A. Lanin I. Fedik

Thermal Stress Resistance of Materials

With 104 Figures

Springer

Professor Dr. Anatoly Lanin
Professor Dr. Ivan Fedik
Scientific Institute of Industrial Association "LUCH"
Zheleznodorozhnaya 24, 142100 Podolsk, Russia
E-mail: lanino5@mail.ru, fedik@sialuch.ru

Library of Congress Control Number: 2007923155

ISBN 978-3-540-71399-9 Springer Berlin Heidelberg New York

Typesetting: Data prepared by the Author and by SPi using a Springer LaTeX macro package
Cover: WMX Design GmbH, Heidelberg

Printed on acid-free paper SPIN 11589501 57/3180/SPI 5 4 3 2 1 0

Preface

In this book, thermal stress resistance of materials is considered comprehensively, in terms of various parameters of thermal loading, defining service conditions of the components of energy generators, machine-building, nuclear power, space technology and products of other industrial fields.

All aspects of thermal stress resistance (including experimental methods of measuring thermal stress resistance, designs for estimation of the thermal and residual stresses), regularity of change of thermal stress resistance and fractures (depending on loading requirements) and the structural conditions of materials (including monocrystals) are all reviewed, together with their complex relationships. The evolution of theoretical concepts about thermal stress resistance from energy as well as about statistical positions and principles of fracture mechanics are analysed. The behaviour of high-temperature materials (carbides, nitrides and oxides) is preferentially surveyed in the temperature range of an elastic–brittle fracture.

Special attention is given to an examination of the influence of thermal loading modes on fracture conditions and the development of thermal stress resistance criteria, both of which are helpful in estimating the bearing capacity of a body in non-uniform and local fields of thermal stresses and at a cumulative thermal-force action. Possible technological expedients and methods for increasing the thermal stress resistance of materials are discussed.

Most part of the data given in this book represents the results of experiments conducted from 1965 to the present time by researchers at LUCH, the scientific research institute of the Agency of the Russian Federation on Atomic Energy.

Podolsk,
January 2008

Anatoly Lanin,
Ivan Fedik

Contents

Symbols IX

1 Introduction 1

2 Evolution of Theoretical Concepts of Thermal Stress Resistance 5

3 Design Estimates of Temperature Fields and Strain Condition of Bodies 13
3.1 Plane Problem of Thermal Elasticity for Bodies with a Volumetric Heat Generation 18
3.2 Effect of Temperature Dependence of Physical–Mechanical Properties on Calculation of Thermal–Elastic Stresses 20
3.3 Thermal–Elastic Stresses in a Finite Hollow Cylinder 24
3.4 Temperature Stresses at Inelastic State of a Body 25
3.5 The Thermal–Elastic Stresses at Local Radiation Loading of a Body 30
3.6 Calculation of Thermal Stresses in the Cylindrical Body Cooled on Lateral Surface in Water 36

4 Methods of Testing for Thermal Stress Resistance 39
4.1 Basic Methods of Testing for Thermal Stress Resistance 40
4.2 Methods of Testing for Thermal Stress Resistance Under Cooling Conditions 41
4.3 Heating Methods of Testing for Thermal Stress Resistance 47

5 Mechanism of Crack Propagation in Non-Uniform Fields of Thermal Stresses 67
5.1 Limit Equilibrium of Edge and Central Cracks in the Thermal-Loaded Disk 67

5.2 Interaction of Growing Cracks and Redistribution of Stresses in the Disk 70
5.3 Energy Fracture Model of Thermal-Heated Bodies 78

6 Influence of Thermal Loading Modes on Fracture 85
6.1 Fracture of Cylindrical Bodies Heated on a Lateral Surface in Liquid Media 85
6.2 Fracture of Cylindrical Body Thermally Loaded on an End Surface 89
6.3 Local Thermal Loading of a Surface Body 90
6.4 Influence of Residual Stresses on Fracture at Thermal Loading 98
6.5 Fracture of Elastic–Brittle Bodies at Combined Thermal and Mechanical Loadings 107
6.6 Influence of Temperature on Thermal Stress Resistance 111
6.7 Fracture of a Body at Cyclic Thermal Loading 115

7 Effect of Structural Parameters on Thermal Stress Resistance 121
7.1 Thermal Stress Resistance of Mono-phase Ceramic Materials . . 121
7.2 Thermal Stress Resistance of Heterogeneous Ceramic Materials 127
7.3 Thermal Stress Resistance of Composites with Fissured Structure 139
7.4 Thermal Stress Resistance of Functionally Graded Materials . . 145
7.5 Thermal Stress Resistance of Anisotropic Bodies 155

8 Elastic–Plastic Deformation Under Local Heating 171

9 Criteria of Thermal Stress Resistance of Materials 179
9.1 Criteria of Comparative Estimation of Thermal Resistibility of Materials 179
9.2 Criterion of an Estimation of Bearing Capacity of Thermally Loaded Body 182

10 Ways of Increasing Thermal Stress Resistance of Ceramic Materials 189

A The General Data on Properties of Constructional Materials 203
A.1 Structural Condition of Materials 203
A.2 Fracture Toughness 206
A.3 Dependences of Strength Change 210
A.4 Creep and Rupture Life 218

References 223

Index 237

Symbols

L	Length, thickness of a sample (mm)
D	Sample diameter (mm)
r	Current radius (mm)
ρ	Dimensionless current radius
m	Index of homogeneity of a material on Weibull
V	Volume (m^3)
T	Absolute temperature (K)
T_{ml}	Melting temperature (K)
T_m	Average integrated temperature (K)
ΔT_m	Average integrated temperature difference (K)
ΔT	Temperature difference (K)
ΔT_f	Fracture temperature difference (K)
Θ	Dimensionless temperature
t	Time (s)
Q	activation energy (J mol^{-1})
q	thermal stream (W m^{-2})
R	(with a coefficient or without it) – criterion of the thermal stress resistance
U	energy (J)
γ	effective surface energy (J m^{-2})
α	coefficient of linear expansion (K^{-1})
Y	volumetric mass, apparent density (g cm^{-3})
ε	relative deformation
ε_c	creep rate
η	coefficient of viscosity (Pa s)
λ	thermal conductivity (W mK^{-1})
a	factor of thermal diffusivity (m^2 s^{-1})
c	thermal capacity (J mol^{-1} K)
E	elastic modulus (MPa)
μ	Poisson's ratio
ν	coefficient of transverse creep flow
$\sigma_t, \sigma_b, \sigma_c$	tensile, bending, compression strength (MPa)

σ_{t}	ultimate strength at thermal loading (MPa)
h	coefficient of heat transfer (W m^{-2} K^{-1})
$Bio = hl/\lambda$	
$Fo = a\tau/l^2$	criterion Fourier
K_1	factor of stress intensity
$K_{1\mathrm{c}}$	fracture toughness (MPa $\mathrm{m}^{-1/2}$)
G	energy for crack spreading

1

Introduction

Refractory metals and compounds, and composites based on them, are widely used in fuel elements and construction of the high-temperature zone of atomic reactors [1, 2], nuclear rocket engines [3, 4] nuclear thermal-emission transformers [5], and in the developed products of military technology [6], designed to operate at high temperature and powerful heat fluxes. Components of the outer skin of space vehicles on entrance into the air atmosphere of the Earth at high speeds undergo strong aerodynamic heating accompanied by the appearance of force and thermal stresses [7].

The desire of designers to increase the specific powers and overall performance of gas-turbine engines due to the increase of temperature parameters encounters the challenge of thermal resistance maintenance of newly developed composites in components such as the rotors of a gas turbine, turbocharger, cams of countershafts, valves, fitting pipes of an exhaust system, etc. [8]. Similar problems of thermal resistance originate in various kinds of heat-exchange apparatus [9]. Use of composite ceramic materials allows operation of heat exchangers at increased temperature up to 1,700 K under exposure of products of fuel combustion with a high content of sulphur, and also under erosive action of the solids contained in products of combustion.[1]

Thermal stresses of a cyclical kind arise in the manufacturing and operation of integrated electronic circuits [10]. Increasing the thermal stress resistance of metal-working materials has crucial importance for prolongation of the service life of cutting tools [11]. Mean temperature on an interface metal–ceramic tool during cutting reaches 1,400 K, according to estimations.

The problem of creation of highly effective elements of a force optics used in high-power laser complexes of continuous or pulse action with energy in an impulse up to 10 kJ becomes more difficult as absorption of even a small

[1] Thermal and corrosion durability of lining ceramic materials traditionally used in blast furnaces and steel melting furnaces significantly depended on the structure and service conditions: temperature, medium and velocity of heating–cooling is observed explicitly in a special reference media [386].

part of the laser radiation by the surface of the optical elements is capable of causing thermal stresses and deformation of a reflecting surface [12].

This incomplete list of the many fields of use convinces of the urgency of the problem of maintenance of an appropriate thermal stress resistance of high-temperature structural materials. The term 'structural materials' incorporates, first of all, a wide spectrum of the ceramic materials prepared by powder metallurgy [13, Application]. The general scheme of production engineering of powder metallurgy includes: a synthesis of powders of the given chemical, phase and grain-size composites, formation of mouldings blanks and high-temperature consolidation. The arsenal of consolidation methods is rather extensive and includes the usual moulding, rolling, extrusion forming, also isostatic moulding, hot moulding, explosion processing and sintering as various alternatives. Such abundance of technological expedients in combination with a variety of regimes allows making materials and products with a sufficient diversity of porosity, parameters of micro- and macro-structures, contents of impurities and flaws of a crystalline structure, and amount of inlet additives. It makes production engineering of powder metallurgy rather universal and forces one to consider the technological parameters of preparation of the properties definition of ceramic materials and to view its structural features carefully.

High-temperature structural materials are based on non-metallic, high-melting point compounds on an oxygen-free basis: carbides, borides, nitrides with melting temperatures of 2,000 K and more, and also oxide systems on the basis of Al_2O_3, SiO_2, MgO, ZrO_2. For such compounds, a mixed ionic–covalent type of inter-atomic chemical bond and high thermodynamic stability is characteristic [14, 15]. These compounds are characterized by high hardness and elastic modulus, chemical stability, refractoriness and a high degree of brittleness caused by features of inter-atomic bonds, and low dislocation mobility (see application A.1). A series of high-melting point compounds, Al_2O_3, ZrO_2, Y_2O_3, possess polymorphic structural transmutations for which the presence of a major thermal hysteresis is characteristic. Transmutation of monoclinic modification $(ZrO_2)_m$ in tetragonal $(ZrO_2)_T$ at heating occurs in the interval temperatures 1,280–1,570 K, and at cooling 1,300–970 K. Borides, nitrides, carbides, hydrides and some oxides featured by the simple formula of type Mx, Mx_2, possess homogeneity areas with a variable relation of metal to non-metal. The diversion from a stoichiometric composite affects occurrence of structural vacancies, ions of other valence, change of overlapping and screen of valence bonds. Compounds with different stoichiometry naturally possess various strength and physical performances. Unlike traditionally used metals, metallic compounds are rather brittle and sensitive to structural defects, but possess high refractoriness that justifies their use in high-temperature technology. Nevertheless, lack of opportunity for plastic deformation in a wide enough temperature range makes them rather vulnerable to originating thermal stresses. High-melting point BCL metals and alloys on the basis of molybdenum, wolfram and chromes widely used in high-temperature nuclear

reactors [16], at certain parameters of loading also appear not plastic enough and subject to thermal fatigue fracture. These conditions require a careful estimation of the thermal stress resistance at construction and maintenance of products from ceramic and refractory materials.

The causes of the thermal stresses are the temperature gradients originating in a body at sharp heating or cooling, and also the non-equilibrium physicochemical processes occurring in a body at its manufacture or during use. Non-uniform drying of gels and aluminous inter-mixtures with non-uniform strain on thickness of a body, or pyrolysis of polymer substances with change of concentration of chemical components, results in the occurrence of elastic stress fields and the subsequent cracking and fissuring. This in turn changes the kinetics of the diffusive process owing to more light transport of gas on the formed flaws in the depth of a body.

Deposition of coats by chemical or physical expedients, in conditions far from thermodynamic equilibrium, causes, as a rule, significant shrinkage strains and the stresses, resulting in fracture. Great stresses and an opportunity for cracking occur in structural constructions at cooling of the concrete mixture.

Thermal stress resistance, as a strength, is not a constant of a material and depends on several factors: the stressed state, loading velocity, size of a body, temperature and environment. Mechanical strength at a force loading has much in common with thermal stress resistance. In both cases, it is expedient to distinguish loading between transient, long-term, and repeated modes. The strains terminating in fracture of a body can be elastic, elasto-viscous or elasto-plastic. At the same time there are essential differences between strength and thermal stress resistance:

- Propagation of flaws in a thermally loaded body always occurs in inhomogeneous fields of the stresses necessarily containing zones of tensile and compressive stresses.
- The thermal stresses set by strain are capable of relaxing promptly in comparison with the force loading, for example with suspended load.
- At a cyclic loading of a body with heterogeneous structure, local stresses originate not only due to an elastic anisotropy, but also due to the anisotropy of thermal expansion of various structural components of a body.

The thermal stress resistance, as well as the strength, changes essentially with temperature and velocity of loading [14–17]. With the evolution of microplasticity and then macro-plasticity at temperatures of 0.3–0.5 of the melting temperature (T_{ml}), the thermal stress resistance increases by a greater degree when the velocity of the loading is lowered [18]. It is necessary to consider a creep flow and a stress relaxation under these conditions [16, 17] and an origination of the residual stresses capable of causing fracture after cooling of the body. In some cases it is necessary to consider also environmental effects on the thermal stress resistance, even at moderate temperatures.

Regularity of the strength and fracture at thermal loading are studied to a much lesser degree than at force stresses, though many studies carried out in the last few decades, deepening the notion of thermal stress resistance, have been published in the proceedings of international conferences [19–24], in a number of monographs [15–18, 25–28], in surveys [29–31] and dispersed in journal articles. This last circumstance has induced us to review various aspects of thermal stress resistance in a single publication. Solving the problems of thermal stress resistance becomes more and more important in view of the extreme states of materials and constructions now coming to the foreground.

2

Evolution of Theoretical Concepts of Thermal Stress Resistance

Winkelman and Shott, who published on thermal stress resistance in 1894, brought the characteristics of thermal stress resistance into criterial form, as the ratio of a material's strength to the value of the thermal stress. This ratio was marked by the first character, R, of the English word 'Resistance'. In the first half of the twentieth century, J.N. Goodier, B.A. Boley, V.D. Kindjery and A.V. Lykov established the basic relations of temperature origin of patterns and thermal stresses, in different bodies on coordinate, time and other parameters. It has been demonstrated in early experimental works [25, 26, 32, 33], that fracture of brittle materials at thermal loading depends on a tension defined by conditions of external thermal effect, size and shape of the body.

The majority of existing theories represent fracture as the instantaneous act occurring after reaching by thermal stresses of the ultimate strength in any point of a body [25, 26], or the critical coefficient of stress intensity, introduced by Irvin in 1957 [34] and subsequently used widely in following works [35]. G.S. Pisarenko of the Ukraine Institute of Strength Problems with colleagues suggested in 1963 [26] to use alongside the R criteria for a simple body, the so-called 'regime factor' Q, describing the shape, size and thermal operating mode of a product. Having estimated the value of Q on the simplified samples, at modes close to operational, it is possible to judge roughly the quantity Q for objects or components of complex configuration. Evaluation Q for the nozzle end of turbine blades was made using analogy parameters Bio, Kn which included some physical quantities describing a material. Criteria of the thermal stress resistance R of complex products were defined from a relation of experimentally measured peak fracture difference of temperatures ΔT, between the medium and the surface of a body, and regime factor Q: $R_{\mathrm{e}} = \Delta T/Q$.

Scientists of the Institute of Physical-Technical problems in Lithuania in the 1970s [16] performed calculations of regime factors of prismatic bodies at various thermal loading modes on the basis of which, for the first time anywhere in the world, a practical method for quantitative assessment of thermal stress resistance of bricks was devised.

Manson [36] in 1955, and in consequence a series of other researchers [17, 26], considered that, in conformity with statistical concepts of strength, the fracture of thermally loaded body should be defined by its maximum loaded field.

It was supposed that fracture of a body becomes instantaneous in that moment when tension stress reaches critical value on an individual micro-crack in any elemental volume of the body. The probability of brittle fracture was defined only by normal tension stresses and did not depend on compression or shear stresses. It was theoretically proved that the stress gradient does not influence the mean fracture limit.

Computational statistical estimates of strength at pure bending, tension, torsion and bending by concentrated force, have shown qualitative conformity with experiments on SiC samples [26]. Strength value under tension has appeared below the strength under bending and torsion, however the quantitative conformity was not observed in all loading modes.

The degree of damage defined by the particular critical number of micro-cracks per unit volume of material, V, was taken as a measure of the material's transition into limiting state [37]. The assumption is made that volume V is characterized by some medial stress and consists of some small enough volumes V_i with non-uniform structure and its stress state is determined by the normal law of distribution.

The limiting stress corresponding to a macroscopic fracture at any complex stress is determined according to the concept [37] of a stationary value of a material which is calculated on results of strength tests at any two elementary modes of stressing, for example, at tension and compression. Though the theory gives the basic capability to estimate strength at the non-homogeneous triaxial stresses, engineering calculations for these cases of loading, have not been conducted owing to their complexity.

The formulas represented in [38] are more convenient for engineering strength estimates at the complex homogeneous and non-uniform stress states. It is accepted that only tension stresses are responsible for brittle fracture and, unlike Weibull's theory, all stress components σ_1, σ_2, σ_3, operating in the body of volume V are considered. Despite the reliability of estimates of strength gained at some views of complex loading, the use of calculated formulas offered [39] with reference to the thermal stress state of bodies with extensive fields of compression is not obviously possible, when the flaws initially formed in a body are arrested, not leaving detectable flaws on the surface.

Thus, existing statistical theories, correctly estimating dispersion of values of thermal stress resistance (for more detail see application A.3), do not allow us to use them for an estimate of strength and the thermal stress resistance in any complex and non-homogeneous complex stress.

Observations of fracture of thermally loaded bodies, using the energy concept of fracture mechanics, have allowed us to recognize the existence of non-equilibrium and equilibrium stages of crack growth. The theoretical concept of fracture offered in 1963 by Hasselman [40] allowed formulation of a close linkage between the start of thermal fracture and the residual strength of a

body. The energy model offered later, in 1969 [41], represented fracture as the kinetic process incorporating the stage of unstable crack growth and the stage of its equilibrium spreading, demanding the continuous increase of thermal loading. This model, reflecting facts of not-one-stage fracture established already by experiments on bodies under thermal load, undoubtedly rendered possible progress on development of the theory of thermal stress resistance.

However, Hasselman's model was based on the assumption, not confirmed experimentally, of simultaneous unstable spreading of many cracks without considering the influence of complexity of stress and size finiteness of a body, and could not explain naturally all the observable variety of thermal fracture. Hundreds of different researchers viewed the thermal fracture on the basis of energy principles in the subsequent years. Scientists of the Institute of Physical-Technical problems in Lithuania, in development of these principles in 1968 [16], introduced the criterial parameter M controlling complete or partial fracture of the solid and hollow disks. These parameters were used successfully for an estimation of the fracture character of ceramics with fissured structure.

Energy models developed in the late 1980s [42, 43] proved experimentally and also theoretically the opportunity of occurrence of a hierarchical structure of cracks at the quenching of heated bodies. According to these models, the free energy of thermal-loaded body W is defined by the sum of strain energy W_{g} and the crack surface energy W_{m}. If the material is characterized by a constant specific crack surface energy γ, the crack surface energy $W_{\mathrm{m}} = \gamma 2a$ is a linear function of the crack length a. As the compliance of a body decreases with increase of crack length, strain energy W_{g} will diminish with crack growth.

Thus, the free energy of system W for thermal loading exhibits a maximum at crack length a_i (Fig. 2.1a). According to Griffith and Irwin [34], crack growth is possible if W decreases with increasing crack length, i.e. under condition $\delta W/a \leq 0$. Considering, that $W/\delta a = K^2/E$ and $K_{\mathrm{c}} = (2E\gamma)^{1/2}$, then $K \geq K_{\mathrm{c}} \rightarrow \delta a > 0$. It means that if the stress intensity factor exceeds critical

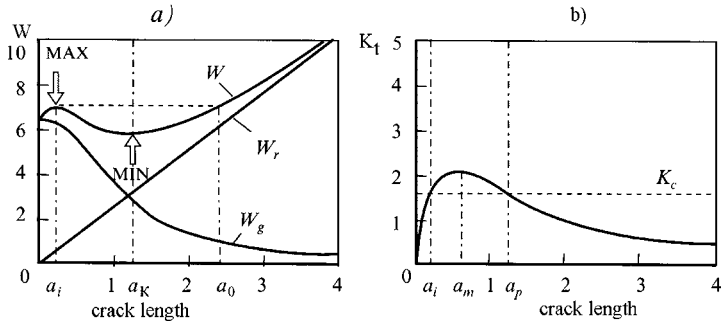

Fig. 2.1. Change of total system energy W, surface energy W_{m} and strain energy W_{g} under thermal loading (in the relative unities) (**a**) and coefficient of stress intensity vs. crack length (**b**) [44]

value of the fracture toughness K_c the crack is capable of propagating. This K–a curve, having a typical maximum at a_m, is presented in Fig. 2.1b. Under thermal loading with strain control, the driving force for crack growth relaxes during crack propagation, and the crack may be arrested. Requirements for the crack arrest correspond to two extreme cases. If the released elastic energy of an unstable propagating crack is instantaneously carried away and dissipated elsewhere, the crack stops immediately, as soon as $K_a < K_c - W/a > 0$ and $\delta a = 0$. If the energy of the body is spent for the crack surface energy, the end length of the crack becomes equal to a_p.

As thermal impact is a transitional process, a time dependence should be taken into consideration. Crack propagation starts as soon as the energy release rate $G = \delta W/\delta a = K^2/E$ on any existing crack surpasses a critical value G_c, and continues extending while this condition is maintained (Fig. 2.2).

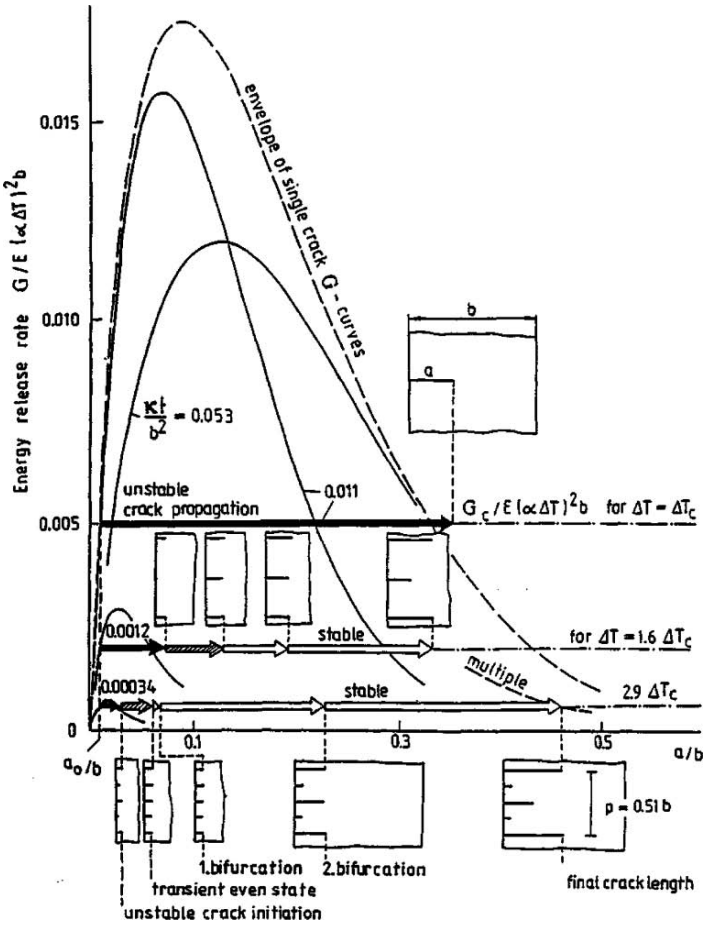

Fig. 2.2. Time-temperature process of spreading cracks for three arbitrarily chosen values of ΔT [43]

For instance, the greatest of existing cracks a_o at certain difference $\Delta T = 1.6\Delta T_c$ starts to propagate when G reaches G_c at normalized time $F_o = \lambda t/b^2 = 0.0012$, where b is the width of a specimen. If it occurs on the upwards slope of the curve, the energy release increases with crack propagation which specifies unstable propagation (black arrow). The moving crack, in the opinion of the authors, owing to dynamic effects, can be driven to where its static G is below G_c. Then the crack stops for a moment until G reaches G_c again. For the propagation of finer initial cracks, G reaches the critical value G_c a little bit later after the start of the greatest existing crack.

Cracks start independently of each other, provided that they are not too close to the initial crack, owing to an unloading of the body in the neighbourhood of the crack. The consecutive cracking is observed in experiments during cooling of glass plates in a water bath after preheating up to various temperatures [43]. The subsequent cracks with increase ΔT appear between growing cracks if the latter are widely spaced. A retardation of cracks (or stability conditions of crack front) has been calculated by a gradient method on the edge of the half plane [43]. In the process of advancing the front of stresses deep into the body, the part of cracks is stopped, so the quantity of moving cracks decreases with growth of their length.

The observed phenomena of formation of stresses and fracture are characterized by certain overall attributes:

- Multiplicity of formed cracks
- Opportunity of transition from unstable crack propagation to stationary one
- Self-organizing process of formation of crack system

These models, correctly reflecting an overall pattern of fracture of a body cooled on a surface, remain appreciably qualitative for other modes of thermal loading as they neglect an aspect of a triaxial stress and, most importantly, the physical differences of crack propagation in fields of tensile and compression stresses.

The computation in the 1990s of a finite element method [45, 46] and weighting functions [47, 48] of zones of a phase change on the tip of a crack in ceramic material undergoing phase changes, became defining for fathoming the process of a fracture toughness raise and an explanation for empirically building R-curves. Volumetric changes induced by the martensitic transformation, lead to an emersion of tensile stresses on the tip of a crack and compression stresses on the line of the crack. The compression stresses interfere with extension of the crack, and for maintenance of a steady cracking motion, a raise of stress intensity coefficient is necessary due to an increase of an exterior loading.

A.G. Lanin, with colleagues of the Russian scientific research institute LUCH, at the beginning of [49], revealed that the cylindrical samples heated on the lateral surface are entirely fractured on separate parts despite the presence of compression stresses in the peripheral zone. At the same time, the

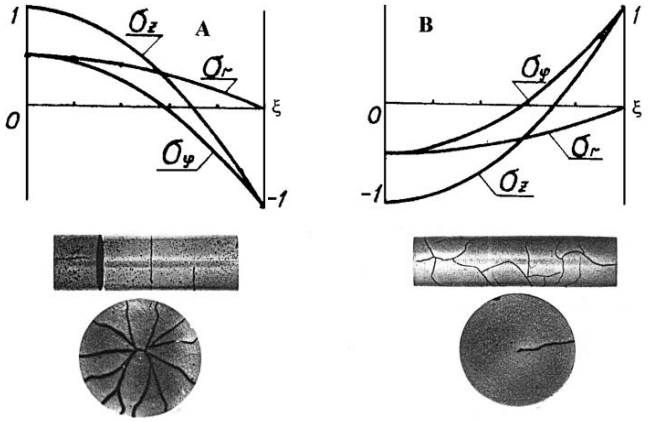

Fig. 2.3. Stress diagram and fracture view at changing of stress state from heating (**a**) to cooling (**b**) of surface of sample [49]

cracks originating on the surface of quench-tested quasi-isotropic polycrystals stop in the compressed central zone; thus complete fragmentation is excluded (Fig. 2.3). Lanin and colleagues introduced a new criteria parameter defining condition of total or partial fracture at the variation of the stress state on the basis of force fracture mechanics. It was established that partial or full fracture of the brittle isotropic bodies is determined by non-uniformity of the stress field characterized by an N parameter which takes into account not only the ratio between the tensile and compression zones, but also distribution of stresses in these zones.

Later, in 1981 [50], they established that the modification of thermal mode in various combinations changes the fracture kinetic. Disintegration of the body under tensile loading takes place as a result of unstable crack propagation after reaching the critical stress intensity coefficient K_{1c}. The crack growth under compression stresses occurs in another fashion. Under thermal loading with rather large zones of compression, the started crack stops in the compression zone, and complete fragmentation may be reached (as in force axial compression) under a load several times higher than the load for starting the crack [51, 52]. (Research results in detail are considered in Chap. 4).

The overall energy store necessary for fracture under compression exceeds many times the level of the stored elastic energy for fracture of the body in a uniform field of tension stress [53]. Fracture of a body under axial compression proceeds with increasing load at certain interaction of growing cracks [53]. The experimental data obtained in testing organic silicate glass, graphite and zirconium carbide show that fracture in compression is of a kinetic nature. Tests were conducted on flat specimens $20 \times 30 \times 4$ mm in size with a central straight initial crack $2L(L = 2-3\,\text{mm})$ in length, positioned at an angle β to the axis of compressive loading at the distance d from each other. A model was developed for the growth and interaction of cracks in brittle solids under compressive

stress state. From the viewpoint of fracture mechanics, this process consists of three conventional stages occurring successively with the increase of compressive load. The first stage is represented by the equilibrium propagation of single cracks which initiate at defects in the material and do not interact with each other. The crack starts at critical stress coefficient depending on initial length and orientation. The crack propagates on the curvilinear trajectory approaching asymptotically the compression axis of loading. The minimum stress σ required for the propagation of the most unfavourably oriented defects (at an angle of 30–45° in relation to the axis of compressive loading) is 2.5–4 times higher than stress σ_t for loading of the initial crack perpendicular to the axis of tensile loading. Subsequent damage accumulation is associated with the development of a system of interacting cracks in which the paired or multiple interactions between the adjacent cracks (the intensity of these interactions continuously increases) may lead to a qualitative change in the nature of their propagation, i.e. from equilibrium to unstable when the relative distance $\lambda = d/2L$ (Fig. 2.4) diminishes to critical value. The final stage of fracture becomes possible at the increased loading after certain multiple interacting cracks, evolved in equilibrium, and increased driving stress intensity with highly unstable crack growth. The load corresponding to fragmentation of the solid material is several times greater than the load at which the first macro-cracks started to develop. Analogous results were achieved later [35, 54, 55].

Data for crack growth under axial compression permit us to explain the fracture peculiarities of samples at thermal loading with large compressive fields. The further evolution of methods of force fracture mechanics by colleagues at LUCH allowed us to view the conditions of crack propagation at

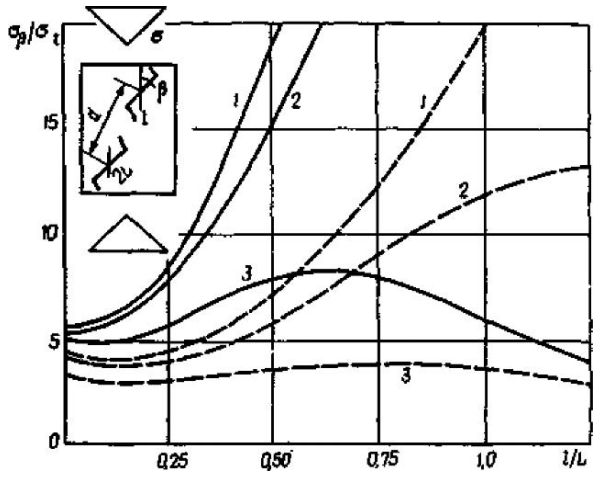

Fig. 2.4. Fracture diagrams for a system of parallel cracks (1) $\lambda = d/2L = \infty$; (2) $\lambda = 3$; (3) $\lambda = 2$ (*solid lines* $\beta = 30°$, broken lines $\beta = 45°$)

cycling compressive loading [56], to examine various kinds of the local thermal fracture [58, 59], to establish the conditions of crack propagation under combined force and thermal loading [60], to consider the thermal fracture of the bodies with residual stresses [61] and to discuss the thermal fracture peculiarities of monocrystal [62].

3

Design Estimates of Temperature Fields and Strain Condition of Bodies

Analytical methods of definition of thermal stresses in bodies are rather informative and are evident enough. The most important advantage of the analytical solution is the opportunity for tracking an effect of physical properties on the character of the solution of a problem. Besides analytical methods, separation of variables, function theories of complex variables, integrated transformations, etc. allow us to compute the value of thermal stresses in any point of a body with beforehand given precision certainly, not above the statistical scatter of initial parameters. As there is an extensive literature on these problems [63–66], description of the mathematical methods is not given here. Unfortunately, analytical problem solving of thermal elasticity is possible to obtain only in extremely rare cases. It refers predominantly to the linear equations of mathematical physics for classical geometrical forms.

Definition of temperature stresses is determined for the majority of practical cases by means of the incoherent quasistatic theory of thermo-elasticity [67]. It is accepted that the deformation of a body does not change the level of its temperature. The disregard of connection of mechanical and thermal energy is quite admissible owing to the insignificance of dynamic effects under the usual non-stationary requirements of heat transfer. It enables us to solve a problem of thermal stresses in two stages: first to solve an equation of heat conductivity, and then, on the discovered allocation of temperatures in a body, to define stress field, as a rule, using the linear equations of the theory of thermo-elasticity.

The quantitative assessment of thermal stress resistance as the same estimation of strength at a force stressing, demands once again definition of the stress and strained state, and then determination of a degree of danger of this state for the bearing capacity of a body. The problem of thermal elasticity in the dimensionless view is reduced to the solution of a boundary-value problem for a heat equation with set initial and boundary conditions. Calculations of temperature patterns by analytical methods are stated in a number of monographs [67–69].

For a prompt and convenient determination of numerical values of temperature and a temperature gradient in solid bodies of the various geometrical forms at various boundary conditions, it is reasonable to use ready design diagrams [70]. All calculations are conducted with use of a so-called principle of the elemental superposition when in all cases boundary conditions, interior sources and thermal–physical characteristics do not depend on the body temperature. Diagrams are given for a plate, a ball, a hollow or continuous cylinder at boundary conditions (BC):

- I mode, if the temperature of a surface of a body is known
- II mode, if the intensity of thermal flow is set
- III mode, if the temperature of the medium which is flowing about a body and the law of heat transfer between the medium and the surface of a body is given
- IV mode originates when the viewed body is in touch with another body having other thermal–physical characteristics

Conditions of heat transfer of a body with exterior temperature sources are characterized by criterion Bi which is equal to lh/λ (where l is 1/2 thickness of a body; h is coefficient of a heat transfer, λ is the thermal conductivity of material). If the quantity Bio is rather high, $Bio \geq 50$, it is possible to neglect temperature resistance of a boundary layer and to accept temperature of the surface of a body equal to temperature of the medium, that is, instead of BC of III mode, to accept the simpler BC of I mode. If values of Bio are rather small, $10 > Bio \geq 0.2$, it means that temperature resistance (thickness) of a boundary layer is relative large and that most of the temperature difference is concentrated at the boundary of the body. A temperature drop inside a body is rather small. As a result the problem of temperature calculation is reduced to definition of the surface temperature.

Heat transfer by radiation is proportional to a difference of the fourth degree of temperatures of a heat source and a surface of a body, i.e. dependence is non-linear. However, if the difference between the source temperature and the surface of a body is large, the solution of a temperature problem is possible to reduce to BC II mode. The temperature pattern of a body can be computed with use of BC I mode if the course of a surface temperature at a radiation heating (or cooling) is known. All analytical solutions are made for an infinitely long cylinder; for a plate, restricted on thickness with length and breadth extended to infinity; a half restricted body is considered as the infinite body restricted only in one direction on one coordinate, and only a sphere has restricted sizes.

Except for the specified BC, the assignment for surfaces of a body of simultaneous boundary conditions of all sorts is also possible: on one part of a surface, temperatures, on other parts, densities of thermal flow or a condition of heat transfer on a Newton's law. Such boundary conditions are termed 'mixed'. There are blended boundary conditions at calculation of temperature in constructions when on one part of a body the condition of a convective

heat transfer is set, and on others thermal flow through a boundary surface is absent.

It is necessary to consider a series of simplifying cases. For example, temperature fields possessing certain symmetry can be featured by functions with one or two independent variables. Reduction of dimensionality of problems essentially facilitates calculations of temperature patterns. Solutions for plates and a half-restricted body completely apply to problems with rods of restricted length if they have a good heat insulation of a lateral surface. The procedure of calculations for flat plates, rectilinear cylinders and rods can be spread to curved plates, cylinders and rods, when their curvature is not too large, namely, that the ratio of thickness of a plate (diameter of a cylinder, thickness of a rod) to the radius of curvature of its surface (an axis of a cylinder or a rod) would be no more than 0.1.

An additional effect of face surfaces can be neglected for a plate with restricted length and breadth or a cylinder with restricted length if the subjected points of calculation are far from the boundary, not less than to 4–5 sizes of radius of the cylinder.

Thermal–elastic stress can be easily determined at known temperature patterns from combined equations of stress and strains with consideration of thermal deformation. Dependences between shear stresses and strains, and also the static and geometrical equations are accepted without modifications on the theory of elasticity [71].

On a calculated mean integrated temperature difference, $\Delta T_{\mathrm{m}} = (T_{\mathrm{m}} - T)$, at the moment of fracture (where T_{m} is mean integrated temperature of a body in cross-section and T is surface or centre point temperature), assuming that properties of a material do not vary and material is elastic, thermal stresses σ are defined by the following relationship:

$$\sigma = E\alpha\Delta T_{\mathrm{m}} K_{\Phi}/(1-\mu), \tag{3.1}$$

Where α is a coefficient of thermal expansion, E is a modulus elasticity, μ is Poisson's ratio, K_{f} is form factor. Derived from the relationship (3.1) at value $K_{\mathrm{f}} = 1$, the complex $\sigma(1-\mu)/Ea = \Delta T_{\mathrm{m}}$ is accepted to name the first criterion of thermal stress resistance R measured in degrees.

Thermal stress resistance is measured as a rule on specimens of a simple shape (disk or cylinder), easily manufactured by powder metallurgy methods. The fields of the thermal–elastic stresses can be obtained by substituting the entries ΔT_{m} in expression (3.1) for the following practical cases:

- The instantaneous change of a surface temperature
- The linear modification of a surface temperature
- A constant thermal flow
- Constant temperature of the heater
- A single-sided or two-sided heating or cooling of the hollow cylinder

Ready numerical value of temperature fields and stresses, on the given properties of materials, are easily defined in existing publications, for example in reference [72].

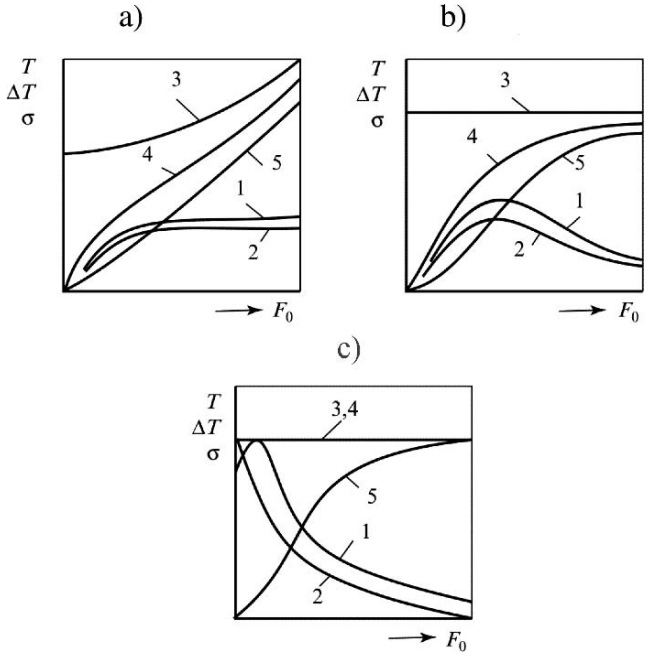

Fig. 3.1. Character of a modification of temperature stresses (1), difference of temperature (2), temperatures of medium (3), temperatures of surface (4) and *centre* (5) for an infinite cylinder which is heated up at boundary conditions of heat transfer $q = \text{const}$. (**a**), h (coefficient of a convective heat transfer) = const. (**b**) and $h \to \infty$ (**c**), $F_o = at/R2$

The maximum thermal stresses originate in all cases of a non-steady cooling or heating after a certain time (Fig. 3.1a,b) the smaller is the more intensive coefficient of heat transfer (h). The surface temperature T_s accepts temperature of medium T_m instantaneously only in an extreme case when intensity of heat transfer is infinitely great $Bio = hl/\lambda = \infty$ (boundary conditions of the first mode) (Fig. 3.1c).

Mean integrated temperature difference ΔT becomes equal to a difference of initial temperature of a body T_0 and the temperature of the medium. The stresses on a surface of a cooled body accept the maximum values in an initial instant. The maximum mean integrated temperature difference and the maximum thermal stresses are less at all finite values than Bio is in an extreme case ($Bio = \infty$). Their values depend, at constant properties of a material, on some function f (Bio), describing temperature pattern and varying within the limits from 0 up to 1.

Analytical methods allow obtaining solutions for a plane stress state of a rod body when, according to the principle of Saint–Venant, all cross-sections of a long body are equivalent, except end sections on which local perturbed stresses diminish rapidly enough. The plane stress state is characteristic of a

body when the characteristic cross-sectional dimension of a body considerably exceeds its size in the longitudinal direction (for example, a thin plate) and in this case when axial stress is absent.

The solution of many non-linear problems of thermal stress states and bearing capacities of a body in serviceable conditions related:

- With variables of thermal–physical and (or) mechanical properties vs. temperature
- With variable and complex dependences of heat transfer on the surface of a body
- With nonuniform distribution of a volumetric or local surface heat sources
- With complex geometry of simply and multiply-connected bodies

becomes possible to resolve only by numerical methods.

Numerical solutions fathom those effects which are gained after the approximate replacement of an initial equation or a field of an existence of a solution. For example, partial derivative note through a finite differences. The main advantage of these methods consists in that they allow the solution of a problem in any case (for example, when the analytical solution is not known).

A differential equilibrium and consistency of equations ensures relationships between stresses and strains in points infinitesimally close to each other. If these equations are solvable, the solution, naturally, gives precise values of magnitudes. In most cases, however, it is impossible to gain the exact solution, therefore it is necessary to resort to a rough method.

Finite element method (FEM) and method of boundary integral equations (BIE) have been widely accepted for solving problems of thermal elasticity [66, 69]. These methods are well mastered, and there are numerous programmes for the analysis of thermal stress states of particular components or construction elements. On the basis of FEM laid variation principles. They are related to the concept of a functional scale which depends on a variation of a function or several functions. The field of the solution of a matching problem of thermal elasticity is divided into small but finite elements. An approximation of functions is spent in each small element. These functions depend linearly on coordinates inside of a finite element. Unknown parameters of approximation express through displacement of a node of a grid in the matrix shape. Finally systems of the linear algebraic equations are received. Each equation includes in an explicit aspect only a part of unknown parameters. Thus, the solution of an initial problem of thermal elasticity is reduced to the solution of a system of linear algebraic equations. Finite elements at the division of the field can have diversified shapes (for example, elements of spherical and cylindrical shells, plates, rods, etc.). Difficulties in using FEM originate at a definition of the thermal stress states in a neighbourhood of interior cavities, micro-cracks and other stress concentrators. These difficulties are partially avoided due to the application of another numerical method, BIE. Its basic difference from FEM is the use of boundary-element approximation. It reduces the volume of scaling essentially as there is a division into elements, not all the area but only

its boundary lines. The important advantage of BIE is scaling of the required function in the arbitrary point of the interior field, and not just in nodes of a grid (as, for example, in FEM). BIE is especially effective for the solution of external problems when the boundary line extends to infinity. Naturally, BIE with all its advantages does not replace but supplements FEM. Therefore the sharing of these two numerical methods with the advantages of each allows an approach to the solution of the task in view from different sides.

As the majority of practically important problems are solved only approximately, the solutions can be obtained by various methods or their combinations which will be observed in the analysis of experimental data of the thermal stress resistance in the sections below.

3.1 Plane Problem of Thermal Elasticity for Bodies with a Volumetric Heat Generation

There are significant gradients of temperatures causing emersion of thermal stresses in the constructive elements of nuclear reactors due to interior volumetric heat generation. The definition of thermal stress is essentially facilitated if the cross section of a fuel element represents a singly connected domain and is restricted by curves of the second order (circle, ellipse). In this case the stress function F (so-called function of Erie) satisfies the non-uniform biharmonic equation

$$\Delta\Delta F = -\frac{\alpha E}{1-v}\Delta T = \frac{\alpha E q_V}{(1-v)\lambda},$$

where

$$\Delta T = -\frac{q_{\mathrm{v}}}{\lambda}, \quad \Delta\Delta = \left(\frac{\partial^2}{\partial x^2} + \frac{\partial^2}{\partial y^2}\right) * \left(\frac{\partial^2}{\partial x^2} + \frac{\partial^2}{\partial y^2}\right), \tag{3.2}$$

and the sign (*) means operational multiplication.

Thermal–elastic stresses are computed by differentiation of stress function F. Stress components in the cartesian axes appear as:

$$\sigma_{xx} = \frac{\partial^2 F}{\partial y^2}; \quad \sigma_{yy} = \frac{\partial^2 F}{\partial x^2}; \quad \sigma_{xy} = -\frac{\partial^2 F}{\partial x \partial y}. \tag{3.3}$$

Thermal stresses in a continuous cylindrical fuel element in radius R with the power of an interior heat generation q_{v} in polar coordinates

$$\left(\frac{\partial^2}{\partial r^2} + \frac{1}{r}\frac{\partial}{\partial r}\right) * \left(\frac{\partial^2}{\partial r^2} + \frac{1}{r}\frac{\partial}{\partial r}\right) F = \frac{\alpha E q_V}{(1-v)\lambda}.$$

Fulfilling operational multiplication, we gain

$$\frac{\partial^4 F}{\partial r^4} + \frac{2}{r}\frac{\partial^3 F}{\partial r^3} - \frac{1}{r^2}\frac{\partial^2 F}{\partial r^2} + \frac{1}{r^3}\frac{\partial F}{\partial r} = \frac{\alpha E q_V}{(1-v)\lambda}. \tag{3.4}$$

Stresses in polar axes are computed in the usual way

$$\sigma_{rr} = \frac{1}{r}\frac{\partial F}{\partial r}; \quad \sigma_{\varphi\varphi} = \frac{\partial^2 F}{\partial r^2}; \quad \sigma_{r\varphi} = \sigma_{\varphi r} = 0.$$

Having noted $F = A(r^2/R^2 - 1)^2$ and having substituted F in (3.4), after simple transformations we define a stress function:

$$F = \frac{\alpha E q_V R^4}{64(1-v)\lambda}\left(\frac{r^2}{R^2} - 1\right). \tag{3.5}$$

This function satisfies the non-uniform biharmonic equation, and boundary conditions on an exterior contour, and consequently is the single solution of the formulated problem. A definition of thermal stresses does not cause difficulties now.

$$\sigma_{rr} = \frac{1}{r}\frac{\partial F}{\partial r} = \frac{\alpha E q_V R^2}{16\lambda(1-v)}\left(\frac{r^2}{R^2} - 1\right),$$

$$\sigma_{\varphi\varphi} = \frac{\partial^2 F}{\partial r^2} = \frac{\alpha E q_V R^2}{16\lambda(1-v)}\left(3\frac{r^2}{R^2} - 1\right). \tag{3.6}$$

If the face surfaces of a cylindrical fuel element are free, the axial stress σ_{zz} looks like:

$$\sigma_{zz} = \sigma_{rr} + \sigma_{\varphi\varphi} = \frac{\alpha E q_V R^2}{4\lambda(1-v)}\left(\frac{r^2}{R^2} - \frac{1}{2}\right). \tag{3.7}$$

The attractiveness of the gained relationships is doubtless. They show that definition of the stationary thermal stresses is carried out without the solution of a problem of thermal conductivity. The level of originating thermal stresses depends on properties of a material ($\sigma E/\lambda$), geometries of a fuel element (R) and parameter of maintenance (q_v). From here the unsurpassed virtue of analytical methods has clearly tracked the possibilities of guidance for thermal stress state elements in nuclear engineering.

The exact analytical solution of a stationary problem of thermal elasticity is also possible for a fuel-rod element with an elliptical cross section. Stress function F is, from the solution of the non-uniform biharmonic equation in the cartesian axes:

$$\Delta\Delta F = \frac{\partial^4 F}{\partial x^4} + 2\frac{\partial^4 F}{\partial x^2 \partial y^2} + \frac{\partial^4 F}{\partial y^2} = \frac{\alpha E q_V}{(1-v)\lambda}. \tag{3.8}$$

Stresses in a fuel element are defined through function F, according to relationships (3.3). The solution of (3.8) can be sought in the form of

$$F = A\left(\frac{x^2}{a^2} + \frac{y^2}{b^2} - 1\right)^2, \tag{3.9}$$

where A is a constant; and a and b are semi-axes of an ellipse. After substitution of (3.26) to (3.25) (see below) we discover a stress function

$$F = \frac{\alpha E q_V}{\lambda(1-v)\left(3\frac{a^4+b^4}{a^2b^2}+2\right)}\frac{a^2b^2}{8}\left(\frac{x^2}{a^2}+\frac{y^2}{b^2}-1\right)^2. \tag{3.10}$$

At $a = b = R$ expression (3.27) coincides with a stress function for a cylindrical fuel element (a relationship as in 3.22). Thermal stress for the free face cross sections is defined, bypassing the solution of the problem of thermal conductivity:

$$\begin{aligned}
\sigma_{xx} &= \frac{4A}{b^2}\left(\frac{x^2}{a^2}+\frac{3y^2}{b^2}-1\right);\\
\sigma_{yy} &= \frac{4A}{a^2}\left(\frac{3x^2}{a^2}+\frac{y^2}{b^2}-1\right);\\
\sigma_{xy} &= -\frac{8Axy}{a^2b^2};\quad \sigma_{22} = \sigma_{xx}+\sigma_{yy},
\end{aligned} \tag{3.11}$$

where

$$A = \frac{\alpha E q_V}{\lambda(1-v)\left(3\frac{a^4+b^4}{a^2b^2}+2\right)}\frac{a^2b^2}{8}.$$

A special case of expressions (3.11) at $a = b = R$ fulfils the conformity principle for thermal stresses in a long cylindrical fuel element. If $a \gg b$ the cross section of a fuel element represents a plate thickness $\delta = 2b$ (certainly, with the certain oncoming). For example, the stress σ_{xx} at $x = 0$ and $y = b$ matches a stress in a plate thickness $2b$ with the power of an interior heat release q_{v}

$$\sigma_{xx} = \frac{\alpha E q_V \delta^2}{12\lambda(1-v)} = \frac{\alpha E q_V b^2}{3\lambda(1-v)}.$$

Thus, due to a modification of the length of the semi-axes of an ellipse it is possible to simulate thermal stresses in fuel elements with different cross sections. If the cross section of a fuel element has an arbitrary shape, derivation of the analytical solution (in the form of formulas, infinite series or integrals) is not obviously possible. In such a case, numerical methods are applied.

3.2 Effect of Temperature Dependence of Physical–Mechanical Properties on Calculation of Thermal–Elastic Stresses

An extensive enough body of literature about the effect of temperature dependences of physical–mechanical properties (α, E, μ) for a field of temperature stresses in bodies of various geometrical shapes is accumulated at the present time. It is possible to obtain the exact solution of thermal–elastic problems in

some cases, for example, for an incompressible material ($\mu = 1/2$) at arbitrary relation α and E vs. temperature, and at $\mu = \text{const}$. $\mu \neq 1/2$ for some individual dependences of these properties on temperature or coordinates [71]. The solution at $\mu \neq 1/2$ is usually complicated, fits poorly for practical application. The solutions gained by a convergence method in the form of some series on extents of small fixed parameters are known. Uses of these solutions in the general case α, E dependences vs. temperature are also rather inconvenient and ineffective.

The problem of searching for the axisymmetric stress state in a body of cylindrical shape with properties depending on temperature can be reduced to the solution of the ordinary differential equation with variable factors [73, 74]. This equation for the plain stress state (a thin flat disk with a homogeneous and isotropic material), when α, E and λ are not constant, has generally an appearance, at the radial temperature distribution, as follows:

$$\frac{\mathrm{d}^2\sigma_\mathrm{r}}{\mathrm{d}\rho^2} + \left[\frac{3}{\rho} - \frac{\mathrm{d}}{\mathrm{d}\rho}(\ln E)\right]\frac{\mathrm{d}\sigma_\mathrm{r}}{\mathrm{d}\rho} + \frac{E}{\rho}\sigma_\mathrm{r}\frac{\mathrm{d}}{\mathrm{d}\rho}\left(\frac{1-\mu}{E}\right) + \frac{E}{\rho}\frac{\mathrm{d}\varepsilon_\mathrm{t}}{\mathrm{d}\rho} = 0. \tag{3.12}$$

An expression for true temperature strain ε_t can be recorded in various fashions depending on the choice of a coefficient of linear expansion. The mean coefficient of linear expansion relative some reference temperature T_r (20°C) is usually used. Temperature strain at modification of a body temperature from T_r up to t is:

$$\alpha E_\mathrm{t} = \int \alpha(t)\mathrm{d}t. \tag{3.13}$$

Equation (3.12) is easily integrated in the case when the modification of elastic constants E and μ on cross section of a body can be neglected. The solution of these thermal–elastic problems is a well-known expression for constant properties, with the replacement $\alpha(t)$ on ε_t.

$$\begin{aligned}
\sigma_\mathrm{r} &= E\left(\frac{1-\frac{i^\mathrm{k}}{\rho^2}}{1-i^2}\int\limits_i^1 \varepsilon_\mathrm{t}\rho\mathrm{d}\rho - \frac{1}{\rho^2}\int\limits_i^\rho \varepsilon_\mathrm{t}\rho\mathrm{d}\rho\right), \\
\sigma_\varphi &= E\left(\frac{1+\frac{i^2}{\rho^2}}{1-i^2}\int\limits_i^1 \varepsilon_\mathrm{t}\rho\mathrm{d}\rho + \frac{1}{\rho^2}\int\limits_i^\rho \varepsilon_\mathrm{t}\rho\mathrm{d}\rho - \varepsilon_\mathrm{t}\right).
\end{aligned} \tag{3.14}$$

For a solid disk it is necessary to assume $i = 0$. The case of a plane deformation at face surfaces free from loadings differs by the presence of a factor $E/1-\mu$ instead of E on the right-hand side (3.14), and also by the third component of stresses σ_z. The expression looks like

$$\sigma_z = \frac{E}{1-\mu}\left(\frac{2}{1-i^2}\int\limits_i^1 \varepsilon_\mathrm{t}\rho\mathrm{d}\rho - \varepsilon_\mathrm{t}\right) = \sigma_\mathrm{r} + \sigma_\varphi. \tag{3.15}$$

It is easy to estimate effect of temperature dependence of a linear expansion coefficient on maximum value of thermal stresses by means of relationships (3.14). Assuming that within the limits of temperature difference on the cross section of a body, this dependence can be approximated in a linear fashion:

$$\overline{\alpha}(t) = \overline{\alpha}(t_i)[1 + \overline{\beta}(t - t_i)], \tag{3.16}$$

$$\alpha(t) = \alpha(t_i)[1 + \beta(t - t_i)] = \overline{\alpha}(2t - 20), \quad \text{where} \quad \beta = \frac{2\overline{\beta}}{1 + \beta(t_i - 20)}.$$

and $\beta = 2\beta 1 + \beta(t_i - 20)$.

We admit that the temperature changes in the manner of a quadric parabola

$$t(\rho) = t_i + \frac{\Delta t}{(1 - i)^2}(\rho - i)^2. \tag{3.17}$$

Such a temperature field is realized in some cases in practice, with the thermal stress testing of specimens and maintenance of components and constructive elements. In particular, it occurs in the continuous or hollow cylinder (disk) at small values ($i \leq 0.1$) or large values ($i \geq 0.9$) with a heat insulated cavity under following conditions on an outside surface:

- Heating with a constant thermal flow, the regular stage of thermal regime
- Heating with an interior heat source ($q_{\text{v}} = \text{const.}$), steady conditions
- Heating (cooling) in fluid medium at heat transfer of moderate intensity ($Bio < 0.2$) during the moment of origination of the maximum stresses

Conversing expressions (3.14) after scaling integrals, it is possible to show that definition of the maximum stresses at variable factors of a linear coefficient of expansion is reduced to the usual calculation at $\alpha = \text{const.} = \alpha^*$ and the necessary value α^* is chosen as follows:

$$\alpha_i^* = \overline{\alpha}\left(2t_i - 20 + \frac{2(5 + i)}{5\,(3 + i)}\Delta t\right) = \alpha\left(t_i + \frac{5 + i}{5(3 + i)}\Delta t\right) \text{ for stresses } \sigma_j(i)$$

$$\alpha_1^* = \alpha\left(2t_1 - 20 - \frac{2(5 + 11i)}{5(3 + 5i)}\Delta t\right) = \alpha\left(t_1 - \frac{5 + 11i}{5(3 + 5i)}\Delta t\right)$$

$$\text{for stresses } \sigma_j(1), j = \varphi z. \tag{3.18}$$

Miscalculation of stresses from the chosen constant value α_{c} is not proportional only to temperature coefficient and temperature drop on the cross section of a body, but is also connected with temperature level in the observed point.

For the general case of α, E and μ on temperature, the dependence within the limits of temperature difference on cross section of a body is represented by the following equations:

$$\begin{aligned}
\alpha(t) &= \alpha_{\mathrm{o}}[1+\beta'_{\alpha}(t-t_{\mathrm{o}})+\beta''_{\alpha}(t-t_{\mathrm{o}})^2],\\
E(t) &= E_{\mathrm{o}}[1+\beta'_{\mathrm{E}}(t-t_{\mathrm{o}})+\beta''_{\mathrm{E}}(t-t_{\mathrm{o}})^2],\\
\mu(t) &= \nu_{\mathrm{o}}[1+\beta'_{\nu}(t-t_{\mathrm{o}})],\\
\alpha_{\mathrm{o}} &= \alpha(t_{\mathrm{o}}); E_{\mathrm{o}} = E(t_{\mathrm{o}}); n_{\mathrm{o}} = (t_{\mathrm{o}})
\end{aligned} \tag{3.19}$$

Where

$$t-t_{\mathrm{o}} = \sum_{k=1}^{N} a_k \rho^{2k}, \tag{3.20}$$

where N and a_k are defined from comparison (3.20) with the exact solution of a boundary-value problem of thermal conductivity so that the lapse of approximation did not exceed a specified value.

Substituting (3.19) in view of (3.20) in (3.11), it is possible to reduce it to:

$$\rho\frac{\mathrm{d}^2\sigma_{\mathrm{r}}}{\mathrm{d}\rho^2}+\left(3-2\sum_{k=1}^{\infty}p_k\rho^{2k}\right)\frac{\mathrm{d}\sigma_{\mathrm{r}}}{\mathrm{d}\rho}-2\sigma_{\mathrm{r}}\sum_{k=1}^{\infty}q_k\rho^{2k-1}+2\alpha_{\mathrm{o}}E_{\mathrm{o}}a_1\sum_{k=0}^{5N-1}A_{\mathrm{o}}\rho^{2k+1}=0. \tag{3.21}$$

Admissible coefficients p_k and q_k for the majority of brittle materials and temperature difference diminish promptly as estimates with increment of a coefficient k demonstrate. It is convenient therefore to seek the solution of (3.21) in the form of an ascending power series ρ. Let

$$\sigma_{\mathrm{r}} = \alpha_{\mathrm{o}}E_{\mathrm{o}}a_1\sum_{k=0}^{\infty}B_k\rho^{2k}. \tag{3.22}$$

Then from equilibrium conditions follows:

$$\sigma_{\varphi} = \alpha_{\mathrm{o}}E_{\mathrm{o}}a_1\sum_{k=0}^{\infty}(2k+1)\rho^{2k}. \tag{3.23}$$

Substituting (3.22) in (3.21) and comparing coefficients at equal ratio we gain for definition B_k a system of linear algebraic equations.

Estimates show that an adequate accuracy of the solution is given usually by the first 2–4 terms of series (3.22) and (3.23), and it is possible at scaling coefficients B_k to be restricted by terms, linear on parameters p_k and q_k.

The lapses of the standard calculation of the limited temperature stresses under formulas for constant properties of a material can be varied depending on their habits. For example, the error can attain 55% for zirconium hydride, while it does not exceed 20% for zirconium carbide in the low-temperature field and 40% at temperature 2,300 K. The greatest understated lapses are obtained at calculation on the medial coefficient of a linear expansion. The least error is on true values of a linear expansion if the medial body temperature is chosen as defining.

The last alternative should be recommended for practice as the lapse of calculation in this case does not exceed 5–15% for the specified materials. It is necessary to use the dependences presented above if higher precision is required.

The state of problems for calculation of thermal–elastic stresses by analytical expedients with a method of perturbations in materials with temperature dependent properties is discussed in [75].

3.3 Thermal–Elastic Stresses in a Finite Hollow Cylinder

As the experimenter always deals with finite bodies, it is obviously necessary to estimate the reliability and possibility of use of the thermal–elastic stress calculations of the infinite body. Two approaches to the solution of an axisymmetric problem of thermal elasticity for the cylinder of an infinite length are now known. Using representation of the solution in the form of decomposites of the Fourier–Bessel series, it is possible to fulfil precisely all the boundary conditions of a two-dimensional temperature field generally as continuous, just as for the hollow cylinder [71]. Deriving numerical results thus is related to the solution of pair infinite system of the linear algebraic equations whose regularity is proved as a rule. The second approach is based on the use of so-called homogeneous solutions, i.e. those which do not give stresses on a part of a surface. Superposition of thermal–elastic solutions for the infinitely long and homogeneous cylinder allows fulfilling problems of necessary boundary conditions either at end faces, or on the lateral surface of the finite cylinder. The application of exact homogeneous solutions practically does not reduce the computing difficulties because of the presence of the infinite combined equations. The approximate homogeneous solutions based on variation principles are more effective.

Expressions for stresses in a finite cylinder can be gained, superimposing on the stress state of an infinitely long cylinder such additional stresses that it was possible to fulfill to the necessary boundary conditions for a terminating cylinder. The method of the homogeneous solutions gains reliable enough results for three typical alternatives of temperature field in the hollow cylinder defined by the following dependences:

$$t(\rho) = \begin{cases} t_i + \dfrac{\Delta t}{(1-i)^2}(\rho - i)^2 (\mathrm{I}) \\ t_i - \dfrac{\Delta t}{\ln i} \ln \dfrac{\rho}{i} (\mathrm{II}) \\ t_1 - \dfrac{\Delta t}{(1-i)^2}(1-\rho)^2 (\mathrm{III}). \end{cases} \tag{3.24}$$

The first case corresponds to heating (cooling) of an outside surface of the cylinder with heat-insulated interior. The second alternative is the known distribution of temperature in stationary state, and the third approximately represents the temperature field at heating (cooling) of an interior surface

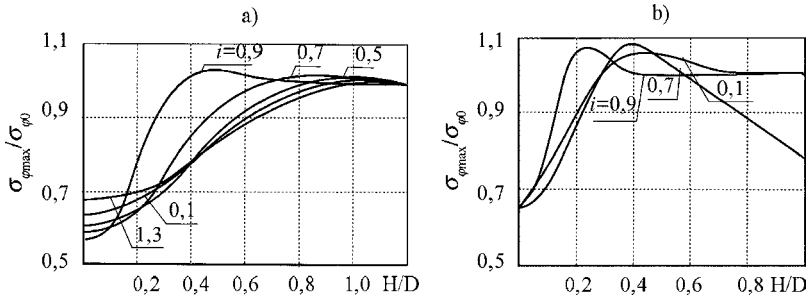

Fig. 3.2. Relationship of the maximum circumferential stresses on the exterior (**a**) and interior (**b**) surfaces of the finite and semi-infinite hollow cylinder depending on relationship of height and exterior diameter H/D for a stationary case of temperature distribution on thickness of a wall of the cylinder with various values $i = d/D$, where d is a diameter of an interior hole

with heat-insulated exterior. These alternatives in the assemblage cover a wide enough range of temperature patterns which can occur in the hollow cylinder.

The maximum circumferential stresses (MCS) that originate on the outside surface of a face cross section of an interior surface are some distance from the end face (Fig. 3.2). If the length of the cylinder is great enough, the maximum of tangential stresses on the interior surface is the same distance from the end faces irrespective of length. The maximum of tangential stresses is displaced to the medial cross section in the short cylinder and stress distribution on height attains a monotonous character.

Thus, use of a relationship for an infinitely long cylinder can result in significant understating values of stresses on an external surface, especially for the thin-walled cylinders, attaining 85% at $\mu = 0.3$. The relation of stresses $\sigma_{\varphi\,\max}/\sigma_{\varphi o}$ on an internal surface poorly depends on thickness of the cylinder wall and on Poisson's ratio and it does not exceed 1.25 for various profiles of temperature fields. It is noteworthy that the magnitude of the maximum stresses increases in the process of transition from the long cylinder to the short one at first a little bit and only then does it start to decrease gradually. This effect is expressed on an external surface poorly (within the limits of 3%), and it is a more appreciable up to 10–13% on the internal surface. These habits of the stressed condition should be noted in consideration of the fracture character of cylinders under thermal load.

3.4 Temperature Stresses at Inelastic State of a Body

The theory of an elastic–plastic deformation of materials under any varying loading conditions, and computational methods of thermal stress resistance of typical structural members (rods, plates, shells), with a simple enough account for the solution of engineering problems, is presented in [76].

We review the most frequently used specimens in the form of the hollow cylinder and the disk in practical experiments. Definition of stresses and strains in thick-walled tubes at axisymmetric strain belongs to a number of classical problems of the plasticity theory and has been observed repeatedly. Solutions are gained on the basis of the deformation theory in the absence of a reinforcement. Calculation of an elastic–plastic state of a thick-walled tube with any axisymmetric temperature pattern in view of the effect of temperature on mechanical properties of a material can be conducted under the deformation theory by means of a method of variable stress parameters, and also by a method of additional strains, using the exact solution at constant elasticity parameters. The satisfactory solution can be gained at the complex loading by means of the theory of a plastic flow.

The problem of definition of the plain stress state of plates in elastic–plastic state assumes use of the Mises or the Treska–Saint–Venant criterion of plasticity [64, 65] on the basis of the deformation theory of plasticity. The most effective computational method for plates is the method of additional strains which allows using an algorithm of elastic calculation that is the complete closed analytical solution.

The convergence method is used for the solution. The complete strains in a plate are expressed in the form of: $\varepsilon_{\mathrm{g}} = \varepsilon_{\mathrm{g}}^{\mathrm{e}} + \varepsilon_{\mathrm{g}}^{\mathrm{o}} \quad \varepsilon_\theta = \varepsilon_\theta^{\mathrm{e}} + \varepsilon_\theta^{\mathrm{o}}$, where $\varepsilon_{\mathrm{g}}^{\mathrm{e}}$, $\varepsilon_\theta^{\mathrm{e}}$ are elastic strains, $\varepsilon_{\mathrm{g}}^{\mathrm{o}}$, $\varepsilon_\theta^{\mathrm{o}}$ are additional strains.

The elastic problem, as a first approximation, is solved at $\varepsilon_z^{\mathrm{o}} = 0, \varepsilon_\theta^{\mathrm{o}} = 0$. The elastic problem in the second stage is solved with additional strains. In the final reckoning, the radial σ_{r} and tangential stresses σ_θ are expressed in the form of:

$$\sigma_{\mathrm{r}} = \frac{E}{1-\mu^2}\left[\frac{N_{\mathrm{r}}}{A} - z\frac{M_{\mathrm{r}}}{D} + \left(\frac{\varsigma_{1\mathrm{T}}}{A} + z\frac{\varsigma_{2\mathrm{T}}}{D} - (1+\mu)\alpha T\right)\right] + \frac{E}{1-\mu^2}\left[\frac{N_{\mathrm{r}}^{\mathrm{o}}}{A} + z\frac{M_{\mathrm{r}}^{\mathrm{o}}}{D} - (\varepsilon_{\mathrm{r}}^{\mathrm{o}} + \mu\varepsilon_\theta^{\mathrm{o}})\right];$$

$$\sigma_\theta = \frac{E}{1-\mu^2}\left[\frac{N_\theta}{A} = z\frac{M_\theta}{A} + \left(\frac{\varsigma_{1\mathrm{T}}}{A} + z\frac{\varsigma_{2\mathrm{T}}}{D} - (1+\mu)\alpha T\right)\right] + \frac{E}{1-\mu^2}\left[\frac{N_\theta^{\mathrm{o}}}{A} + z\frac{M_\theta^{\mathrm{o}}}{A} - (\varepsilon_\theta^{\mathrm{o}} + \mu\varepsilon_{\mathrm{r}}^{\mathrm{o}})\right],$$

where $N_{\mathrm{r}}^{\mathrm{o}}$, N_θ^{o} are additional forces per unit length of cross sections, and the moments $M_{\mathrm{r}}^{\mathrm{o}}$, M_θ^{o}, E, are a modulus, α and μ both coefficients of linear expansion and the Poisson, $\varsigma_{1\mathrm{T}}$, $\varsigma_{2\mathrm{T}}$ are temperature terms, and A and D are the terms considering modifications of a modulus on width of the disk.

The elasto–plastic stress state is homogeneous, in this connection the values of stress and strain intensity coincide with values of principal stresses and, accordingly, with strains in the peripheral and radial directions. The discovered solution can also be used under condition of creep. The computation is analogous to elastic–plastic calculation, however, instead of deformation

curves isochronous creep curves are used [64]. A method of additional strains is used expediently in this case. The loading is divided by time into a series of small stages within the limits of which the effect of stress change on strain rate of creep appears incidental. The calculation is carried out for the elastic cylinder in the presence of additional strains.

The calculations of the thermal stresses in bodies in view of all actual inelastic properties are generally rather complex, even if one of the models of inelastic behaviour is chosen – a plastic straining or elastic–viscous deformation [67]. Considering that the majority of refractory materials have rather restricted plasticity, and the duration of thermal loading in their operation and maintenance is usually great in comparison with the short-term mechanical trials on which the theory of plasticity is based, use of the equations of the creep theory is quite expedient (see Application A.4).

The temperature stress calculations of axisymmetric hollow cylinder under thermal load at the given stationary temperature difference between interior T_1 and external wall T_2 (Fig. 3.3) are carried out in [16]. The authors made an assumption that the deviator of stresses is similar to the deviator of velocities of strains in view of the extent of effect of a medial rated stress on the process of creep.

We accepted also that the modification of a body's volume is considered by introduction of the coefficient of the transverse creep υ. Strains $\varepsilon_\theta, \varepsilon_r, \varepsilon_z$ were determined by the equations (3.24); The radial σ_r, tangential σ_θ and axial σ_z are accepted as the principal stresses.

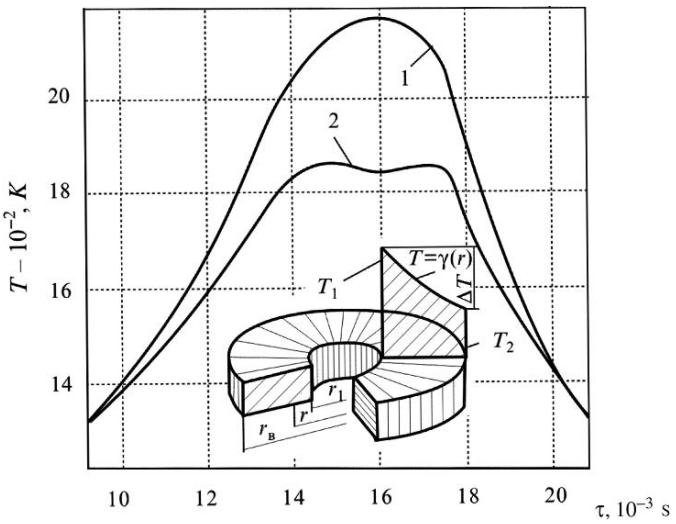

Fig. 3.3. A modification of temperature T_1 on interior and T_2 on an external wall of a ring specimen during testing [16]

$$\left.\begin{aligned}
\dot{\varepsilon}_\theta &= \alpha\dot{T} + \frac{\dot{\sigma}_\theta}{E} - \mu\frac{\dot{\sigma}_r + \dot{\sigma}_z}{E} + C(\sigma_\theta^n - \nu\sigma_r^n - \nu\sigma_z^n)\exp\left(-\frac{Q}{kT}\right),\\
\dot{\varepsilon}_r &= \alpha\dot{T} + \frac{\dot{\sigma}_r}{E} - \mu\frac{\dot{\sigma}_\theta + \dot{\sigma}_z}{E} + C(\sigma_z^n - \nu\sigma_\theta^n - \nu\sigma_z^n)\exp\left(-\frac{Q}{kT}\right),\\
\dot{\varepsilon}_z &= \alpha\dot{T} + \frac{\dot{\sigma}_z}{E} - \mu\frac{\dot{\sigma}_\theta + \dot{\sigma}_z}{E} + C(\sigma_z^n - \nu\sigma_\theta^n - \nu\sigma_r^n)\exp\left(-\frac{Q}{kT}\right).
\end{aligned}\right\} \tag{3.25}$$

Besides, the static and geometrical equations [65] were applied.

Both derivatives on time and on radius are included in the gained combined equations and therefore their solution is extremely complex. It is impossible to gain the analytical solution of this system even at some simplifications. Therefore, the numerical method of the solution of the differential equations of Euler–Cushy is used.

The radius of a specimen has been divided notionally into small sections, Δr, and stresses are computed through short time periods, Δt:

$$\left.\begin{aligned}
(\sigma_\theta)_{m+1} &= (\sigma_\theta)_m + \Delta t(\dot{\sigma}_\theta)_m,\\
(\sigma_\mathrm{r})_{m+1} &= (\sigma_\mathrm{r})_m + \Delta t(\dot{\sigma}_\mathrm{r})_m,\\
(\sigma_z)_{m+1} &= (\sigma_z)_m + \Delta t(\dot{\sigma}_z)_m,
\end{aligned}\right\} \tag{3.26}$$

where $(\sigma_\theta)_{m+1}$, $(\sigma_r)_{m+1}$ and $(\sigma_z)_{m+1}$ stresses in the end time period, and $(\sigma_\theta)_m$, $(\sigma_r)_m$ and $(\sigma_z)_m$ in the beginning of the same period.

As the solution of an elastic problem for the hollow cylinder exists, the stress derivatives on a time are convenient to express in the form of addends. The augend should consider a derivative of an elastic component which is computed under known formulas of an elastic problem. The addend considers stress relaxation. As the extent of the stress relaxation strongly depends on temperature in more heated parts, the stresses relax much more quickly. However requirements of a static balance demand, that a tangential stress and an axial stress are counterpoised by themselves in the volume of a specimen, therefore the high rate of stress relaxation in most heated places leads to disproportionation of stresses in the whole volume. Stress velocity disproportionation should be considered by the third addend, not dependent on the current radius. The radial stresses are kept from touching, as they are not counterpoised. The above reasoning is recorded in the form of the equations:

$$\left.\begin{aligned}
\dot{\sigma}_\theta &= \dot{\sigma}_{\theta y} + \dot{\sigma}_{\theta n} + K_\theta,\\
\dot{\sigma}_r &= \dot{\sigma}_{ry} + \dot{\sigma}_{rn},\\
\dot{\sigma}_z &= \dot{\sigma}_{zy} + \dot{\sigma}_{zn} + K_z,
\end{aligned}\right\}. \tag{3.27}$$

As magnitudes K_q and K_z do not depend on the current radius they can be computed in the end of the mth period from requirements of a static balance.

$$\int_{r_1}^{r_2} (\sigma_\theta)_{m+1}\mathrm{d}r = 0, \int_{r_1}^{r_2} (\sigma_z)_{m+1} r\mathrm{d}r = 0. \tag{3.28}$$

The known equations must be differentiated for definition of elastic components. From (3.25) it follows that

$$\left.\begin{aligned}
\dot{\sigma}_{\theta m} &= -CE(\sigma_\theta^n - \nu\sigma_\theta^n - \nu\sigma_z^n)\exp\left(-\frac{Q}{kT}\right),\\
\dot{\sigma}_{rn} &= -CE(\sigma_r^n - \nu\sigma_\theta^n - \nu\sigma_r^n)\exp\left(-\frac{Q}{kT}\right),\\
\dot{\sigma}_{zn} &= -CE(\sigma_z^n - \nu\sigma_\theta^n - \nu\sigma_r^n)\exp\left(-\frac{Q}{kT}\right).
\end{aligned}\right\}$$

The following simplifications are accepted at the accomplishment of stress calculations:

1. Parameters α, E and λ are independent of radius on medial integrated temperature, but they are considered with transition to a following time period and with modification on temperature.

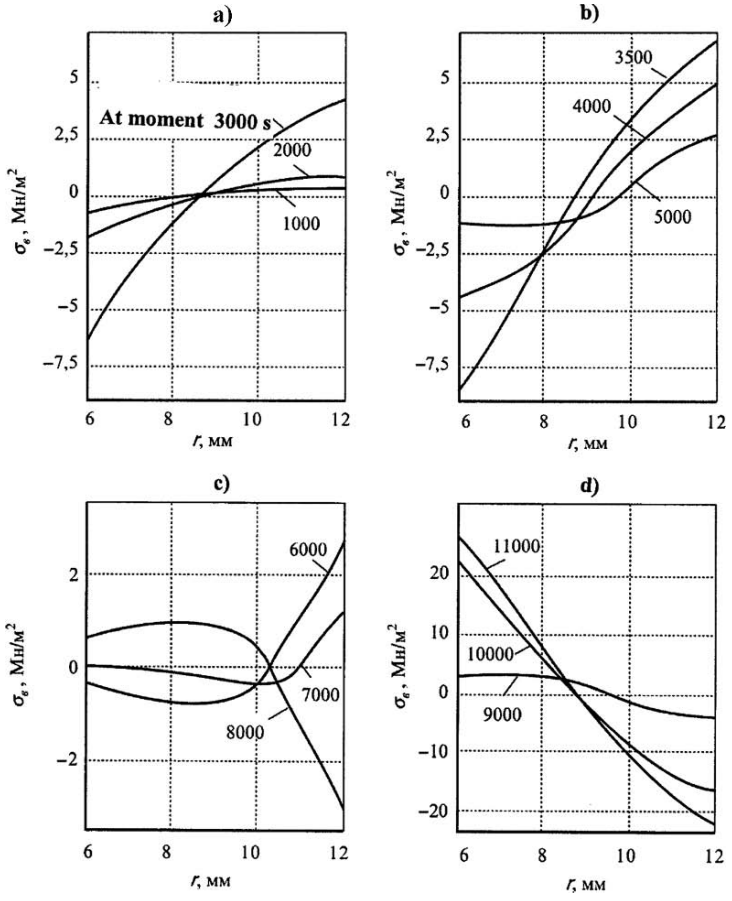

Fig. 3.4. Distribution of tangential stresses on radius of ZrO_2 specimen during different moments of one test [17]

2. Stress derivatives on time in period Δt remain stationary, spasmodically varying at transition to a following period. For best accuracy calculations, interval Δt with an increase of temperature is diminished, that it is called by the strong speed-up of stress relaxation with an increase of temperature.

Results of the calculation are presented on Fig. 3.4. In the beginning of a test (Fig. 3.4a), the stresses are increased with increment of a temperature difference according to Fig. 3.3, as the temperature is still low and stresses do not relax in practice. However, from some moment (Fig. 3.4b), despite the further increase of temperature difference, the stresses are diminished quickly owing to the elastic–viscous flow and the stress relaxation. At the moment of greatest temperature difference (Fig. 3.4c), the stresses diminish to rather small values as the temperature at this time is high. The residual tension stresses originated on an inner wall, comparable with an ultimate strength, after removal of thermal load at rather low temperatures, causing fracture of the material (Fig. 3.4d).

The experiments performed on ring-shaped ZrO_2 specimens under matching regimes have confirmed reliability of the design estimates.

3.5 The Thermal–Elastic Stresses at Local Radiation Loading of a Body

Considering the wide opportunities of thermal stress resistance measurement at local radiation heating and the necessity of an estimation of a bearing capacity of devices (laser power optics, pulsing nuclear reactors) at impulse thermal exposures, due attention should be given to examination of calculation methods of local fields of the thermo–elastic stresses.

A calculation of the thermal stresses for specimens of finite sizes is connected with significant mathematical difficulties. Even known solutions for half space [27] demand a great volume of computations. However, simple enough expressions [77] are gained at certain limitations on the size of a specimen.

Let us accept that allocation of density of a heat flow q in a spot of loading in radius ω is presented by a relationship

$$q = q_{\mathrm{o}} \exp(-kr^2), \tag{3.29}$$

where $q_{\mathrm{o}} = 2Q/\pi\omega^2$.

The radial σ_{r} and tangential stresses determined from known simple relationships [67, 78] in case of axisymmetric non-stationary heating of a flat specimen of width $\delta < 2\omega$ when a component σ_z can be neglected

$$2\sigma_{\mathrm{r}}/\alpha E = T - T_{\mathrm{r}}; \quad 2\sigma_{\varphi}/\alpha E = T + T_{\mathrm{r}} - 2T, \tag{3.30}$$

where α is the coefficient of a linear expansion and E is a modulus of elongation, respectively.

$$\overline{T}_{\mathrm{r}} = 2r^{-2} \int_0^r Tr\mathrm{d}r; \quad \overline{T} = \overline{T}_{\mathrm{r}}. \tag{3.31}$$

At $r = D/2$; D is the diameter of a specimen.

The stress state of a specimen is quasi-plane, i.e. it depends on coordinate z, but it is represented by usual expressions for plane stress state. The stresses σ_{r} and σ_{φ} on irradiated surface at $r = 0$ are compressing; at increase of values r the stresses change sign.

At the beginnings of a loading, when the temperature field has not yet extended up to the boundary lines of a specimen, it is possible to observe a specimen as half space. The solution of thermal conductivity problem for half space is known [68] at the probable distribution law of a heat density flow.

$$\theta(\rho, \xi, \tau) = \int_0^{\sqrt{\tau}} \exp\left[-\left(\frac{\rho^2}{4x^2+1} + \frac{\xi^2}{4x^2}\right)\right] \frac{\mathrm{d}x}{4x^2+1}, \tag{3.32}$$

where in the dimensionless view

$$\theta = \frac{\pi\sqrt{\pi}(T - T_0)\lambda\omega}{2\sqrt{2}Q}; \rho = \sqrt{2}\frac{r}{\omega}; \xi = \sqrt{2}\frac{z}{\omega}; \tau = \frac{2\alpha t}{\omega^2};$$

λ, a are coefficients of thermal conductivity and thermal diffusivity respectively; T_0 is the reference temperature of a specimen; τ is the time of a loading. Temperature at the centre of a spot of thermal loading

$$\theta(0, 0, \tau) = 0{,}5\mathrm{arctg}2\sqrt{\tau}. \tag{3.33}$$

It is possible also to determine a depth

$$z = \omega(2\sqrt{\tau}), \tag{3.34}$$

where the temperature at the given value τ makes about 10% of the maximum temperature on the surface of a specimen and, on the contrary, at $z = \delta$ up to a boundary value τ_1 it is possible to use expression (3.32).

We determine the maximum values of tensile tangential stresses σ_{m} on the surface of a specimen, as fracture of brittle materials happens from tensile stresses. The requirement of a maximum of expression (3.30) in view of (3.32) is:

$$\frac{\rho^2}{4\tau + 1} \cong 3.21 \tag{3.35}$$

accordingly we gain for stresses σ_{m} at the moment of fracture

$$(1 - \mu)\frac{\lambda\sigma_{\mathrm{m}}}{\alpha \mathrm{E}} = (1 - \mu)\frac{Q}{\omega}\left[0{,}028\mathrm{arctg}2\sqrt{\tau_{\mathrm{p}}} + 0.52\left(\frac{\omega}{D}\right)^2\sqrt{\tau_{\mathrm{p}}}\right]. \tag{3.36}$$

For temperature in a place of occurrence of stresses σ_{m}:

$$T - T_0 = 0.01 \frac{Q}{\lambda\omega} \mathrm{arctg} 2\sqrt{\tau_{\mathrm{p}}}, \tag{3.37}$$

where $\tau_{\mathrm{p}} = 2at_{\mathrm{p}}/\omega^2$ and μ is Poisson factor.

The augends in expression (3.36) can be neglected, as its contribution becomes less than 10% at trial of specimens not limited to a round form with defining size $D > 10\omega$. The experimental definition accepted now for the first R and the second R' criteria of thermal stress resistance through the parameters of thermal action producing emersion of stresses, appropriate to the ultimate strength of a material:

$$R = \frac{(1-\mu)\,\sigma}{\alpha E}; R' = \frac{(1-\mu)\,\sigma\lambda}{\alpha E}, \tag{3.38}$$

allows us to use a design relationship (3.37) for the immediate determination of the second criterion of the thermal stress resistance R' at known values μ and a, set for the given time to failure τ_{f} to parameters of thermal action Q and ω.

Reliability of the design estimates of the thermal stresses of specimens of zirconium carbide disks of 26 mm diameter and 1 ± 0.1 mm width are approved by trials. The tests carried out on the cathode-ray installation [77] with a loading spot ($\omega = 2.7$ mm) at two values of initial specimen temperature: $T_0 = 20$ and -195°C. The time of specimen fracture, τ_{p}, varied from 0.3 to 0.005 s at the assignment of a heat flow Q from 100 up to 840 W.

Specimens in these trials failed on two to six fragments, and, as a rule, cracks do not propagate from a central point, which confirms the initial assumption of presence of an annular domain of the maximum tensile stresses around a zone of thermal action on the surface of a specimen.

The second criterion of the thermal stress resistance is equal to $1.3 \times 10^3\,\mathrm{W\,m^{-1}}$ at coefficient of a variation of 15% irrespective of the level of thermal loading Q. Accordingly, the value of the first criterion of the thermal stress resistance $R = 65$ degrees. The observable spread of the thermal stress resistance is usual for a brittle fracture of zirconium carbide. Estimates of temperature values on relationships (3.33) and (3.37) demonstrate that the increase of temperature at the centre of a specimen by the moment of fracture made 700–800°C, but in a fracture zone 25–30°C, depending on a level of a loading.

The tests of disk specimens, 24 mm in diameter, were conducted to check the data gained by a heating method using a bath of melted tin [79]. Fracture of specimens occurred at a temperature of 850 ± 50°C. The mean values $R' = 1.3 \times 10^3\,\mathrm{W\,m^{-1}}$, $R = 65$ degrees were determined at temperature in a fracture zone of $25, \ldots, 30$°C after calculation with use of the experimentally discovered value of the coefficient of a convective heat transfer in melted tin $2.5 \times 10^3\,\mathrm{W\,m^2\,K^{-1}}$. The good agreement of the data among themselves allows us to consider that this computational method ensures reliable results.

Experimental data on the thermal stress resistance of zirconium carbide represented by criteria $R' = 2.6 \times 10^3\,\mathrm{W\,m^{-1}}$ and $R = 65$ degrees in the sub-zero temperature field at cooling of a back surface of the disk by liquid nitrogen are obtained for the first time. Obviously, at the precise solution of thermal conductivity problem, in view of temperature dependences $a(T)$ and $\lambda(T)$, these values will be reduced a little, but are above the room temperature value. The similar result is in good conformity with direct calculation of criteria of the thermal stress resistance on expressions (3.38) with use of a coefficient of linear expansion, modulus of elongation and an ultimate bend strength of a material. The measured values of bend strength for ZrC at the temperature of the liquid nitrogen appeared practically equal to matching magnitudes at 300 K. It is known that the modulus in the field of the sub-zero temperatures does not vary, and the coefficient of linear expansion is reduced [14]. Therefore the criteria of the thermal stress resistance calculated directly from expressions (3.38), should be above the results of the experiments conducted. We note also that the thermal stress resistance data obtained for zirconium carbide coincides with results in references [14, 79] if considering the possible dispersion of the physical–mechanical properties, determining the thermal stress resistance criteria.

Calculation capabilities for calculation of the thermo–elastic stresses in a thin disk heated at any point eccentrically oriented relative to its centre at the given power of a heat source are observed in [80].

Calculations are carried out for a body in the form of a circle, but the solutions can be used easily for bodies of other geometry with application of methods of conformal mapping. The solution is conducted on the basis of the classical theory of the linear thermo-elasticity. It is accepted that a material is homogeneous and isotropic, both from thermal and mechanical points of view, and all physical properties do not depend on temperature. Allocation of temperatures in the disk after thermal shock is determined by superposition of a matching Green function and the function, satisfying a simple equation of thermal conductivity. The appropriate stress fields and strains on the discovered field of temperatures are assigned by means of the Goodier function for the thermo–elastic potential of displacement and Erie's stress function [67]. The solution is gained in the form of double promptly converging infinite series. Numerical calculations are given for a case history.

The value of a convective heat transfer h on air is accepted as being stationary, though the heat transfer factor is a function of a surface temperature and a character of a modification of temperature at a point where gauging is made. The modification of heat transfer evokes very small effect on the numerical calculations in view of the low duration period of a heat input to the disk and the relative time lag of ambient air. The extensive numerical results are given by way of illustration on diagrams, but the experimental check of calculations was not performed.

The thermo–elastic stresses at any point of an end surface of the disk locally heated by an arc discharge are counted in [81].

Distribution of temperature $T(r,t)$ on radius r during t:

$$\frac{1}{k}\frac{\partial T}{\partial t} = \frac{1}{r}\frac{\partial}{\partial r}\left(r\frac{\partial T}{\partial r}\right) + \frac{q}{k}, \tag{3.39}$$

$$T\,(r,0) = 0, \frac{\partial T\,(b,t)}{\partial r} = 0, \tag{3.40}$$

where a heat flow $q = q_{\mathrm{o}}$ for values $0 = r \le a$ and $q = 0$ when $r \le R$; a is the radius of a heating spot, R is the radius of the disk

The solution for the temperature field is presented in the form of:

$$\frac{T}{Q_0} = \left(\frac{a}{b}\right)^2 \tau + 2\left(\frac{a}{b}\right)\sum_i J_0\,(m_i r/b)\frac{J_1\,(m_i a/b)}{m_i^3\left[J_0(m_i)\right]^2}\left[1 - \exp(-\tau m_i^2)\right], \tag{3.41}$$

where summation is made on all positive roots $J_1(m) = 0$ and

$$Q_0 = q_{\mathrm{o}} b^2/\lambda \tag{3.42}$$

$$\tau = a\tau/b^2. \tag{3.43}$$

Thermal radial stresses σ_{r} and circumferential σ_θ in the thin disk

$$\sigma_{\mathrm{r}} = E\alpha\left(\frac{1}{b^2}\int_0^b \mathrm{Trd}r - \frac{1}{r^2}\int_0^r \mathrm{Trd}r\right), \tag{3.44}$$

$$\sigma_\theta = E\alpha\left(\frac{1}{b^2}\int_0^b \mathrm{Trd}r + \frac{1}{r^2}\int_0^r \mathrm{Trd}r - T\right). \tag{3.45}$$

We gain a stress distribution having substituted values (3.41) in (3.44) and (3.45) and having conducted the necessary integration:

$$\sigma_{\mathrm{r}}/E\alpha Q_0 = 2\left(\frac{a}{b}\right)\sum_i J_i\left(\frac{m_i r}{b}\right)\frac{J_1(m_i a/b)}{m_i^3\left[J_0(m_i)\right]^2}\left[1 - \exp(-\tau m_i^2)\right]\frac{b}{m_i r}. \tag{3.46}$$

$$\sigma_{\mathrm{o}}/E\alpha Q_0 = 2\left(\frac{a}{b}\right)\sum_i \left[J_1\left(\frac{m_i r}{b}\right)\frac{b}{m_i r} - J_0\left(\frac{m_i r}{b}\right)\right]\frac{J_1\,(m_i a/b)}{m_i^3\left[J_0\,(m_i)\right]^2} \times \left[1 - \exp\left(-\tau m_i\right)^2\right]. \tag{3.47}$$

Numerical estimates of allocation of thermal stresses with eccentric loading spot ρ oriented on the thin disk of width l and the account of requirements of heat transfer [78] are presented in Fig. 3.5 and in the normalizing tables [81] convenient for particular estimates of thermal stress resistance of materials by the user.

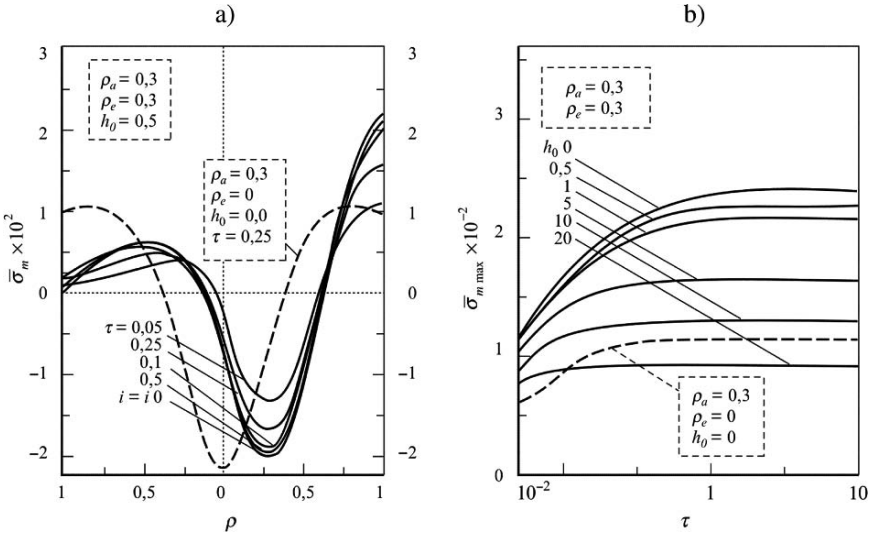

Fig. 3.5. Dimensionless distribution of tangential thermal stresses σ_θ in a disk in radius R, with relative radius of a loading spot $\rho_a = a/R$, with relative magnitude of spot eccentricity $\rho_e = e/R$, oriented on distance e from centre, at heat transfer value *Bio* – $h = 0.5$ for the dimensionless instant $\tau = 0.5$ (**a**). Modification of the maximum dimensionless values of tangential stresses depending on the dimensionless time at a variation of values of heat transfer h (**b**) [78]. *Dotted curves* represent values σ_θ with a central loading spot $\rho_e = 0$ and value of heat interchange $h = 0$

The real magnitude of stresses at substitution of performances of materials E, α, λ in the dimensionless complex of stresses $\tilde{\sigma}_{\max}$ is easily determined from the relationship:

$$\sigma = E\ \alpha\ Q_0\ \tilde{\sigma}_{\theta\theta\max}/\lambda\ \pi(a/R)^2 l, \tag{3.48}$$

Where Q_0 is heat generated at the arc heating in a volume of a loading spot of width l and radius a. Radial stresses are compressive all over the radius. The maximum is attained in a central field depending on the eccentricity of a loading spot. The tangential compression stresses in a central part change sign and attain the maximum values on the rim of the disk. These tensile stresses produce emersion of flaws on a surface at reaching critical coefficient of stresses K_{1c} and an ultimate strength of the material.

The convective heat transfer at the arc heating up to 1,000°C air temperature, characterized by values *Bio* at a level of 0.5 have a rather feeble influence on thermal stresses. These sharply vary during initial instants, attaining constant value for the dimensionless time $\tau \geq 0.25$.

The experimental estimates of the thermal stress resistance of brittle materials, including graphite and composites with carbon fibres, have confirmed the reliability of this computational method.

3.6 Calculation of Thermal Stresses in the Cylindrical Body Cooled on Lateral Surface in Water

Non-stationary temperature patterns and thermal stresses in a body are very often necessary for determining when the coefficient of a convective heat transfer depends on surface temperature. The estimate of thermal stresses at non-stationary cooling is impeded, owing to inaccurate knowledge of difficult dependence of heat transfer in boiling condition (see Chap. 4). The exact analytical solution of a transient heat problem for such non-linear problems is not gained. The various approximate cases of calculation are developed for a system of an arbitrary relation of a convective heat transfer coefficient on time: an integral method, perturbation method, a variation method and other methods reduced to integral equations [68]. The solution of a non-linear transient heat conduction problem using the existing approximate analytical computational methods would be ineffective, and it would be reasonable to use numerical methods, or methods of electro-model operation [82]. Fields of temperatures and stresses in a body cooled in water are counted by the FEM with the use of a program, ANSIS 6.0 [83].

Calculation of temperature stresses at which the damage to a cooled specimen began was conducted by the numerical method in a wide temperature interval, down to 1,250°C [84]. The estimate of thermal stress resistance is represented by magnitude of thermal fracture stress σ_{t} and (or) the value of mean integrated temperature drop $\Delta T_{\mathrm{m}} = T - T_{\mathrm{s}}$. The basic error in estimation ΔT_{m} is introduced with the definition *Bio*; the error is summed from measuring errors h and λ. Accepting the indeterminate assignment of *Bio* of 20%, an estimate of the experimental values $R_{\mathrm{e}} = \Delta T_{\mathrm{m}}$ for ZrC specimens, $d = 6\,\mathrm{mm}$ and $\lambda = 5$–$50\,\mathrm{W\,m^{-1}\,K^{-1}}$ will be within the limits of 2–10%.

The lapse of thermal stress definition provoked by origination of local stresses σ_{l}, which can originate at boiling on a stage equal to the size of a steam bubble, is not great. These values σ_{l} counted for a half space by a Laplace method [67], under the effect of a local heat flow q_{l} inverse on a sign to a flow q, uniformly distributed on the whole cooled surface, do not exceed $10^{-2}\alpha E T_0$. Validity of a design estimate is confirmed by experimental data indicating that during the life of steam bubble on a surface, which is less than $10^{-4}\,\mathrm{s}$, local oscillations of temperature do not exceed 6°C [85]. Thus, definition of thermal stress resistance does not meet insoluble difficulties at the developed process of bubble boiling action.

Non-stationary cooling of the lateral surface of a disk or a solid or hollow cylinder does not cause complete loss of bearing capacity. Cylindrical ZrC specimens first heated up to temperature $T_{\mathrm{i}} = 600\,\mathrm{K}$ are damaged only fractionally after cooling in a water bath at $T = 300\,\mathrm{K}$. The depth of a crack penetration on average makes $0.55R$, a figure that is agreed for design estimates [50].

Table 3.1. Thermal fracture stresses σ_t, and mean integrated fracture difference ΔT_m of specimens of various forms tested by cooling in water

Material, Number	Sample size (mm)	MPa σ_{ts}	MPa σ_b	$E \times 10^{-4}$ (MPa)	$\alpha \times 10^6$ (K^{-1})	λ ($W\,m^{-1}K^{-1}$)	ΔT_m (K)	σ_t (MPa)	σ_t/σ_b
$ZrC_{0.93}$, $N = 52$	cylinder, $d = 3$, $l = 30$	–	280	3.5	6	30	60	126	0.45
$ZrC_{0.93}$, $N = 35$	disk, $d = 25$, $h = 3$	90	260	3.4	6	28	50	102	0.39
Sapphire, $N = 32$	tube, $\delta = 2$, $d = 13$, $l = 9$	–	690	4.5	7.2	18	72	280	0.41
Al_2O_3, $N = 45$	cylinder, $d = 1$, $l = 30$	–	245	4.0	6.4	16	54	138	0.57

Reliability of the quantitative definition of thermal stress resistance in the case of a non-stationary cooling method is confirmed by data measured on specimens of various different forms and sizes (Table 3.1).

Observable differences ΔT_m within the limits of 15–25% are caused first of all by natural dispersion of properties of ceramic materials. The choice of zirconium carbide as the basic experimental material is due, first of all, to the stability of properties $\sigma, \Delta T$ and complex αE in a temperature range from 20 up to 1,500°C, and also the corrosion stability of ZrC at boiling in water. Second, the presence of sufficient experimental data gained by other methods for which the measurement error is not higher than non-stationary cooling method in water.

Reliability of design estimates of thermal stresses $\boldsymbol{\sigma}_t$ and effects of a temperature hysteresis of boiling condition on their level are also confirmed convincingly by regularity of ZrC specimen damage, heated up to different initial levels of temperature T_0 from 150 up to 1,200°C. The delayed transition from a film boiling condition to bubbling at $T = 200$°C, observable on heating of specimens of $d = 3$ mm above 1,000°C confirms the lack of strength decay (Fig. 3.6).

The average level of strength of specimens after heating them up to 1,100–1,200°C and cooling in water is compared with initial values of strength as thermal stresses σ_t have appeared below σ_{ts}. The capability of ZrC to strengthen at heating up to temperatures of 1,000–1,220°C is avoided as the relaxation of thermal stresses and emersion of compression stresses becomes

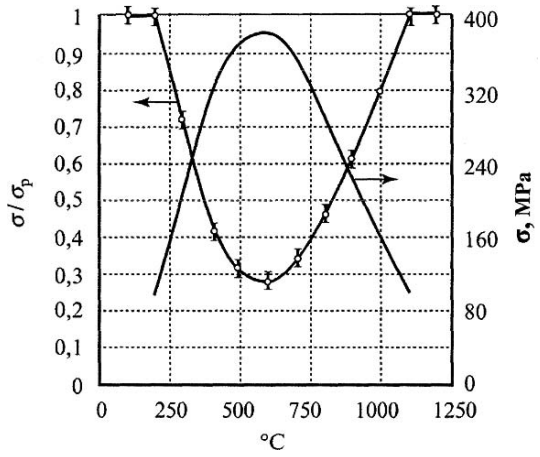

Fig. 3.6. The relative decay of strength at non-stationary cooling in water of cylindrical specimens of ZrC, with $d = 2.2\,\text{mm}$ and $l = 45\,\text{mm}$; and a modification of thermal stresses σ_t at a heating up to temperature T_0 [84]

appreciable only at a heating above 1,500°C and a weaker cooling mode, for example, by a gas blowing across a specimen. The maximum decay of strength is attained at a heating of specimens up to 400–600°C, when thermal stresses reach their maximum. The complete exclusion of damage after cooling in water is observed also after heating of cylindrical specimens 1.2 mm in diameter up to $T_0 = 1{,}300$–$1{,}400$°C.

Studies in the 1990s [86, 87] modified the method of non-stationary cooling by using specimens with preliminary induced indenter imprints. The estimation of critical temperature drop ΔT_c in this case is carried out provided that not less than 25% of all cracks available in a specimen should grow after cooling by not less than 10% from their initial length. Accomplishment of these requirements secured a reliable and reproduceable estimate of thermal stress resistance of a material with rather a paucity of specimens of any form and sizes. Estimation of thermal stress resistance was conducted in [87] on parameter $R_\text{c} = \Delta T_\text{c}\sqrt{C}$, where C is the half length imprint of the Knoop indenter, and ΔT_c is a temperature drop, causing growth of cracks.

4

Methods of Testing for Thermal Stress Resistance

The methods of testing for heat resistance currently used in practical research are not yet properly classified (let alone standardized); however, attempts in this field have been reported occasionally [19, 29–31, 88–91].

The standards adopted in various countries are mainly concerned with methods that give a qualitative characterization of heat resistance only. In conformity with the standards of Russia, Great Britain, U.S. and France [17, 92], ceramic articles (bricks, refractory panels, etc.) or cylindrical or prismatic specimens of specified size are heated to a certain temperature in air and, after a period of time, are cooled in a steam of water or air. Finally, the number of such thermal test cycles is determined that lead to loss of weight or to cracking, spalling or fracture.

The advent of new technologies (especially in space, aviation and nuclear power engineering) and the use of new materials and products operating under severe conditions make it necessary to develop quantitative methods for the evaluation of heat resistance and classification and appropriate methodology of testing mimicking real thermal loading conditions [92].

In the present chapter, an attempt is made to classify, in broad outlines, the existing methods for determination of heat resistance; by convention, two classification aspects are considered which are based on the heat flow direction (a) away from the surface of the body on cooling, and (b) into the interior of the body heated on the surface. The methods used are evaluated in the following terms:

- Feasibility of a quantitative characterization of heat resistance
- Accuracy of measurement by a given method
- Temperature range of testing
- The range within which heat resistance is measured
- Feasibility of measuring the thermal loading rate
- Test medium
- Size and shape of specimens tested
- Availability of equipment and complexity of testing

4.1 Basic Methods of Testing for Thermal Stress Resistance

Experimental quantitative methods of heat resistance are concerned with the measurement of a temperature field in the body as early signs of imminent failure become apparent. The temperature field in the body is determined either experimentally (using contact or contactless techniques), or theoretically (by computation). In the latter case, computations are carried out taking into account the boundary conditions of heat exchange.

In most cases, the temperature fields under non-linear heat-exchange conditions are found using numerical methods, which is easily done if appropriate software facilities are available.

The mean integral temperature drop $\Delta T_{\mathrm{m}} = T_{\mathrm{m}} - T$ as calculated at the instant of failure (where T_{m} is the mean integral temperature through the body cross section and T is the temperature at an arbitrary point, either on the surface or in the bulk) is used to determine the thermal stresses

$$\sigma = \alpha E \Delta T_{\mathrm{m}} K_{\mathrm{f}}/(1-\mu), \tag{4.1}$$

where E is Young's modulus; α is the coefficient of linear expansion μ is Poisson's ratio; K_{f} is the form factor.

The term $\sigma(1-\mu)/E\alpha = \Delta T_{\mathrm{m}}$ obtained from (4.1) for $K_{\mathrm{f}} = 1$ is conventionally called the first criterion of heat resistance R (measured in degrees). The term $R\lambda$ (λ is the thermal conductivity) is called the second criterion of heat resistance R' (measured in W deg^{-1}); it characterizes the ability of the material to sustain linear heat flow without damage [93].

For commonly used test specimens in the form of a solid or a hollow cylinder, ball, or disk, the values of K_{f} are 1, 1 and $1-\mu$, respectively, when the entire surface is cooled; when the surface is heated, the corresponding values of K_{f} are 1, 2/3 and $1-\mu/2$. In the case of a thermal loading applied locally to specimens of simple shape or to specimens of irregular (axially asymmetric) shape, thermal stress analysis either becomes a complicated procedure, or leads to uncertain results. Certain techniques permit the direct measurement of the stress or strain leading the specimen to failure [93].

Value R calculated on physical–mechanical parameters $E\alpha$, σ and μ as a rule is higher then experimentally measured $R_{\mathrm{e}} = \Delta T_{\mathrm{m}}$, because for calculation a bending strength is used as the most easily measured property for brittle ceramic materials. Actually, body fracture at thermal stress begins, in most cases, at stresses, close to ultimate tension strength, and termination of fracture happens at stresses noticeably exceeding initial.

Some researchers characterize thermal stress resistance with maximum temperature drop $\Delta T_{\max}$ between surface of a body and a coolant, leading to fracture. Such quality estimate of thermal stress resistance of different materials is possible to conduct only at equal sizes of specimens as, decrease of basic size of specimen at the same $\Delta T_{\max}$ lead to natural reduction of temperature stresses capable to call fracture.

Therefore thermal stress resistance of materials on specimens of different sizes should be estimated by values of stresses determined on mean integrated difference ΔT_{m}.

Expression ΔT_{m} acquires in view of fracture toughness and a crack size c a following aspect:

$$\Delta T_{\mathrm{m}} = \sigma(1-\mu)/E\alpha = K_{1\mathrm{c}}/\sqrt{c}.$$

The temperature range of testing and the feasibility of evaluating heat resistance in quasi-brittle, visco-elastic or viscoplastic states are determined by the technique chosen for thermal shock. Heat resistance, like strength, has been shown to be a function of the temperature and thermal loading rate [16, 17, 51]. In the temperature range of $(0.3-0.5)T_{\mathrm{m.p}}$($T_{\mathrm{m.p}}$ - melting point), the material develops successively micro-plastic and a macroscopic behaviour, concomitant with the increase in heat resistance, more pronounced at lower thermal loading rates. Under such conditions, creep and stress relaxation must no longer be ignored [16, 17, 94], as well as the residual thermal stresses potentially capable of causing damage. Occasionally, the effect of the medium was observed even at moderate temperatures. For example, the heat resistance of Al_2O_3 specimens and certain glasses, heated and then cooled in water, was observed to decrease appreciably as compared to that for the same material cooled in air. Thus, in evaluating the carrying capacity of thermally loaded elements, the choice of a testing method should be made with due account of the operating conditions.

4.2 Methods of Testing for Thermal Stress Resistance Under Cooling Conditions

The experimental methods for determination of heat resistance by cooling in water [32, 33, 43, 84, 94–97], organic media [98, 99], molten salts [99–101] and metals [102], gas [102, 103] or gas–dust media [32, 104] are based on the creation, in pre-heated specimens, of a temperature drop detrimental to material continuity. Technically, the testing methods are rather simple. The required items are a furnace for heating the specimens in air or in an inert atmosphere; cooling chambers with automatically or manually operated delivery of specimen heated to the desired temperature; as needed, an acoustic sensor for monitoring cracking of the specimen. Electrically powered furnaces with a maximum heating temperature of 1,000°C are preferably used. Conventional test specimens are cylinders or beams of rectangular cross section; occasionally, disks or hollow cylinders can be used.

If for some reason the use of an acoustic sensor for failure monitoring is not feasible, the testing procedure involves stepwise heating of the specimens (in steps of 10–20°C) until visible signs of damage become apparent in the specimen as the difference ΔT between the heating temperature and the

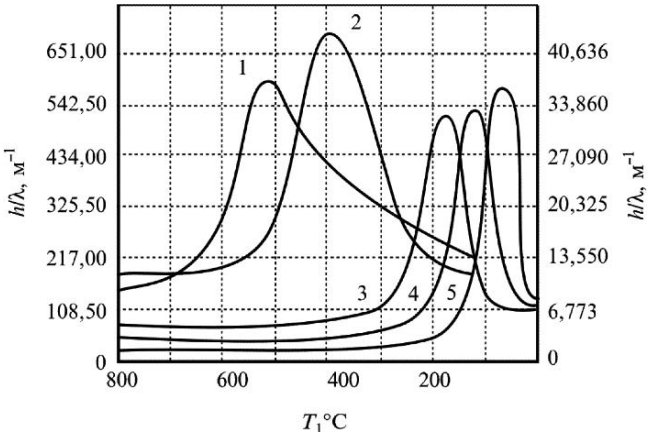

Fig. 4.1. Dependences of heat-transfer ability h/λ for different fluidic medium vs. temperature of a cooled surface [107]. (1) heavy oil; (2) light oil; (3) water at 20°C; (4) water at 60°C; (5) water at 100°C. Scale for curves (3)–(5) is on axis ordinates at the *left*; Scale for curves (1) and (2); is on the *right*; h is coefficient of a convective heat exchange, λ is coefficient of thermal conductivity

ambient temperature reaches a critical value. The loss of integrity in specimens cooled in liquid medium without boiling can be recorded either by a sharp change in the amplitude of the acoustic signal [94, 380], or visually by inspecting the specimen for surface cracks [94]. In many cases, the loss of integrity is evaluated by the relative drop in strength σ_i [94, 105] measured with respect to the original strength σ_i, or by use of non-destructive testing techniques – by measuring the damping decrement or electric resistance [106] for conducting materials.

The nature of the coolant and eventual boiling during cooling are factors that affect, in an unpredictable manner, the heat transfer coefficient (Fig. 4.1), and insufficient knowledge of this relationship can pose problems for the quantitative evaluation of heat resistance. If the temperature dependence for the heat transfer coefficient in the given medium is known, then the mean integral temperature drop in the cross section of the specimen is $\Delta T_{\mathrm{m}} = \Delta T f(Bio)$, where ΔT is the difference between the initial temperature of the heated specimen and the temperature of the medium T_{m}; Bio is a criterion defined as $Bio = lh/\lambda$ (h is the heat transfer coefficient; λ is the thermal conductivity; l is the characteristic size of the specimen); in the general case, it can be determined by numerical computation starting from boundary conditions of the third kind [68]. The main error in ΔT_{m} (composed of the errors in h and λ) is associated with the Bio criterion. If the uncertainty in Bio is 20%, then the error in evaluating ΔT for cylindrical specimens of size $d = 6\,\mathrm{mm}$ and with $\lambda = 5 - 50\,\mathrm{W\ m^{-1}\,K^{-1}}$ lies within 2–10%.

Cooling in Water

Water, frequently used as a coolant in testing materials for heat resistance, is capable of generating destructive temperature drops in small-size specimens. In early works [19, 32, 94, 105] the estimate of thermal stress resistance was realized on maximum temperature drop ΔT between a surface of a body T_s and temperature of medium T_m, at constant value $Bio = hl/\lambda$. Actually, coefficient of a convective heat exchange is function of the surface temperature and assumption of constancy h calls an error in definition of temperature difference in a specimen up to 20% at mean $Bio \gg 1$.

In greater extent lapse of definition of the thermal stress resistance depends on chosen value of a convective heat exchange h. Values of the stationary heat exchange $h = 3 \times 10^4\,\mathrm{W\,m^{-2}\,K^{-1}}$, and a critical heat flow $q_m = 1.5 \times 10^6\,\mathrm{W\,m^{-2}}$ for the water boiling at atmospheric pressure are the next according to [108]. At underheating of water on 80°C up to boiling temperature increases q_{cr} up to $6 \times 10^6\,\mathrm{W\,m^{-2}}$ and further raise $q > q_{cr}$ transforms boiling condition to steady film regime, reducing h up to $1.2 \times 10^3\,\mathrm{W\,m^{-2}\,K^{-1}}$.

Regrettably, the available data on heat exchange in water are contradictory. The computational data in [90, 91] show that the maximum values of $h = f(T)$ lie in the range of $1\text{–}4 \times 10^4\,\mathrm{W\,m^{-2}\,K^{-1}}$($T$ = 130–150°C) and depend on the size, shape and surface condition of the specimen. Direct measurements of a silver ball of diameter $d = 20$ mm cooled in a nonstationary regime showed [107] that heat transfer qnefficient h reaches a maximum value of $2.8 \times 10^4\,\mathrm{W\,m^{-2}\,K^{-1}}$ for an initial temperature of the specimen of 220–240°C and then gradually decreases to a constant value $2 \times 10^3\,\mathrm{W\,m^{-2}\,K^{-1}}$ at temperatures higher than 500°C.

Detailed studies of heat exchange on the surface of specimens heated to 1,200°C were carried out in bubble and film boiling regimes in water [84]. The determination of the non-steady heat transfer on the surface of hot specimens quenched in a large volume water was performed by:

(a) The measurement of the temperature in the centre of a small specimen during cooling when Bi < 0.4.
(b) The measurement of the temperature fields registered for a period of time by a system of thermo-couples fixed in a large specimen.
(c) The measurement of temperature over a period of time by one or two thermo-couples fixed in small or large specimens of known thermal–physical properties. The heat transfer in this case is determined by solving the inverse problem of the thermal conductivity [109].

The specimens as balls, solid and hollow cylinders having the diameter from 2 to 60 mm made of Cu, Ni, stainless steel, graphite with different surface finish, were used to measure the heat transfer. The temperature was measured in all tests by chromel–alumel thermo-couples ($d = 0,1$ mm) covered with an insulating layer. The thermo-couples were soldered using a silver alloy to the inner wall (0.5 mm in thickness) of the hollow cylinder. The specimens

as hollow cylinders were thermally insulated and tightly sealed using a fitment in order to prevent the heat transfer from the tube face surface. The junction of the thermocouples was fixed in a drilled orifice of the solid cylinder filled with an In–Ga liquid alloy. The insulated thermo-couples were incorporated into the graphite ball sample <60 mm in diameter using a mixture of furfuryl alcohol and graphite powder followed by curing and graphitization at a high temperature. The thermo-couples junctions were pinpointed from X-ray photographs made in three projections. Measurement of the thermal heat transfer was made on a special installation. A sample is heated in an inert atmosphere of a furnace, the temperature measured by the thermo-couple was recorded by a logging potentiometer. A device to automatically transfer the sample into a water-bath and an oscilloscope for thermometering the sample during quenching are switched on simultaneously with the help of a relay, when a pre-set temperature is attained. The shift of the boiling regimes is fixed by the change of the amplitude of the acoustic emission signal detected by a transducer operating in the frequency range 1–20 of K_c. The so-called exponential method [107] derived from the time varying measurements of the sample temperature at small values of $Bio < 0.4$ was used as a basic method. In this special case, the temperature in the sample's centre somewhat differed from the surface temperature and the quantity of heat Q from the cooling surface S of a body having an m mass and a c heat capacity in a time $\mathrm{d}\tau$ is expressed by the relation:

$$Q\mathrm{d}\tau = mc\mathrm{d}T = h(\tau)(T_s - T_w)S\mathrm{d}\tau$$

and the coefficient of heat transfer is given by:

$$h(\tau) = (mc/S)(\mathrm{d}T/\mathrm{d}\tau)l/(T_s - T_w),$$

where T_s and T_w are, respectively, temperatures of the sample's surface and water.

The smooth temperature curve attests the existence of pure bubbling on the surface. The drastic point of inflection on the temperature curve and the increase in the amplitude of the acoustic signals are evidence of the regime change from film to bubble boiling. The transient heat transfer in quenching hot samples from the temperature level $T = 250°\mathrm{C}$ occurred exclusively through bubbling. When the samples were heated in the range 250–350°C the heat transfer may occur both through pure bubble boiling and also through alternating boiling regimes.

It is shown that the intensity of heat transfer of heated body at 300°C was reduced from $3.7 \times 10^4\,\mathrm{W\,m^{-2}\,K^{-1}}$ to $0.5 \times 10^4\,\mathrm{W\,m^{-2}\,K^{-1}}$ with the water bath temperature rise from 20 to 100°C. The sample movement velocity changed from 2 to 25 cm $\mathrm{s^{-1}}$ in the temperature range of the developed bubble boiling had no effect on the coefficient of heat transfer.

The coefficient of film heat transfer statistically varied between 0.3 and $0.7 \times 10\,\mathrm{W\,m^{-2}\,K^{-1}}$ independently of the sample size and thermal–physical properties in accordance with [110].

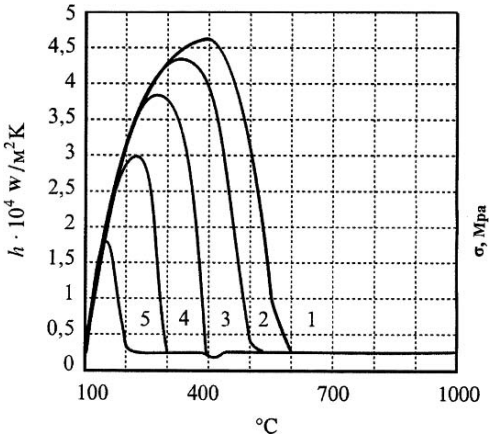

Fig. 4.2. Temperature dependences of non-stationary heat transfer factor h of samples heated up to T, when samples with various thermal–physical complex (rc/λ) cooled in water of great volume ($T = 20°\mathrm{C}$). 1. $T_{\mathrm{cr}} - 600°\mathrm{C}$, 2. $T_{\mathrm{cr}} - 500°\mathrm{C}$, 3. $T_{\mathrm{cr}} - 400°\mathrm{C}$, 4. $T_{\mathrm{cr}} - 300°\mathrm{C}$, 5. $T_{\mathrm{cr}} - 200°\mathrm{C}$

Using a regular regime method [111], the temperature dependence of the heat exchange process was established (Fig. 4.2) and evidence was obtained showing that the heat transfer coefficient in the bubble-boiling temperature range is virtually independent of the size, thermal characteristics and surface condition of a specimen heated to 600°C.

The obtained relations $h = f(T)$ permit quantitative evaluation of the heat resistance of specimens heated to 600°C and cooled in water at 25°C with an accuracy no worse than 15%. If heat resistance tests are carried out at specimen temperatures higher than 700–900°C, one must take into account the thermal hysteresis of heat transfer in transition from film to bubble boiling regime, markedly affected by the thermal–physical complex rc/λ of the tested sample in radius r [84]. Neglect of these features may lead to wrong estimates of heat stress resistance R and R'.

It should be noted that the heat transfer relation $h = f(T)$ was obtained on tests carried out in distilled water. Mineral salts dissolved in water assist in breakup of the vapour film on the surface of the specimen which causes a change in the bubble-boiling temperature range and maximum attainable heat transfer. This property can be used for increasing both the cooling rate and the temperature drop in the specimens. Thus, addition of 5 wt% of NaCl to distilled water increases the cooling rate nearly twofold and shifts the heat transfer maximum towards higher temperatures by about 300°C [107]. The test method using intensive cooling without boiling of water on surface of a specimen, is offered in [112].

The cooling method in which heat from the heated specimen is rapidly removed by the boiling water makes it possible to test heat resistant materials

($\Delta T_m = 300$–$400°C$) using specimens of various shapes; however, here the temperature range is rather narrow (100–600°C) and the heat loading rate varies little. Cooling in water and other media causes the appearance of cracks in the specimen, however, without its disintegration, which makes visual observation of failure uncertain and necessitates the use of indirect methods for assessing failure, for example, by measuring the loss of strength [94], or the change in the damping decrement [106] or electric resistance [18] or thermal diffusivity [113].

The procedure of an estimation of the thermal stress resistance at crack spreading from imprints of the indentor, saves from necessity of trial of a great quantity of specimens for construction of probability allocation of the thermal stress resistance and besides allows to characterize fracture toughness of a material [52, 93, 114].

Cooling in Mineral Oils or Polymeric Media

The use of mineral oils of varied viscosity as cooling media does not make heat exchange under boiling conditions a simpler process; here, as compared with water, the heat transfer coefficient decreases appreciably (Fig. 4.1). For this reason, the use of oils is recommended only if water has a corrosive effect on the tested specimen. Recently, aqueous solutions of organic compounds have been used as quenching media; for example, 5–10 wt% solutions of polyvinyl alcohol, sodium polycrylane, etc., are several times more efficient as coolants than mineral oils, especially at elevated temperatures up to 600–800°C. However, to the best of our knowledge, no polymeric solutions have been used in testing for heat resistance.

Cooling in Molten Salts and Metals

In the use of this technique of cooling, no boiling occurs, and the heat transfer coefficient usually shows a weak monotonic dependence on the temperature. For this reason, quantitative evaluations of the heat resistance give results more reliable than those for cooling in water and aqueous inorganic and organic solutions. Furthermore, tests can be carried out at higher temperatures if, for example, there is need to evaluate the heat resistance of the material in the visco-elastic state, since the boiling or decomposition points are high enough, and the heat transfer coefficient in a melt at high temperatures is higher than in mineral oils under the same conditions.

Cooling in Gas–Dust Media

Testing materials for heat resistance in gas–dust streams requires the use of more sophisticated equipment. Cylindrical specimens 6–25 mm in diameter and up to 70 mm in length, pre-heated to the desired temperature in a furnace, are placed in a chamber with air-borne particulate matter, either Al_2O_3

(particle size of 38–231 μm) [32], or silicon carbide (particle size of 150–170 mesh) [104].

Direct measurements at different air flow rates showed that the heat transfer coefficient changes smoothly from 0.3×10^3 to $0.8 \times 10^3\,\mathrm{W\,m^{-2}\,K^{-1}}$ according to [104] and from 0.4×10^3 to $0.6 \times 10^3\,\mathrm{W\,m^{-2}\,K^{-1}}$ according to [32]. The temperature drop to failure ΔT was determined either visually [32, 104], or by measuring the sharp drop in the strength of the test specimen [32]. ΔT was the statistical mean of the results for five specimens at least. Since the heat transfer coefficient is determined by direct measurements with a sufficiently high accuracy, the quantity ΔT is used [68] to calculate the integral mean drop ΔT_m, and the breaking thermal stress σ_t is found with a reasonably small error.

Cooling in Gas Streams

Cooling with gas streams is carried out using facilities adapted for testing large, low heat-resistance specimens [103], or pre-cracked specimens [115]. In both cases, disk specimens are used; in [103], the side face of the disk is cooled through annular spaces, keeping the disk edges thoroughly insulated, whereas in [115], the central zone of the edge face of a thin disk 50 mm in diameter is cooled. Methods of local cooling of a surface by velocity gas stream [116–118] are used. Also, tests were conducted where no gas stream was used, and cooling of the specimen surface was through radiation [18]. The temperature drop to failure ΔT is determined either visually [18, 103, 115], or by a sharp decrease in strength [115] as the temperature was allowed to rise. Furthermore, in [115] a finite-element method was used (with allowance for uncertainty in the heat transfer coefficient over the disk face) to determine temperature drop and thermal stresses in the radial direction of the specimen.

The gas-stream method technically is more complex than the water-, gas- and melt-cooling methods and should preferably be used only if the gas medium is an important factor for evaluating heat resistance.

The air-cooling technique is also used in cyclic tests of specimens or full-scale parts heated in spacious and complex gas-dynamic test benches which will be discussed later.

4.3 Heating Methods of Testing for Thermal Stress Resistance

Technically, the heating methods are more varied than the cooling methods; along with the traditional techniques of radiation heating using furnaces, gas streams and molten metals, they include new advanced techniques (heating by plasma, laser radiation, electron beam, arc and induction) that permit the stress state to be varied at higher temperatures, higher heating rates, and in various corrosive media.

Testing by Radiation Heating

Hasselman and coworkers discussed non-uniform temperature fields and stresses; generated by radiation heating and capable of causing failure in opaque [119] and semi-transparent materials [120]. The accomplished theoretical analysis with instances of rated estimates of a thermal stress resistance gives the useful ground for development of the experimental methods.

The experimental methods for radiation heating of brittle materials and quantitative evaluation of heat resistance were considered systematically and comprehensively in [16, 17, 26, 121]. It was noted that the current methods of radiation heating are convenient to classify by the types of specimens used.

Methods for Testing Hollow Cylinders or a Set of Annular Specimens

A widely used technique of long standing is the method of radiative heat flow in which hollow cylinders of different length [122] or a set of cylindrical rings [16, 122–125] heated from the inside by a hot rod are used; heating is done either in air [123, 124], or in a vacuum [16, 122]. The testing unit has for its main component a high temperature furnace (power of 3–6 kW) equipped with a rod-like heater of graphite, silicon carbide [123] or tungsten [16]. A set of annular specimens with height $H \geq 8R_{\mathrm{h}}$ (R = 20–35 mm) are mounted coaxially with respect to the central heater using a micrometer [124] or centering bushings which serve simultaneously as internal heat shields to moderate axial flow [16].

The heat resistance of the material is determined by the breakup temperature drop at the instant of the specimen's failure; the instant of failure is recorded by rupture of a conducting film applied to the surface of the non-conducting specimens [123, 124], or visually through an inspection window in the water-cooled casing of the furnace, or (if failure is clearly distinctive) acoustically [16]. As the temperature profile through the cross section of the specimen is thus known, the integral mean temperature drop ΔT_{m} is easily found [16, 122].

The temperature range under steady-state conditions of testing is rather narrow and has an upper boundary of 400°C on the inner surface of the specimen. Under non-stationary conditions, it extends to 700–800°C for a maximum heater temperature of 1,250°C [124]. Under program-controlled conditions with the heating rate close to linear [16, 124], accelerated tests can be carried out with an accuracy of measurement no worse than that under stationary conditions. Numerical analysis of the thermal stresses in this case poses no problems.

All of these experimental units with radial heat flow are more complex in design than those using fluid coolants. Furthermore, special specimens of rather large size are needed for testing, which does not make testing of new

materials a quick procedure. However, unlike with the cooling methods, failure is clearly fixed as the specimen breaks up into parts on reaching the ultimate load.

Method for Testing Cylinders and Disks

A unit for heat resistance testing by radiation heating under nonstationary conditions includes, as a rule, a hot and a cold chamber. In the unit described in [16], the tungsten heaters in the upper hot chamber (required power of 7 kW) permit the temperature of the specimen to be raised to 2,200°C in an inert gas or in a vacuum, whereas in a cold chamber with a molybdenum heater, the specimen can be preheated to 300–900°C. To ensure a sharper temperature drop, the lower heater can be replaced by a water-cooled coil. Transfer of specimens from the low to the high-temperature chamber and the opposite way is affected by an electro-mechanical drive.

The authors of [126] used an uncommon technique in which heating is done by means of a film heater applied to the side face of a disk specimen. The change in the radial temperature profile over time to failure is monitored by six radially arranged thermocouples. Testing of the electroconductive ceramics used in varistors is performed by means of transmission current of various force through a specimen and making temperature drops and stresses down to an emersion of the first indications of fracture [127].

A unit was described in [98] where the specimen in the hot chamber (Fig. 4.3) is heated in an inert medium or in a vacuum to 2,000°C by means of heater 1, which is a hollow graphite cylinder placed inside an inductor. The heater is shielded from the surroundings by water-cooled double quartz tubes. In order to create a uniform temperature field along the length of the graphite heater, the heater's edges were protected by molybdenum or graphite shields. The temperature of the heater is monitored by an optical pyrometer. After the heater has reached the desired temperature, specimen 2 (protected on the side face by shield 3) is transferred pneumatically from the cold chamber to the hot chamber as piston 4 is driven by pressure applied from beneath. After the specimen has been positioned in the middle of the heater, shield 5 is released and allowed to drop by gravity, and the side face of the specimen is exposed to the heater. The instant at which the specimen fails is recorded by a piezoelectric sensor connected to the specimen through a sound duct; the signal from the sensor is transmitted through an amplifier to a recording oscillograph which is switched on automatically after shield release.

The transfer of heat from the heater at temperature T_h to the specimen's surface at temperature T_s can be treated in terms of constant heat flow $q =$ const. with an accuracy better than 5% if the surface temperature is not in excess of 0.475 T_h [119]; this makes determination of the heat resistance a much simpler procedure.

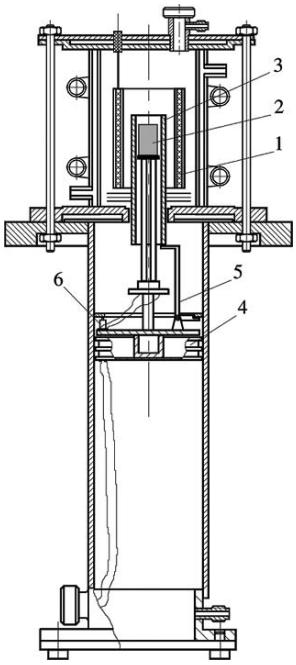

Fig. 4.3. Radiation heating unit for testing cylindrical specimens for thermal stress resistance

The heat flow is determined experimentally in a regular regime [111] by measuring the temperature over time at a single point of the specimen:

$$q = C\gamma l/2(\mathrm{d}T/\mathrm{d}\tau), \tag{4.2}$$

where the heat capacity per unit of volume $C\gamma$ is known.

The maximum relative error in measuring the temperature does not exceed $\pm 0.7\%$; this error is associated with the thermocouple calibration error ($\pm 0.3\%$), measuring device error ($\pm 0.05\%$), and delay effect error ($\pm 0.3\%$) which is caused by the heat resistance at the thermocouple–specimen contact through an In–Ga eutectic at temperature change rates of $<100\,\mathrm{K\ s^{-1}}$. As the heat flow for the system 'heater–specimen' is known, the integral mean temperature drop to failure is determined by merely measuring the heating time to failure τ_f.

The total relative error in the heat resistance composed of the time-to-failure error, heat flow error, temperature extrapolation error and thermal parameter errors does not exceed 10% with a probability of 0.68. As a rule, failure is manifested by complete disintegration of the specimen.

It should be noted that the cylinders and disks used as test specimens are more convenient than hollow cylinders or rings. However, in both cases heat

resistance of the material in terms of ΔT_{m} does not exceed 100°C, and the temperature at failure can be varied only within 300–700°C.

Testing of Prismatic Specimens

Prismatic specimens (note that the prism is a pattern of which numerous commercial refractory articles are made) are conveniently prepared by cutting them out of the full-scale bricks used for lining furnaces. For anisotropic materials, the specimens are prepared in different directions with respect to the anisotropy axes.

Methods have been developed for radiation heating under steady-state and non-steady-state conditions [16, 17]. In the, experimental unit in [17], two flat heaters are used with heat-insulating material applied to two sides of the prismatic specimen. The temperature field of the specimen is monitored by means of thermocouples, and the time of failure is recorded either visually or with an acoustic sensor. Under steady-state heating conditions (Fig. 4.4a), the specimen is heated along the z-axis on edge side $2b$ by a plate heater of width $2r$, and its faces of width $2d$ are cooled by natural convection. Under non-steady-state conditions (Fig. 4.4b), the specimen is intensively heated on the faces of width $2d$ along the z-axis; the other faces are heat insulated. In the former case, tensile stresses and failure occur on the periphery of the cooled surface, and in the latter case, in the central part along the z-axis.

In [17], a unit was developed (Fig. 4.5) for heat resistance testing of prismatic specimen 4 in which one face on one side was heated by electric bar heater 3. Other faces of the specimen were coated with heat-insulating materials 2 held in steel frame 1. The specimen can be heated linearly at a rate of up to $300\,\mathrm{K\,min^{-1}}$ set by a programmed controller; the temperature profile cam be measured using thermometric unit 6 positioned close to the specimen. The temperature having been measured at several points of the thermometric block, one can determine the heat flow using (4.2), here knowledge of the heat transfer coefficient is not necessary.

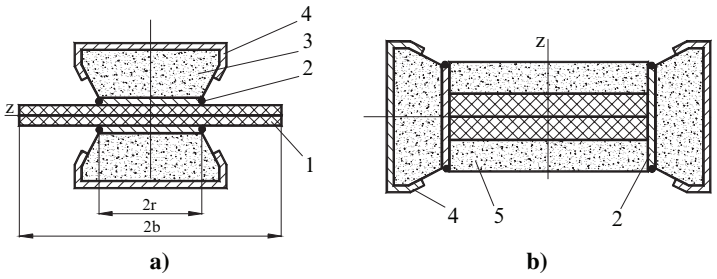

Fig. 4.4. Loading schemes for prismatic specimens in steady-state (**a**) and non-steady-state (**b**) heating: (1) specimen; (2) heater; (3) heater insulation; (4) casing; (5) specimen insulation

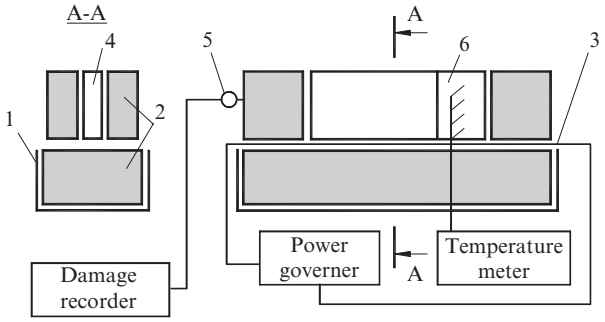

Fig. 4.5. Flow chart of a unit for one-sided heating of prismatic specimens

The heat flow and time to failure (recorded by acoustic sensor 5) are used to calculate the integral mean temperature drop ΔT_{m} and the maximum tensile stress σ_{t}. Because of the simplifications adopted for the heat transfer conditions and thermal stress analysis of a prismatic body of finite dimensions, the evaluation of the thermal breaking stress for prismatic specimens is less reliable as compared with cylindrical axially symmetric specimens.

Method for Testing Specimens Heated in a Gas Stream

The wide use of ceramic materials in aviation and aerospace engineering under conditions of high-temperature gases of different oxidizing ability necessitated the development of methods for testing these materials using various gas-dynamic testing units [16, 128–131]; these units, although costly and complex in construction, permit one to set conditions closely mimicking real operating conditions.

In the unit in [16], tests for heat resistance are carried out under steady-state conditions using specimens in the form of a hollow ring or a cylinder heated to 2,200°C in a gas jet of propane–butane–oxygen mixture. Several ring specimens 50 mm in diameter with a total length of about 8 diameters are placed in a steel casing lined with a refractory material. The specimens are heated by a gas jet under controlled conditions to reach the desired temperature and temperature drop. As a rule, the Reynolds number of the gas jet lies within 3,000–6,000, with minimum risk of erosive surface damage.

In another unit [128], tests are carried out in a non-steady-state heating regime under conditions of the third kind at a constant temperature of the gas jet (kerosene + air).

The time of failure is recorded either visually, or by measuring the resistance of the conducting film applied on the (non-conducting) specimen; the corresponding temperature drop is measured by means of thermocouples fitted in the specimen.

The gas-fired (propane + air mixture) unit described in [130] is equipped with a heat flow meter which permits determination of the gas-to-surface

heat transfer coefficient, thermal conductivity, and cross-sectional temperature profile in specimens 25 mm in diameter. The heat resistance tests are carried out in a heating-and-cooling cycle regime; the specimen is cooled with a jet of cold air to different temperatures until visible signs of failure become apparent.

Gas burners operating on oxygen (or air)–kerosene mixtures are also used in the study of heat resistance or surface crumbling in rocks [131].

A simple unit convenient for use in the laboratory for testing materials with $\Delta T_m < 100°C$ was described in [132]; here the specimen is heated in a jet of hot air (750°C) powered by a 2 kW electric heater. The air jet with a flow rate of $15\,l\,h^{-1}$ and a velocity of $90\,m\,s^{-1}$ is directed from a nozzle onto the face of a disk specimen, 19 mm in diameter and 2–3 mm thick. The radial temperature drop is measured by means of thermocouples fitted into the water-cooled rear face of the specimen; the time of failure is recorded either visually or by a sharp rise in the temperature. The unit permits measurement of the temperature profile and consequently determination of the integral mean temperature drop.

Method of Testing for Heat Resistance by Heating in Molten Salts and Metals

The equipment for conducting such tests is rather simple. Most commonly, a furnace equipped with a Ni–Cr alloy (to 800°C) or a silicon carbide heater (to 1,000–1,100°C) is used for melting salts and metals. The vessel for holding molten salts is made of stainless steel, and for molten metals, of ceramic refractory or, possibly, of stainless steel also; however, in this case there is a risk that the molten metal may interact with the material of the vessel. The test specimens in the form of a ball [100, 133], a disk, a cylinder (solid or hollow) or a beam [51] with asbestos-insulated edges, kept at room temperature or, as needed, precooled (down to a maximum of −200°C in liquid nitrogen) or preheated (up to a maximum of 600°C) are quickly placed in a bath with the molten medium. The time to failure T_f is recorded either acoustically [133], or using a sensor operating in the frequency range of 1–20 kHz [51]. Failure can be determined visually [100] using penetrating dyes for inspection of specimens heated stepwise (in intervals of 10–15°C) in the melt. The failure temperature is assumed to be the temperature at which 50% of the ten specimens tested fail. The temperature field at failure is determined by the numerical method, using the known properties of the specimen (thermal conductivity λ, thermal diffusivity a), and the measured temperature of the medium T and time to failure T_f or the failure temperature alone (on the basis of 50% failed specimens). In [133], heat transfer coefficient h was assumed to be constant ($0.8 \times 10^4\,W\,m^{-2}\,K^{-1}$) over the entire temperature range. Glass spheres 24.5 mm in diameter precooled to −200°C failed within 1–8 s after they were placed in a bath of molten tin at 700°C, so that the temperature at the center of the sphere at the time of failure was virtually

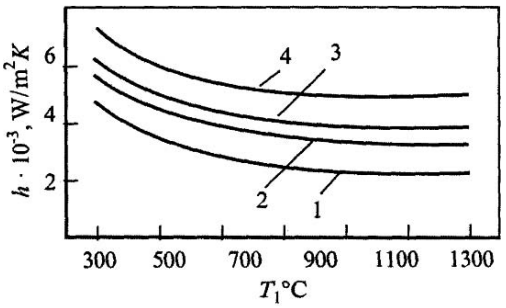

Fig. 4.6. Heat transfer coefficient of a cylindrical specimen heated in molten tin as a function of the temperature; 1–4 refer to $B/\lambda = 8 \times 10^{-4}$; 4×10^{-4}; 3×10^{-4}; 1.5×10^{-4}, respectively (B is the wall thickness; λ is the thermal conductivity)

constant. The relative error in determining the breaking tensile stress at the center of the sphere due to possible relaxation of surface stresses and a change in the material properties with the temperature does not exceed, according to [133], 10%.

In [51], heat transfer coefficient h was determined with an error not in excess of 10%. The temperature curves were measured by a regular heating method [111] and treated by graphic differentiation; thermocouples were used for measuring the temperature of the test specimens, which were solid and hollow cylinders with different wall thickness B and thermal conductivity λ. For an accurate analysis of the temperature field, the non-linear temperature dependence for h and the dimensional term B/λ should be taken into account (Fig. 4.6). The error in ΔT_{m} and the thermal stresses as estimated within the framework of the decoupled quasi-static theory of thermoelasticity [67] was 15% and was mainly associated with the uncertainty in measurement of the heat transfer coefficient. The temperature range for measuring the heat resistance was $\Delta T_{\mathrm{m}} = 300$–$400°\mathrm{C}$.

By varying the initial temperature of the specimen, one can determine the heat resistance within a temperature range bounded from above by the melting point of the metal. In [51], the heat resistance of titanium, yttrium and zirconium hydrides was measured in the temperature range of -200–$700°\mathrm{C}$, with the maximum temperature of the tin melt not exceeding 950°C; no visible corrosion effect was observed. The tin bath method permits testing of highly porous materials, as was successively demonstrated on specimens of ZrC and Si_3N_4 with porosity reaching 70%; molten tin, because of its high viscosity and low wettability, does not enter the pores. As in all heating methods, as the thermal tensile stresses in the central zone of the specimen attain a critical value, the specimen, as a rule, disintegrates [49]. However, under the conditions of high thermal loading and a short time to failure, the peripheral zone of the disk specimen undergoes spalling because compressive stresses reach the critical value [134].

Plasma Method of Heating in Testing for Heat Resistance

Most plasma testing units [135–138] are used for the comprehensive evaluation of the heat resistance as well as the erosion resistance and volatility of the materials and elements of the interior wall of nuclear reactors subjected to powerful plasma pulses of short duration; the tests are carried out in a single stepwise thermal loading regime or a cyclic thermal loading regime until visible signs of failure become apparent. A plasma torch of 32 kW power was used for testing heat-protective composite materials in the corrosion–erosion medium of an argon plasma with varied addition of oxygen [137]. A plasma beam 10 mm in diameter was directed, for a specified period of time, onto the surface of a disk specimen 30 mm in diameter and 5 mm thick at a distance of 50 mm from the nozzle edge. The side faces of the specimen were heat insulated. The temperature range of testing is bounded from above only by the melting point of the material tested and in most cases does not go beyond 1,500°C. The temperature on the front face was measured by an optical pyrometer, and on the water-cooled back face, by thermocouples. The temperature of the water supplied at a known rate was used to measure the mean heat flow. The thermal stresses at failure in the composite specimen were determined using a special finite-element program [136] starting from measurements of the temperature drop between the front and back faces of the specimen and the heat flow.

A unit equipped with an electric-arc plasma torch capable of generating heat flow in the range of 1×10^5–$5 \times 10^7\,\mathrm{W\,m^{-2}}$ was designed for testing materials for heat resistance under laboratory conditions [139]. The diameter of the argon plasma jet was 10–12 mm. The edge face of the test specimen 8–9 mm in diameter and 30–50 mm long was heated uniformly, and the side face of the specimen was shielded from heat by a graphite screen. Under such heating conditions, a non-steady-state temperature field is generated along the length of the specimen. Plasma heat flow is measured prior to testing by a water calorimeter. During testing, the water-cooled flap placed in the path of the plasma jet was opened, the time to failure was recorded by a piezoelectric sensor, and the temperature was measured by means of two loop-type thermocouples at two points on the specimen surface. The error in the time to failure recorded by an electric stopwatch did not exceed ±3%; the time-to-failure constant was 0.045 s.

Using the temperatures measured at two points in the heated zone of the specimen, the temperature field was determined by extrapolation. The temperature field can also be evaluated by the constant heat flow q measured during the experiment. An approximate (within ±20%) solution of the problem of thermal elasticity for a semi-infinite cylinder with an arbitrary temperature profile along the length was given in [80]. The axial tensile stress

$$\sigma_z \approx 0,119\alpha EqR/\lambda$$

reaches the maximum at the axial point spaced by distance $Z = 0.78R$ from the end face at time $\tau \approx 0.26R^2/\lambda$. In [140], a more accurate estimate of the thermal stresses (±5%) throughout the volume of the cylinder was given. This method, applied to specimens of aluminum oxide and zirconium carbide, showed good agreement between the experimental and computational values of the time to failure and the surface failure coordinate. The ultimate failure stress σ for this type of loading was identical to the bending strength.

A convenient method of cyclic thermal loading by means of a plasma torch was described in [141]. Here a set of 15 beam-like specimens >40 mm in length, fixed vertically in a cylindrical rotating holder, were heated to about 2,000°C within 2 s. Thermal loading was controlled by varying the distance between the torch nozzle and the specimen and the rotation rate of the holder. The temperature at the surface and at a depth of 0.35 mm was measured by refractory-coated thermocouples with a time constant of 0.3 s. The probable error in measuring the transient temperatures did not exceed 20%. The temperature and stress fields and the probability of failure were calculated using a special computer program. Plasma heating techniques permit testing of high-refractory materials with $\Delta T_m > 900$°C with varied heating rates; however, the experimental units, especially those of high power, are costly and require sophisticated equipment, and their use is justified in special studies of plasma-generated thermal loadings and corrosion–erosion effects.

Laser and Electron Beam Methods of Testing

The advent of new high-intensity sources of energy stimulated the development of new methods of testing for heat resistance using laser [136, 137, 141–145] and electron beam [58, 134, 146, 147] units. In these methods, the quantitative analysis of heat resistance is carried out using advanced techniques of measuring temperature fields, heat flows, occurrence time and propagation of cracks in a thermally loaded body.

In one of the widely used methods, the central zone of a disk specimen is heated by an electron beam (Fig. 4.7). This electron-beam method, suitable for testing conducting materials implemented in 1972 features a vacuum chamber (no higher than 0.003 Pa) and an electron gun (electron beam 10–15 mm in diameter with smoothly controlled output power of up to 5 kW by varying the cathode temperature and electron energy of 20 keV) [77]. The test specimens were disks 20–40 mm in diameter and 4 mm thick, the hot-spot diameter could be varied within 3–8 mm and the heat flow density q (measured by calorimeter 1) could reach 8 MW m^{-2}. The q profile across the hot spot was close to normal. As needed, the back face of the specimen could be cooled (using water, liquid nitrogen, or an inert gas). To generate a symmetric thermal loading zone, the axis of the specimen could be aligned with the axis of the electron gun (see Fig. 4.8). Movable water-cooled diaphragm 6 with a hole for transmitting the central part of the electron beam was placed in front of specimen 4. Movable water-cooled shutter 5 between the diaphragm and the

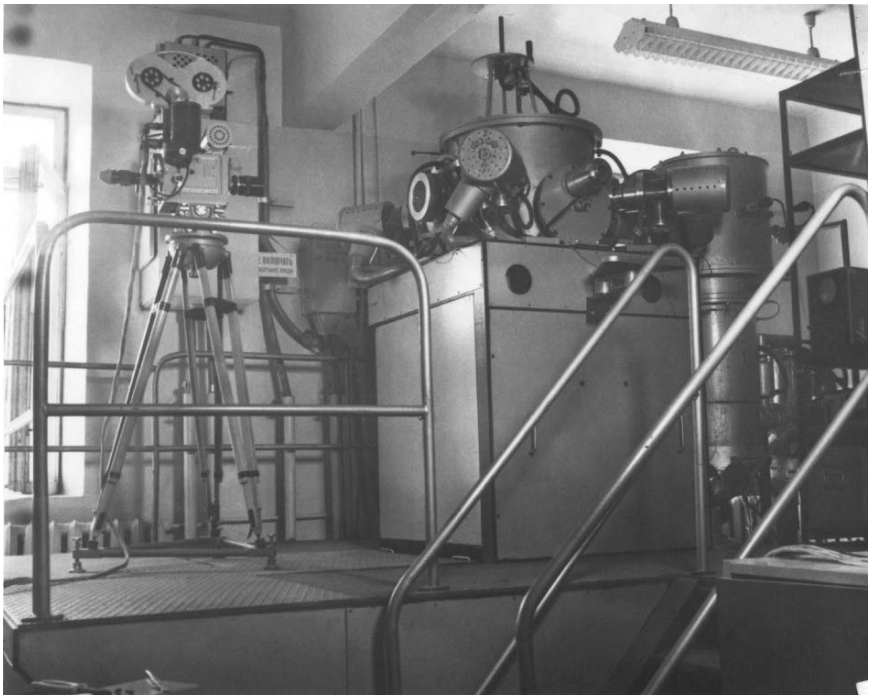

Fig. 4.7. General view of electron-beam unit

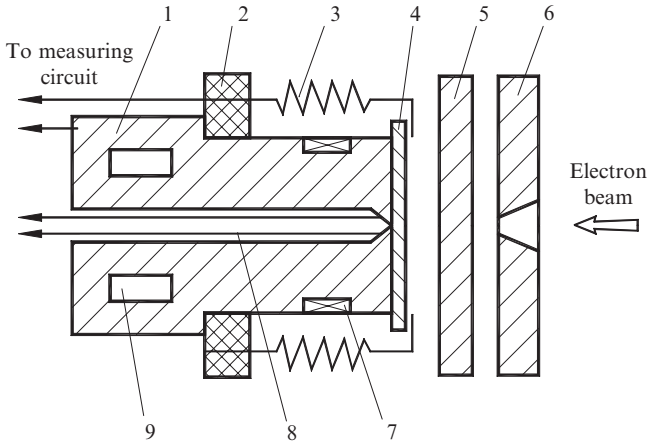

Fig. 4.8. Schematic diagram of a unit for electron beam heating of disk specimens

specimen is used for aligning the electron beam relative to the diaphragm and for tentative setting of the thermal loading level.

After removing the shutter the specimen was loaded with the needed amount of heat. The amount of heat per unit of time Q is determined by the energy parameters of the electron beam:

$$Q = \rho U I_0,$$

where U is the electron gun accelerating voltage; I_0 is the current passing through the specimen and recorded by a loop oscillograph; ρ is a coefficient that takes into account the reflection of electrons as a function of the atomic number of the material studied. With an accuracy of $\pm 10\%$, the value of ρ can be set at 0.95 for a wide range of materials. The heat flow can be determined with satisfactory precision calorimetrically by measuring the flow rate of the cooling agent (flowing through channel 9) and its temperature (measured by a battery of thermocouples with electrode diameter of 0.2 mm was used). The mean square error in measuring the heat flow did not exceed 6%. The initial temperature of the specimen cooled by liquid nitrogen was about –190°C; to raise it to 1,000°C, electric heater 7 was used. The initial temperature of the specimen was measured by thermocouple 8. The time of failure was determined by the break in the electric connection between calorimeter 1 and the specimen, pressed against the body of the calorimeter by means of springs 3 and insulating sleeve 2.

Heating of thin disks ($H/R < 0.1$, where H is the height (thickness) and R is the radius of the disk) generates a plane stressed state in them [77]. For the case of $H/R > 0.2$, that is, virtually for a finite cylinder, stress analysis becomes more complicated [58, 59].

In intense heating of short duration, the failure of brittle materials is confined within a narrow zone of compressive stresses and is kinetic in character. The ultimate thermal loading in the compressive zone is determined by the compressive stress gradient [51, 58, 59].

The critical duty rating of thermally loaded structural elements, for example, laser mirrors of copper, molybdenum, tungsten, etc., depends on irreversible changes associated with plastic strain [148–150] rather than on brittle failure as is the case with ceramics. Therefore, in cases where local thermal loading comes from electron beam or laser sources, a laser holographic interferometer [148] is used to control hot-spot movements on of the specimen surface. In the elastic strain region, normal displacements of the heated surface and thermoelastic stresses in a finite cylinder determined analytically are in agreement with experimental data. The circuit design of an interferometer is assembled directly on electron beam installation (Fig. 4.9). Elements of optics are fixed on steel slabs, one of which 8 is disposed inside of the camera and is rigidly interlinked to its inferior cap, another 9 is fixed on a jamb 6 supporting a vacuum chamber. The pulsing multimode ruby laser OGM-20/10 is used as a light source which generated radiation pulses by duration of 30 ns with energy 0.6 J. The interferometer is built on the two-beam circuit design

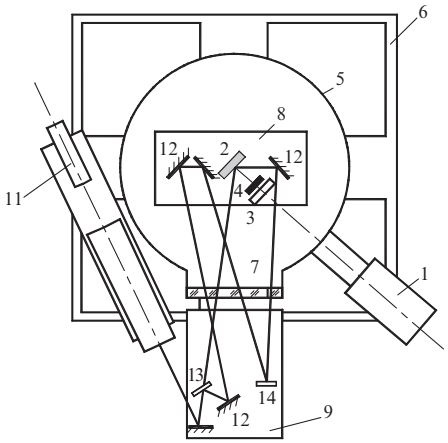

Fig. 4.9. The circuit design of the unit [148]: (1) electronic gun; (2) specimen; (5) diaphragm; (4) cut-off plate; (5) vacuum chamber; (6) jamb; (7) window; (8, 9) slabs; (10) laser OGM-50; (11) laser LG-78; (12) mirrors, (13) beam splitter, (14) photoplate

in which the laser radiation beam dilated by means of a telescope is divided on two waves, one of which is guided on a specimen, another on a reference mirror. The waves reflected from rotary mirrors interfered in a plane of a photoplate. Orientation of an objective beam, under an angle 35° to a specimen surface is provoked by necessity to ensure normal slope of an electron beam on a specimen and thus providing axisymmetric thermal loading.

Starting up of the laser implemented in the given instant by a signal from impulse generator G5-82 synchronized with control oscillator of electron beam. Adjustment of the optical scheme is executed by means of the He–Ne laser which beam is put in the circuit design through the ruby laser after removal from it of a prism of complete interior reflection. Mention should be made, that for obtaining enough contrasting holographic structure by means of the multimode laser radiation is necessary to combine precisely the structure of subject and reference beams.

The image reconstruction is made by hologram illumination of collimated radiation beam of the He–Ne laser. Copying of interferograms implemented with photographic camera. At interpretation of the interferograms copied on photographic paper, graphical build-up of a displacing profile is used. Value of displacements W concerning edge of a specimen was determined by formula

$$W = n\lambda/2\cos\beta$$

Where n is the order of a dark strip, $\lambda_0 = 0.694$ – laser wavelength, β is an angle between an objective beam and a normal line to a sample surface. The measuring error of normal displacement of a surface is sized up within the limits of $\pm 0.2\,\mu$m.

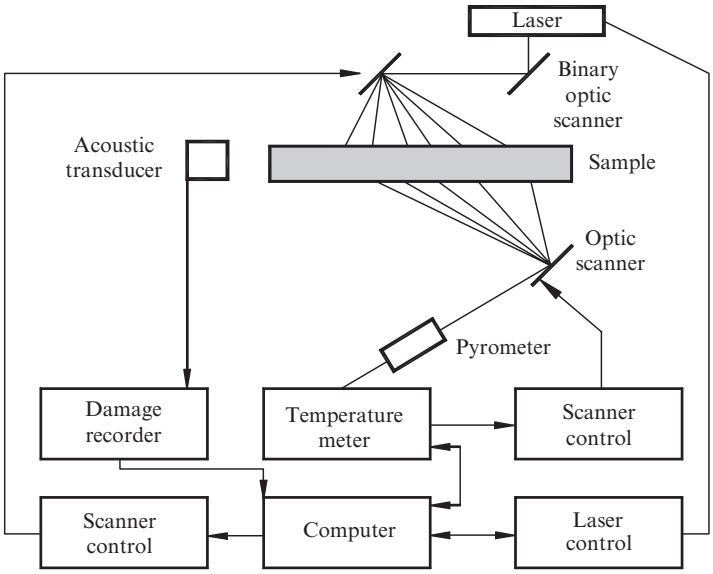

Fig. 4.10. Block diagram of a unit for heat resistance testing of laser-heated specimens

Normal displacement of a heated surface and the thermoelastic stresses of the finite cylinder in the field of an elastic deformation, calculated analytically coincide with experimental data.

In [142], a rather complex laser testing unit was described (Fig. 4.10); this unit, equipped with advanced instrumentation, provides the possibility of testing both conducting and non-conducting materials for heat resistance over a wide temperature-range with varied heating rates and thermal stress distributions throughout the bulk of the specimen.

The specimen (a thin disk) is heated briefly (0.3–0.5 s) with a Nd–YaG laser beam ($A = 1.06$ jam) with output power of 1 kW. Two electronically controlled mirrors permit the laser beam to scan the front face of the specimen and thus to form the desired temperature field. The temperature field on the back face of the specimen is measured by means of a fast-response pyrometer into which the measuring beam is directed from the scanned face via a computer-controlled mirror. During a scan time of 1 s, some 50 measuring points can be recorded. The failure of the specimen is recorded by an acoustic system coupled to a personal computer which makes it possible to measure the temperature field at failure and thus to determine the stress field.

Another, somewhat simpler system for measuring heat resistance was described in [138]. Here the surface of the specimen is heated by a continuous-wave laser beam 6 mm in diameter (λ 10.6 μm, output power of 50 W). A rotating shutter with a slot in it for the laser beam is used to control the heating time. At each measurement, the total beam power and the power profile across

the hot spot (roughly Gaussian) are determined. The temperature at a given point on the face of the specimen is measured by an optical pyrometer; the temperature on the water-cooled back face is measured using thermocouples; the time of failure is recorded acoustically. From the measured heat flow and time to failure, the temperature and stress fields can be determined. Tests for heat resistance are conducted in a single or a cyclic thermal-loading regime; after each load, the specimen is inspected for thermal damage.

Laser and electron beam methods provide for the ample possibility of testing materials with $\Delta T_{\mathrm{m}} > 900^{\circ}\mathrm{C}$ for heat resistance over a wide temperature range with different heating rates and varied localization of the heating zone. However, the electron beam method can be applied to conducting materials only, and the laser method still fails to provide for sufficiently high heating power.

Radiation Methods of Heating with Use of Focusing Mirrors

These methods are based on heating the specimen with a focused beam of radiant energy from high-temperature sources: electric-arc [135], solar radiation [151, 152], high-energy gas-filled lamps [153–156]. In [157], a unit was described featuring an ac carbon arc with power of 4–6 kW and an elliptical cylindrical silver-coated copper reflector with a height of 20 mm and focal distance of 51 mm; in this unit, a cylindrical specimen 5 mm in diameter could be heated to 2,000°C within 4–5 s. Tests for heat resistance were carried out in a cyclic heating regime using water, an air–water mixture, or a compressed inert gas for cooling. The unit is complex in design since it requires automatic instruments to control the arc and rotation of the specimen for uniform heating. The error of analysis is uncertain; presumably, the major sources of error are associated with non-uniform heating of the specimen and with uncertain measurements of the temperature and heat transfer coefficients.

In large and complex units using mirrors 2 and 2.8 m in diameter for focusing solar energy, one can reach heat flows of 8 and 15 $\mathrm{MW\,m^{-2}}$ in a focal spot 10 mm in diameter, respectively, [151]. The heat flow, controlled by means of an adjustable shutter, is measured by a water-cooled stationary calorimeter, the surface temperature is measured by an optical pyrometer, and the time of failure is identified by the drop in the diagram of radial expansion of the specimen. For quantitative evaluation of heat resistance, disk specimens 40–50 mm in diameter and 4–5 mm thick, shock-heated in a central zone with a radius of 5 mm, are used [136].

The units with mirrors for focusing radiant energy from powerful gas-filled lamps appear to be convenient and promising tools for testing. In such a unit [155], disk specimens 30 mm in diameter and 6–8 mm thick are first heated in a vacuum chamber from a xenon-filled arc lamp with power of 30 kW equipped with reflecting mirrors and then cooled with liquid nitrogen (Fig. 4.11). The temperature on the specimen surface (measured by an optical pyrometer) can be raised to 2,000°C with a through-the-thickness temperature

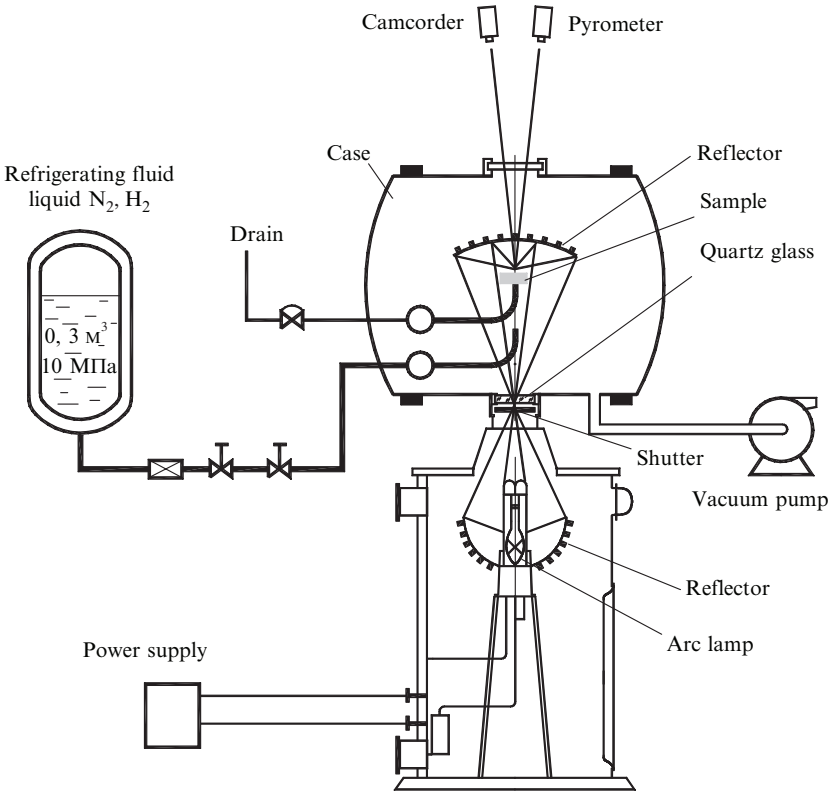

Fig. 4.11. Unit for heat resistance heating of specimens heated by a lamp with focusing mirrors

drop of up to 1,000°C. Testing is rather qualitative in character and mimics the aerospace conditions of thermally loaded refractory materials.

Best suited for quantitative evaluation of heat resistance is the unit in [156] where a disk specimen 11–15 mm in diameter and 0.2–0.3 mm thick is heated on two sides by 150 W lamps positioned at the focal point of ellipsoid reflectors. The temperature profile in the heated central zone of the specimen is measured by a scanning infrared pyrometer. The temperature profile thus measured can be used for determining thermal stresses and the critical stress factor for peripheral radial stresses whose length in the steady-state growth stage is monitored by a stereomicroscope with a resolving power of 5 μ coupled to a high-speed video camera. Regrettably, the power of the light source is not sufficiently high to enable testing of full-scale specimens and materials with higher heat resistance. Methods for testing specimens heated by arc discharge and electric current. In testing conducting materials for heat resistance, methods are used in which the specimen is heated either by passing current through it [158, 159], or by arc discharge [160].

For testing high-refractory materials such as graphite ($R = 500 - 800\,\mathrm{K}$), a unique unit was developed [158] which allows thermal and mechanical loading simultaneously. The specimen (a hollow cylinder with an outside diameter of 40 mm and wall thickness of 6 mm) is heated by passing current of industrial frequency through it. The heated specimen is able to expand freely in the axial direction owing to the use of floating current leads. To increase the radial temperature drop, the specimen is cooled with a mixture of nitrogen and water dust blown from nozzles. The temperature drop between the outer and inner faces of the specimen is measured by tungsten–rhenium thermocouples in contact with the surface. The accuracy of temperature measurement by the contact thermocouples can be assessed by reading off a special scale in the measuring unit containing soldered-in thermocouples.

For an inner face temperature of 2,100°C, the drop through the wall can reach 900–1,500°C depending on the material. However, for high-refractory graphite materials even such a high temperature drop can be insufficient to produce failure; to achieve this, a tensile load is applied to the specimen. Since in this method the temperature profile through the wall thickness remains unknown, there is no way of determining the integral mean temperature drop.

Making use of the known distributions for temperature and stress fields in cylindrical specimens heated by internal sources [67] by passing current or from nuclear reactions in the material [160], the authors of [161, 162] proposed, on an experimental and computational basis, a quantitative method of testing conducting materials for heat resistance using arc discharge.

Disk specimens of graphite or graphite-based compositions with a diameter of $D = 80\,\mathrm{mm}$ and thickness of 3–5 mm are heated by the ac arc from a 30 kW welding apparatus using graphite electrode of radius $r = 8\,\mathrm{mm}$ positioned on both sides of the disk at a distance of 0.5 mm.

In testing for heat resistance, the arc discharge power W was increased in steps (7–8 specimens were used) until radial cracks could be visually detected in the disk periphery (tensile stress region). The measured quantity W is used to determine

$$R = \sigma\lambda/\alpha E = \sigma_0 W f(Bi)/\pi(4r/D^2),$$

where $\sigma\varphi$ are the tangential thermal stresses that can be as high as the ultimate tensile strength at a certain time during heating. The *Bio* criterion is determined indirectly by the calculated computational and experimental temperatures at one or two points of the specimen. Knowledge of the *Bio* criterion makes it possible to evaluate the thermal losses and the thermal power $W \sim f(Bio)$ spent on heating the disk. Simultaneously, one can determine the thermal diffusivity; furthermore, in testing disk specimens radially notched on the periphery, one can determine the fracture toughness. It is clear that the arc discharge and electric current methods can be used for conducting materials only; note that arc heating causes surface erosion in the specimen tested. However, for high-refractory graphites with $\Delta T_\mathrm{m} > 900°\mathrm{C}$ intended specifically for work under erosion conditions, the use of this method is quite justified.

Testing of Materials by Induction Heating

The induction heating method is used for heat-resistance testing of high-refractory conducting materials [163–166] in a wide temperature range, up to 2,500°C; the test specimens usually have the form of axially symmetric cylinders, (solid or hollow), disks and rings.

In the unit (Fig. 4.12a) described in [163], the side face of disk or ring 4 is heated in a vacuum or inert medium by inductor 5 through the quartz walls of air-tight chamber 6. The specimen is accommodated in water-cooled copper concentrator 3 which serves for increasing the specific power and simultaneously as a screen preventing the walls of the quartz chamber from overheating. The radial temperature drop arising in the disk at temperatures >1,500°C owing to radiative removal of heat from the end face causes failure in the specimen on reaching the critical power level W. The time of failure is recorded as breaking of the electrical connection between three needles on which the specimen is mounted. If a larger temperature drop is needed, for example, in destructive testing of graphite, a ring specimen is used (Fig. 4.12b) whose inner face is cooled with a stream of water. With the cooling water flow rate being known, one can, by measuring the inlet and outlet water temperatures by means of thermocouples 7, determine heat flow q. In both cases the radial temperature profile in the specimen is measured by an optical pyrometer through inspection windows 1, 2, or by means of thermocouples 8.

The quantity q at failure (with allowance made for the non-uniformity of heat transfer through the thickness of the specimen) is used to determine the heat resistance criterion $R^l = \Delta T\lambda$ with an error not in excess of $\pm 10\%$ [163]; if the thermal conductivity of the material is known, one can determine the integral mean temperature drop ΔT_{m}. The thermal fracture stress in induction-heated disks 40–55 mm in diameter and 5 mm thick can be measured directly

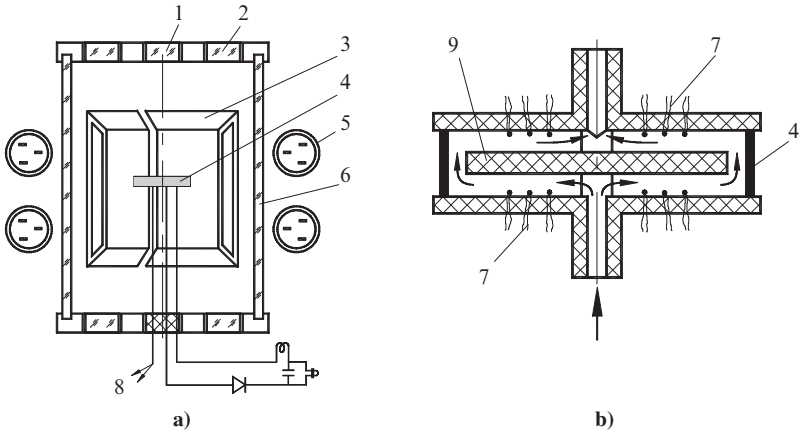

Fig. 4.12. The circuit design of unit for thermal stress resistance testing of cylinders, disks (**a**), and rings (**b**), heated by an induction method

by means of strain gauges cemented in the central zone where tensile stresses are generated. At the time of failure (for Fourier criterion values smaller than 0.05), the temperature of the central part of the specimen remains virtually unchanged, so the stress can be measured using strain gauges with an accuracy of $\pm 4\%$ at least [164].

Interesting data on the heat resistance of graphite material with non-linear strain characteristics were reported in [165] where rings with a diameter of 44 mm and wall thickness of ∼15 mm, inductively heated on the outer face, were tested. A distinctive feature of this method is the use of a contactless laser-based technique for measuring the radial strain of a hole in two orthogonal directions with an accuracy of 2 µm as the specimen is heated to 2,200°C. Simultaneously the temperature on the inner surface of the ring is measured by means of a thermocouple with an accuracy of 4°C at 800°C. The method of an estimation rather thermal stress resistance materials on ring specimens cooled on an interior surface and heated in a inductor coil on an exterior surface is observed in [167].

Under real operating conditions, no single method can be recommended for testing materials for heat resistance. For evaluating the bearing capacity of thermally loaded (as well as mechanically loaded) structures, methods must be used that provide an adequate description of the operating conditions with respect to the type of load, temperature, environment and heat resistance of materials (see Table 4.1).

However, for a comparative evaluation of the heat resistance of newly developed or upgraded materials, one can recommend the use of one of two simple methods that do not require special instrumentation: a method in which a specimen heated to 600–700°C is cooled in water, and a method in which the specimen is heated to 1,000°C in a bath of molten metal or salt. The specimens to be used for that purpose should be of simple geometric shape: a cylinder (solid or hollow), disk, ring or ball.

For evaluating the heat resistance of materials at temperatures higher than $(0.3–0.5)T_{\mathrm{ml}}$ where the material can develop micro- or a macro-plastic behaviour and creep, technically more sophisticated methods should be used: heating by induction, by electron or laser beams, or by the focused light from powerful lamps. These methods permit variation and monitoring of the profile of the temperature fields and their parameters such as the heating rate and cycles and thus provide the possibility of testing materials for heat resistance in the visco-elastic state under conditions closely mimicking real operating conditions at high temperatures.

For testing materials for heat resistance under the conditions of thermal loading and, simultaneously, corrosion or erosion effects produced by a plasma medium or a combustion gas jet, special units, most complex in design, are needed.

It can be inferred therefore that in order to predict the bearing capacity of thermally loaded structural elements depending on their shape, material and thermal loading conditions, one must choose an adequate test method

Table 4.1. The characteristic of test methods on aspects of thermal loading and thermal stress resistance

Source (heating or cooling)	Maximum heat flow ($MW\,m^{-2}$)	Temperature range (°C)	Heating rate ($K\,s^{-1}$)	Class of materials for testing
Methods of testing by cooling				
Water, aqueous salt solutions	16	120–600	300–900	A, B, B
Mineral oils	3	200–700	50–200	A
Melted metal	9	300–1,000	200–500	A, B
Gas–dust mixture	2	600–1,500	10–50	A
Radiation	1	1,500–2,500	−20	A
Methods of testing by heating				
Radiation (electric furnace)	1	300–700	50	A
Gas jet*	2	500–2,500	50–100	A
Molten metal bath	9	200–700	200–500	A, B
Plasma*	150	300–>2,500	300–>1,000	A, B, C, D
Electron beam	80	300–>2,500	50–>1,000	A, B, C, D
Laser	1	300–1,500	30–>1,000	A, B, C, D
Solar energy	15	500–2,000	500–>1,000	A, B, C
Focusing mirror method	100	500–2,500	100–>1,000	A, B, C, D
Electron arc*	300	1,500–>2,500	800–>1,000	B, D
Electric current	15	1,500–2,500	50–800	B, D
Induction	80	200–2,500	30–>1,000	A, B, C, D

Remarks: A – refractories, mono-phase oxygen and oxygen-free compounds with thermal stress resistance $R = \sigma(1-\nu)/E\alpha$ = 30–100 K; B – cermets on the basis of WC, TiC, SiC with thermal stress resistance R = 150–200 K; C – composites on the basis of Si_3N_4, SiC, ZrO_2 with thermal stress resistance R = 300–450 K; D – graphite and composites on its basis with thermal stress resistance R = 500–900. * – the capability of erosive interacting

from those currently in use most of which have not yet been standardized. For the comparative evaluation of the heat resistance of various materials, one will need quantitative methods of testing based on cooling of specimens in water and their heating in molten metals and necessarily standardized at an internationally accepted level.

5

Mechanism of Crack Propagation in Non-Uniform Fields of Thermal Stresses

5.1 Limit Equilibrium of Edge and Central Cracks in the Thermal-Loaded Disk

One of the paths of further development of fracture theory is elaboration of the evaluation methods of the thermal stress state of bodies with finite dimensions with single and multiple cracks, and establishment of the effect of these factors on the fracture kinetics and the load-bearing capacity. Investigation of the fracture of a finite body under thermal load in a non-uniform stress field was conducted in 1973 on the principles of fracture mechanics [49].

For the sake of simplicity of description, we examine a solid thin disk that is axisymmetrically cooled from the periphery. In this case the stages of appearance of the first macro-cracks and fragmentation are characterized by considerably differing levels of the thermal loads, and this makes it possible to trace the different stages of fracture development [50]. This example is sufficiently general to make it possible to reveal characteristic features of the fracture process in an inhomogeneous field of thermal stresses. A single boundary crack situated along the radius is formed when the critical thermal load has been reached [50]. We trace the nature of the development, assuming that the crack is heat-insulated from the environment. In this case the crack does not distort the temperature field because the vector of the heat flux is parallel to its plane. Thermal stresses in a disk with a crack whose lips are free from loadings is possible to define by solving the force problem for a case when the stresses on the lips of the crack are equal in size and opposite in sign to thermal stresses in a disk without a crack, and then use principle of superposition [64].

We assume that the material is homogeneous and isotropic and that its properties do not depend on the temperature. The boundary crack of length l is situated on the x-axis of the cartesian system of rectangular coordinates whose origin lies at the centre of a disk with radius R whose periphery is free

of loads. On the basis of Muskhelishvili's method we can reduce this problem to the solution of the following system of singular integral equations:

$$\sigma_{yy}^{\mathrm{T}}(x) + \frac{E}{4\pi}\int\limits_L M_1(x,t)\mu_1(t)\,\mathrm{d}t = 0; \tag{5.1}$$
$$\sigma_{xy}^{\mathrm{T}}(x) + \frac{E}{4\pi}\int\limits_L M_2(x,t)\mu_2(t)\,\mathrm{d}t = 0, x \in L,$$

where σ_{ij} are the thermal–elastic stresses in the disk without cracks;

$$M_1(x,t) = \frac{1}{t-x} + \frac{(1+x^2)(1+xt)}{x^3} + \frac{x}{1-xt} - \frac{(1-x^2)(2+x^2)}{x^3(1-xt)^2} + \frac{(1-x^2)^2}{x^3(1-xt)^3};$$
$$M_2(x,t) = \frac{1}{t-x} - \frac{1-x^2}{x^3} + \frac{3-2x^2}{x^3(1-xt)} - \frac{3(1-x^2)}{x^3(1-xt)^2} + \frac{(1-x^2)^2}{x^3(1-xt)^3}, \tag{5.2}$$

and the region of integration L is the segment $[t_0, 1]$, where $t_0 = 1 - l/R$. Here, the functions $\mu_{1,2}(t)$ are the jumps of the derivative of the components of the displacement vector at the upper and lower lips of the notch:

$$\left(\frac{\partial u}{\partial x} + \mathrm{i}\frac{\partial v}{\partial x}\right)^+ - \left(\frac{\partial u}{\partial x} + \mathrm{i}\frac{\partial v}{\partial x}\right)^- = \mu_2(t) + \mathrm{i}\mu_1(t), \quad t \in L. \tag{5.3}$$

In the case of an axisymmetric temperature field

$$T(\rho) = T_0 + \Delta T\rho^n, \quad 0 \le \rho = r/R \le 1, \tag{5.4}$$

where ΔT is the temperature gradient over the cross section, we have the following distribution of thermal–elastic stresses in the disk without cracks:

$$\sigma_{rr}^{\mathrm{T}} = \frac{\sigma_{\mathrm{o}}}{n}(\rho^n - 1); \quad \sigma_{\varphi\varphi}^{\mathrm{T}} = \frac{\sigma_{\mathrm{o}}}{n}[(n+1)\rho^n - 1]. \tag{5.5}$$

Here, $\sigma_{\mathrm{o}} = \alpha En/n+2/\Delta T/$ is the maximum tensile stress (at the periphery of the disk). The approximate solution of (5.1) is written in the form:

$$\mu_1(t) = \frac{4\pi\sigma_{\mathrm{o}}}{E}\left(\frac{c}{\sqrt{t-t_0}} + \sqrt{t-t_0}\sum_{k=0}^{m} a_k t^k\right), \tag{5.6}$$
$$\mu_2(t) = 0$$

and the coefficients c, a_K were found by the collocations method, with the collocation points being uniformly distributed over the segment $[t_0, l]$:

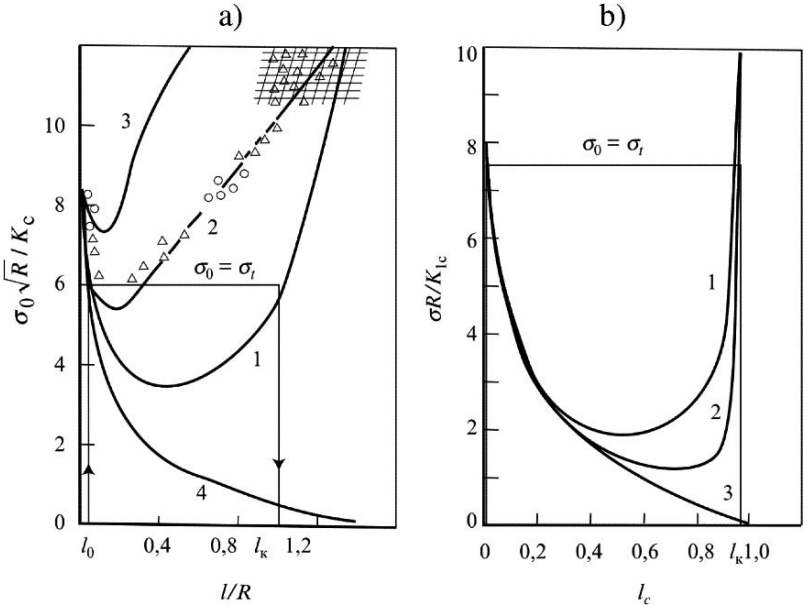

Fig. 5.1. Curves of limit equilibrium of a boundary crack in the disk: (1) $n = 2$; (2) $n = 6$; (3) $n = 10$; (4) uniform tension

$$x_i = t_0 + \frac{1 - t_0}{1 + m} i, \quad i = 0, 1, \ldots, m + 1. \tag{5.7}$$

The accuracy of determining the coefficients depended chiefly on the magnitude of m. For instance, when c was calculated with an error of not more than 1%, $m = 3$ for $I \leq 0.9R$, and $m \approx 20$ for $l \approx 1.75R$.

Figure 5.1 shows the curves of limit equilibrium plotted on the basis of the equality of the stress intensity factor K_1 and its critical value in a state of plane stress K_c, where K_1 was determined from the relationship:

$$K_i = \lim_{x \to t_0 - 0} (\sqrt{t_0 - x}\sigma_{yyty=0}) = \pi c \sigma_o \sqrt{R}. \tag{5.8}$$

We find a substantial difference for the crack propagation nature in an inhomogeneous thermal-stress field (unstable, changing into equilibrium (curves 1–3)) compared with uniform tension (unstable (curve 4)).

We represent the development of thermal crack in the following manner: σ_0 attains its critical value of the limit thermal stresses σ_t with increasing thermal load. Under these circumstances, the crack increases jump up to the length l_k, which is determined by the right-hand branch of the curve of limit equilibrium. The final length l_k depends on the profile of the temperature field, the dimensions of the disk and the properties of the material. For instance, it is smaller, the larger the inhomogeneity of the temperature field (i.e. the larger n is); this is fairly obvious if we bear in mind that the tensile zone becomes

shorter. An increase in the final length is associated with an increase of the complex $\sigma_t\sqrt{R}/K_c$, i.e. it manifests itself when the strength of the material or the disk dimensions increase or when the fracture toughness decreases. Quasi-static examination reveals partial rupture at the critical thermal load ($\sigma_o = \sigma_t$) since the final length of the crack does not exceed the size of the disk. When the thermal load increases ($\sigma_o > \sigma_t$), the crack grows in equilibrium ($l_k^1 > l_k$) but in such a way that the fragmentation of the disk is not attained at any finite load level.

Calculation of the limit equilibrium of a central crack in the disk under thermal load is performed in a procedure analogous to the calculation for an edge crack in a quasi-static statement [52].

The curves of the limit equilibrium plotted for radius R with a central crack with length of $2l$ at parabolic temperature pattern: $T = T_0\Delta T(r/R)^n$ are presented in Fig. 5.1b. Where ΔT is temperature difference on cross section, r is current radius, and $\sigma_o = \alpha E/\Delta T//n + 2$ is the maximal tensile stresses at the centre of the disk without a crack. It is visible that curves of the limit equilibrium, as well as for the disk with an edge crack, have the characteristic minimum, to the left of which only an unstable fracture is possible (a load is dropped with rise of crack length), and on the right only equilibrium evolution damage is observed.

Stresses σ_o attains critical value of the limiting thermal stresses σ_t with increase of thermal load. The crack is incremented up in steps to length l_k defined by the right branch of the curve of limit equilibrium. The final length l_k depends on the temperature profile, size of the disk and properties of the material. At increase of thermal load $\sigma_o > \sigma_t$, a crack with $l > l_k$ grows in equilibrium, but does not attain the boundary line of the disk at even its final level. Though at parabolic temperature distribution $n = 2$ the non-equilibrium evolved crack is stopped down on the close distance ($l = 0.95R$) to boundary line of a body. It is apparent that the curves are qualitatively similar from the comparison of curves of limited equilibrium of the disk with a central notch (Fig. 5.1b) and the disk with an edge crack (Fig. 5.1a). In both cases, the crack after unstable growth is capable of being passed round equilibrium at the infinite increase of loading.

5.2 Interaction of Growing Cracks and Redistribution of Stresses in the Disk

The distribution of an edge crack in the disk proceeds in a complex fashion. When the thermal load exceeds the critical value, examination must include the secondary macro-cracks whose position and instants of appearance are determined with a view to the stress redistribution caused by the first crack. The curve presented in Fig. 5.2 makes it possible to trace the change in stresses at the periphery of the disk when the length of the crack increases. These stresses were determined from the expression

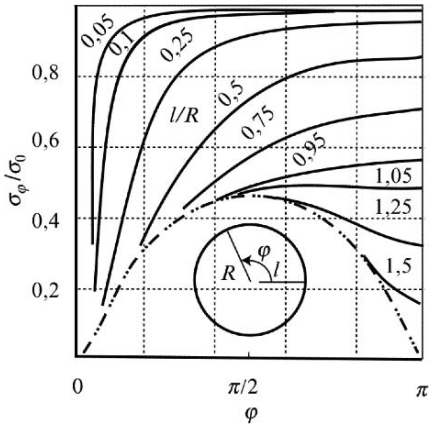

Fig. 5.2. Thermal–elastic stresses at the periphery of a disk with boundary crack ($n = 2$)

$$\sigma_{\varphi\varphi t/\rho=1} = \sigma_{\mathrm{o}} + \frac{E}{2\pi}\int\limits_{L}\left[t + \cos\varphi + \frac{4t\sin^2\varphi(t\cos\varphi - 1)}{(1 + t^2 - 2t\cos\varphi)^2}\right]\mu_1(t)\ \mathrm{d}t, \quad (5.9)$$

where φ is the polar angle measured from the Ox-axis. The existence of a crack less than $0.3R$ length has practically no effect on the magnitude of the maximum stresses at the periphery. A longer crack, however, noticeably changes the state of stress throughout the entire volume of the disk. The level of the maximum stresses decreases gradually with increasing length of the crack up to $l \leq 1.2R$, and then it becomes stabilized, amounting to about $0.47\sigma_{\mathrm{o}}$ (for $n = 2$). The point with the maximum stresses with $l \leq R$ lies at the end of the diameter that passes through the line of the crack, and it abruptly shifts into a position perpendicular to the crack if $l > R$.

Assuming that the secondary cracks originate at the peripheral points where the stresses are maximal, we examine the pattern of the further fracture development. If $l_1 < R$, then the second crack line will be on the same diameter as the first one. When $R \leq l_{\mathrm{t}} \leq 1.1R$, the appearance of a secondary crack is equiprobable in the sector $\pi/2 \leq \backslash\varphi\backslash \leq \pi$. When $l_1 > 1.1R$, two secondary cracks, perpendicular to the first one, have to appear.

In connection with that, we trace the simultaneous development of several boundary cracks in the disk. To simplify the analysis, we will examine two cases: two equal cracks lying on one diameter and four pairwise equal cracks lying on two mutually perpendicular diameters.

In the case of two cracks with length l, (5.10) after substitution of the variables $t^2 = \eta, x^2 = \xi, t_0^2 = \varepsilon$ is reduced to the following:

$$\sigma_{yy}^{\tau}(\xi) + \frac{E}{4\pi}\int\limits_{\varepsilon}^{1}\tilde{M}_1(\xi,\eta)(\mu_1\eta)\ \mathrm{d}\eta = 0, \quad \varepsilon \leq \xi \leq 1,$$

where

$$M_1(\xi,\eta)=\frac{1}{\eta+\xi}+\frac{1+\xi}{\xi}+\frac{\xi}{1-\xi\eta}-\frac{(1-\xi)(5+\xi)}{\xi(1-\xi\eta)^2}+\frac{4(1-\xi)^2}{\xi(1-\xi\eta)^3}, \quad (5.10)$$

and its solution assumes the form

$$\mu_1(\eta)=\frac{4\pi\sigma_{\rm o}}{E}\left(\frac{c\sqrt{\eta}}{\sqrt{\eta-\varepsilon}}+\sqrt{\eta(\eta-\varepsilon)}\sum_{k=0}^{m}\alpha_k\eta^k\right). \quad (5.11)$$

In case of four cracks we arrive at the following system of equation:

$$\sigma^{\tau}_{\varphi\varphi}(\xi)+\frac{E}{4\pi}\int_{\varepsilon_1}^{1}\tilde{M}_1(\xi,\eta)\mu_1^1(\eta)\,{\rm d}\eta+\frac{E}{4\pi}\int_{\varepsilon_2}^{1}M_{12}(\xi,\eta)\mu_1^2(\eta)\,{\rm d}\eta=0,\quad \varepsilon_1\le\xi\le1; \quad (5.12)$$

$$\sigma^{\tau}_{\varphi\varphi}(\varsigma)+\frac{E}{4\pi}\int_{\varepsilon_2}^{1}\tilde{M}_1(\varsigma,\eta)\mu_1^2(\eta)\,{\rm d}\eta+\frac{E}{4\pi}\int_{\varepsilon_1}^{1}M_{12}(\varsigma,\eta)\mu_1^1(\eta)\,{\rm d}\eta=0,\quad \varepsilon_2\le\zeta\le1,$$

where

$$M_{12}(\xi,\eta)=\frac{1+\xi}{\xi}+\frac{1}{\eta+\xi}-\frac{2\xi}{(\eta+\xi)^2}-\frac{\xi}{1+\xi\eta}-\frac{5+\xi^2}{\xi(1+\xi\eta)^2}+\frac{4(1-\xi^2)}{\xi(1+\xi\eta)^3} \quad (5.13)$$

and it is taken that $\xi=y^2$, $\varepsilon_{1,2}=(l-l_{1,2}/R)^2$, where the subscripts 1 and 2 relate to horizontal and vertical cracks, respectively. The solution of system (5.12) is written in a form analogous to (5.11), and the collocation points were placed uniformly on the segments $\varepsilon_1\le\xi\le1$ and $\varepsilon_2<\xi<1$. An error of less than 1% in the calculation of the thermal load limits and thermal–elastic stresses was ensured for $l_{1,2}\le0.7R$ with $m\le10$.

The curves of limit equilibrium (Fig. 5.3) reveal a substantial dependence of the final length of the cracks on their number with an unchanged temperature field. The existence of two or four equal cracks leads to a decrease of l_K to one-half or one-third, respectively, compared with the single crack. Thus the interaction of boundary cracks is an obstacle to the penetration of rupture into the bulk of the body and makes complete fracture more difficult. The thermal loads, which are indispensable for maintaining the equilibrium development of cracks, increase abruptly with an increasing number of cracks. For instance, with $l=0.6R$, the ratio of critical thermal loads is 1:1.7:4.5 for one, two and four cracks, respectively.

In disks with four cracks, the effect of the second pair of cracks (vertical ones) begins to manifest itself noticeably at the final length and the critical loads corresponding to the equilibrium growth of the horizontal cracks, with

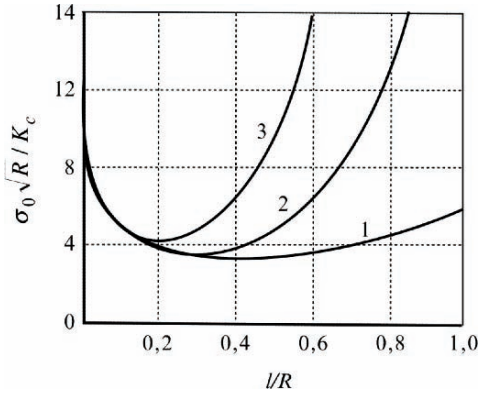

Fig. 5.3. Curves of limit equilibrium for a disk with one (1), two (2), and four (3) equal boundary cracks ($n = 2$)

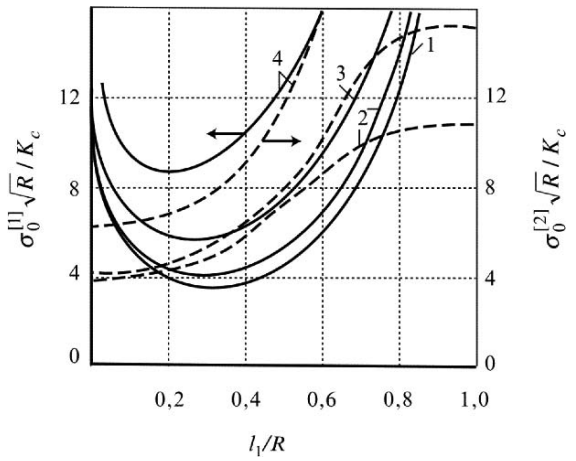

Fig. 5.4. Curves of limit equilibrium for a disk with four pairwise equal boundary cracks ($n = 2$): (1) $l_2/R = 0$; (2) $1_\varepsilon/R = 0.2$; (3) $l_2/R = 0.4$; (4) $1_2/R = 0.6$

the vertical cracks being more than $0.2R$ length (the solid lines in Fig. 5.4). Analogous is the change in the limit loads that are indispensable for the growth of the vertical cracks, depending on the length of the horizontal ones (the dashed lines in Fig. 5.4).

When the lengths are small ($l_{1,2} \leq 0.2R$), the system of cracks affects the magnitude of the maximum stresses at the periphery which is equivalent to the effect of a single crack with the total length. The largest unloading effect ensured in the case of a single crack for $l \geq 1.2R$ is attained at $l \geq 0.75R$ for two, and at $l \geq 0.5R$ for four cracks. For two and four cracks, the maximum stresses at the periphery become stabilized at the level of 0.47 and $0.28\sigma_{\text{o}}$, respectively.

The experimental study of the fracture kinetics was carried out with disks of 15–55 mm diameter and 1.5–2 mm thickness, made of zirconium carbide. The chemical composite of the specimens was as follows, 87.8 wt% Zr; C_{tot} 11.3; porosity 6–8%, mean grain size 66 μm. The specimens had the following properties at 20°C: density of 6.16 g cm^{-3}; electrical resistivity 26 μΩ cm; modulus of elasticity $E = 335$ Gpa; Poisson ratio $\mu = 0.24$; thermal conductivity ∼45 W m^{-1} K^{-1}; coefficient of linear expansion in the range 100–300°C $\alpha = 6.5 \times 10^{-6}$ deg^{-1}; bending strength 224 MPa; fracture toughness $K_{1c} = 3.6\,\text{MPa}^1/^2$.

The radial boundary notches 0.2–0.3 mm wide were produced in the specimens by the electrospark method, and then they were tightly packed with mica. Crack growth was observed and the length of the cracks measured on a microscope type PMT-3 on one of the end faces of the disk which was previously polished.

The tests were carried out by cooling the specimens in water at room temperature, after the specimens, with their end faces heat-insulated, had been uniformly heated. The initial temperature of the specimen was increased in steps of 5–10°C, and thus the appearance of a crack starting at the apex of the notch was attained. The initial length of the crack (taking the size of the notch into account), with the notch size changing between 0.4 and 6 mm, fluctuated between 1.6 and 7.2 mm. Further experiments were carried out analogously. The crack gradually grew, increasing in length jumpwise by 0.1–3 mm and not entering the snowballing stage of development.

Figure 5.5 presents the results of tests with 30 specimens in the range of initial temperatures 120–500°C. On one specimen we succeeded in obtaining five to ten experimental points (denoted by crosses) corresponding to the jumplike change of the length of the crack. These points are situated on the equilibrium section of the curve of limit equilibrium. On the branch of this

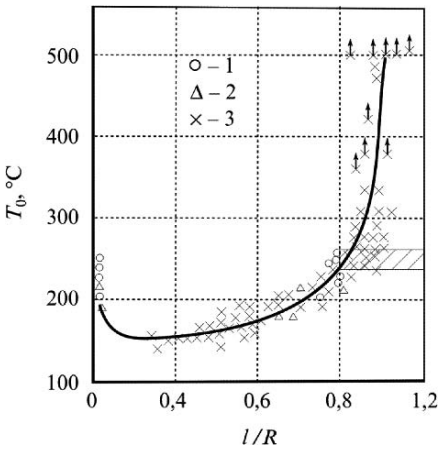

Fig. 5.5. Dependence of the limit thermal load on the length of the crack; (1) initial disks; (2) indented disks; (3) disks with a crack

curve corresponding to the beginning of unstable growth we succeeded in obtaining two groups of points.

The first group expresses the results of tests with disks without induced cracks, the second group represents disks with initial cracks 20–40 μm deep, obtained with the aid of a micro-hardness tester PMT-3 by pressing in a diamond pyramid under a load of 200 g_f. The indentations were situated on the lateral surface of the disk, 40 μm from each other, in such a way that the cracks emerging from them took up the entire height of the disk. The final height of the cracks forming in disks without an initial crack was on an average 8.8 mm at $T_0 = 224°C$, and in indented disks 8.0 mm at $T_0 = 202°C$. These data fit fairly well around the right-hand branch of the curve of limit equilibrium, and this indicates how small is the contribution to the final crack length of the dynamic effects accompanying the unstable crack development before its cessation. In other words, the experiments confirm the applicability of the quasi-static approximation used previously in the theoretical analysis. With $l \sim 1.3R$ and $T_0 = 250$–$260°C$, secondary cracks appeared at the periphery of the disk or moving perpendicularly away from its path (dashed area in Fig. 5.5).

It can be seen that the interaction of the secondary cracks with the primary crack substantially slows down the rate of equilibrium growth of the main crack, which is in agreement with the results of theoretical analysis. This analysis also showed that developed macro-cracks led to a considerable change in the field of thermal–elastic stresses in the disk. The configuration of the forming cracks therefore depends, generally speaking, on the state of the specimen before the thermal loading (whether it contains cracks, their disposition and size), and also on the sequence (history) of the loading in the case of repeated tests. At an initial temperature of less than 250–260°C, when only a single crack can develop in the disk, the sequence of loadings does not affect the final length of the crack (Fig. 5.6a). At higher temperature, the repeated loading is characterized by the presence of one more developed crack against the background of a network of shorter cracks (Fig. 5.6b). In one-time loading (with the same initial temperature as had been attained in the last cycle of repeated loading), the configuration of the cracks is more symmetrical (Fig. 5.6c).

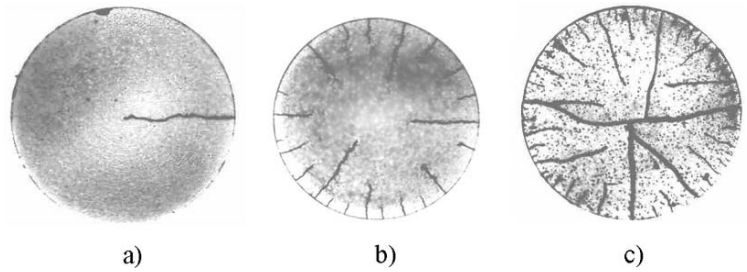

Fig. 5.6. Nature of the fracture of disks in repeated (**a**, **b**) and one-time (**c**) loading: (**a**) $T_0 = 150$–$240°C$; (**b**) $T_0 = 260$–$500°C$; (**c**) $T_0 = 600°C$

The loading history has also a substantial effect on the limit load-bearing capacity of the disks; by this we mean the thermal load causing fragmentation. In one-time loading, full fracture occurred at $T_0 \approx 600°\mathrm{C}$, whereas in repeated loading and at the same temperature, the through crack did not appear. As a rule, in full fracture, two fragments formed as a result of the merging of the cracks developing towards each other from diametrically opposite points. The maximum thermal load characterized by the σ_t and causing the formation of fractures is approximately 3.5–4 times higher than the level corresponding to the appearance of the first macro-cracks in the initial disks ($T_0 \approx 224°\mathrm{C}$, $\sigma_\mathrm{o} \approx 160\,\mathrm{MPa}$).

The experimental dependence of the parameter of thermal load on the length of the crack (see Fig. 5.5) taking the calibrating curves (see Fig. 5.1) into account is suitable for determining the fracture toughness. The temperature field was calculated by the formulas for Bio = const., with the introduction of the effective heat exchange coefficient in water $h = 10^5\,\mathrm{W\,m^{-2}\,K^{-1}}$ and the effective temperature of the medium $T_\mathrm{ef} = 100°\mathrm{C}$, obtained as a result of the experimental investigation of heat exchange in identical specimens with built-in thermocouples. For $Bio \approx 16$ adopted for the calculation, the temperature field at the instant of occurrence of σ_omax was approximated by a parabola of sixth degree. With a view to these data, the fracture toughness in the interval of crack lengths (0.2–0.8) R was $4\,\mathrm{MPa}^{1/2}$, which is close to the above-mentioned value obtained in three-point bending of specimens in the form of notched beams cut out from the initial disks. This method is attractive because it provides the possibility of using the specimens many times, which is a fairly difficult problem when such materials as carbides of high-melting point metals are involved.

The capability of the asymptotic analysis of multiple cracking of a cooled body was conducted in [168]. The unit cell of the crack system for the developed process can be gated out in the form of a beam, which basically are lips of parallel cracks. Then the evolution of a system of parallel cracks can be presented as an assemblage of individual cracks, each propagates in a median plane of the effective beam. As in real processes of a brittle failure, all cracks in the hierarchical system are practically rectilinear, shift components of stresses in their apexes are unessential. In the absence of superposed forces, it means that thermal–mechanical loadings are applied on cracks symmetrically relative to their planes and, hence, each crack propagates really along a median plane of the effective beam, and the transverse displacement on lateral faces of a beam is forbidden (Fig. 5.7). It is convenient for such a scheme of fracture to use a method of compliance [169] at definition of stress intensity coefficient K_I.

The obvious assumption is accepted, that evolution of cracks occurs in a regime ensuring the maximum value of stress intensity coefficient in its apex, i.e. for a dissipation of an elastic energy of the beam in the optimum regime. Interconnection between effective width of a beam (H) and length of a flaw (l)

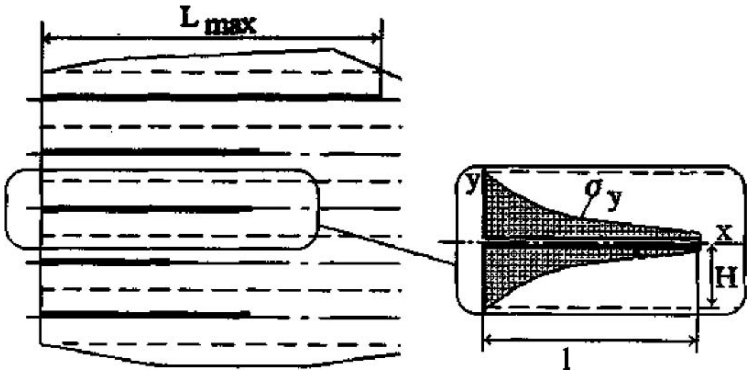

Fig. 5.7. The design scheme for definition of the limiting equilibrium of cracks [168]

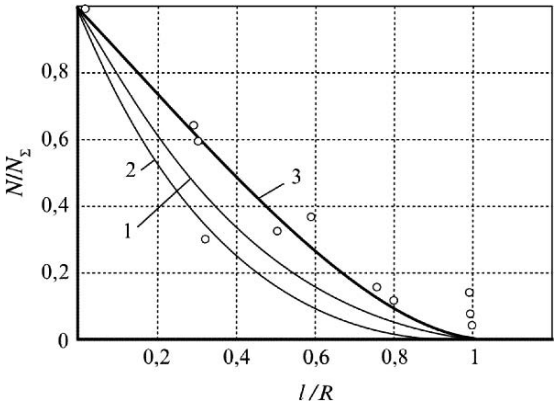

Fig. 5.8. Dependence of a relative crack density on the length of cracks for disks in radius R. Calculations for variants of parabolic (curves 1, 2) and logarithmic (curve 3) allocations of temperatures. *Open circle* is experimental data [50]

$$L = \left(\frac{AH^{3/2}}{K_{1c}}\right) \times \sqrt{2\frac{a}{l}} \ldots\ldots (15). \tag{5.14}$$

The interconnection between a relative density of cracks (a ratio of number, of cracks whose length exceeds some size (l) to the common number of cracks $N_{\sum}$) and the relative length of cracks (a ratio of a size (l) to the maximum size of cracks $l_{\max}$ in the system) is used for the integral performance of the crack system in:

$$N(x > l)/n_{\Xi} \approx 1 - \{l/l_{\max}\}^m \tag{5.15}$$

where $m = 8/3$ for logarithmic allocations.

The results of numerical calculations of a problem about many cracks in thin disk in comparison with experimental data are presented on Fig. 5.8.

The logarithmic law of distribution corresponds to experimental data better than parabolic. Probably, it is connected with conditions of a heat transfer on a cooled external surface of a disk.

Other notations of relationships of a universal character can be used approximately featuring the parameter of a hierarchical system of cracks in the integrated form in practical problems of thermal loading.

5.3 Energy Fracture Model of Thermal-Heated Bodies

The energy necessary for the evolution of a crack at thermal loading is scooped entirely from a reserve of elastic energy from strain accumulated in a body. The quantity of freed energy is determined by redistribution of the temperature stresses field, depending on the position of apexes of originating cracks and their paths.

The path of a surface crack on the generalized geodetic line and cleavage surface inside a body coincides with the generalized minimal surface [170] for the case of a steady crack extending with equal velocity of energy absorption and power supply. Such lines are circles and direct generators for a cylindrical surface.

According to this, the zone of fracture of the homogeneous brittle body at thermal loading should transit on a set of geodesic lines which divide the body in fragments with the minimal total strain energy. It is necessary to note that coordinates of a fracture surface in real brittle bodies, also as well as their strength, have some dispersion about a mean value, depending on quantity and distribution of micro-flaws in a body.

This point of view is verified in [171] with an axisymmetric heating of a lateral surface of a long solid cylinder. The maximum axial stresses σ_z stationary on the significant distance along an axis of the cylinder in tensile zone ($\rho = 0$), far from the end faces, exceed twice the component σ_φ and σ_r (Fig. 5.9).

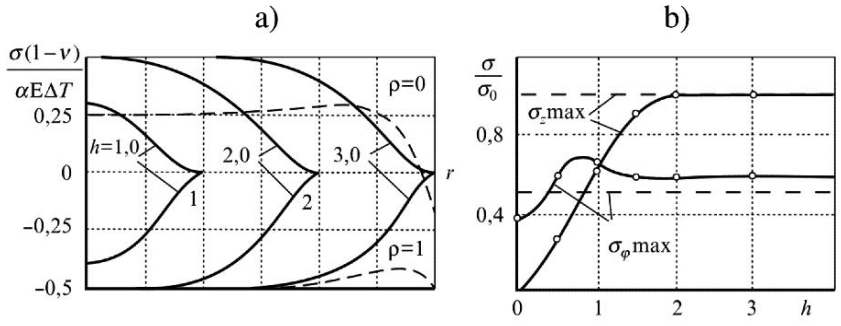

Fig. 5.9. Allocation of maximum stresses σ_φ (*full lines*) (**a**) and dependence of maximum tensile stresses vs. the height of cylinder ($\rho = 0,\ \mu = 0,25$) (**b**). *Shaped lines* are the condition of plane deformation

Therefore the plane of crack propagating from a central band of cross section in a direction to a surface should transit perpendicularly to an axis. Considering the influence of end effect on distribution of the thermal–elastic stresses, it is possible to guess that the quantity of a released energy depends on the distance between a crack plane and an end face of the cylinder. It is possible to discover a point on an axis of the initial cylinder with the maximum energy release varying height of one of formed fragments.

The problem of determination of a crack's trajectory is reduced in such a statement to calculation of the strain energy in a finite-length cylinder. Assuming that the time of crack propagation is not long enough, in comparison with the characteristic time of a modification of the temperature field, the latter is possible to accept constant during fracturing.

Let us asume, for simplification, that a temperature distribution in a homogeneous isotropic cylinder with properties independent of temperature is featured by a quadratic parabola

$$T = T_0 + \Delta T \rho^2, \tag{5.16}$$

where $\Delta T > 0$ is the temperature difference between a surface and an axis of the cylinder.

The dimensionless coordinates (origin of coordinates in the centre of gravity of the cylinder) are hereinafter entered.

$$0 \le \rho = r/R \le 1;\ -h \le \xi = z/l \le h;\ h = H/2R;\ h_1 = H_1/2R \tag{5.17}$$

where R and H are the radius and height of the cylinder, respectively; H_1 is the height of the smaller cylinder at fracturing on two parts.

Using the known expression of the total energy of an elastic deformation [63]

$$W(h) = \frac{\pi R^3}{E} \int\limits_{-h}^{h} \mathrm{d}\xi \int\limits_{0}^{1} [\sigma_r^2 + \sigma_\varphi^2 + \sigma_z^2 - 2\nu(\sigma_r\sigma_\varphi + \sigma_\varphi\sigma_z + \sigma_z\sigma_r) + 2(1+\mu)\tau_{rz}^2]\rho \mathrm{d}\rho, \tag{5.18}$$

and also dependences for the thermal–elastic stresses, gained for the temperature field (5.16) in the form of the Fourier–Bessel series, we have after necessary scaling and some transformations

$$W(h) = W_\mathrm{o} \left[\frac{2h}{3}(1-\nu) - 8(1+\mu) \sum_{i=1}^{\infty} A_i \alpha_i^{-4} \right]. \tag{5.19}$$

Here

$$W_\mathrm{o} = \frac{\sigma_\mathrm{o}^2 \pi R^3}{E},$$

where

$$\sigma_\mathrm{o} = \frac{\alpha E \Delta T}{2(1-\mu)}$$

gives the maximum axial stresses (on an axis of the long cylinder far from its end faces).

Coefficients A_i are defined from the infinite system of linear algebraic equations.

$$\sum_{j=1}^{\infty} F_{ij} A_j = G_i, i = 1, 2, \ldots, \tag{5.20}$$

where

$$F_{ij} = \frac{1}{16\alpha_i^3}\left(cth\alpha_i h + \frac{\alpha_i h}{sh^2\alpha_i h}\right)\delta_{ij} + \sum_{n=1}^{\infty} \frac{\beta_n^2(\alpha_i^2+\beta_n^2)^{-2}(\alpha_j^2+\beta_n^2)^{-2}}{h\left[1+\frac{2(1-\mu)}{\beta_n^2}-\frac{I_0^2(\beta_n)}{I_1^2(\beta_n)}\right]};$$

$$G_i = (1-\nu)\alpha_i^{-4}; J_1(\alpha_i) = 0; 0 < \alpha_1 < \alpha_2 < \ldots.; \beta_n = \pi n h^{-1}; \tag{5.21}$$

$n = 1, 2, \ldots.; J_1$ is the Bessel's function of the first kind; I_0, I_1 is the Bessel's functions of imaginary argument.

The results of the calculation of strain energy W/W_0 executed with use of the reduction method at the solution of system (5.20) are presented in [71]. Being restricted to values i, j, within the limits of $1 \leq i$, $J \leq 40$–50, it is possible to gain exactly the first five signs of magnitude W/W_0. At $h \leq 1.0$ strain energy non-linearly depends on height of the cylinder, at large values of h this dependence is rather close to linear. We may define this quantity by means of the gained data

$$\Delta W(h, h_1) = W(h) - [W(h_1,) + W(h - h_1)] \tag{5.22}$$

describing the modification of the total energy of an elastic deformation at transition from one state (the cylinder of height H) to another (two fragments of height H_1 and $H - H_1$). In consequence of a problem symmetry, the curves for field $0.5 \leq -h_1/h \leq 1.0$ are a specular reflection relative to the line position $h_1/h = 0.5$.

The maximum of an energy release is observed at $h < 2.7$ when the cylinder is fractured in two equal parts (curves 1, 2 in Fig. 5.10). Two maximums of the energy release appear with increase of the initial height of the cylinder in the range of $2.7 \leq h \leq 6.0$ displaced aside of the end faces and symmetrically oriented at a point $h_1 = h/2$ (curve 3 in Fig. 5.10). The position of maxima is determined by values $h_{1\,\max}^{(1)} \approx 1.15$ and $h_{1\,\max}^{(2)} \approx h - 1.15$. Magnitude $h_{1\,\max}^{(1)}$ varies inappreciably (within the limits of 1.1–1.2) at a variation of a Poisson's ratio over the range $0 < \mu < 0.5$.

The third local maximum, described by a value $h_{1\,\max}^{(3)} = h/2$ (curve 4 in Fig. 5.10) appears at $h \geq 6.0$. Its magnitude does not exceed matching values for bands near to the end faces at $6 < h < 21$. Therefore existence of the third maximum does not influence the trajectory of cracks in the indicated range h.

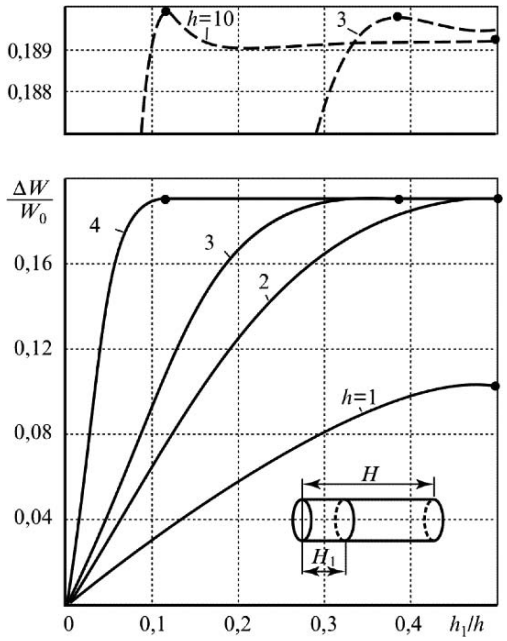

Fig. 5.10. Dependence of freed strain energy at fracture of the cylinder on two parts vs. the height of a smaller fragment. *Shaped lines* are sections of curves in a larger scale, the points are the position of maxima

Let us assume that the cracks are formed sequentially one after another when the level of the maximum tensile stresses attains some critical value, σ_{t}. We assume also that temperature difference on a cross section of a body is gradually incremented and, having achieved the magnitude at which the first crack explicates, it does not vary further.

Regarding only origination of the transverse cracks relative to an axis, we restrict consideration to cylinders with value $h > 1$, as tangential stresses (see Fig. 5.10) predominate at smaller height of the cylinder. The stresses growing in the process of increase of cylinder height from $h = 2.0$ are close to level σ_{o}, matching to a plane deformation. Appearing fragments with $h_i < 2.0$ do not fail after fracturing cylinders with $h > 2.0$, as greater temperature difference is necessary for crack evolution.

It is possible to estimate fracture character of specimens depending on their height (Table 5.1). The results for specimens with a relationship of sizes $h < 2.7$ and $2.7 < h < 3.15$, for which the theory predicts transition from symmetric fracture to asymmetric, is interesting.

Specimens of zirconium carbide of sizes $D \times H = 15 \times 30$ and 15×45 mm, with 30 pieces in each batch, were used for testing. Thermal loading of specimens is executed by heating a lateral surface at stationary heat flow. The specimen is placed for this purpose in a tubular radiator, heated up with eddy

Table 5.1. Character of fracture depending on height of the cylinder

Height of the initial cylinder	Quantity of fragments	Sizes of fragments
$1.0 \le h \le 2.7$	2	$h_1 = h_2 = h/2$
$2.7 < h < 3.15$	2	$h_1 = 1.15$ $h_2 = h - 1.15$
$3.15 \le h \le 3.85$	3	$h_1 = 1.15$ $h_2 = h_3 = (h - 1.15)/2$
$3.85 < h < 4.3$	3	$h_1 = h_2 - 1.15$ $h_3 = h - 2.3$
$H \ge 4.3$	≥ 4	

Fig. 5.11. Fracture character of specimens: $a - h = 2$; $b - h = 3$

currents to 1,500–2,000°C by means of a high-frequency unit [164]. The fracture moment is fixed by the piezoelectric transducer, whose signal is recorded on a strap of the oscilloscope. The cracks are revealed on a specimen surface by a method of penetrating colours.

Magnitude of heat flow is incremented stepwise so that the level of limit stresses is attained at the thermal regular stage (criterion Fourier $F_o = \alpha\tau/R^2 \ge 0.25$) to which there corresponds parabolic temperature distribution (5.16). However it is not always possible, and fractures happened basically at an earlier stage of heating ($F_o \approx 0.05 \ldots 0.18$).

Measurement of coordinates of fracture surface (Fig. 5.11) displayed good enough correspondence to theoretical and experimental data. Average height of one of the fragments is 15 mm ($h_{1p} = h/2$) at a root mean square deviation about 3 mm for specimens with $h = 2$ that failed on two parts.

Specimens with $h = 3$ at origination of transverse cracks failed on some parts whose quantity changed from two to four. The peaks are registered sequentially on the oscillogram, fixing the moment of fracture in case of origination of numerous cracks. The height of the fragments formed about the end faces of the cylinder is approximately 13 ± 3 mm ($h_{ip} \approx 0.87$). Some difference of the obtained value h_{ip} from the theoretical $h^{(1)}_{i\,\max} \approx 1.15$) is apparently possible to explain by the abrupt temperature profile at the fracture moment ($F_{of} \approx 0.1$) in comparison with that accepted (5.16) in calculation. Nevertheless, obtained data testify to the existence of an end effect of fracture, even when allocation of temperature along the radius differs from a quadratic parabola.

Thus, the results obtained allow calculation of an effective surface energy in requirements of thermal loading, including that all strain energy generated

at fracture of the cylinder into two parts is outlaid for formation of a new surface ($2\pi R^2$), according to Fig. 5.10 at $h \approx 3$–5 we have

$$\gamma_{\text{eff}} \approx 0.095 {\sigma^2}_{\text{t}} R/E, \tag{5.23}$$

where σ_{t} *is* the limit of temperature stresses. Considering, that for explored specimens $\sigma_{\text{t}} \approx 95\,\text{MPa}$, $E \approx 350\,\text{GPa}$, we gain $\gamma_{\text{eff}} \approx 1.8$–$10^4\,\text{erg/cm}^2$.

The latter determines, apparently, the upper boundary of a specific energy of fracture for zirconium carbide as an energy loss on excitation, sound and elastic vibrations are not considered in the calculation. Nevertheless the obtained magnitude γ_{eff} in a sufficient measure is characteristic for rather brittle materials, such as Al_2O_3, SiC, etc. [18].

This page intentionally blank

6

Influence of Thermal Loading Modes on Fracture

The modification of thermal loading modes in different combinations with simultaneous variation of the forms and sizes of specimens can influence kinetics and the character of fracturing appreciably. Choice of the thermal loading modes determines both the temperature range of tests, and the capability of an estimation of thermal stress resistance at quasi-brittle either elastic–viscous, or a viscous–plastic state.

6.1 Fracture of Cylindrical Bodies Heated on a Lateral Surface in Liquid Media

The energy approach, confirming the observable kinetic regularity of various fractures at an individual view of a loading by cooling of a heated body, is not able to explain the fracture of a body at its surface under heating.

The damage of the cooled body with multiple formation of surface crack and partial loss of bearing capacity essentially differs from the fracture of an axisymmetric heated body when crack spreading begins in a central zone at reaching critical stress intensity, K_{1c}, completed with total fracture of the body into parts.

A stress field with a tensile zone at the centre and compression in the circumferential field arose at heating the lateral surface of disk specimens in a bath of melted tin. Numerical calculation in view of temperature dependence of heat transfer *Bio* demonstrates that magnitudes of the maximum tension and compression stresses vary in time not synchronously (i.e. with unequal tempo) and attain extremes at different moments (Fig. 6.1a), thus their ratio changes in a wide range, attaining enormous values at a small loading duration (Fig. 6.1b) [134].

Results of heating tests, using melted tin, of a lateral surface of ZrC specimens with diameters of 46 and 54 mm and width of 3 mm, heat-insulated on their end faces (Table 6.1) display a capability of qleavage fracture of a narrow

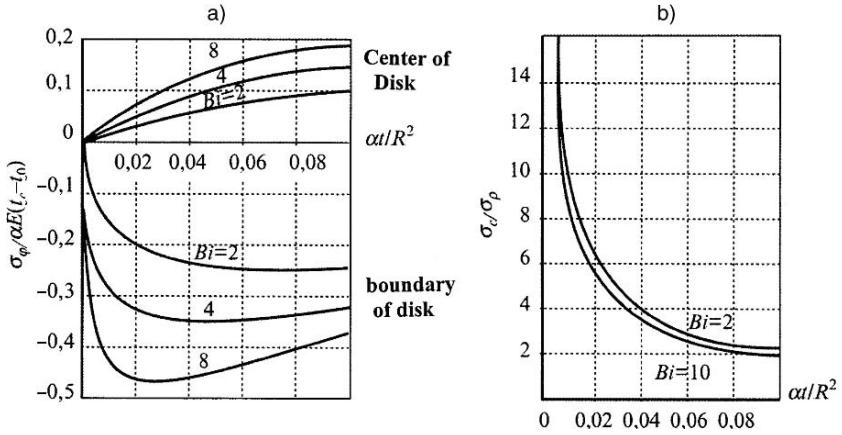

Fig. 6.1. Modifications of the maximum stresses at heating of the disk in the melted tin, tensile at centre and compression stresses in circumferential part of the disk (**a**) and the ratio of compression stress level σ_c to tensile stress σ_t vs. the dimensionless time (**b**)

Table 6.1. Parameters and fracture character of ZrC disks in the melted tin

Temperature of fracture T_f (°C)	Time of fracture τ_f (s)	Maximum of temperature and stress in zones				View of fracture
		Compression		Tension		
		T (°C)	MPa	T (°C)	MPa	
420	3.5	163	−356	51	163	Fragments
590	2.3	220	−480	76	159	Fragments
870	0.9	355	−810	65	137	Cleavage fragments
1,100	0.65	420	−960	65	130	Cleavage fragments
1,100	0.9	360	−1,050	65	140	Cleavage fragments
1,340	0.9	540	−1,247	65	140	Cleavage fragments
1,400	0.5	530	−1,120	65	140	Cleavage
1,400	0.55	550	−1,260	65	140	Cleavage

circumferential area of the disk, due to compression stresses increasing with temperature and simultaneous stay time reduction of the specimen in melt.

Compression and tension stresses of thermal fracture attain, respectively, 1,075 and 137 MPa. For comparison, bending strength at 20°C is on the average equal to 230 MPa with a variation coefficient of 10%, and compression strength at a room temperature of 870 MPa and 970 MPa at 1,000°C with a variation coefficient of 9%.

The fracture of specimens by cleavage is non-homogeneous, sections fitting to end faces are cleaved off at a distance noticeably greater (2,. . . ,3 mm) than in medial disk layers (Fig. 6.2b). The single separate cleavage on the square 1,. . . ,3 mm and on depth some tens of micrometers preceded to the final stage of overall cleavage.

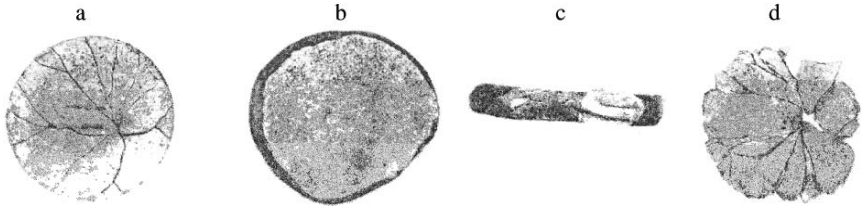

Fig. 6.2. Fracture view of ZrC specimens after thermal loading in the melted tin: (**a**) fracture from tensile stresses, (**b**) and (**c**) cleavage from compression stresses, (**d**) the mixed fracture

The character of the fracture in the compression field is conditioned on the kinetic character of evolution of cracks, studied in more detail in the context of force loading under compression loading [53]. The load corresponding to fragmentation of the body is several times greater than the load at which the first crack started to develop.

Mixed form of fracture (Fig. 6.2d) becomes possible with increasing the time period of the disk in the bath of melted tin, when after cleavage of the peripheral parts of the disk, thermal stresses appearing in a central zone, comparable with tensile strength, disintegrate the whole body. The simultaneous increase of time and decrease of temperature of melt causes the typical form of fracture – the complete fragmentation of a body with radial cracks (Fig. 6.2a) due to tangential tensile stresses in a central part of the disk.

Comparison of test results for thermal stress resistance of specimens with complete fragmentation at various heating methods [172] is presented in Table 6.2.

Observable differences of ΔT within the limits of 15–25% are caused, first of all, by natural scattering of properties of ceramic materials. Thermal stresses σ_{th} exceed tensile strength σ_{t} a little and make 0.32–0.57 of bend fracture stresses σ_{b}. Analysis of combined test data at heating indicates an essential dependence of fracture character and a level of the fracture thermal stresses of a body on parameters of thermal loading (Fig. 6.3).

The limit curves form different fields of the fracture initiation on a coordinate plane: time/loading temperature. So, fracture will begin in the tension field if the time of the loading and magnitude of the loading temperature are equal to values of coordinates of the point P. The parameters of a loading matching the band C, lead to fracture in the compression field. Band CP initiates practically simultaneous fracture in both fields. Reduction of the test time and rising of the thermal loading up to the magnitudes lying in band C ensure compression fracture.

The fracture mechanics based on consideration of propagation kinetics of a single crack in a body under load cannot predict the scattering values of strength and thermal stress resistance, observed in real materials. Statistical failure theories [26, 36], built on the concept that a solid material contains

Table 6.2. Thermal stress resistance (ΔT) and characteristics of ZrC specimens: tensile σ_t, and bend strength σ_b, modulus E, coefficient of linear expansion α, thermal conductivity λ and thermal fracture stresses σ_t

Material	Method	Sample size (mm)	Strength (MPa)		$E \times 10^{-4}$ (MPa)	$\alpha \times 10^{6}$ (K^{-1})	λ ($W\,m^{-1}\,K^{-1}$)	ΔT (K)	σ_t (MPa)	σ_t/σ_b
			σ_t	σ_b						
$ZrC_{0.94}$ $N = 20$	I	cylinder, $d = 15$, $l = 45$	60	148	3.0	5.2	25	50	98	0.53
$ZrC_{0.93}$ $N = 7$	II	Disk $d = 35$ $h = 2.5$	100	290	3.2	5.2	28	61	93	0.32
$ZrC_{0.96}$ $N = 30$	III	cylinder, $d = 15$, $l = 45$	80	260	3.4	6.0	25	57	117	0.45

(I) induction heating, (II) heating in melted tin, (III) radiation method of heating, N quantity of the tested specimens

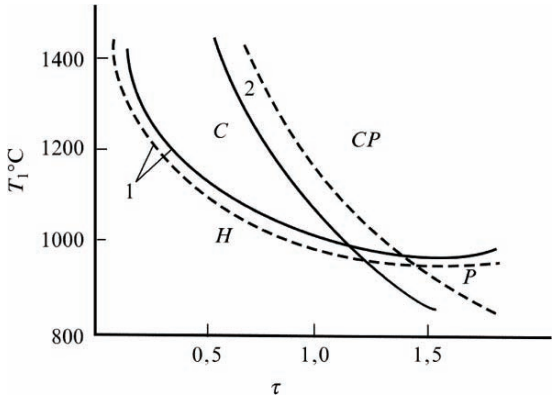

Fig. 6.3. Cartogram of the body fracture mode at heating in melted tin. *Limiting curves* of thermal loading at reaching ultimate tensile strength (1) and compression strength (2); Bands of fracture: from compression stresses C, from tensile stresses P, mixed fracture CP, absence of fractures H. *Unbroken curves* refer to disks with diameter of 46 mm, *dashed curves* are disks with diameter of 58 mm

a great many primary elements with different inherent defects and various physical–mechanical properties, allow us to present the allocation of strength values.

Scattering regularity of thermal stress resistance values, as also strength characteristics of brittle materials at a force loading, represent great practical value, doubtlessly. In particular, allocation of thermal stress resistance R obtained at stationary tests of a batch of ring specimens of zirconium dioxide stabilized 6% CaO is characterized by exponential Weibull's distribution. The mean of criterion R_m makes 43 grad., $R_{max} = 62.3$ grad., $R_{min} = 29.6$ grad.

and root-mean-square deviation $S = 7.6$ grad [16]. The variation coefficient of thermal stress resistance $W = 17.5\%$ is close to the matching value for this material at strength test by a force loading.

Mass tests for thermal stress resistance of the carbide and hydride specimens [173] and aluminum oxides [174] confirm the above fixed regularity of distribution of thermal stress resistance values. The fixed scattering values of thermal stress resistance are interlinked to structural inhomogeneity, inevitable in the preparation of a batch of specimens, even from the same production run.

The scale effect of change of strength predicted by statistical theories is manifested in the certain limits for all materials. It is connected with increase of sizes, which increases probability of appearance of dangerous flaws. The modification of strength is especially great when sizes of surface micro-cracks are commensurable with the width of a body. At reaching the certain volume, further size increase of specimens ceases to affect their strength and consequently the design estimates of strength made on the basis of test data of medium-sized specimens appear much underrated for a body of greater volume [175]. Results of estimations of size effect on thermal stress resistance, in our judgement, are not authentic enough owing to the use of the approximate dependences of a convective heat transfer of specimens cooled in water [176–178], and also with disregard of a change stress state at test of disk, and cylindrical specimens of finite sizes [179].

6.2 Fracture of Cylindrical Body Thermally Loaded on an End Surface

In practice in an operation, there are cases of thermal loading when cylindrical articles heated on an end surface fail. The precise solution of the thermal–elastic problem for the semi-infinite cylinder at any axial allocation of temperature is presented in the form:

$$\sigma_j = \sigma_j^{(0)} + \sigma_j^{(1)} (j = r, \varphi, z); \;\; \boldsymbol{t}_{rz} = \boldsymbol{t}_{rz}^{(0)} + \boldsymbol{t}_{rz}^{(1)} \tag{6.1}$$

where stresses with a coefficient 1 are caused by action at an end face of tangential stresses equal in magnitude and in opposite direction to stresses τ_{rz}.

The effective solution of a problem is gained [140] by means of the variation methods developed with reference to the given class of problems. The performed calculations have shown that the greatest tensile stresses originate in instant $F_{\mathrm{o}\max} = a\tau/R2 = 0.55$ apart from the end face $\xi = z/R = 1.04$ and are determined by a relationship

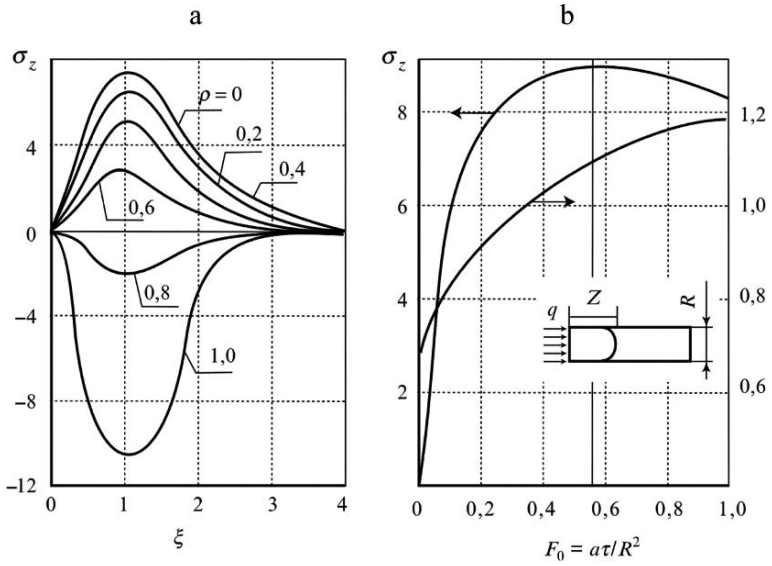

Fig. 6.4. Stress distribution on length of the cylinder for different points on radius $\rho = r/R$ at $F_o = 0.55$ (**a**), a modification of the maximum values of stresses σ_z and possible fracture point ξ=Z/R in time (**b**)

$$\sigma_{z\,\max} = \sigma_z(0, \xi_{\max}, F_{o\,\max}) = 0.086 \frac{\alpha \mathrm{E} q R}{(1-\nu^2)\lambda}, \tag{6.2}$$

where λ, a are coefficients of thermal conductivity and thermal diffusivity, α is coefficient of linear expansion, μ is the Poisson coefficient, E is module of elasticity, q is thermal flow, R is radius of the cylinder.

Allocation of axial stress σ_z on radius in cross section $\xi = \xi_{\max}$ is close to a quadratic parabola. Transition of tensile stresses σ_z to compression stresses is in point $\rho = 0.72$. The curved path of fracture (diagrammatically figured on Fig. 6.4) is caused by a field of compression stresses in peripheral layers of the cylinder.

The crack originating in a central band of the cylinder ($\rho = 0$) is passed round the whole cross section of the cylinder non-equilibrium, overcoming the impeded effect of compression stresses, and forms two fragments at the maximum value σ_z exceeding an ultimate tensile strength of a material by 2–2.5 times.

6.3 Local Thermal Loading of a Surface Body

High-intensity energy sources – electrical discharge, electronic and laser beams – [180] have all been applied recently more widely in the processing of materials. The significant thermal stresses induced during processing can

exceed the ultimate strength of a material with insufficient toughness and lead to cracking in a heating band and even bring about the complete fracture of a component. The magnitude of fracture stresses and character of fractures are changed essentially with variation of stress state [49].

The planar stress state [69, 181, 182] is observed in a number of the space problems of thermoelasticity under some requirements in prototype systems. For example, it originates in the half space, exposed to axisymmetrical heat flow, and also in an elastic layer when the temperature field is presented by a harmonic function.

Fracture of thin disks happens by the extension of radial cracks in case of heating at planar stress state [77] due to the tangential component of stresses. The stress state becomes essentially three dimensional with increase of width of a disk that leads to a modification of the fracture character of specimens. Unlike a half space, the tensile stresses occur in the cylinder behind a heating spot. The tensile stresses value grows all over again with increase of the heated up field, and then is reduced to null and the magnitude of compression stresses is continuously diminished (Fig. 6.5). Thus, requirements of half space in the cylinder are realized only when tensile stresses in comparison with compression can be neglected, i.e. in case of spots, essentially smaller than $0.1R$.

From comparison of the stress solution for the thin cylinder ($H < 0.5R$) with the matching solution obtained under the theory of plates, it follows that precision of the latter depends on the extent of the heating locality (i.e. from ratio of a heating spot radius r_o to R) and width of cylinder H. The allocation of stresses is noticeably different only inside a heating band (up to 10%) at small H and $r_o < 0.2R$. Increase of the heating spot radius leads to the approaching of the results. Precision of the solution under the theory of plates is reduced with growth of the cylinder height. For example, the error

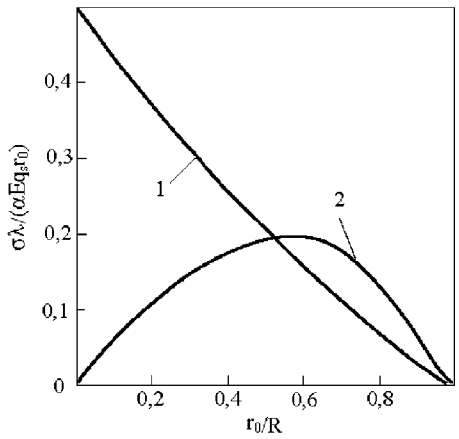

Fig. 6.5. Dependence of the maximum values of compression (1) and tensile (2) stresses in the finite cylinder ($H = 2R$) vs. size of a heating spot [69]

is equal to 15% in the case of the height of the cylinder of $0.5R$ at $r_0 = 0.7R$, and the error attains 85% at $r_0 = 0.1R$ [69].

Investigations of fracture modes of the finite cylinder under local thermal loadings were accomplished in [58]. The stress state in a specimen is calculated in the following statement of the problem. The cylinder of radius R and height H free from mechanical loadings is heated up instantaneously on an end face by axisymmetric heat flow whose density obeys the Gauss probability law

$$q = q_o \exp(-2\varepsilon^2/\omega^2)$$

where ω is effective radius of a beam. Physical–mechanical properties of a material do not depend on temperature. The temperature field is determined in the finite cylinder from thermal conductivity equation with application of the Laplace and the Hankel transformations. The components of a stress tensor caused by these fields and the vector of displacement were discovered from equilibrium equations and the Hooke equations in the displacement converted on the basis of an initial functions method [63, 69] to the system of the differential equations of the infinite order. The stresses and displacement at any cross section of the cylinder were adjusted with boundary conditions on lateral and end surfaces. After representation of the unknown quantities sought for in the form of rows on Bessel's functions of the first kind of real and imaginary arguments and their substitutions in view of orthonormalized systems of the cylindrical and trigonometrical functions, the transcendental combined equations indicated above are reduced to the complete infinite system of the algebraic equations relative to the unknown coefficients at Bessel's functions.

The solution of algebraic combined equations for particular sizes of the finite cylinder ($H/R = 0.2$; $\omega/R = 0.225$) executed with error not exceeding 2% showed that apparent stress field in dimensionless state $\sigma\lambda/\alpha Eq\omega$ is specified by different localization of compression (A) and tension (B and C) zones changing with time. The solution obtained coincides practically with available data for half space for a short time of loading when the boundary of the finite cylinder does not yet have an affect on distribution of the temperature fields. For example, under specified time $\tau = 0.04\,\mathrm{s}$, the intensive two-axis compressive stresses in surface layers (zone A) border with the three-axis tension (zone B) at the distance from the top surface, $\xi \approx 0.3$. The tension stress level in zone B is an order lower than the compressive stresses (Fig. 6.6a). The compression zone is observed again since $\xi > 0.7$, down to an inverse surface. The compressive stresses σ_φ, σ_r in radial direction on the surface ($Z = 0$) change to the tensile tangential stresses σ_φ (zone C) at $\rho = r/R = 0.2$ and reach a maximum at $\rho = 0,4$ (Fig. 6.5b).

It should be noted that the tensile stresses in zone B are nil at short time loading $\tau \leq 0.02\,\mathrm{s}$ and tensile stresses σ_φ, σ_z totally disappear at $\tau > 0.1\,\mathrm{s}$. The only tensile stress σ_φ remained in zone C and there is no axial stress σ_z. The level of $\sigma_\varphi^{\max}$ increases essentially with time.

The local heating was carried out in a vacuum chamber of an electron beam device by electron beam of 20 keV with smoothly controlled output power q

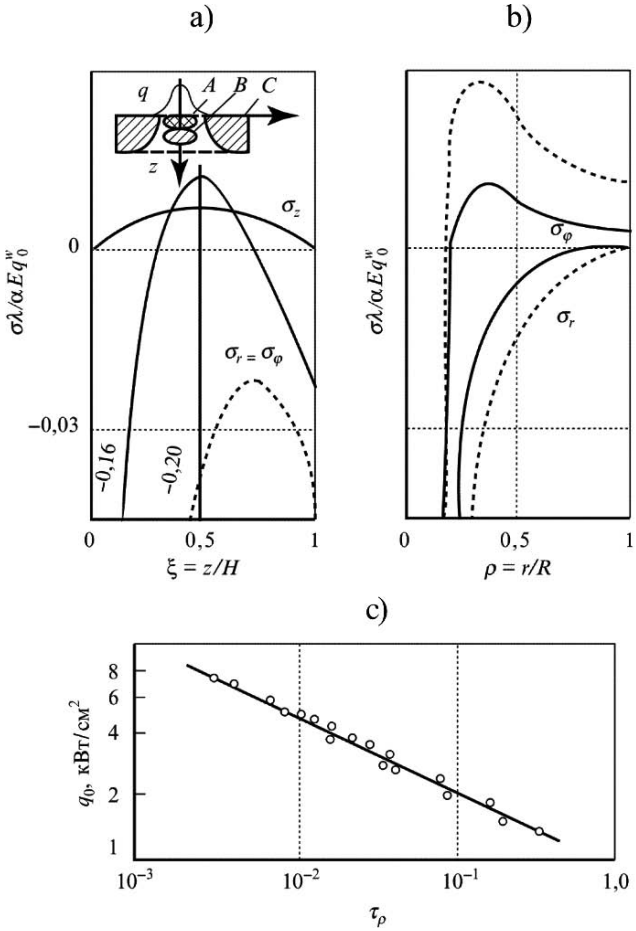

Fig. 6.6. Distribution of calculated values of stresses on an axis at $r = 0$ (**a**) and on radius of a specimen at $z = 0$ (**b**). (*Full lines* are obtained at $\tau = 0.04$ s, shaped at $\tau = 0.02$ s); (**c**) the relationship between a specific heat flow and time to failure of $ZrC_{0.9}$ specimens (Points are experimental data)

of up to 5 kW [77]. The test specimens were ZrC or SiC disks 15–20 mm in radius (R) and 4 mm thick (H), the hot spot diameter ω could be varied within 3–8 mm, and the heat density q could reach 8 kW cm^{-2}. A moveable water-cooled diaphragm with a hole for transmitting the central part of the electron beam was placed in front of the specimen. A movable water-cooled shutter between the diaphragm and the specimen was used for aligning the electron beam relative to the diaphragm and tentative setting of the thermal loading level. The amount of heat per unit of time, q_o, is determined by the energy parameters of the electron beam: $q_o = \beta U I_0$, where U is the electron accelerating voltage; I_0 is the current passing through the specimen and

recorded by the loop oscillograph; β is a coefficient accounting for electron reflection and adopted to be 0.95 for ZrC. More exact measurement of the heat flux was performed by calorimetric technique accounting for water flow rate and for water heating by thermocouple bank. The mean root square error in measuring the heat did not exceed 6%.

The thermal loading q_o and time to failure of a specimen were determined during tests. It is more convenient to observe regularity of fracture relative time τ_f. Basically, with the same outcome, tests can be executed in another sequence: the exposure loading time is set and value q_o, leading to a specimen fracture is selected.

The experimental data indicating linkage between time to failure τ_f and magnitude of a heat flow, q_o, are presented by a constant $q_o \sqrt[3]{\tau_f} = \text{const}$. characterized almost in logarithmic coordinates on Fig. 6.6c. The observable scatter of values q_o within the limits of 30% from the fixed average value is natural for brittle materials and similar to dispersion of strength values in the same limits at a force loading. The maximum stresses for some characteristic zones of a specimen have been calculated with use of the obtained dependence $q_o - \tau_f$ for different values τ_f.

The complicated and complex change of the stress state vs. loading time defines the kinetics and type of fracture. Three characteristic views of fracture are observed at modification τ_f and accordingly a stress state. Under high heat density ($q \cong 7.2\,\text{kW cm}^{-2}$) and at low loading time ($\tau \cong 0.004\,\text{s}$), the local fracture originates at the cost of axial compressive stress σ_z (Fig. 6.7a). The apex of this pyramid is located apart from a surface $\xi = 0.15$–0.25. The multitude of cracks parallel to the top appeared within the layers of 15–20 µm without reaching the surface, as can be observed in relatively transparent sublimated SiC specimens (Fig. 6.9). The final spalling occurs from the loss of stability of the surface layer with parallel cracks at critical stress equal to the compressive strength of the material. The calculated value of spalling agrees well with the experimental value of the compressive strength.

At higher loading time ($\tau \approx 0.01\,\text{s}$) under $q = 5$–$7\,\text{kW cm}^{-2}$ the tensile stresses in the zone B cause the formation of a crater in the central part of

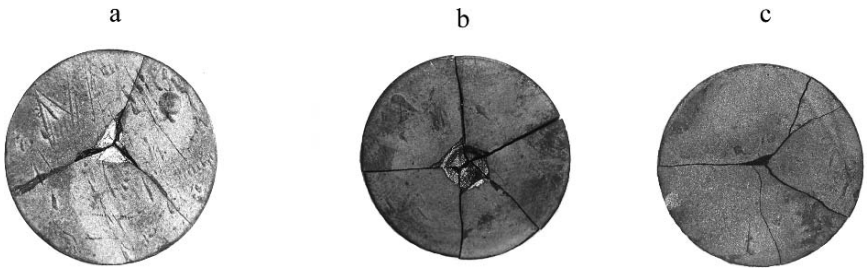

Fig. 6.7. View of the tested $ZrC_{0.93}$: specimens from (**a**) $q_o = 7.2\,\text{kW cm}^{-2}$, $\tau_f = 0.004\,\text{s}$; (**b**) $q_o = 2.9\,\text{kW cm}^{-2}$, $\tau_f = 0.035\,\text{s}$; (**c**) $q_o = 1.4\,\text{kW cm}^{-2}$, $\tau_f = 0.184\,\text{s}$

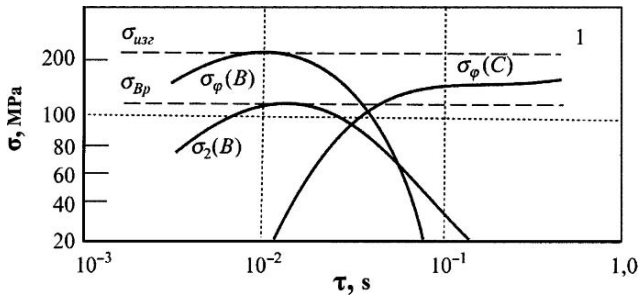

Fig. 6.8. Computed maximum values of stress. (B, C are bands of tension, see Fig. 6.6)

the disk. Because of the limited localization of the tensile stresses in the zone B and their high gradient both on the radius and along thickness, the crack incipient in the zone B propagates along the surface of a cone at an angle to the top of the disk by-passing zone A and reaching the top surface at $\rho = 0.2$ where the component σ_φ is tensile. After that the cracks propagate at the cost of tensile stress σ_φ in zone C (Fig. 6.7b). The peak of the crater is formed at a distance of $\xi = 0.3$–0.5 from the top of the cylinder. This corresponds to the points of appearance of the maximum tensile stresses. The level of tensile stresses in zones B and C corresponding to the fracture lies in the range between tensile and bending strength (Fig. 6.8). The craters are not formed with increase of time τ_f (up to 0.1 s and more). Fracture occurs owing to propagation of two-six radial, some curved, cracks without originating the crater (Fig. 6.7c), similarly to fracture of the local loaded thin disks [77].

The complex character of the fractures in the specimens in the cases observed above is caused undoubtedly by non-uniform triaxial stress. For the most simple case of fracture at times $\tau_\mathrm{f} \geq 0.1$ s, when a single tensile component in a specimen is tangential stress (Fig. 6.6, band C), the crack originates at a point of the maximum values $\sigma_\varphi^{\max}(\xi = 0, \rho = 0.4)$ and spreads radially, i.e. in a perpendicular plane, to the direction of the maximum tensile stress. The crack is able to overcome the restrictedly stretched compression zone ($p = 0$–0.2) and disintegrate a specimen in case of a stretched area of stresses ($p = 0.2$–1.0). Similar regularity of partial or complete fracture depending on a relationship of the tensile and compression bands are recognized in [50] at non-stationary aspects of thermal loading of ZrC disk specimens.

The modification of thermal loading condition influences not only the character of the fracture, but also the magnitude of fracture stresses. All modifications of the level of the limiting thermal loadings are caused only by triaxial stress on a body. A stress level $\sigma_\varphi^{\max}$ responsible for fracture is close to the bend strength value of zirconium carbide (Fig. 6.8) at short times $\tau_\mathrm{f} < 0.01$ and at the most acute inhomogeneity of a stress state on cross-section, when the field of tensile stress is insignificant.

The limiting values of stresses become near to ultimate tensile strength at time $\tau_f > 0.04$ s when firstly all three components of σ_r, σ_φ and σ_z, in zone B are tensile and then a more stretched band of tensile stresses occurs in zone C.

Electron beam loading of SiC specimens confirms the influence of a stress state of a body on fracture character [59]. Disks of 22 mm in diameter are damaged by various fashions: from local brittle cleavage to complete separation of a specimen into parts at variation of a level of thermal loading up to 10 kW cm^{-2}, changing diameter of the electron beam spot from 3 up to 7 mm and loading time within the limits of 1×10^{-3}–10 s. Local surface cleavage of a material is possible only at sizes of thermal loading band of 3 mm, due to the compression component of thermal stresses with magnitude 500–760 MPa exceeding ultimate compression strength, while the level of tension component of thermal stresses is far from ultimate tension strength.

Brittle cleavage extending to a depth of 20–30 μm with formation of a system of parallel cracks changing the path on the boundary of grains is observed well owing to a transparence of the material (Fig. 6.9).

The mechanism of spalling formation is adequate to the mechanism of fracture under compression loading [53] and is determined by the evolution of an ensemble of interacting micro-cracks on trajectory, parallel to the compression axis, with their subsequent avalanche union and origination of the damage sites. The damage sites are merged and incremented on the area until the stress level does not become critical on loss of stability during rise of thermal loading, forming cleavage. The disks are disintegrated in parts at sizes of thermal band up to 7 mm and loading time > 0.1 s.

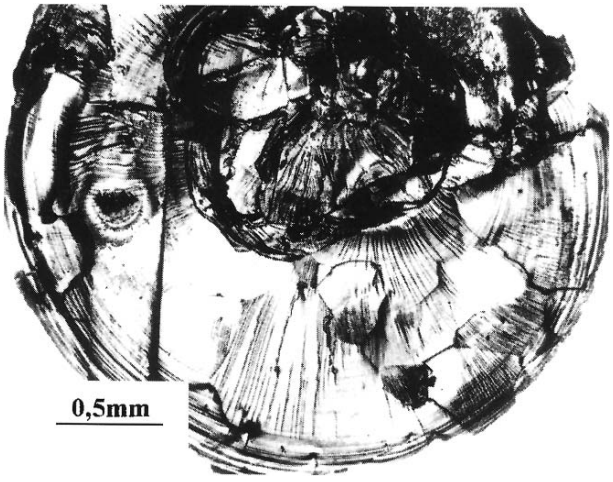

Fig. 6.9. Character of a fracture of sublimed silicium carbide after local thermal loading, $q = 10.5$ kW cm^{-2}, $\tau = 0.01$ s

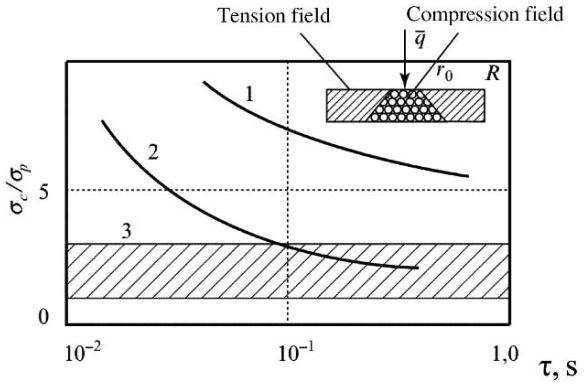

Fig. 6.10. A ratio of the maximum values of compression components of stresses in specimen SiC to tensile varying with time at non-stationary thermal loading (1) $2r_0 = 3$ mm; (2) $2r_0 = 7$ mm; (3) σ_c/σ_t

The character of fracture of specimens is determined by a relationship of the maximum compression and tensile components of stresses during thermal loading in relation to the limiting characteristics of a material's strength (Fig. 6.10).

Considering that a ratio of compression strength and tension for SiC is within the limits of 1–3 (see Fig. 6.10 field 3), fracture of a SiC specimen at the diameter of thermal loading band of 3 mm happens only from the compression component of stress in the restricted volume of a body (curve 1) at >0.1–0.2 s. Fracture of a specimen at the diameter of thermal loading band of 7 mm (curve 2) is possibly from the tensile component of stress on the rim of the specimen.

Fracture of zirconium carbide at analogous test conditions happens only due to the tensile component of thermal stresses since a ratio $\sigma_c/\sigma_t = 8$–10 above that of SiC and, besides, it is constant over the range of temperatures up to 1,400 K.

Results of the local loading of ZrC and SiC disks confirm considerations about the essential effect of inhomogeneity and complexity of a stress state on the character of a brittle failure [50], once again proving the necessity of use of the force approach of fracture mechanics instead of existing energy methods. As a matter of fact, for the exact description of all fracture patterns of locally loaded specimens (formation of cracks and craters) it is necessary to consider the history of a loading and the kinetics of disproportionation of the thermal–elastic stresses at all intermediate stages of crack evolution.

6.4 Influence of Residual Stresses on Fracture at Thermal Loading

The thermal stress resistance and bearing capacity of thermally loaded bodies can change significantly at variation of an aspect and level of the residual stresses originating during manufacture of ceramic articles or at their maintenance in non-uniform temperature fields with different heating and cooling rates.

Residual Stresses of a Technological Origin

The reasons for formation of macro-stresses during sintering of the high-melting point materials prepared by methods of powder technology can be inhomogeneity of a chemical and phase composite on cross section of the ceramic blank part and the temperature gradients originating during sintering and cooling [183–185]. The presence of wide areas of homogeneity at many materials of interstitial type at variation of a chemical composite leads to modification of the lattice constant, dislocation and diffusive mobility and physical–mechanical properties, in particular a coefficient of linear expansion [14].

The appreciable modification of a chemical composite of the surface layers of the ZrC, NbC stock materials leads to emersion of a noticeable gradient of a coefficient of linear expansion and the residual macro-stresses even in the absence of temperature gradient. The level of residual stresses σ_{r} is determined predominantly by the magnitude and character of a modification of a coefficient of linear expansion on a cross section of the stock material.

Residual stresses originate at a stage of cooling from the temperature of brittle-plastic transition $T_{\mathrm{b-p}}$ to room temperature, as stock materials are sintered at high temperature ($T_{\mathrm{s}} > 2{,}300\,\mathrm{K}$) and cooled at a low speed (200–$300\,\mathrm{K\ h^{-1}}$). The magnitude and sign of residual stresses are determined by the gradient character of a coefficient of linear expansion [184, 185].

The following expression for the maximum values of stresses is obtained using experimentally derived data of a change of a coefficient of linear expansion on the cross section of a stock material and known dependences of thermal stresses vs. modification of properties [71]

$$\sigma_{\max} = \sigma_{\varphi} = \sigma_z = \frac{\Delta\alpha \Delta T E}{3(1-\mu)} \left(1 + \frac{r_0}{R} + \frac{r_0^2}{R^2}\right),$$

where $\Delta T = T_{\mathrm{b-p}} - T$; E is modulus of elasticity, μ is a Poisson's ratio; R is radius of stock material; $r = R - l$ (l is distance from a surface); $\Delta\alpha$ is the maximum difference of the linear expansion coefficient in different layers of the stock material. Even minor gradients of linear expansion coefficient lead to formation of the significant tensile stresses (Fig. 6.11) in high modulus carbides having high temperature of brittle–plastic transition. These stresses

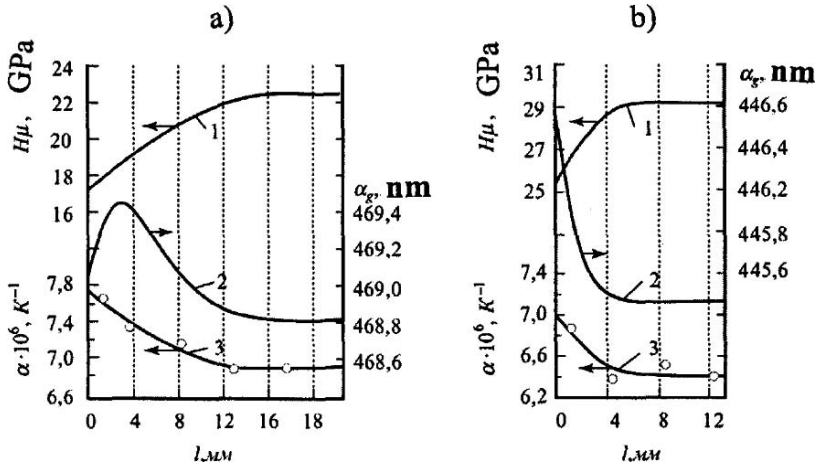

Fig. 6.11. A modification of micro-hardness (1), lattice constant (2) and a coefficient of linear expansion (3) on cross sections of stock materials $ZrC_{0.91}$ (**a**) and $NbC_{0.76}$ (**b**)

during manufacture can produce emersion of cracks, or reduce the thermal stress resistance by 40–80% in the subsequent tests by cooling in water.

Formation of residual stresses in glass during its cooling from melted state is caused by non-uniform distribution of temperature and viscous-fluid deformations and is due also to a gradient of density on a section of glass [186]. The occurrence of so-called structural stresses is connected with fixing non-equilibrium glass structure with various densities, which takes place if separate layers harden with unequal speed. The value of structural stresses is an order below viscous-fluid stresses. Measurement of residual stresses in glass is conducted by a method of birefringence, by means of quartz wedges or by the mechanical method, based on definition of size of a sample's deflection at unilateral removal of surface layers, owing to imbalance of residual stresses in the tempered sheet.

The significant residual local stresses originate in the coating sprayed on a substrate. Local stresses are estimated by calculation [187], by an X-ray method [188, 189] and on shear of lines of fluorescent spectroscopy [190]. A major effect on the quality of large objects from industrially electro-melted refractory processes influences the residual stresses, appearing during decrease of temperature after isothermal exposure. The temperature field differs with the greatest irregularity in objects during cooling. The temperature and moisture gradients on cross section of an object cause cracks [191].

Measurements of results of residual stresses around an indenter's imprints have allowed us to explain the habits of sub-critical distribution of cracks and created an observable level of thermal stress resistance [192–195]. There are methods of liquidation or sharp decrease of a temperature gradient (for

example, preliminary electrode and induction electro-warming of a mixture) at the stage of a warming up refractory. It is necessary to conduct controlled annealing for decrease of residual stresses after cooling of moulded objects whose regimes are determined by optimization methods of the deformed solid mechanics [196, 197].

The surface residual stresses measured by a $\sin^2\omega$ method on the end surfaces of disk specimens of aluminium oxide after coarse and thin abrasion are increased respectively up to 150 and 90 MPa. Strength at a biaxial bend loading thus matches 300 and 220 MPa. The thermal stress resistance estimated at cooling of heated disks by a jet of cold air has appeared to be 25% below the thermal stress resistance of disks with a smaller level of residual stresses [198]. The cracks that originated in the central band of tensile stresses, stopped in the field of compression stresses on the rim of the disk. Some unexpected decrease of difference in fracture temperature of specimens with a higher level of residual stresses is motivated simply by test conditions. The increased convective heat transfer from a rougher surface led to decreasing of fracture difference. An apparent contradiction in calculations is removed by accounting for this condition.

The residual stresses appearing in disk specimens made from an alloy of chromium after heating of a lateral surface and the subsequent cooling bring about brittle fracture [199]. It is caused because many BCC metals [200] possessing relatively high strength and sufficient fracture toughness at the uniaxial loading are inclined to brittle behaviour in non-homogeneous and complex fields of the stresses' proper thermal loading.

Application of temperature differences down to $\Delta T = 1{,}123$ K do not cause fracture of disks (with exterior diameter of 45 mm and a central hole with diameter of 4 mm). However, easily visible cracks originate on the rim of disks after the first cooling with velocity 30 grad min^{-1}, owing to emersion of the thermal–elastic tangential compressive stress at heating, sufficient for a plastic flow of the material and origination of residual tensile stress. The number of thermal cycles for fracture is incremented with reduction of a temperature drop and at $\Delta T = 873$ K specimens fail after ten thermal cycles. Measurement of residual stresses in disks by a known X-ray $\sin^2\psi$ method established the character of distribution of residual stresses on the radius of the disk. The residual tensile stresses ∼150 MPa appeared on the rim of the disk after double loading with difference $\Delta T = 873$ K, and compressive stresses ∼100 MPa in a central band. The cracks propagate radially at this aspect of stress distribution due to a tangential component of residual stresses and preferentially up to half the radius of the disk, i.e. up to a band of compression of residual stress.

The retardation of cracks at the approach to a band of compression stresses testifies to the unfavourable conditions of their extension that is inherent in a brittle fracture of solids in a non-uniform field of stress. Brittle character of fracture of disks as a result of a loading is confirmed also by the characteristic pattern of cleavage fracture typical for a brittle spalling, without appreciable indications of a tough fracture.

It is clear that the complex field of residual stresses, unlike axial extension of smooth round specimens, restricts plastic deformation of an alloy and leads to brittle fracture. Processing of materials which involves thermal loading, besides the harmful effect of residual stresses, may increase the bearing capacity by the directional formation of compression residual stresses on the surface of articles by methods used for reinforcement incrementing resistance to the beginning of thermal fracture (see observations in Chap. 9)

Structural anisotropy of a material, phase changes [201, 202] and the essential presence of various kinds of flaws in the structure of a sintered material [203–205], result in emersion of a different sort of (conventionally independent) technological micro-stresses: σ_l localized in the sections embracing separate groups of grains, σ_i inter-granular, σ_s spherically symmetrical stresses in the grains set-up by a gradient of linear expansion coefficients on the grain body and peak micro-stresses σ_p in the mouth of micro- and submicro-cracks [206].

Two different procedures are used for estimation of a local level of stresses in large-grain ZrC materials. One method is founded on gauging inter-planar distances d_{hkl} for the same planes (hkl) for the major number of grains by scanning the surface of a specimen on a diffractometer with focusing on Bregg–Brentano [204]. The second method implies measurement of the disjointed reflexes from local sections of grains by means of micro-beams [203]. Both procedures reveal local stresses over a wide range. The stresses are raised from 130 up to 380 MPa with increase of grain size from 8 up to 60 µm and cause decrease of bending strength from 460 to 180 MPa. The further increase of grain size led to emersion of the cracks exceeding their size [203]. Change of thermal stress resistance of specimens with different grain size, tested by cooling in water, followed the modifications of strength.

Examination of composites based on Al_2O_3 with inclusions of particles of SiC and stabilized ZrO_2 have established the essential effect of local stresses on fracture toughness [205]. Stresses measured by a piezoelectric method varied from grain to grain being counterpoised in the volume of a specimen. The increase of grain size of mono-phase ceramics Al_2O_3 owing to lattice anisotropy increases the level of local stresses and the slope of the R-curves characterized by the value of coefficient χ, and leads to magnification of the crack path length L enveloping grains (Table 6.3). The low level of residual stresses in specimens of Al_2O_3 with grains of a small size is caused by the increased relaxation ability due to accelerated inter-granular diffusion.

Introduction of SiC particles, owing to the negative difference between coefficients of linear expansion particles of SiC and Al_2O_3 matrix, led to emersion of tensile stresses in Al_2O_3 grains, and decreasing the grain size reduces the capability of a fracture toughness to rise sharply with increase of the content of SiC particles. As opposed to this, a ZrO_2 composite, with a higher value of coefficients of linear expansion in relation to Al_2O_3, creates additional domains of compression stresses incrementing with rise of ZrO_2 content and increasing the efficiency of the action of bridge stresses. Nevertheless, introduction of

Table 6.3. Modification of level of residual stresses, the relative path length of cracks L enveloping grains and (or) particles, slope coefficient χ of R curves depending on grain sizes and contents of particles SiC and ZrO_2 (wt%) in aluminium oxide

Contents of particles, wt (%)	Grain size (μm)	Residual stresses σ (MPa)	L (%)	χ
0	3	63	3	0.44
0	19	79	11	0.66
0	28	108	25	1.0
0	40	110	40	1.6
0	65	126	65	1.9
0	5	−188	51	0.8
SiC-10	1.6	+13	0.5	0.4
SiC-20	1	+77	0.1	0.2
SiC-30	0.8	+169	0	0.06
0	∼19	+79	11	0.7
$ZrO_2 + 10$	∼2	−82	0.4	0.07
$ZrO_2 + 10$	∼18	Not measured	11.1	1.03
$ZrO_2 + 20$	∼2	−148	0.05	.003
$ZrO_2 + 30$	∼2	−195	0	−0.07

Coefficients of linear expansion: ZrO_2 $12 \times 10^{-6}\,K^{-1}$; α-SiC $3.5 \times 10^{-6}\,K^{-1}$; Al_2O_3 $9.0 \times 10^{-6}\,K^{-1}$

30 wt% ZrO_2 does not increase the fracture toughness owing to decrease to nil of a trajectory of cracks L enveloping grains.

The temperature cycling of high dispersed polycrystals on the basis of boron nitride phases with lattice of wurtzite (BN_w) and blende (BN_{sf}) produced explosive fracture on particles with sizes of 10–20 μm, owing to the presence of a high level of local stresses (1.5 Gpa), which originated during synthesis of the polycrystals at high temperature and pressures of more than 5 GPa [202].

Modelling of Residual Stress Formation in Operating Conditions

Research into the origination conditions of residual stresses in ceramic articles depending on temperature, irregularity of temperature pattern, heating and cooling rates and their definition is of interest for an estimation of the bearing capacity of constructional elements in operating conditions [207, 211].

The formation of dangerous residual stresses (RS) is possible in the production of refractory ceramic materials in non-uniform temperature fields at high temperatures. These RS may appear in ceramic heating elements, nuclear ceramic rods, ceramic lining of spacecraft, metallurgical furnaces, etc.

Modelling of the origination of residual stresses was implemented in [61] by heating ZrC specimens over the range 1,300–2,000 K by two expedients:

electron beam and induction heating methods. The schema of RS origination is as follows:

- Heating of the disk with the establishment of radial temperature gradient
- Exposure of the disk with preservation of the constant value of temperature gradient at a particular temperature
- Cooling of the disk after reduction or elimination of temperature gradient

In the case of the electron heating method [77], the electron beam was focused at the centre of the disk with the electron spot diameter $d = 0.3\,D$, where D is the disk diameter within the limits of 20–24 mm and height of 1–2 mm.

The side surface of the ZrC disk of the same dimensions was heated up by the induction method [208]. The radial temperature gradient forming in the course of heating can easily be controlled by the electrical power of the device. The temperature field on the radius of the disk is measured by a fast response pyrometer. The measurement time of the temperature field in 20 points comprises 0.02 s. The error of measurement does not exceed 12% in this case. The distribution of thermal stresses in the disk is calculated on the measured temperature field in the same way as in the case of electron beam heating. The values of the calculated stresses in elastic approximation for ZrC are valid for a wide temperature range. The stress–strain diagrams under tension and compression are linear for ZrC up to 1,500 and 2,300 K, respectively, at the moderate stress rate of $10^{-3}\,\mathrm{s}^{-1}$ [Application 3]. The ZrC is brittle even at 3,000 K at a higher stress rate of up to $10^{-1}\,\mathrm{s}^{-1}$. We emphasize that thermal stress resistance of ZrC is constant in the temperature range 300–1,600 K at the rate of thermal loading 1–40 MPa s^{-1}. The thermal stress resistance increases at temperatures above 1,700 K, with the lower rate of thermal loading owing to the relaxation of the local stresses. It should be noted also that the long term loading of ZrC can cause the measurable creep at 1,600 K [Application 4].

The exposure of samples to the non-uniform temperature field induces relaxation of thermal stresses in most heated parts of the disk and the redistribution of the stress components throughout the whole volume. Residual stresses with diagrams opposite in signs to thermal stresses occur after some exposure of the samples under thermal load and subsequent cooling by radiation heat transfer from the face side of the disk. The schema of distribution of the residual stresses under induction heating and electron-beam heating are given in Fig. 6.12. The tensile stresses appear in the opposite zones of the disk.

The thermal–elastic stresses are computed under the incoherent theory of thermal elasticity with error of 12% on temperature patterns. Theoretical estimation of relaxed stresses under thermal loading even in a simplified manner is rather bulky. Numerical calculation of residual stresses was conducted provided that the relaxation rate in a complex field of thermal stress is similar to creep at the uniaxial loading. An exponent of a stress n is 3.2 in the

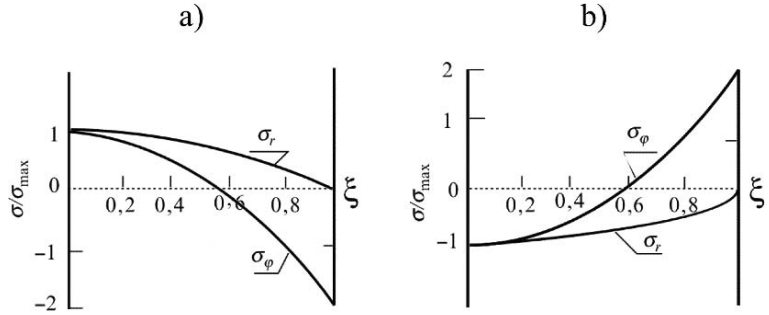

Fig. 6.12. Distribution of residual tangential σ_φ and radial stress σ_r vs. ξ coordinates after electron-beam heating of central zone of the disk (**a**) or induction heating of lateral side (**b**) $\xi = r/R$ is the scaled disk radius

equation of creep and an activation energy $Q = 95\,\mathrm{kJ\ gmol^{-1}}$ for ZrC over the range of temperatures of 2,000 K.

$$\dot{\sigma}_{\theta\mathrm{m}} = -CE\left(\sigma_\theta^n - \nu\sigma_r^n - \nu\sigma_z^n\right)\exp\left(-\frac{Q}{kT}\right), \tag{6.3}$$

The residual tangential stresses were evaluated experimentally by an X-ray $\sin^2\psi$-method [209] with an error of 15 MPa for such high-module material as ZrC. In some cases the stresses were determined by the measurement of a slit entered into the stressed sample. General principles of determination of residual stresses are given in [210]. There is practically a linear relationship between the disclosure and residual stresses measured by the X-ray $\sin^2\psi$-method and so the residual stresses can be estimated by a less tedious method. For example, the disclosure of the slit of 25 μm corresponds to 240 MPa.

Thermal stress resistance is determined by two methods:

- By water cooling of the lateral surface of a previously heated disk with thermally insulated end faces, or
- By heating the same disk assembly in melted tin

The temperatures of the sample or the tin bath increased stepwise through 25 K up to the temperature of quenched samples T_0 or the temperature of melted tin, T_t, causing their fracture. The maximum difference, $\Delta T_\mathrm{m} = T_\mathrm{m} - T$, is calculated numerically on the temperature dependence of heat transfer in water or in melted tin and temperatures T_0 or T_t at the moment of fracture. The T_m is the mean integrated temperature over cross section of the disk and T is the temperature of any point of the disk. Thermal stress is evaluated on the ΔT_m value:

$$\sigma_\mathrm{f} = \alpha E \Delta T_\mathrm{m} K_\mathrm{f},$$

where K_f at heating of a central band of the disk and of a lateral surface are equal, respectively, $1 - \mu$ and $1 - \mu/2$.

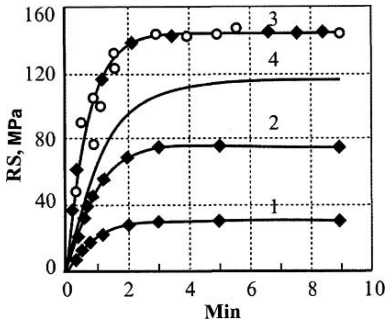

Fig. 6.13. Dependence of residual stresses on time of exposure and heating temperature under thermal loading by induction of ZrC disks. The RS are measured by X-ray $\sin^2\psi$ method after temperature exposure; (1) 1,600 K; (2) 1,800 K; (3) 2,300 K; (4) Calculated estimations of residual stresses on creep data. *Open circle* is calculated values of RS with use of the relation (6.3)

Application of a temperature drop in disks leads to emersion of the residual stresses on opposite sign to thermal stresses, acting during high-temperature stand-up. Magnitude of residual stresses is determined by heating temperature and exposure time (Fig. 6.13).

The first signs of thermal stress relaxation in the zirconium carbide are observed at a temperature of 1,300℃. The appearance of plastic deformation at the mechanical loading by bending is higher (1,800℃) [13]. The rate of relaxation with temperature rise increases and the process of relaxation and formation of residual stresses at 2,000℃ finishes in some minutes. The value of RS can vary not only by temperature level but also by exposure period under thermal load. The formation of tension stress components on the periphery of the disk reduces the thermal stress resistance measured by the quenching method more the higher is the level of residual stresses (Fig. 6.14).

The change of the thermal stress resistance is governed by summation of the residual stresses with the tension thermal stresses during the quenching test. The compressive RS increases the thermal stress resistance and the tension RS decreases it. The disks can crack spontaneously without thermal loading if the tension RS achieve the strength limit.

As the thermal stress resistance changes nearly proportionally to the residual stresses value, we propose to estimate the RS by a method of calculation using the difference of thermal stress resistance values ΔT_{im} and ΔT_{m}, respectively, for samples with and without residual stresses.

$$\sigma_{\mathrm{r}} = \alpha E(\Delta T_{\mathrm{im}} - \Delta T_{\mathrm{m}}). \tag{6.4}$$

The comparison between calculated and measured σ_{r} testifies their consistency (Fig. 6.13). Calculated estimations of residual stresses on creep data are lower than experimental measurements in consequence of disregard of the unsteady creep part.

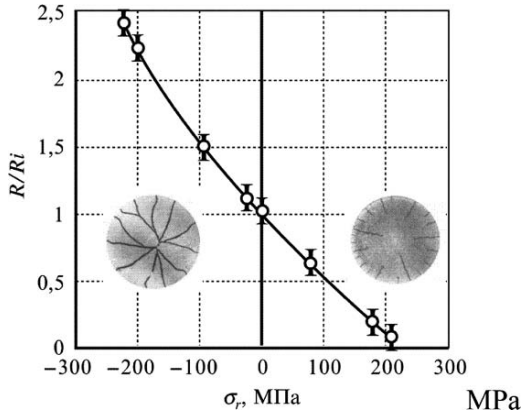

Fig. 6.14. Influence of the surface residual stresses measured by quenching on the thermal stress resistance of ZrC disk

The formation of tension residual stresses exceeding the strength limit results in appearance of radial cracks in the peripheral zone of the sample without total fragmentation (Fig. 6.14). In the case of formation of compressive residual stresses in the peripheral disk zone, the thermal stress resistance is increased by up to 2–2.5 times (Fig. 6.14). Any further increase of the thermal stress resistance due to compressive stresses appears to be impossible because of the increase of the tension stress components in the central part of the sample up to the strength limit. In this case the sample is fragmented completely. Various kinds of fracture on the residual and thermal stresses are determined by non-uniform stress field with a different ratio of tension and compressive zones and distribution of stresses in these zones. Such heterogeneity of the stress field can be expressed on the basis of force fracture mechanics by a parameter N [49], which characteristic is explicitly observed in Chap. 8.

The residual tension stresses formed in the peripheral zone of the ZrC disk after induction heating are stable in samples at temperatures of annealing less than 1,600 K. A higher temperature and longer exposure of the annealing causes residual stresses to decrease readily (Fig. 6.15).

It is very interesting to compare the measured relaxation rate with data from other authors, but investigations on thermal relaxation are in fact very scarce. Fortunately, our colleague, Prof. P.V. Zubarev performed the investigation of relaxation of ZrC under bending in a temperature range of 1,900–2,500 K. The curves of relaxation have a similar form to ours, but the rate of the relaxation at related temperature is lower by a factor of 10. Such a difference is moderate for creep and relaxation and may be associated first of all with the distinction of stress state and with variance of composite and structure of the sample material.

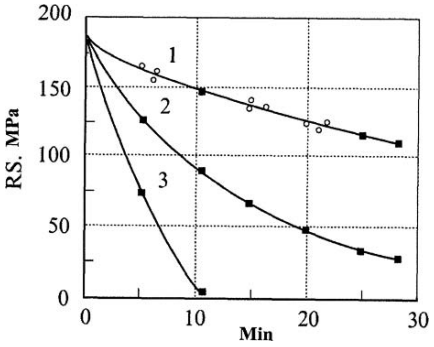

Fig. 6.15. Residual stresses in ZrC disks measured by X-ray $\sin^2\psi$ method after annealing. (1) 1,600 K; (2) 1,800 K; (3) 2,300 K; *Open circle* is the values of RS determined by the disclosure of the slit

To decrease dangerous residual stress level after complete cooling down of the thermo-stressed products, it is necessary to anneal them at an intermediate temperature level. The time of annealing must be sufficient for the partial relaxation of stresses at the chosen temperature.

6.5 Fracture of Elastic–Brittle Bodies at Combined Thermal and Mechanical Loadings

Components of engineering constructions operated at high temperatures, for example, blades of gas turbines or devices in space installations, can be subjected to simultaneous thermal and mechanical loadings. Realization of specialized research on the basis of force principles of fracture mechanics [60] is required for the estimation of the bearing capacity of a body under such combined loadings.

The study of growth of cracks in linear-elastic material does not meet additional mathematical difficulties in calculation under combined thermal and force loading, as the influence of thermal and mechanical loads can be considered separately, and the outcome of their joint operation is then determined on the principle of superposition.

The findings considered below are obtained for two cases. The first corresponds to a cylinder with an edge slit under thermal load and homogeneous tension load P per unit of lateral area. In the second variant, uniform pressure of the value P is applied to the lateral area of the cylinder. These cases are simplified, but nevertheless are rather important, as allowing evaluation of the order of values of mechanical loads, which essentially change the fracture characteristics of the body under combined loading in comparison with the thermal effect alone.

The curves of the limiting equilibrium represented in Fig. 6.16 were obtained similarly to the curves plotted in Fig. 5.1. The value of maximum

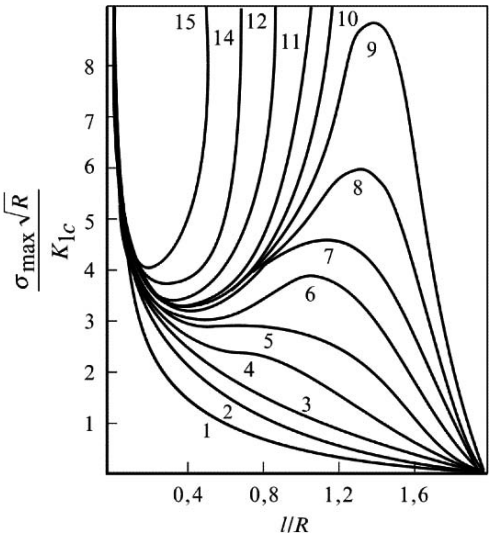

Fig. 6.16. Curves of the limiting equilibrium for a cylinder with an edge slit under the combined effect of thermal stresses with tension (curves 2–9) or compression (curves 11–15) load on the lateral area

tension stress on the lateral area of the cylinder without cracks is still designated as $\sigma_{\max} = \sigma_o \pm P$ (signs $\pm$ are, respectively, for tension and compression), where σ_o is maximum thermal stress. The parameter $\chi = p/\sigma_o$ on each curve for simple loading is constant.

The values P and σ_o are connected with $\sigma_{\max}$ by the following relation:

$$\sigma_o = \sigma_{\max}/1 \pm \chi; \qquad P = \sigma_{\max}/1 \pm \chi.$$

An essential influence of the mechanical loads under combined effect on the body fracture type and final length of the crack is seen from Fig. 6.16. Under the superposition of homogeneous tension value 10% and more than the level of maximum stresses ($\chi \geq 0.1$, curves 2–5) the sites of equilibrium cracking disappear; the crack becomes unstable over the range of length $l \geq l_0$ and total fracture happens. Under a lower level of tension, $0 < \chi < 0.1$, the sites of equilibrium crack growth are retained, as in the case of thermal loading only, however, up to a quite certain value of the load $\sigma_{\max}$. For example, under $\chi = 0.01$ (curve 9) the equilibrium growth of the crack happens in the range $3.2 \leq \sigma_{\max}\sqrt{R}/K_{1c} < 8.6$. The crack comes to rest without entering the surface in this range of loads. The crack moves unstably down to the boundary of the body if, with the same $\chi = 0.01$, the load is $\sigma_{\max}\sqrt{R}/K_{1c} \geq 8.6$. Thus, the total fragmentation of the body becomes possible under superposition of a homogeneous tension of any final magnitude in contrast to thermal loading only. The value of this ultimate load, describing transition from partial fracture to total fragmentation under known parameter χ, can be determined with the help of the curves in Fig. 6.16.

The superposition of homogeneous compression stress on the lateral area of the cylinder results in a decrease of the final crack length in comparison with the only thermal loading (curves 11–15). For example, under the level of compression 0.1–0.2 from the maximum thermal stress and $n = 2$ this length decreases approximately twice.

From the principles of energy, the force loading of the thermally loaded body with tension or compression loads up to an identical level is bound to have a similar effect on the process of fracturing. Actually, as follows from the limiting equilibrium curves, the levels of thermal fracture loads and the kinetics of fracture appear to be different under superposition of tension or compressive loads.

In support of the calculations, experiments with thermally loaded disks under simultaneous superposition of the force load were conducted. To realize a force load upon the thermally loaded disk is practicable only by bending. Samples of ZrC disks, with a diameter of 15.5 mm and thickness h of 1.4 mm were loaded in a special device by axisymmetrical bending momentum at the expense of the force created by a spring. The load value is determined on the displacement of the spring tip, which was previously graduated. The bending of the sample under loading is carried out in ring punches. The diameter D of the outside punch is 14 mm, and the internal diameter d is 4 mm. The thermal loading is carried out by cooling the lateral area and thus creating a radial temperature difference in the disk, which was covered on its face surfaces with heat-resistant rubber and asbestos insulation. The level of tangential stress from a force load was determined by the relation in [212]:

$$\sigma_\varphi = \pm(3P/4\pi h^2\beta)[(1-\mu)(\beta - 1/\beta) + 2(1+\mu)\beta ln\beta]$$

with $0 \le \rho \le 1$

$$\sigma_\varphi = (3P/4\pi h^2)[(1-\mu)(1-\beta^2)]$$

with $\rho = \beta$, where $\rho = 2r/d, \beta = D/d$.

The mean integrated temperature difference ΔT_m and thermal stresses were determined by water quenching [213]. The measurements of crack length were conducted using a microscope on the face surface of the disk, which was polished prior to the experiment. Cracks of 3–7 mm in length were created under thermal loading of disks with initial radial slit 0.5–3 mm long and 0.2–0.3 mm wide. The temperature of the sample under thermal loading was increased stepwise in 10° intervals in the range of temperatures 100–600℃, fixing, after each cycle of heating and cooling, the alteration of crack length. The bending stress was maintained constant during the whole test.

The theoretical estimations of crack length vs. the dimensionless thermal load value and the experimental results on 30 samples tested under thermal loading and on 15 samples under combined loading are shown in Fig. 6.17. It is apparent that the development of the crack under thermal loading and under superposition of transversal bending by the load of 20 N happens similarly up to the relative length value $\lambda = l/R = 0.5$–0.6.

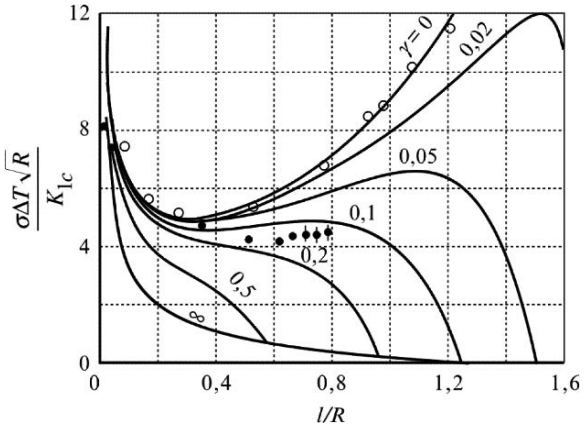

Fig. 6.17. Curves of the limiting equilibrium for a disk with an edge slit under the combined effect of thermal stresses ($n = 6$) and bending. Experimental data under combined loading (*filled circle*) and at simple thermal loading (*open circle*)

In both cases the crack grows in equilibrium, increasing in length by steps, and the magnitudes of the steps are approximately identical and change within the limits of 0.1–4 mm. At the same time, the tendency to the increase of the crack length is observed under combined loading as compared with only thermal loading at the identical thermal load. Beginning with $\lambda \geq 0.6$, the cracks located in the operative range of maximum bending stresses deviate from the main trajectory in the perpendicular direction. The rate of rectilinear growth of the main crack is essentially decelerated up to the moment of its deviation by about 90°, or at the appearance and accumulation of secondary perpendicular cracks. This is caused by the emerging significant radial stresses on the line of the main crack, when it passes the zone of maximum bending stresses at the centre of the disk. The further increase of thermal load and, respectively, the λ up to 0.65–0.7 result in total fracture of the disk into 2–3 parts.

The experimental data on combined loading nevertheless disagreed slightly with the calculated curves for the combination of the thermal and bending loads. The appropriate calculated curve of the limiting equilibrium, $\gamma = 3P\sqrt{R}/2h^2K_{1c} = 0.126$, under the bending load $P = 20$ N lies a little below the average level of data points. This is explained by two reasons. The first is associated with emerging secondary cracks, partial unloading of the body and shift of the limiting equilibrium curves towards the increase of the required load for equilibrium crack growth that was not taken into account in this simplified calculation. The second reason is that this curve was plotted for a maximum stress on the surface of the disk, disregarding the stress gradient across the disk thickness.

Another pattern is observed under thermal loading of disks. The growth rate of the only main crack is maintained up to $\lambda = 1$ to temperatures of 250–260℃, then it is decelerated in connection with emergence and develop-

ment of secondary cracks. The total fragmentation into separate parts does not happen until the temperature reaches 600℃ at $\lambda \cong 1.2$–1.4, when the interaction of cracks spreading towards one another from diametrically opposite points of the disk becomes possible.

Thus, the obtained data indicate the importance of the various roles of interaction of the cracks under combined loading and under thermal loading only. In the former case, the interaction of cracks results in earlier fracture into separate parts, in the latter case the moment of fragmentation is retarded.

This data can be useful used in the analysis of bearing capacity of ceramics in the atomic, space and thermonuclear technologies working in supercritical modes, supposing occurrence of partial loss of bearing capacity of components.

6.6 Influence of Temperature on Thermal Stress Resistance

The regularity of thermal stress resistance with temperature represents a topic of significant interest. However, the data of direct measurement of thermal stress resistance at different temperatures are extremely restricted, so the temperature dependences of the thermal stress resistance criteria R and R' for some high-melting point compounds (Fig. 6.18) were obtained by calculation using the most reliable values of their physical–mechanical properties. Borides and silicium carbide have the greatest values R and R'. Various composites on the basis of these materials, and also mixtures of ZrB_2–SiC are applied in the manufacture of different components whose operation involves sharp thermal cycles [214].

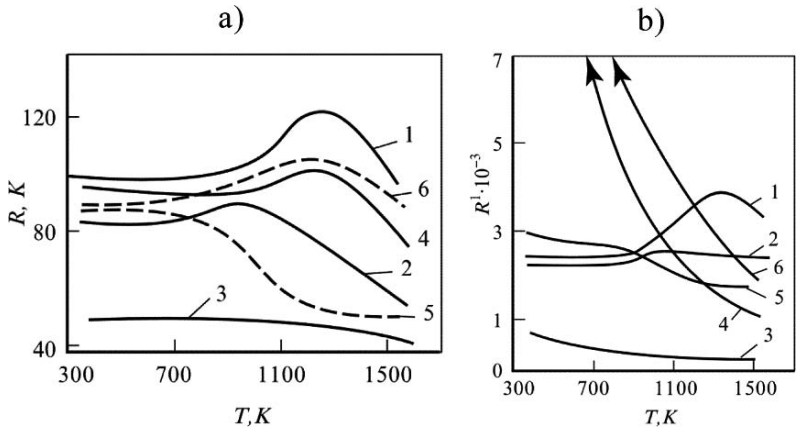

Fig. 6.18. Design temperature dependences of criterion of thermal stress resistance R **(a)** and R' **(b)** some high-melting point compounds: (1) HfB_2; (2) ZrB_2; (3) ThO_2; (4) BeO; (5) ZrC; (6) SiC

The majority of high-melting point compounds do not manifest appreciable macro-plasticity from room temperature up to $0.5T_{\mathrm{m}}$, therefore use of design criterion R and R', based on the linear theory of elasticity, is justified. The decay of values of R in an initial part of a temperature range observable for some materials, for example ZrC and MgO, is caused by increase of a coefficient of linear expansion. The influence of a ratio σ/E on criterion of the thermal stress resistance R with a modification of temperature is more complex. Temperature dependence of strength of high-melting point compounds can have a diversified character. The ratio σ/E of some materials at an increase of temperature down to emersion of macro-plasticity is gradually diminished or saved at stationary values. Other materials vary irregularly, due to some increment of strength owing to emersion of micro-toughness or due to more slump of a modulus at practically constant values of strength in this temperature band (see Application A.2). The modification of criterion R' with temperature depending on the class of material is manifested variously. The decrease of R' of oxides (MgO, BeO) is connected with a slump of thermal conductivity. The thermal conductivity of carbide or boride materials with increase of temperature, as a rule, are raised that determines accordingly character of a criterion modification R'.

Comparison of temperature dependences of thermal stress resistance obtained experimentally during a stationary loading of ring disks of ZrO_2 and MgO [16, 26], displays satisfactory coincidence with the calculations to temperatures of 1,500–1,600 K (Fig. 6.19). An exception is represented by fissured

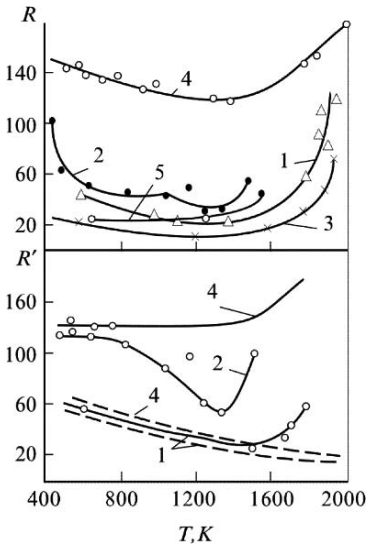

Fig. 6.19. Temperature dependences of thermal stress resistance criteria R and R' [16, 26], obtained at stationary loading of specimens of stabilized ZrO_2 : $P = 22\%$ (1), $P = 4\%$ (2) and $P < 0.5\%$ (3), with the fissured structure containing 20–26% of monoclinic phase, $P = 20\%$ (4) and MgO $P = 11\%$ (5). *Dotted lines* (1, 4) refer to design data

ZrO_2 materials, containing up to 15–20% of a monoclinic phase, whose experimental values for thermal stress resistance exceeds design values by 3–5 times. The increment of thermal stress resistance in the field of temperatures above 1,600 K is due to the occurrence of macro-toughness, and as a consequence, explicit discrepancy of design criteria R and R' is observed. The character of fracture of thermally loaded specimens of porous and dense ZrO_2 varies from transcrystalline to inter-crystalline fracture simultaneously with an increase of temperature from 1,000 K. Fracture occurs practically completely at the grain boundaries at temperatures above 1,900 K.

Observable non-coincidence of design and experimental estimates of thermal stress resistance of fissured materials is due to the essential influence of structural inhomogeneity. The level of thermal stress resistance of heterophase compounds of MgO rises with an increase of temperature, and more noticeably for compounds containing more than 4 wt% Al_2O_3 (Fig. 6.20).

Temperature dependences of thermal stress resistance are investigated in the most detail in [18]. The increase of temperature and emersion of microplasticity in ceramics increases the level of thermal stress resistance due to relaxation of local stresses. Ability of stress relaxation and, hence, thermal stress resistance, is increased with decrease of loading velocity. The thermal stress resistance of zirconium carbide with modification of temperature from room temperature to an emersion of micro-toughness at 1,700 K remains at stationary value; further heating increments the value R at decreasing of

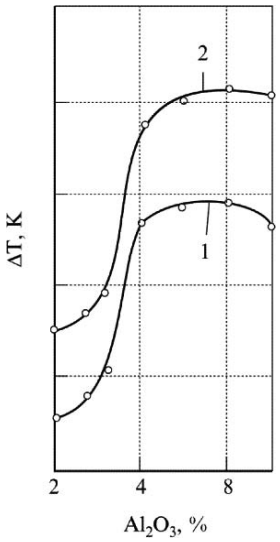

Fig. 6.20. Fracture temperature difference ΔT at a stationary loading of heterophase specimens from magnesium oxide depending on the component of aluminum oxide; (1) at moderate temperatures of up to 1,300 K, and (2) at high temperatures ~2,000 K [16]

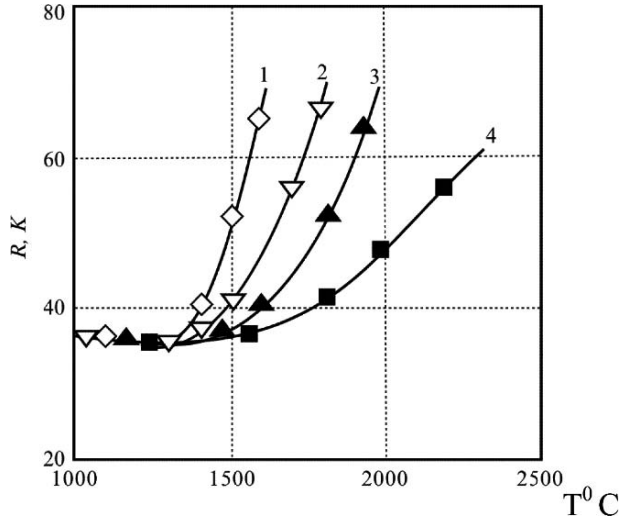

Fig. 6.21. Dependence of thermal stress resistance of samples of ZrC on temperature at different heating rates: (1) 10 K s^{-1}; (2) 50 K s^{-1}; (3) 100 K s^{-1}; (4) 200 K s^{-1}

heating rates from 400 down to 210 K s^{-1}, matching to loading rate from 40 to 1 MPa s^{-1} (Fig. 6.21).

Constancy of R values from 300 up to 1,700 K is explained by an invariance of strength and αE value. The sample cannot be fractured at temperatures greater than 2,000 K and especially at low loading rate, when a stress relaxation becomes possible. However, the significant plastic deformation causes emersion of dangerous residual stresses which destroy the body after removal of thermal loading during cooling, i.e. at temperatures below T_{bp}. Optimization of temperature regimes of laser cutting, in view of the velocity of emersion and localization of a melt band, allows avoidance of brittle failure of a material due to residual stresses [215].

Consideration of thermal stress resistance of hydride materials is significant from the point of view of materials science and for practical purposes. Hydrides of transition metals are an unusual class of materials with variable contents of hydrogen. Metals absorbing hydrogen strongly increase in volume and become brittle. Many of them, at sorption of hydrogen, are cracked or even scattered in a dust. The content of hydrogen in some metals or alloys can be so great, that it exceeds its contents in the same volume of fluidic hydrogen. High content of hydrogen in hydrides is explained by the location of hydrogen atoms in interstitial sites of a crystal lattice of metals. Hydrogen is capable of being retained in hydrides of some metals up to 400–500℃, and up to 800℃ and more at adoption of special measures preventing hydrogen yield.

The nuclear characteristics of hydrogen allow its use as a neutron moderator in nuclear reactors, and the ability of hydrides to retain great amounts of hydrogen allow us to observe them as capacities for storing hydrogen and

as a source of a hydrogen fuel, for example, in automobile engines. The development of nuclear small-sized high-energy installations primarily for jobs in space undertaken in the 1960s has demanded creation of neutron moderators working at temperatures exceeding 550–600℃. Designers of nuclear reactors decided first of all to use zirconium and yttrium hydrides [216, 217].

The original temperature dependence of thermal stress resistance is observed in zirconium and yttrium hydrides obtained through saturation [51] (Table 6.4). The thermal stress resistance practically does not vary in a temperature interval of 20–600°C, despite a doubling of strength. The invariance of the measured thermal stress resistance is confirmed by constancy of design criterion R_{d} as the magnification of strength and decay of a modulus with an increase of temperature are compensated by essential increment of the true coefficient of linear expansion. The experimental values for R_{e} exceed those of the design. A heat flow breaking the specimen determined by criterion R^1, is increased feebly with temperature for zirconium hydride and is diminished for yttrium hydride, according to modification of thermal conductivity coefficient of these materials.

The considerable decay of fracture resistance of the zirconium and yttrium hydrides, characterized by criterion R'', is undoubtedly compensated by emersion of micro-plasticity and increment of the fracture toughness. However, scattering of values R and σ proper to a brittle failure of hydrides at room temperature remains almost constant and up to 900 K.

The low value of the yttrium hydride criterion R, more than three times lower then zirconium hydride, is explained by the low strength and greater magnitude of modulus $YH_{1.97}$. At the same time, criterion R' for $YH_{1.97}$ is only twice below the matching criterion for $ZrH_{1.85}$ at 300°C, that is effected by the rather high level of thermal conductivity of yttrium hydride.

6.7 Fracture of a Body at Cyclic Thermal Loading

Thermal stresses have different effects on extent and character of damage of a body at repeated actions, depending on heterogeneity of the structure, aspects and parameters of thermal loading and, above all, on the temperature band of the test [218].

Various kinds of flaws in the form of pores, grain boundary inclusions, micro-cracks and also the local stresses originated owing to thermal expansion anisotropy and modulus of crystals are always present in the polycrystalline ceramics prepared by usual powder metallurgical techniques. As a result, the accelerated growth of flaws becomes possible with lack of micro-plasticity, due to decrease of propagation resistance of cracks in the defective areas of many structural ceramics at a cyclic loading and at relatively low temperatures.

The thermal fatigue mechanism of mono-phase, not transformation-strengthened ceramics, is connected with progressing degradation of the bridge linkage of grains in the volume of a body in the neighbourhood of a crack

Table 6.4. Effect of temperature on thermal stress resistance and physical–mechanical properties of $ZrH_{1.85}$ and $YH_{1.97}$ [51]

t°C	σ_b (MPa)	$E \times 10^4$ (MPa)	$\sigma/E \times 10^3$	$\alpha \times 10^{-6}$ (K^{-1})	λ (W m^{-1} K^{-1})	$\overline{R}_{exp}$, K	R_{dsn}, K	R' ($\times 10^2$ W m^{-1})	R''', (MPa^{-1})
$ZrH_{1.85}$ ($d \approx 500$–$1{,}000\,\mu m$)									
−190	–	–	–	(4.0)	–	85	–	–	–
20	29.4	6.86	0.4	6.0	28	70	50	20	112
200	40.2	6.08	0.7	0.8	32	70	52	22	54
400	53.9	5.29	1.0	12.8	34	70	56	24	26
500	55.9	4.61	1.2	14.7	32	75	58	24	21
600	60.8	4.41	1.4	16.6	30	–	58	–	17
$YH_{1.97}$ ($d \approx 270$ MKM, $C_o = 0.10$ mass%)									
20	16.7	13.5	0.12	8	–	20	11	–	–
300	29.4	12.9	0.23	11	51	20	14	10	214
500	27.4	12.5	0.22	13	31	25	12	6.2	235
600	29.4	12.3	0.24	14	32	–	12	6.4	204
800	30.4	–	–		26	–	–	–	–

Remarks: Strength is determined for hydride specimens obtained by hydrogenation of metal specimens

tip at an inter-crystalline fracture [219, 220]. Stress of grain linkage at loading during opening up of a crack is changed sharply from the compression stresses, normally present in ceramics, to the tensile stresses breaking bridge linkages between grains. The residual compression stresses in grains result from anisotropy of thermal expansion after cooling of a body from its operating temperature. A grain slip on boundaries and fracture of bridge linkages is accompanied by gradual decrease of σ_{r}. The expended energy on drawing down of grains in view of friction promotes increase of fracture toughness. Structural inhomogeneity and presence of defects of ceramics bring about appreciable temporal and geometrical irregularity of crack evolution. The increase of the length of a crack occurs by steps prepared by processes of structural rebuilding in the volume of the body in the neighbourhood of a crack. Slowing down of crack growth is observed at the formation of bridge linkages between grains down to its almost complete stop, and again a build-up of growth rate occurs at degradation of a bridge band. The acceleration of crack growth also becomes possible owing to shear of the adjacent surfaces of grains, origination of the contact local stresses leading to micro-cracking, 'reactivation' of the halted cracks, and hence to a branch or sharp alteration of their extension. Parts of micro-cracks can be merged during a loading or the subsequent stage of unloading. The different alternatives of cyclic fatigue determining variance of strength, either decrease or increase of strength, can be realized depending on a relationship of the energy costs of formation of a local fracture band and energy diffusion. The local fracture mechanism is determined by the initial structure and the presence of inherent ceramic defects, a level of residual stresses, temperature, circumambient aspect and the parameters of a loading.

The loading of mono-phase ceramics in a temperature interval down to $0.3T_{\mathrm{m}}$ restricts development of the fatigue process due to blunting of a crack tip, observable in plastic metals. The strength of mono-phase ZrC specimens drops almost three times and resistance ρ increases after the first cycle of a loading (Fig. 6.22a).

The depth of crack penetration on the radius of the cylinder is not incremented with increase of the number of cycles, owing to the fact that the bearing capacity of specimens remains constant. While resistance ρ with increase of cycles prolongs to be incremented with the delayed tempo due to formation of secondary surface cracks and growth of their total area; though secondary cracks are shallower in depth than primary ones, due to the unloading effect. The coefficient of a strength variation $W = \Delta\sigma/\sigma$ (where $\Delta\sigma$ is scattering of values, and σ is the mean strength) becomes above values of W for initial specimens with statistically distributed flaws after the first loading cycle. Coefficient W is sharply reduced in the subsequent cycles and at emersion of cracks in every section relaxed by cracks, at almost constant mean strength (Fig. 6.22b). Similar regularity of thermal damage is characteristic for other mono-phase ceramics without the expressed structural anisotropy.

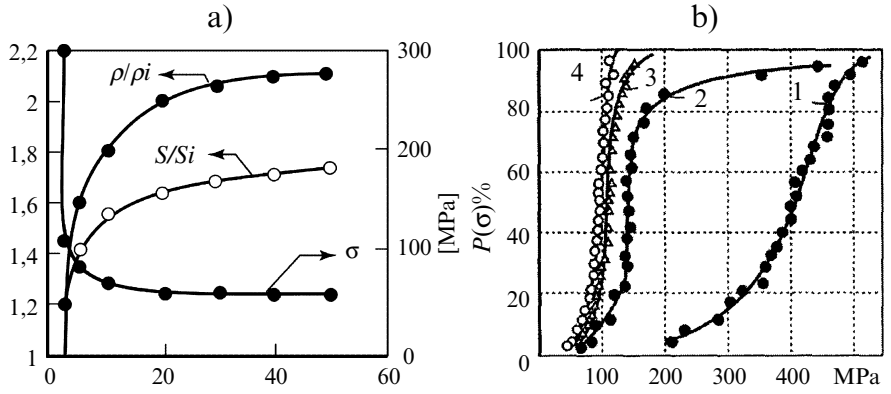

Fig. 6.22. Cyclic decay of strength σ, increase of resistances ρ and the total crack area S of small-grained specimens of ZrC 2.2 mm in diameter, 50 mm in length, heated up to 300°C, with subsequent cooling in cold water (**a**) and statistical strength distribution of specimens (**b**) in an initial state (1), after the first loading (2), after 10 cycles (3) and 50 cycles [18]

The cracks of 100 µm in length in plate specimens of aluminum oxide after indenting did not undergo any gain after 600 thermal heating cycles and cooling by an air flow with temperature difference of the order of 900°C [221].

Fracture of the heterogeneous refractory material almost always progresses at repeated loading, especially in a temperature cycle when low-melting phases at the grain boundaries become more softening. Repeated thermal loading causes broadening of a crack, with consequent decrease of strength and elasticity [222].

Research results of specimens of zirconium dioxide and aluminum oxide after repeated thermal loading (Fig. 6.23) demonstrate that, after three thermal cycles, appreciable decrease of the residual strength is observed. The strength of specimens is determined by cohesion forces of the separate parts contoured by thermal cracks, and also by the strength of these parts. The further thermal cycles lead to already minor loosening of a specimen; so, for example, the subsequent 12 thermal cycles reduce strength only by 5–10%. This is connected with decrease of stress in separate parts of the specimen after the first thermal cycles, in comparison with stresses in the initial unimpaired specimen.

Features of a structural condition of composites determine their behaviour at cyclic loading. Specimens of mono-phase silicium nitride and composites on the basis of aluminum oxide with particles of SiC (Al_2O_3/SiC_p) after 100 repetitive cycles of heating up to 1,473 K and cooling in a flow dust–gas medium down to room temperature did not undergo modifications of strength. While test specimens Al_2O_3 with the introduced whiskers (Al_2O_3/SiC_w) and fibres ($Al_2O_3/SiC_{f)}$ were noticeably damaged under the same conditions [223].

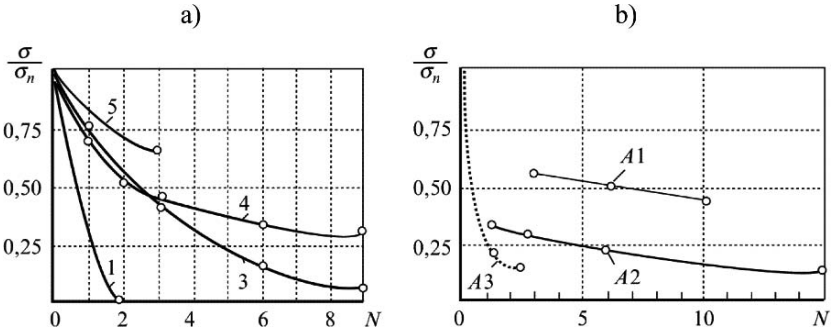

Fig. 6.23. A modification of the relative residual strength at diametrical compression of ring specimens of zirconium dioxide stabilized with CaO depending on quantity of thermal cycles, N, in a regime (T = 300–2,500–300 K). (**a**) (1) 100% cubic phase, (3) 80% of cubic +20% monoclinic, (4) 74% cubic +26 monoclinic phase, (5) 70% cubic +30 monoclinic phase. (**b**) A modification of the relative residual tensile strength of aluminium oxide with various porosity (P) (A1) P 20%, (A2) P 4%, (A3) P 1% in a cyclic regime (T = 300–2,100–300 K) [16]

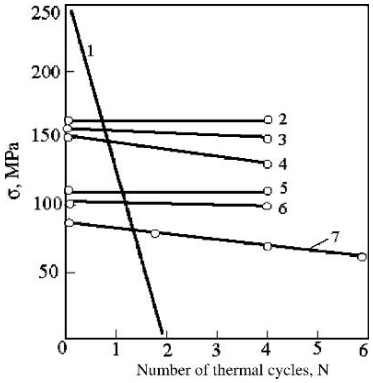

Fig. 6.24. Modification of strength after cyclic thermal loading of specimens of composites of Al_2O_3 reinforced by molybdenum fibres in diameter, d, and length, l: (1) Al_2O_3 without additives; (2) Al_2O_3 + 20 vol% Mo, d = 0.05 mm, l = 12.7 mm; (3) the same, l = 3.2 mm; (4) 10 vol% Mo, d = 0.05 mm, l = 3.2 mm; (5) 20 vol% Mo, d = 0.25 mm, l = 12.7 mm; (6) the same, l = 3.2 mm; (7) 4 vol% Mo, d = 0.05 mm, l = 3.2 mm

Composites with metal inclusions were subjected to an essentially stronger effect of cyclic loading. Resistance to fracture of a sample of hot-pressed thorium dioxide reinforced by molybdenum fibres of 50 μm diameter and 3,000 μm length at a cyclic loading (heating up to 1,300 K with the subsequent cooling in mercury) was increased [224]. Substantial improvement of cyclic thermal stability is observed from reinforcement of Al_2O_3 by molybdenum fibres. The strength of the hot-pressed composite, however, is always downgraded due to emersion of cracks owing to difference in coefficients of

linear expansion of a matrix and fibre. The rupture strength increased noticeably (Fig. 6.24) at cyclic heat-cooling in air from 1,500 down to 300 K. It is possible, only in a few cases, to obtain a small reinforcement with simultaneous improvement of thermal stress resistance, for example, reinforcement of alumina with mullite from molybdenic fibres [225].

The residual strength of composite on the basis of SiC matrix with graphitic fibres was 83% from the initial after 50 cycles of heating-cooling in a range 300–1,300°C in air and remained constant at the subsequent 50 loading cycles [226]. Thermal fatigue of specimens of aluminum oxide increased sharply, with magnification of the length of an initial crack at increments of temperature drop and number of cycles [227].

In composites of nickel–chromic matrix with 25 and 50 vol% of stabilized zirconium oxide at cycling in temperature range 100–1,000°C, the original fatigue micro-cracks are merged, therefore thermal stresses between layers are reduced, not allowing lamination of an composite [228].

The majority of metal materials in a plastic state fail only under the repeated effect of temperature stresses. The experimental procedure of heating of the restrained specimen [229] and special methods of thermal stress calculation and durability characterized by thermal fatigue limit is used [230] for metal bodies in a plastic state, namely at temperatures above $0.01T_{\mathrm{ml}}$ and velocities of a loading considerably below velocities of acoustic wave propagation.

Consideration of these test methods and thermal fatigue of plastic materials is beyond the scope of this book, though undoubtedly there is an area of overlap with ceramics when they transfer into elastic–viscous state at temperatures 0.7–$0.9T_{\mathrm{m}}$.

7

Effect of Structural Parameters on Thermal Stress Resistance

7.1 Thermal Stress Resistance of Mono-phase Ceramic Materials

The criteria of thermal stress resistance R for the majority of a dense high-melting point compounds with porosity of 5–15% is within the limits of 30–100 grades, only on occasion are values of$R$ increased to 400 degrees. The differences between the materials, determined by criteria R', are more appreciable – they vary almost by two orders from $500\,\mathrm{Wm}^{-1}$ for example, for such low heat-conducting materials as Al_2O_3, up to $5{,}500\,\mathrm{W\,m}^{-1}$ for SiC (Table 7.1). The thermal stresses σ_t producing emersion of the first cracks (using a test method in fluidic medium), lie over the range of values 0.45–0.57 from ultimate bend strength σ_b, and variation coefficients of thermal stress resistance are comparable to values W measured at a force loading.

It is characteristic that the thermal stress resistance of the same materials produced by various experimental studies is not essentially equal. It is no wonder, since thermal stress resistance, a structurally sensitive characteristic similar to strength, depends on the strength bond between grains, geometry and size of flaws and pores, and content and allocation of impurities in a body, all changing with the variation of technological regimes of manufacture [14, 231].

Influence of Grain Size

Influence of grain size on the thermal stress resistance of different materials is manifested in an ambiguous fashion. As a rule, the strength of ceramic materials drops at a force loading with increase of a grain size [14, 232–234]. Brittle strength does not change with grain variation when chemical impurity composite and presence of defects on grain boundary remain at a stationary value, for example, after primary crystallization [235]. In some cases, diverse character of strength dependence on grain size is observed, in connection with

Table 7.1. Estimated characteristics of thermal stress resistance R and R' for typical ceramic materials

Material	σ_b (MPa)	$E \times 10^{-4}$ (MPa)	$\alpha \times 10^6$ (K^{-1})	λ ($W\,m^{-1}\,K^{-1}$)	R (K)	W (%)	R' ($W\,m^{-1}$)	σ_t/σ_b
ZrC	260	3.4	6.0	28	50	22	1,400	0.45
NbC	255	3.6	4.7	25	45	24	1,120	0.51
SiC	230	3.3	2.8	80	70	25	5,600	0.55
Si_3N_4	370	3.0	3.1	30	390	19	–	0.45
ZrB_2	220	4.2	6.2	70	58	20	4,060	–
B_4C	370	3.6	4.8	25				
Al_2O_3	260	3.6	6.4	14	54	23	756	0.57

precipitation of impurities and pore formation at the grain boundaries. The dimensional change of grain in sintered specimens can lead to a modification of the interacting character of cracks and pores. More round pores inside grains, as a rule, create lower stress concentration. The boundaries of grains in high-melting point compounds can be enriched by impurities, and this should work upon crack resistance. The differentiated effect of the noted factors on fracture toughness is studied insufficiently, therefore a survey of data about the effect of grain size on crack resistance is not straightforward. We only note that the crack resistance increases for UO_2 with powdering of grain, and there are both analogous and opposite dependences for MgO [14].

Generally speaking, the value of crack resistance undoubtedly reflects the ability of a material to oppose fracturing. The fracture toughness remains an empirically defined characteristic by virtue of great structural responsivity depending (as well as other mechanical properties) on conditions of loading, form and size of a body, and conditions of its attachment (see more detail in Application A.2). Research into thermal stress resistance of the ceramic Si_3N_4, with indenter imprint on the surface of specimens, demonstrated [236] that the least decay of strength after cooling in water was experienced by the low strength specimens with large elongated grains, having almost on 40% greater fracture toughness, than fine-grained specimens. The observable fact of rise of the residual strength and fracture toughness with growth of a loading temperature from 500 up to 700°C, accompanied by decrease of density of the surface micro-cracks and modification of local stresses from tensile to compression in the neighbourhood of an imprint, is interesting.

The level of residual strength drops with decrease of initial strength of dense polycrystal Al_2O_3 (porosity no more than 2%) at consecutive transition to specimens with grains of 10, 34, 40 and 85 μm [237]. Damage to sapphire and polycrystal specimens with grains of 10, 34, 40 μm is also characterized by a drop of strength at reaching a critical temperature difference, unlike the monotonous decrease of strength of a large-grained specimen ($d_g = 85\,\mu m$).

An appreciable effect of the character of a microscopic structure on thermal stress resistance is observed by some researchers [237–239]. It is shown in [238] that fine-grained specimens of Si_3N_4, doped with 10 vol% Yb_2O_3 and 0.5 vol% Al_2O_3 with elongated grains and crystalline grain boundary phase, display decreased strength, unlike large-grained specimens. A similar effect of a grain configuration on thermal stress resistance of sialon is noted in [239].

Inhomogeneity of grain sizes in a sample of ZnO and the different current conductivity bound with it provoke local modifications of temperatures and bursts of thermal stresses leading to faults of the varistor [240].

An appreciable effect on thermal stress resistance and strength in a sample of silicium carbide with various grain sizes is traced in [59]. The microscopic structure of reaction-sintered silicium carbide (SiC_{rs}) at 1,650°C represents the continuous carbide skeleton with 14 mass% of free silicium inclusions, grain size no more than 35 µm and common porosity of 10%, (Fig. 7.1). The

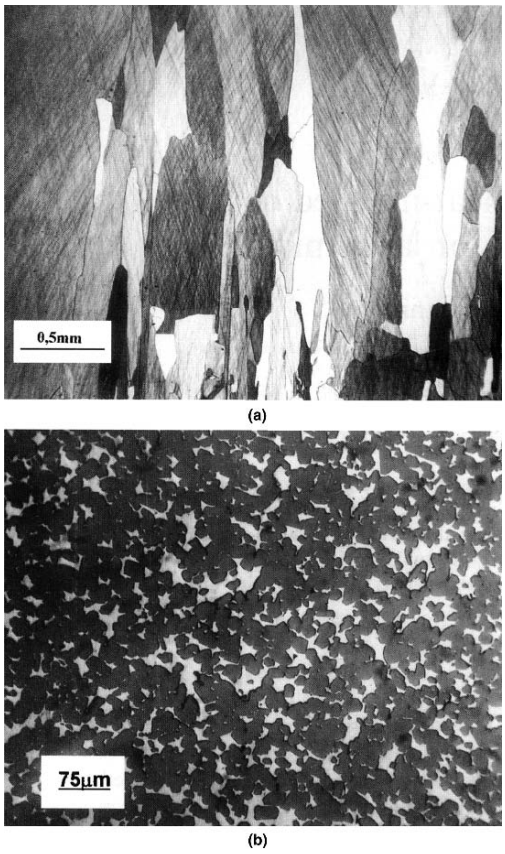

Fig. 7.1. Microscopic structure of sublimating SiC_s (*transparent view*) and reactionary-sintered silicium carbides of SiC_{rs} (in reflected light)

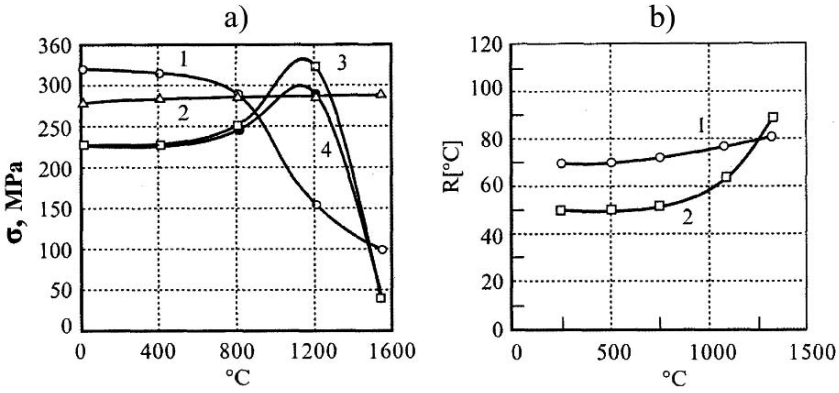

Fig. 7.2. (**a**) Temperature dependence of strength for sublimated specimens of SiC_s cut out in a perpendicular direction (1) and a parallel direction (2); and reactionary-sintered silicium carbides SiC_{rs} tested with deformation velocities of 3×10^{-4} (3) and $3 \times 10^{-3}\,C^{-1}$ (4). (**b**) Thermal stress resistance of sublimated SiC_s (1) and reactionary-sintered SiC_{rs} (2)

structure of sublimating silicium carbides SiC_s (containing 0.6 mass% of Si) has a strongly pronounced columnar crystal character. Grains from 500 up to 5,000 µm in dimension are drawn down in the direction of deposition of a heated mixture of silicium and carbon on substrate. The total of pores does not exceed 0.3%. The localization of free silicium in interlayers at the grain boundaries determines a sharp temperature decay of the bend strength of specimens (cut out in a direction, transversely to a direction of growth) owing to the increase of plasticity of the silicium with temperature.

Thermal stress resistance up to 800°C is determined by cooling heated disk specimens in water, and by two methods of heating: by electron beam or in an induction-heating installation at higher temperatures [58, 163]. Thermal stress resistance of a stronger sublimated SiC_s (Fig. 7.2) is above the thermal stress resistance of reactionary-sintered silicium carbide SiC_{rs} in almost all temperature bands. However, the thermal stress resistance of SiC_{rs} increases with increase of temperature, owing to a relaxation of the thermal–elastic stresses, and exceeds thermal stress resistance of SiC_s at temperatures greater than 1,300°C.

Effect of Porosity

The effect of porosity on fracture of materials under thermal loadings is manifested in various fashions. Irregularity of distribution of pores can lead to a random weakening of body cross section and, hence, increment of stresses acting in this cross section, and decay of strength. This effect of irregularity can be manifested especially noticeably, in a rather small cross section of a specimen and at a significant magnitude of porosity.

Though porosity weakens cross section of a body and reduces its strength, it renders a beneficial effect on thermal stress resistance as the evolution of cracks is slowed down [25]. Experimental data show that increase of porosity diminishes the thermal stress resistance (R and R') or, at the best, leaves it approximately at the same level [26]. Such inconsistent explanation of the role of porosity in thermal fracture is due to the fact that a modification of porosity in a body entails a simultaneous modification of some other structural parameters; size and configuration of grains, and the form and allocation of the pores [241] which are frequently not considered by researchers.

Interaction of cracks at various aspects of a loading can lead to modification of a stress state and the process of fracture of the defective body depending on the character of the porous structure and the alignment of cracks. A series of examinations conducted by modelling specimens of glass with spherical inclusions imitating pores, demonstrate that strength appears to be dependent not only on the quantity of inclusions (pores), but also on their sizes that determine features of the stress state around inclusions [242].

The forms and sizes of pores in sintered bodies are closely bound to the magnitude of grains and the available design relationships, and the joint effect of these factors are confirmed experimentally [14]. It is necessary to note that surface condition and possible presence of non-uniform porosity fields can cause a much greater effect on strength, than the average value of porosity. Volumetric flaws in the form of great pits with a medial size of 200 µm are the reasons for the fracture only in 40% of all cases of fracture of mono-phase compounds. Fracture at lower loadings in 10% of cases originates in zonal structural isolations appearing during the non-homogeneous compacting and the subsequent non-uniform process of shrinkage [243]. A greater part of fracture sites are the short, thin, hairline flaws hardly observable at magnifications of 1,000×, but with radius of a rounding on orders smaller than that of rounded large pits, and hence able to produce a dangerous stress concentration.

The strength of ceramics is reduced, as a rule, with growth of grain size, especially with the anisotropic cell, frequently owing to a segregation of impurities and emersion of discontinuity flaws at the grain boundaries. Emersion of pores and definitely oriented flaws increases thermal stress resistance in some polyphase materials. At the same time, the increase of porosity of mono-phase materials, as a rule, leads to decrease of thermal stress resistance R and R'. The thermal stress resistance of ceramics characterized by criterion R' is diminished more sharply with a modification of porosity owing to decrease of thermal conductivity. A case with criterion R is more difficult as, simultaneously with decrease of specimen strength with specific porosity (Fig. 7.3a), the modulus is reduced also.

Thermal stress resistance R and ratio σ/E is incremented at the leading decay of a modulus in comparison with strength (Fig. 7.4a).

Observing a porous material as a two-phase composite, [244] demonstrates that strength is determined only by structure of a continuous phase, while the modulus depends on properties of both phases. The modification of criterion R

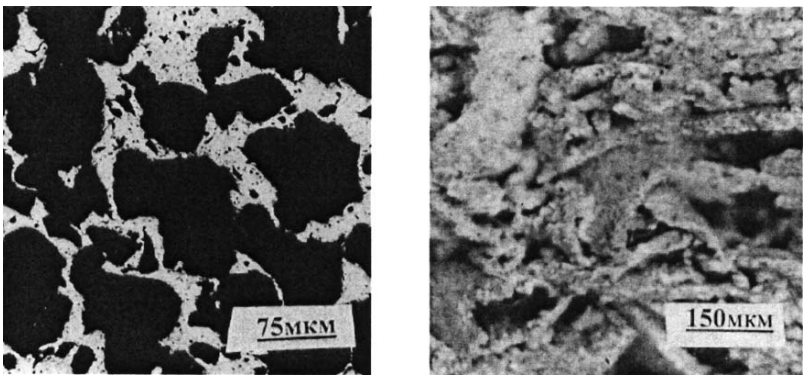

Fig. 7.3. Microscopic structure of (**a**) ZrC with porosity of 75% and (**b**) Zr_3N_4 with porosity of 65%

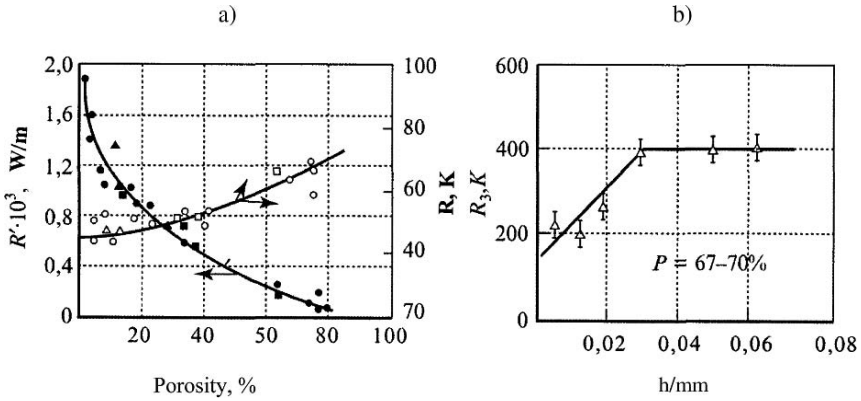

Fig. 7.4. Modification of (**a**) thermal stress resistance criteria R and R' vs. porosity of ZrC and (**b**) thermal stress resistance R of silicium nitride depending on width of elements h of a carcass at a mean porosity of 68–72%

to a large extent is determined by the structural parameters of ceramics. The capability of increase of thermal stress resistance of porous silicium nitride with the expressed structural anisotropy is observed in [245, 246]. Silicium nitride with porosity of 14% and oriented elongated grains possesses heightened thermal stress resistance and has almost seven times greater fracture toughness than more isotropic material of the same porosity [18].

The original manner of preparation of high porosity Si_3N_4 allows changing the structure of porous carcass Si_3N_4 determining stiffness and strength of a body [247, 248]. The production process consists of warm shaping of porous stock material from previously manufactured elements from thermal–plastic slip on the basis of a silicium dust with a subsequent distillation of a binder at

750°C in air and reactionary sintering in nitrogen at 1,400–1,600°C [248]. An optimum structure of a porous carcass from lamellar bent elements of various widths is selected for reaching a high thermal stress resistance. The thermal stress resistance of Si_3N_4 increases almost twice with a modification of the elements of width of a carcass from 0.005 up to 0.03 mm, for example, at a fixed level of porosity $\sim$ of 70%, remaining at the further increase of element width up to 0.6 mm constant (Fig. 7.4b). Use of thicker elements changes the character of contacts at sintering that leads to the prevailing decay of stiffness of carcass in comparison with its strength. This increments the relationship σ/E.

The increase of temperature in testing porous ceramics in a brittle state is determined by variability of complex σ/Ea. Criteria R for specimens of ZrC with porosity of 60–75%, at increase of temperature from 800 K up to 2,100 K remains constant, owing to invariability of complex $\sigma/E\alpha$ as the strength of porous ZrC in this temperature band is constant, and the increment of value α is compensated by appropriate drop of E. The variation coefficient of thermal stress resistance $W = \Delta R/R$ at increase of temperature up to 2,100 K remains constant at a level of 22–24%, confirming the brittle fracture character of porous ZrC at the heightened temperature. Allocation of values of R for testing of 400 specimens of ZrC is submitted to the normal law.

The residual strength of quenched ceramics on the basis of Al_2O_3 combined with 8.75% Na_2O (so-called-β-oxide aluminium) is reduced by ≈25%, at modification of porosity from 5 up to 37%, but the character of strength decay appears essentially different [249]. Strength after loading of highly porous specimens with increase of temperature monotonically diminishes, unlike specimens with porosity of $\leq$5%, for which an abrupt drop of strength is characteristic. Liability to damage of highly porous β-oxide aluminium is due to separation of powdered conglomeratic while dense thermal-loaded specimens form the dense grid of face cracks.

7.2 Thermal Stress Resistance of Heterogeneous Ceramic Materials

Introduction of a various kinds of inclusions into ceramics appears the most effective way of increasing their fracture strength. One of the major aspects of the problem of thermal stress resistance is the determination of linkages between structural parameters and the ability of materials to stand thermal loadings without fracturing. One of the paths to solution of the problem is the introduction of brittle high-melting point particles, whiskers or fibrils in materials without decrease of a temperature level of maintenance.

Increase of the strength, thermal stress resistance and fracture toughness of a composite is determined by requirements of crack initiation and spreading, and also by redistribution of an elastic deformation between particles and matrix. The size of particles, presence of 'whiskers', and orientation of fibres

determines the predominating mechanism of crack interaction. It may be the processes bound with overcoming of forces hindering crack opening at a drawing down of fibres from a matrix, or procedure with reorientation of a crack at its interaction with an interface particle–matrix. Both of these processes are accompanied by a modification of local intensity coefficient of stress and magnification of the surface fracture area.

Existing theoretical concepts about fracture of ceramic composites and micro-mechanical fracture models are observed in a number of theoretical and experimental works [250–252]. Crack extension in composite materials happens with a much more expressed effect of increasing R-curves than in mono-phase ceramics.

Thermal Stress Resistance of Composites with Ceramic Inclusions

The greatest number of the works published on composites with greater thermal stress resistance is devoted to materials based Al_2O_3, ZrO_2, MgO, SiC, Si_3N_4, BN and carbides of transition metals. The thermal stress resistance of ceramics with chaotically oriented lamellar particles of a size of 25–70 μm, as a rule, is reduced despite incremented fracture toughness and, in some cases, rise of R-curves. The introduction of whiskers with a diameter of 0.5–2 μm increases at the same time thermal stress resistance and fracture toughness (Table 7.2).

An appreciable effect of the residual stresses on crack resistance and bearing capacity of a body of composite material under thermal load, explicated at cooling of the body from sintering temperature to a room temperature, is caused by the difference of temperature expansion coefficients and elasticity

Table 7.2. Comparative characteristic of refractory material by dispersible-strengthened whiskers [262]

Matrix	Contents of composite Dispersion phase		σ_c (MPa)	σ_b (MPa)	Fracture energy (J sm^{-2})	N^a
	Whiskers	%				
Al_2O_3	–	–	1,200–1,500	120–150	0.12–0.25	1–2
Al_2O_3	α-Al_2O_3	5–8	1,400–1,500	360	0.85–0.9	100
ZrO_2	–	–	800–1,000	50–60	0.08–0.09	1
ZrO_2	ZrO_2	15–20	1,200	320	0.45	200
MgO	–	–	1,200–1,500	60–70	0.08–0.12	1–2
MgO	MgO	15	1,200–1,500	120	0.6	50
AlN	–	–	186	75	0.18	9
AlN	$3Al_2O_3 \cdot 2SiO_2$	20	420	135	1.8	500
BN	–	–	190	46	0.25	12
BN	$3Al_2O_3 \cdot 2SiO_2$	40–50	280	95	2.2	86

[a]Number of air thermal cycles for fracture in temperature range 20–1,200℃

characteristics of the matrix and whiskers. Residual stresses are compressive on the whiskers and tensile in a matrix.

The level of these stresses on design estimates [253] can attain 1.5 GPa. Residual stresses can be calculated approximately in the fibres:

$$\sigma_r = 2\sigma_\theta = \Delta T\,(\alpha_1 - \alpha_2)\left[\frac{1+\mu_1}{2E_1} + \frac{1-\mu_2}{E_2}\right]^{-1}\left(\frac{R}{r}\right)^2, \qquad (7.1)$$

where α_2 and α_1 are coefficients of linear expansion of a fibre and a matrix; μ_2 and μ_1 are Poisson's coefficients; E_2 and E_1 are matching values of modulus; T is temperature.

Residual stresses in the matrix, caused by anisotropy of thermal expansion, can be estimated using the relationships:

$$\sigma_r = \frac{E(\alpha_r - \alpha_\theta)\Delta T}{2}\ln\left(\frac{r}{b}\right),$$
$$\sigma_\theta = \frac{E(\alpha_r - \alpha_\theta)\Delta T}{2}\left[1 + \ln\left(\frac{r}{b}\right)\right], \qquad (7.2)$$

where b is the normalizing coefficient, at $r = b$, $\sigma_r = 0$.

According to the model, the friction stress at the drawing down of a whisker from the matrix is proportional to the level of compression stresses. At the same time, the increase of a fracture toughness and thermal stress resistance performances of composites with particles is due to processes of crack reorientation on interfaces particle–matrix and micro-cracking of a matrix. The contribution of particles extracting from a matrix is inappreciable on dissipation energy.

Dependence on mechanical characteristics vs. the contents and inclusions sizes is variable. For example, the presence of a chemical bond on the interfaces between matrix and fibre reduces expenditures of energy on drawing down of fibre from a matrix, impeding the increase of fracture toughness. Barrier coats are superimposed on whiskers or fibres for elimination of this phenomenon. Formation of residual stresses can essentially reduce the efficiency of a composite strengthening at less than optimum sampling parameters of reinforcement, owing to the difference of temperature expansion coefficients and modulus of a matrix and inclusion.

Decrease of this negative effect is possible using composites with nanocrystalline inclusions of a size of 20–50 nm, allowing increasing strength of aluminium oxide ceramics with ultra dispersion particles of SiC up to 1,000 MPa [254].

Strength and fracture toughness are essentially increased with the formation of nanocrystalline structures of composites on the basis of Al_2O_3, with the introduction of only 1 vol% of SiC nanoparticles [255]. Mechanical characteristics are analogously increased by adding SiC nanoparticles to silicium nitride [256].

It is established in other work [257], that the dimensional change of particles of a composite $Al_2O_3 + 20\%$ SiC within the limits of from 3 up to 23 μm

causes sharp transition from hardly noticeable cracking to mass fracture, at reaching a critical particle size of $10 \pm 3\,\mu m$. Exceeding this size leads to emersion of radial micro-cracks around particles. The average level of thermal stresses in particles (measured by a neutron diffraction method) was reduced from 1,275 to 800 MPa after cracking.

Boron nitride and composites based on it are represented as a prospective thermal stress resistance material. The low coefficient of linear expansion secures high enough thermal stress resistance. The composites obtained by an elevated-temperature compaction on the basis of ZrB_2 and HfB_2 with 20–30 vol% SiC and up to 10 vol% C have strength and thermal stress resistance performances considerably higher in comparison with borides without additives.

The introduction of filamentary mono-crystalline mullite in quantities of 35–40 vol% in boron nitride increases the impact strength and thermal stress resistance at a cyclic thermal loading [250]. Components of boron nitride added to aluminosilicate refractory also promote an essential increment of cyclic thermal stress resistance.

Specimens of hot-pressed composite $Al_2O_3 + 5$ vol% WC possess a greater thermal stress resistance and fracture toughness than mono-phase aluminium oxide (Table 7.3).

Modification capabilities of properties of mechanical composites by optimum sampling of composite and structure are illustrated in the instance of a composite on the basis of Al_2O_3 with components of two aspects of soda lime glasses with lower and higher values of linear expansion coefficients relative to aluminium oxide [259]. In the first case, the composite with tension stresses on grain boundaries possesses high strength, despite having low fracture toughness. In the second case, the composite with compression stresses fails on grain boundaries and fracture toughness appears higher than mono-phase oxide.

Substantial growth of thermal stress resistance is observed with the introduction of aluminium components and Al_2O_3 in magnesium oxide. The significant drop of strength, modulus and coefficient of linear expansion occurred with the increase of thermal stress resistance. It is appears that the included aluminium oxide, interacting with MgO produces spinel ($MgAl_2O_4$) which leads to emersion of cracks.

Table 7.3. Thermal stress resistance and mechanical characteristics of mono-phase ceramics Al_2O_3 and a composite on the basis of Al_2O_3 with included particles of WC 7–8 μm in size [258]

Material, grain size (d_3), μ	σ (MPa)	E (GPa)	R (K)	$R'''' \times 10^{-6}$	K_{1c} (MPa m$^{1/2}$)
Al_2O_3, $d_3 = 2.8$	520	390	135	59	3.5
$Al_2O_3 + 6$ vol% WC, $d_3 = 1.5$	580	407	147	100	5.1

An essential increase of thermal stress resistance and strength in comparison with composites of usual structure is observed in nanocomposites on the basis of Si_3N_4, containing up to 15% dispersed particles of hexagonal boron nitride homogeneously distributed in a matrix [260]. Similar improvement of thermal stress resistance is observed in a composite on the basis of aluminium oxide with introduction of submicron particles of an aluminum nitride, tested by cooling of heated specimens in glycerin [261].

Reinforcement by fibres increases fracture energy and resistance to crack extension at thermal loading [262]. Critical magnitude of strain during the moment of the composite's fracture, as a rule, is increased in comparison with unreinforced material. This is due to a series of factors, including a multiple crack branch in a matrix, and the elastic–brittle or plastic deformation of fibers leading to blunting and crack stop. Titanium carbide with carbon fibres included possesses the higher criteria R and R'''' measured experimentally in comparison with the monolithic TiC [263].

The strength of silicium nitride composite with introduced fibers of boron nitride after specimens heated up to 1,000°C were cooled in water was not much reduced, unlike the strength drop of mono-phase specimens [264]. Silicium carbide reinforced by three-dimensional carbon fibers after some 100 cycles of heating-cooling of specimens from 1,300 to 300°C, retained 83% of it strength from an initial level [265].

The thermal stress resistance of a composite on the basis of Si_3N_4 with BN fibers and included SiC particles is increased in comparison with monophasic Si_3N_4, owing to formation of yieldable BN cellular structure on the phase boundary [266].

The accelerated evolution of nuclear power and space engineering has demanded the development of a new class of high-temperature and thermal stress resistant composites on the basis of graphite. Work in the 1960s determined the expediency of application of high-melting carbide–graphite composites possessing high levels of thermal stress resistance. Quality estimations of the serviceability of materials derived from silicium carbide, wolfram and, on the other hand, zirconium and hafnium carbides with graphite particles in a plasma jet have shown the significant advantages of the last [267].

Mechanical characteristics, thermal stress resistance and habits of fracture of heterogeneous composites (Fig. 7.5) on the basis of a brittle carbide matrix with brittle carbon particles at force and thermal loading are observed explicitly in [268].

The thermal stress resistance is estimated on mean-integrated temperature drop ΔT_m at a non-stationary loading of disks 35 mm in diameter by a lateral surface heated in the bath of melted tin. Zirconium and niobium carbides with different contents of a carbon component in the form of carbon black (up to 5 wt%) and in the form of mineral scaly graphite inclusions of grade KLZ by a size of 50–150 μm (up to 10 wt%) are used as materials of research.

Introduction of both views of carbon inclusions in the carbide matrix invariably reduces strength and modulus of composites. However, carbon black

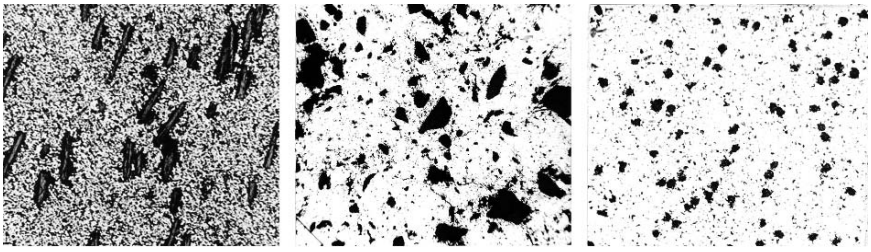

Fig. 7.5. Micro-structure of heterogeneous composites: (**a**) ZrC+5 mass 5% carbon black (150 µm); (**b**) ZrC + 5 mass 5% graphite KLZ (150 µm); (**c**) ZrC + 5 mass 5% diamond particles (50 µm)

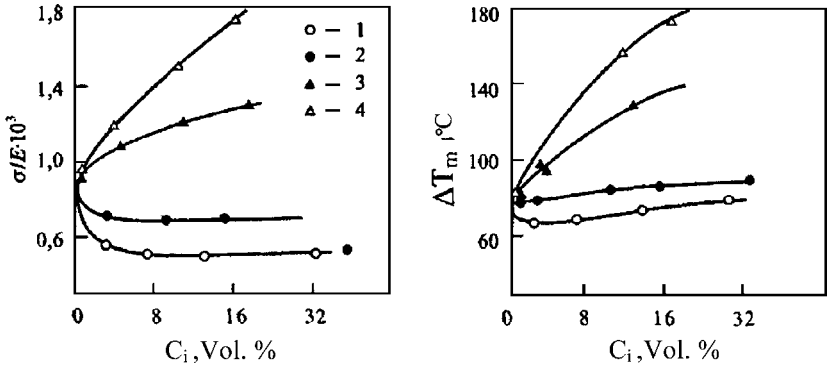

Fig. 7.6. Modification of values of (**a**) σ/E and (**b**) thermal stress resistance ΔT_{m} in composites based on zirconium carbide (1, 4) and niobium carbides (2, 3) depending on the contents of the carbon component in the form of carbon black (3, 4) and graphite (1, 2): (1) ZrC + graphite; (2) NbC graphite; (3) NbC + carbon black; (4) ZrC + carbon black [268]

inclusions in comparison with graphite cause a less sharp drop of strength and greater decrease of a modulus. The Poisson's ratio practically does not depend on the contents of the carbon component and is equal to approximately 0.2. The critical intensity coefficient $K_{1\mathrm{c}}$, depending on the contents of carbon inclusions varies similarly to strength values. At the same time, the effective surface energy $\gamma = K_{1\mathrm{c}}/2E$, computed on measured values $K_{1\mathrm{c}}$ and modulus E, is diminished with increase of the contents of carbon black and it does not vary practically with the introduction of graphite. Thermal stress resistance ΔT_{m} with increase of the contents of carbon inclusion up to 5 wt% is increased two to three times in case of use of carbon black, or remains without modifications for composites with graphite, unlike strength. Thus, value ΔT_{m} depending on the contents of carbon inclusion varies similarly to magnitude σ/E, describing an ultimate strain of a body (Fig. 7.6). The ratio σ/E is the main parameter which determines the behaviour of observed carbide composites at thermal loading. Really, design values of criterion $R = \sigma(1-\mu)/E\alpha$ are

similar to measured values ΔT_{m} and as the coefficient of linear expansion of composites is practically identical, modifications of thermal stress resistance are defined only by magnitude of a ratio σ/E. In turn, the criterion of thermal stress resistance $R''' = E/\sigma^2(1-\mu)$, whose magnitude is inversely proportional to the elastic energy reserved in body, determines fracture character. The less criterion R''' is, the more probable is the fracture of a body into number of fragments in the melted tin.

Thermal stress resistance of composites with carbon black appear in this respect to be more inclined to fragmentation than less thermal stress resistant composites with graphite. The criterion of thermal stress resistance $R'''' = E\gamma/\sigma^2(1-\mu)$, considering besides reserved energy also the effective energy γ expended on fracture, leaves correlative linkage with a fragmentation practically the same, though in comparison with criterion R''' the difference between composites by criterion R'''' are decreased a little.

The ability of a body to stand the heat flows without fracture, determined by criterion R', is invariably diminished with increment of a carbon component. And intensity of decay is more appreciable for composites with carbon black, caused by differences in character of the modification of thermal conductivity of composites with carbon black and those with graphite. The leading decrease λ and major increase of resistance of composites with carbon black are due to lack of cohesion of the carbon black component with a matrix.

Fracture of composites is realized without noticeable tracks of a microplastic deformation at rather low temperatures (up to 1,300 K) both at force and at thermal loading. The diagram of deformation under bending and tension rises linearly to the point of fracture for all composites explored. The fracture surface of composites with carbon black is more developed than composites with graphite. The relief of a rupture surface becomes complicated with an increase of temperature. Strength of the carbide composites increases and attains a maximum at emersion of the first indications of a residual deformation ($T = 2{,}500$–$2{,}650$ K). The further evolution of macro-plastic deformation brings about a significant decay of strength. Such character of strength dependence on temperature is typical enough for interstitial compounds [14, 18]. However, at constant aspects of a loading and strain velocity temperature of emersion of a macro-plasticity in hetero-phase composites in comparison with mono-phase carbides increases by 200–250 grad.

Fracture of composites under thermal loading comes at the magnitude of a maximum tensile stress above the tensile strength value, but below that of bending, which follows from comparison of experimental and design criterion R values of thermal stress resistance.

Scattering of strength and thermal stress resistance values of heterogeneous composites in a temperature range of their brittle failure appears higher than for mono-phase carbides. So, the variation coefficient of strength at 300 K for ZrC is equal to 22%, and for composites on the basis of zirconium carbide with 5 wt% of black carbon and graphite it is, respectively, 28 and 35%. Variation

coefficients of thermal stress resistance do not differ practically from those discovered under force loading.

The introduction of carbon inclusions that are 40–50 times less rigid into a carbide matrix should inevitably diminish an effective modulus and strength of a composite, as to unload a matrix due to transferring of a greater part of a common loading on low-modulus particles is impossible, as follows from the theory of reinforcement of composites [262]. Modulus of composites with restricted plasticity lie, as a rule [262, 269], between the extreme values discovered under the condition of equal strain of phase components, or equalities of stresses.

The measured values of modulus of carbide–graphite composites E_c, lead as a matter of convenience for comparison to pore-free state E_o, on relationship $E_c = E_o\ e^{-b1v}$; where b_1 is the empirical coefficient accepted as equal to 4, and p is porosity, are presented in Fig. 7.7.

Curves of design estimations of modules and literary data about modulus of zirconium carbide–graphite [270] are plotted in the same figure. All values of modules are within the limits of design boundary lines: They are closer to the inferior design limit for composites with carbon black; modules for composites on the basis of zirconium carbide with graphite are at the upper level. The latter could be partly due to a capability of a plasticity of graphitic inclusions in their hydrostatical constraint condition by the rigid matrix.

Observable differences of values for E_c are caused to a great extent by modification of stress concentration owing to a variation of the form and alignment

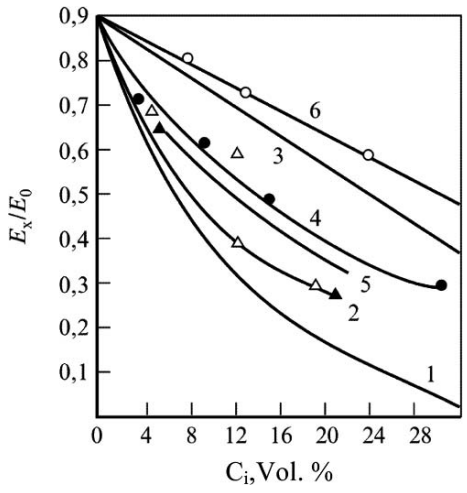

Fig. 7.7. Effect of carbon inclusions on the relative modification of a modulus of composites: (1) and (6) design values at equality of stresses and strains correspondingly on phase components, (2) ZrC + carbon black, NbC + carbon black; (3) and (5) according to [270], (4) NbC + graphite, (6) ZrC + graphite

of inclusions. Low values of E_c for composites with carbon black are determined by lack of the cohesion of a carbon component with a matrix, and also by inhomogeneity of its distribution. Empirical relationships for description of modulus and strength of composites with greater content of a low-modulus phases were deducted for porous materials [14]:

$$E = E_0 e^{-b_1 v}; \tag{7.1}$$

$$\sigma = \sigma_o e^{-b_2 v}; \tag{7.2}$$

where E_0 and σ_o are modulus and strength of a matrix, v is the content of the second phase (inclusions or pores); b_1, b_2 are empirical coefficients, changing as a function of form, alignments and extents of the inclusion cohesion with matrix. Sharper drop strength of composites with graphite, in comparison with the modification of strength of composites with carbon black, is determined by origination of thermal stresses in carbide–graphite composites. The occurrence of the radial tensile stresses are able to produce emersion of ring cracks around inclusions because of the extreme anisotropy of graphite and the greatest subzero difference in values of a coefficient of linear expansion of a matrix and inclusions ($\Delta\alpha = \alpha_m - \alpha_\nu < 0$). Ring cracking in composites with graphite, as indicated here, in most cases really occurs (Fig. 7.8), this explains the low level of their strength.

The essential and negative effect of carbon inclusions as stress concentrators is manifested not only in decrease of strength, but also in magnification of strength scattering at measuring of the specimens, and also in an increase of temperature at the beginning of macro-plasticity. The presence of local and extremely non-homogeneous stress concentrations in composites also set-up a more complex character of evolution of cracks than in mono-phase carbides, and as a result other quantitative dependence of strength on an aspect of a loading [263].

The phenomenon of maintenance of constancy of fracture energy in composites – with the introduction of up to 15 vol% of graphite, apparently, is due to the course of two competing processes. The first is caused by stress concentration and, hence, the facilitated capability of evolution of cracks, the

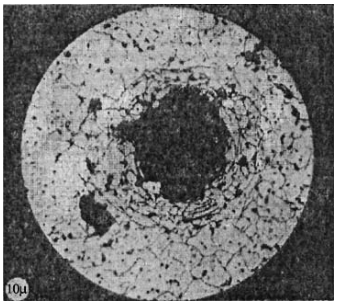

Fig. 7.8. Ring cracks around graphite inclusions in zirconium carbide matrix

second is provoked, probably, by interaction of a crack front with inclusions and rise of fracture energy. The capability of a similar process behaviour is proved by the study on composites of glass; $A1_2O_3$, Si_3N_4 – SiC [262].

The strength improvement at introduction of particles of $A1_2O_3$, ZrO_2, observable in some modelled composites based on glass, due to limitation of a dangerous size of a matrix flaw for composites with carbon inclusions is not confirmed. It is explained partly by the following: the most probable distance between particles for composites with carbon inclusions of >50 μm appears compared with size flaws of a matrix even at maximum composite contents.

Introduction of low-modulus carbon inclusions at appropriate regulating structure can noticeably increase the thermal stress resistance of composites on the basis of a brittle carbide matrix and reduced propensity to fragmentation due to increase of ultimate strain, and the decrease of stored elastic energy in unit volume of the composite.

Investigation of the path of thermal stress resistance improvement and fracture toughness of ceramic high-melting point materials by intrusion of carbon particles into the carbide matrix is discussed further in reference [271]. The size of particles, along with their volumetric contents, is one of the major factors influencing the properties of two-phase composites. Paths of increase of physical–mechanical performances are associated with decrease of particle size of the second phase [262]. A wide enough spectrum of particle sizes of carbon phase in carbide composites, such as natural graphite, carbon black or coke, complicates the interpretation of experimental data at detection of a linkage of composite properties with inclusion sizes. Application of synthetic diamond powders appears effective for obtaining composites of the carbides – carbon as the positive volumetric modification of diamond at structural transmutation causes a straining of the carbide matrix and has an activating effect on the compacting process of a composite at sintering [272]. Synthetic diamond possesses the highest density of all known carbon substances, creating favourable conditions for a uniform distribution of carbon inclusions in the carbide matrix. Finally, powders of synthetic diamond are classified by coarseness into classes with a narrow spectrum of graininess that allows formation of composites with secure inclusion sizes.

Carbide–diamond composites were prepared by blending powders of zirconium carbide with synthetic diamond of grade ACM with medial sizes of particles 0.2, 0.6, 6, 17 and 50 μm. Specimens in the form of disks 25 mm in diameter and 2.5 mm in width, manufactured by the method of a moist moulding with initial density of 52–57%, were sintered in argon medium at a temperature of 2,600°C within 1 h. Specimens with inclusions of natural graphite flake of 50–150 μm and artificial graphite PGI of 80–150 and 150–300 μm were manufactured analogously. The specimens with an intermixture of small (0.6) and large (50 μm) particles of synthetic diamond were prepared beside the composites containing inclusions of a single coarseness. Small additions (0.5 mass%) of carbon particles practically do not render an obstruction to coarsening of the carbide matrix. The increase of their contents leads to

a reinforcement of the blocking effect on coarsening, which is expressed more appreciably, the less the size of the inclusion.

Strength tests were conducted by a three-point bend method on specimens in the form of a rectangular bar with cross-section sizes $1.25 \times 2.5 \times 20$ mm. The fracture toughness is determined on specimens with an edge 0.1–0.15 mm in breadth and 0.5–0.8 mm in depth. The thermal stress resistance is determined by a non-steady heating of disks with a central hole of 4–6 mm in diameter in the bath of melted tin. A heat-insulated specimen from end faces was subjected to repeated immersions in a stannous bath whose temperature stepwise increased through 50°C.

Low-modulus carbon inclusions, whose strength is lower than the carbide matrix, act similarly to the pores diminishing the cross section, and reducing the strength properties of a composite the more strongly, the higher are their volumetric contents. The transcrystalline character of a fracture indicates a sufficient cohesive resistance of inclusions with a matrix. A higher level of strength properties, with inappreciably expressed maximum at C_i 2–2.5 mass%, in composites with small-sized inclusions (0.2–6 μm), in comparison with large inclusions (50 μm), is caused by decrease of grain size of a matrix and the effect of volumetric straining. More favourable condition for crack forming and decrease of strength appear in composites with large particles owing to rise of the elastic energy reserve connected to the difference of thermal expansion of a matrix and particles. Raising of fracture toughness of composites with small-sized particles promotes increase of surface fracture toughness.

Decay of strength at increase of contents C_f from above 2.5 mass% is the more severe, the greater is the particle size, whereas the tempo of a fracture toughness depression does not depend on particle size (Fig. 7.9).

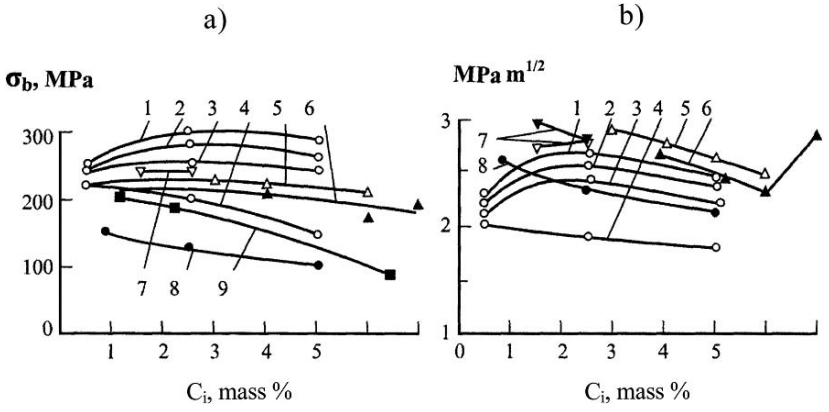

Fig. 7.9. Strength (**a**) and fracture toughness (**b**) of composites with a synthetic diamond (1–7), graphite KLZ (8) and graphite PGI (9) at room temperature. Particle size: (1) −0.2 μm; (2) −0.6 μm; (3) −6 μm; (4) 50 μm; (5) diamond mixture 2 + 4; (6) diamond mixture 3 + 4; (7) diamond mixture 1 + 4

Thus, the effect of particle size on strength is intensified with increase of their contents. So, strength in practice does not depend on coarseness at $C \sim 0.5$ mass%, and increase of a particle size from 0.2 up to 50 μm at $C = 2.5$ and 5 mass% is accompanied by decrease of strength, respectively, by 1.5 and 2 times. The fracture toughness is reduced thus approximately by 1.4 times.

The presence of large inclusions in mixtures leads to decrease of strength by the usual mechanism, but at the same time increases fracture toughness. This is due to additional energy consumption by the fracture, owing to complication of the fracture relief and an elongation of the crack front in bending around large inclusions. The contribution of this last factor is manifested noticeably if the grain size of a matrix is essentially less than inclusion size.

The character of a strength modification in a temperature range 20–1,500°C depends very little on the size of small inclusions (0.2–6 μm) and is determined primarily by their volumetric contents, with whose magnification linearly decreasing temperature dependence of strength is converted gradually into linearly increasing temperature dependence by 30%. Modifications of fracture toughness at higher temperatures in common are analogous to a modification of strength. Strength and fracture toughness of composites with large inclusions (50 μm) decrease with increase of temperature, irrespective of carbon content. Determination of the interconnection of strength and fracture toughness allows the forecasting of fracture toughness by the results of more simple strength tests. Direct proportional dependence between the indicated characteristics is observed for composites with carbon content of less than 5 mass%.

The modification of the second criterion of thermal stress resistance R' is characterized by the weak rate of growth with increase in carbon, R' in practice does not depend on the particle size, varying within the limits of from 0.2 μm up to 6 μm (Fig. 7.10). Large inclusions (50 μm) reduce R' approximately by 15% in comparison with small-sized particles and, at their presence in intermixtures, by 20–25%.

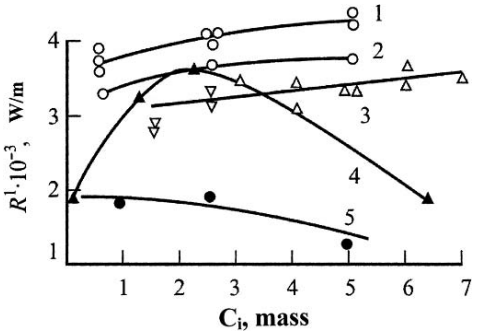

Fig. 7.10. Thermal stress resistance R' of composites with a synthetic diamond (1–3), graphite PGI (4) and graphite JLZ (5). (1) 0.2–6 μm; (2) 60 μm; (3) intermixtures 1 and 2

Observed data testify to the essential effect on strength properties of a carbon component. Low strength of composites with inclusions of graphite KlZ and PGI, and higher rate of decrease in strength with increase of carbon C_f (Fig. 7.9a, curves 8, 9) is caused not only by the size of carbon particles, greater than in composites with synthetic diamond, but also by a higher matrix damage under radial thermal stresses.

A sharper drop of strength is due to magnification of matrix damage at the increase of quantity of inclusions. Decrease of strength in composites with graphite KLZ, in comparison with graphite PGI, is probably caused by the additional effect of the property of anisotropy, leading to increase of thermal stress level. The beneficial effect on fracture toughness renders complication of fracture relief due to local cracking of a matrix. This is confirmed by the fact of increased fracture toughness of composites with graphite particles KLZ in comparison with composites with synthetic diamond (Fig. 7.9b, curves 4, 8).

Introduction of a carbon component in zirconium carbide can result, depending on the type of carbon, in the rise of thermal stress resistance by 1.5–2 times (synthetic diamond, graphite PGI) or in its decrease (graphite KLZ). Raising of thermal stress resistance in carbide–graphite composites with synthetic diamond and PGI is attained, according to the relationship $R' = \sigma\lambda/E$ at the expense of increase as ultimate strain of a material σ/E, and its thermal conductivity. Decrease of thermal stress resistance in the case of graphite inclusions KLZ is caused by a decline of thermal conductivity at saving of a ratio σ/E at the same level.

The choice of optimum relationships of structure parameters such as view, size and contents of carbon particles allows one, generally, to obtain the given spectrum of strength characteristic.

7.3 Thermal Stress Resistance of Composites with Fissured Structure

Technological methods of composite preparation, using phase components with various volume changes at sintering (for example, chromite and magnesite, monoclinic and stabilized zirconium dioxide, periclase and spinel, fireclay and chamotte) result in the creation of a so-called fissured microstructure [17, 250] which is characterized by a partition of a body into chaotic structural elements separated by cracks. The properties of these materials essentially change at variation of their chemical composition and the technological parameters of manufacturing.

Partial stabilization of ZrO_2 by alloying additions MgO, CaO with conservation of a fixed quantity of a monoclinic phase can raise the thermal stress resistance by two to three times. The thermal stress resistance of completely stabilized ZrO_2 remains low, partly owing to increment of linear expansion, in comparison with monoclinic zirconium dioxide. It is established that the

optimal contents of a monoclinic phase in hot-pressed samples is in the limits of 7–10%.

Displacement of an optimum of phase composition is caused by the technological habits influencing a series of other structural parameters; size of grains, density, the form and distribution of pores. However, partial conservation in ZrO_2 of a monoclinic phase, irrespective of the production regime of engineering, causes emersion of cracks in the material's structure which reduce strength, and an elastic modulus. Design values of the criterion of thermal stress resistance R are nevertheless sometimes increased. Values R and R' are not changed essentially in the majority of cases, but they are largely missing from the experimental data [17]. Observable rise of thermal stress resistance is connected to fixed favourable orientation of the cracks precluding spreading of the destructive main crack. The divergence of experimental data on thermal stress resistance of fissured materials compared with calculations is connected with the fact that criteria R and R' are inferred from a condition of quasi-homogeneousity and isotropy of a body, and do not characterize the local events occurring in a material. Composites with dispersed particles of zirconium dioxide possess increased stability to subcritical crack propagation and increased thermal stress resistance.

The behaviour of fissured materials reflects criterion R''' in greater measure. So, for example, for samples ZrO_2 with various contents of monoclinic phases [17] direct correlation between reduction in durability is revealed at a tension, compression and criterion R''' after cyclic thermal loading (Fig. 7.11).

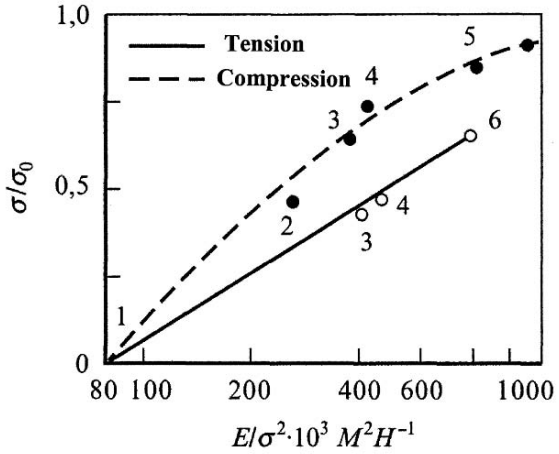

Fig. 7.11. Correlation dependence between relative drop of tensile and compression strength and criterion $R''' = E/\sigma^2$. Completely stabilized ZrO_2 (1). Partly stabilized ZrO_2, with the contents of a monoclinic phase of 8–10% (2), 15–20% (3), 20–26% (4), 30–40% (5), 40% (6). Samples have been subjected to triple thermal loading in the interval temperatures 300–2,500–300 K [17]

An attempt is made to fix the conditions of braking of a local crack and its spreading before complete body fracture on the basis of the concept of energy [17]. Calculation of the strain energy accumulated at thermal loading by heating of ZrO_2 samples is carried out with this purpose and fracture parameters M_1 and M_2 for continuous and hollow disk, respectively, are proposed as analogous to criterion R'''.

$$M_1 = \frac{4K_1 E\gamma_i}{\pi r_{\mathrm{H}} \sigma_{\mathrm{B}}^2}, \cdots M_2 = \frac{2K_2\gamma_i}{\pi(r_{\mathbf{B}}/r_{\mathrm{H}})\sigma_{\mathrm{B}}^2},$$

where K_1 and K_2 are the coefficients depending basically from distribution of temperature stresses in a specimen. A crack is braked at parameter value $M_{1,2} > 1$, it is extended without stopping, in the case of $M_{1,2} < 1$ causing complete fracture of a body. These design estimates of fracture characters introduced for various structures and phase compositions of specimens of ZrO_2 have shown good conformity with experimental results. The parameters $M_{1,2}$, as a matter of fact, anticipated the estimates of fracture character on R-curves introduced in the 1980s [42, 43].

A series of heterogeneous ceramic materials on the basis of aluminium, yttrium and zirconium oxide at thermal and mechanical loading indicate non-linearity of the strain diagram. The consideration of these phenomena is carried out by use of the brittleness measure introduced by Gogotsi [273], characterized by the ratio of a specific elastic energy accumulated in a material at the fracture moment to the total spent energy. Fracture features of materials can be considered also by the character of modification of fracture energy with length of a growing crack at loading of a body on constructed, so-called, R-curves [42].

Thermal stress resistance of heterogeneous materials (HTM) on the basis of aluminum and yttrium oxides are investigated in a summary paper [274]. The inelasticity of HRL is primarily connected with the multiple micro-cracks formed at a mechanical or thermal loading. Specimens of HTM materials on the basis of yttrium oxides (at $\chi = 1$) tested for thermal stress resistance detect drop of strength at thermal gradient ΔT_{c}, while specimens Y-4 with value $\chi = 0.64$ reduce strength continuously at a rise of ΔT, with formation of a dense grid of cracks on the surface.

At first, specimens of aluminum oxide (A-3) with stabilizing agents do not change strength with increase of thermal gradient ΔT, but a continuous decay begins on reaching ΔT_{c} accompanied by continuous acoustical radiation, owing to the specimen cracking at its incremented strain ε (Fig. 7.12).

Hollow coaxial cylindrical samples of alum earth without alloy additives were tested for thermal stress resistance and the same ceramics with 5, 10 or 20% of α-Al_2O_3 plates to find out the decrease of temperature drop ΔT_{c} with a small introduction of this additional agent. Difference ΔT_{c} and strain ε_u start to be incremented with simultaneous decrease of χ only after adding α-Al_2O_3 plates to ceramics more than 20% (the similar effect earlier was observed in a

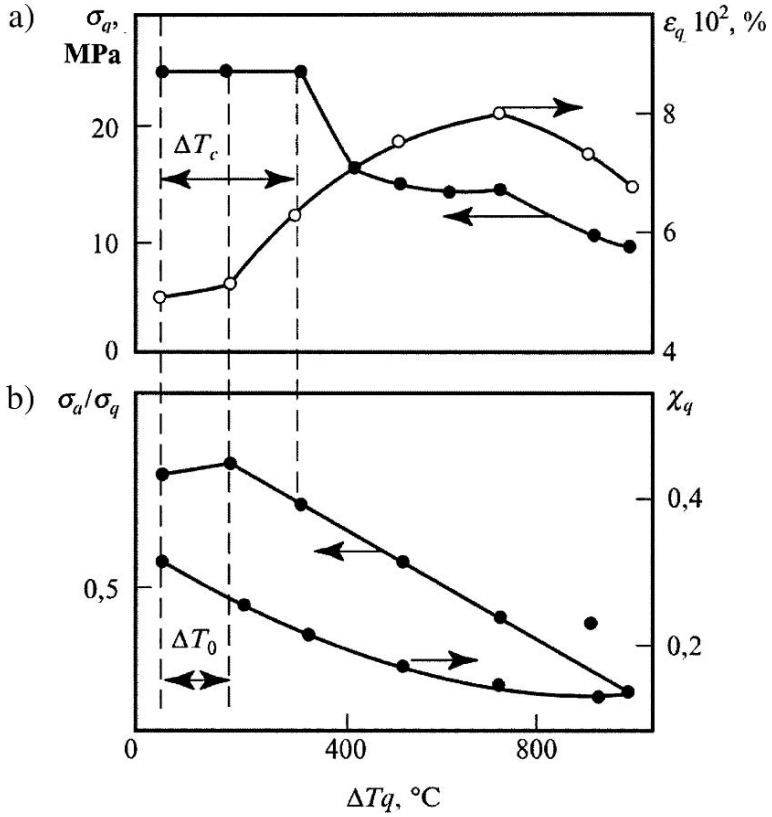

Fig. 7.12. Modification of strength σ_q, specimen strains ε_q of aluminum oxide with 4% of not stabilized zirconium dioxide and 1.9% of chrome oxide (**a**) and the relative values of strength σ_a/σ_q with a brittleness measure of aluminum oxide specimens χ having various compositions (**b**) depending on thermal gradient ΔT_q at cooling in water

boron nitride with components of aluminum oxide [14]). The high content of components of Al_2O_3 results in multiple cracking and coalescence of cracks.

Attempts to establish a connection between the thermal stress resistance characterized by drop of strength of the heated-up sample at cooling, character of the stress–strain diagram, fracture toughness and the kind of R-curve of a material have been undertaken in [275–278]. The analysis is carried out on summary experimental data of tested HTM mainly on the basis of ZrO_2 stabilized with magnesium oxide (Mg-PSZ), and the tetragonal polycrystalline ceramics containing yttrium oxide (Y-TZP). Basically, qualitative linkage between these four characteristics of the investigated materials is observed. Obviously growing steepness of the R-curve and non-linearity of the stress–strain diagram is accompanied by increase of fracture toughness and decreasing recession of strength after thermal loading. Deviation from linear

deformation with loading for the majority ceramic is connected with micro-cracking. Non-linearity of the diagram and increase of fracture toughness and steepness of the R-curve is a direct consequence of phase transformations for metastable tetragonal ZrO_2 ceramics [279]. Nevertheless, a number of deviations from the general laws is observed. For example, HTM Mg-PSZ with obviously expressed non-linearity of the diagram and gradual recession of strength after thermal loading has a flat R curve. Single-phase ceramic Al_2O_3 with the linear deformation characteristic can possess a rather abrupt R-curve and do not demonstrate gradual recession of strength after thermal loading. Attempts to explain such deviations by the presence of local stresses on inclusions able to cause branching of micro-cracks and their interaction are done, finally, resulting in decrease of the module of elasticity and drop of the general energy stock of a body. The ambiguous connection between the investigated characteristics of thermal stress resistance and fracture toughness, most likely is determined also by the not always correct estimation of experimental thermal stress resistance at non-stationary cooling in water. Considering that occurrence of cracks in refractory operation is accepted if they do not cause partition of a body, the authors [17] suggest to carry out a comparative estimation of thermal stress resistance of materials on size of temperature difference R_{50}, corresponding to 50% strength drop. The great value for practice represents certainly the dispersion law of thermal stress resistance values. In particular, distribution of thermal stress resistance values R received at stationary test of a set of ring samples of zirconium dioxide, stabilized with 6% CaO, is characterized by the known exponential Weibull distribution [17]. The average value of criterion R_{m} is 43°, $R_{\max} = 62.3°$, $R_{\min} = 29.6°$, and root-mean-square deviation $S = 7.6°$. The factor of variation of thermal stress resistance $w = 17.5\%$ is close to the corresponding value received for this material in mechanical testing. The established dispersion of thermal stress resistance values is connected with structural heterogeneity, inevitable at preparation of a set of samples even on the same technology.

Thermal Stress Resistance of Composites with Metal Inclusions

Introduction of plastic metal inclusions, insoluble in a ceramic matrix, results in essential increase of fracture toughness and bearing capability of thermal loaded composites. In view of this, investigations of mechanisms of crack distribution in composites on the basis of a brittle matrix with plastic metal particles or fibres [251, 252] are represented as being rather interesting.

Theoretically constructed models of crack distribution in composites with metal inclusions [252] have established the ratio between bridge stresses and size of the mouth of a crack and a determinant kind of R-curve.

Bridge stresses, as opposed to the stresses arising at the loading of a body, reduce crack formation. The results of calculated models are confirmed by experiments on the opening of cracks on aluminium oxides composites with fibres of aluminium in diameters 130 and 340 μm [252].

Strength and deformation characteristics of hard alloys of the tungsten group are defined not only by the Co contents in an alloy, the size of grain WC or thickness of a binding phase layer, but also, appreciably, by the connectivity and contiguity of carbide grains, and durability of interphase border [280]. Reduction of connectivity and contiguity of WC crystals in composites WC–Co with increase in content of the metal additive results in strength increase, owing to restriction of distribution of a crack in brittle carbide particles. The number of thermal loading cycles before occurrence of cracks essentially grows. Significant improvement of thermal stress resistance R' of composites on the basis of a brittle matrix with introduction of metal additives is shown irrespective of an elasticity modules ratio and factor of phases linear expansion, owing to an increase in thermal conductivity and fracture toughness. So, an appreciable increase of thermal stress resistance was observed with the introduction in ZrO_2 and HfO_2 of metal additives up to 15 mole% Ti, Zr; additives of nickel and cobalt in carbides of transitive metals [281] or with creation of a laminated structure in aluminium oxide with additives of a nickel–copper alloy [282].

It is necessary to mention separately the basic capability of a reinforcement, by magnification of a rupture work at introduction of dispersed metallics of submicron size. The dispersed inclusions of molybdenum particles in Al_2O_3 with size less than 1 nm, with the overall content of 5 vol%, hinders coarsening at an elevated temperature compaction or sintering [283].

Grain refinement results in strength improvement, and the possible retardation of cracks on uniformly distributed dispersion particles increases an effective surface energy [283]. Aluminum oxide with 20 volumetric % of molybdenum, with the coarse elongated particles of molybdenum, due to formation of bridge bonds, possesses greater fracture toughness than composites with dispersion particles [284].

Hydride compounds of transition metals Zr, Y and Ti, used as high-temperature moderators of neutrons in space and nuclear high-temperature reactors, experience essential thermal loadings. Mono-phase hydrides ZrH, YH and TiH in a maintenance temperature range in a nuclear reactor up to 900 K are brittle and do not have enough thermal resistance [173].

The formation of hydride composites at introduction of a metal phase to 20–40 vol% increases thermal stress resistance by two to three times, due to a relaxation of local stresses, increase of a fracture toughness and the relationship σ/E (Table 7.4).

Stress relaxation and crack resistance are largely determined by size and uniformity of distribution of inclusions, and also by plasticity of the metal phase. Composites of TiH (Fig. 7.13) with small-sized and ductile inclusions of titanium appear to be the most efficient.

Table 7.4. Modification of thermal stress resistance and mechanical characteristics of hydride composites with metal inclusions

Content	Inclusion size, $l/t\,\mu$	σ_b (MPa)	$\sigma/E \times 10^{-3}$	K_{1c} (MPa m$^{1/2}$)	R (K)
$ZrH_{1.8}$ $d_3 = 500\,\mu m$	–	30	0.43	1.7	80
$ZrH_{1.6} + 27$ vol% Zr	120/200	140	1.9	2.2	120
$ZrH_{1.7} + 19$ vol% Al	150/300	130	1.9	3.0	160
$ZrH_{1.5} + 30$ vol% Al	130/100	136	1.9	4.0	190
$ZrH_{1.7} + 22$ vol% Be	70/40	450	4.7	2.5	95
$YH_{1.9}$ $d_3 = 250\,\mu m$	–	20	0.15	1.5	21
$YH_{1.1} + 40$ vol% Y	100/110	45	5.6	4.0	40
$TiH_{1.6}$ $d_3 = 20\,\mu m$	–	150	1.3	2.2	75
$TiH_{1.2} + 18$ vol% Ti	150/3	390	3.5	3.4	140
$TiH_{0.8} + 40$ vol% Ti	30/5	840	7.6	7.6	300

l, t are length and width of particles, d_g is aggregate size

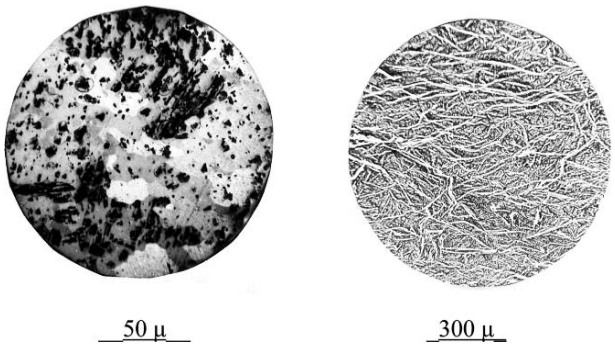

Fig. 7.13. Microscopic structure of not-doped large-grain $ZrH_{1.85}$, with martensitic structure (**a**) and fine-grained composite TiH with metal Ti components (**b**)

7.4 Thermal Stress Resistance of Functionally Graded Materials

A special place among composites is occupied by multilayer materials which consist of ceramics, metal and intermediate layers, whose composition and structure functionally varies from brittle ceramics up to ductile metal. Such composites with functionally gradient materials (FGM) have found wide application in space exploration, atomic technology and the engineering industry. Skins of a composite construction should resist heating up to a high temperature and the effects of an oxidizing atmosphere, and inner layers must be cooled intensively, thus creating a heavy thermal gradient in a structure. It is necessary to refer here to a single coating, as a particular case. Optimization of FGM structure and directional coating on rise of thermal stress

resistance is intensively carried on by design methods, model operation and experimental techniques.

There are two analytical approaches to calculation of a stress state of heterogeneous materials, one of which is a crude method, which inducts an assumption that heterogeneous materials can be substituted by multilayer homogeneous plates. The other represents the so-called precise solution, proceeding from the assumption that modifications of material properties can be presented by the functional mathematically dependent forms. The first approach of a stress state calculation proceeds from the multilayer theory presented in references [285–287]. Calculations of temperature and distribution of the thermal–elastic stresses in the non-uniform multilayer cylinder [285, 286] and in the multilayer plate [287] are carried out by analytical methods for cases where a layer thickness is infinitesimal and the number of layers tends to be incremented ad infinitum. It is shown that the modification of volume content of ceramics noticeably influences thermal coating stresses, and they are essentially diminished in case of the uniform directional distribution of ceramics. The thermal–elastic–plastic stresses originating during manufacture of a plate from FGM with injected reinforcing particles are computed by a finite element method [288]. Macroscopic and microscopic stress components are estimated taking into account modification of material properties from temperature and possible layer damage. The optimum profile of a volumetric relationship in layers of ceramic and metal components is determined by the results of calculation.

The principles of optimum design of multilayered constructions consist in sampling some set of materials at the given power and temperature loadings by a certain measure [69]. It is obvious that the optimization of a structure essentially depends on its assignment, regimes of maintenance and other specific habits. If the strength balance of all layers is necessary, then the optimization criterion is recorded:

$$\frac{\sigma_1^{\max}}{\sigma_{\text{o}}^1} = \frac{\sigma_2^{\max}}{\sigma_{\text{o}}^2} = \cdots = \frac{\sigma_n^{\max}}{\sigma_{\text{o}}^n} = k, \ldots, \max k,$$

where σ_{o}^i is a marginal stress for i layer. If it is necessary to reach the maximum strength of a structure, the requirement of optimality will look like

$$\min \left\{ \max_i \frac{\sigma_i^{\max}}{\sigma_{\text{o}}^i} \right\}.$$

Other optimization forms of a structure are also possible. The formulated problem results in searching for a global extreme of some function depending on discrete and integral-valued parameters. Practically all modern methods of searching for a global extreme of multiextreme functions are characterized by statistical properties [289].

There is an efficient combined method of searching for a global extreme at the complex view of multiparameter function, when starting conditions are

random. Searching for an individual extreme at such approach is conducted with the use of some local method, but each time from randomly chosen starting conditions. The local maximum result of each stage is stored and compared with local maxima of the subsequent stages from which the greatest global maximum is chosen. Repeated use of a local method with random starting conditions allows determination of the global extreme with a high probability by the numerical method.

We observe the problem of optimum design of four-layer coats of micro-fuel elements of high-temperature gas cooled reactors by way of illustration. Leak resistance of such micro-fuel elements in relation to fission products is attained by deposition on spherical fuel corpuscles of buffer low-density pyrolytic layer (PyQ), with both high density layer PyQ and silicon carbide (SiC) adding to a coat's necessary strength (Fig. 7.14).

The measure of optimization of a micro-fuel element on the basis of a maximum strength is stated as follows: Among every possible construction of protective coatings is that for which the requirement is satisfied by optimum

$$\min \left\{ \max_i \frac{\sigma^i_{\varphi\varphi}}{\sigma^i_{\mathrm{o}}} \right\}, \; i=3,4.$$

Thus radii of a core R_1 and micro-fuel element R_5 are set, and widths of surface layers are bounded below

$$R_{i+1} - R_i \geq h_{i+1}.$$

(Values of constants h_i are determined, as a rule, by technological capabilities).

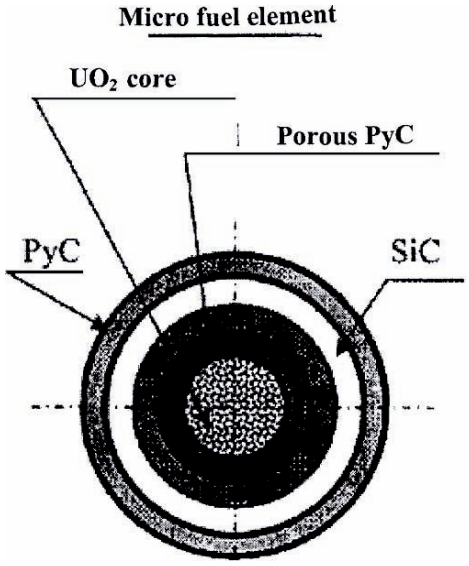

Fig. 7.14. Diagram of a four-layer construction of a micro-fuel element

Table 7.5. Performances of basic and optimum constructions of a protective coating of reactor VGR-50 [290]

Layer	Thickness (μm)	
	Basic construction	Optimum construction
PyC (buffer)	90	100
PyC (dense)	60	30
SiC (power)	50	90
PyC (dense)	50	30

The optimum construction of a micro-fuel element is characterized by enlarged widths of buffer layer and a silicon carbide layer and, accordingly, by decrease of widths of the second and fourth layers from pyrolitic carbon (Table 7.5). The increase of the buffer layer results in pressure decrease of gaseous fission products and relief of the protective coating as a whole. The magnification of width of a carbide layer diminishes the radial movement of this layer and as a consequence, all remaining strata of a protective coating as the carbide layer is the basic bearing layer in a coat. From here it follows that the increase of thickness of SiC causes the stress decrease in this layer and automatically decreases stresses in all remaining layers.

The effect of various factors on the thermal stress state of FGM, subjected to thermal shock, is studied in [291, 292]. This used the elastic–plastic solution for calculation of plane-strain condition of the composite containing intact particles and pores. The metal stratum is strained elasto-plasticly on Mises principals and the isotropic reinforcement requirements; the ceramic material is strained elastically. The statistical distribution of parameters of a bond lift-off or particle fracture is presented by a function depending on the maximum level of tensile stresses in a particle. The level of the residual stresses occurring during manufacture of a composite is estimated by the finite element method at various rates of cooling and requirements of heat transfer [292].

The numerical model operation of damageability which is estimated on modification of stiffness of a loaded cell system is designed for coatings of aluminium oxide on a titanium substrate by finite element method on code NASTRAN within the limits of continuum fracture mechanics. Design surface temperature at a heat flow with a maximum $2\,\mathrm{W\ mm^{-2}}$ and the given convective heat transfer mounts from room temperature up to 1,600°C for some seconds. The majority of the surface elements, at accepted small sizes of FGM of 12 mm in length and a heat flow $2\,\mathrm{W\ mm^{-2}}$, fail after 0.7 s, while damage of all coats and elements on an interface do not attain such levels even after 4 s of thermal loading. The average level of damageability is incremented with increase of porosity.

Originating residual stresses on the boundary line between a coat and substrate FGM at thermal loading are able to produce damage of various characters (Fig. 7.15), owing to the difference of coefficients of linear expansion

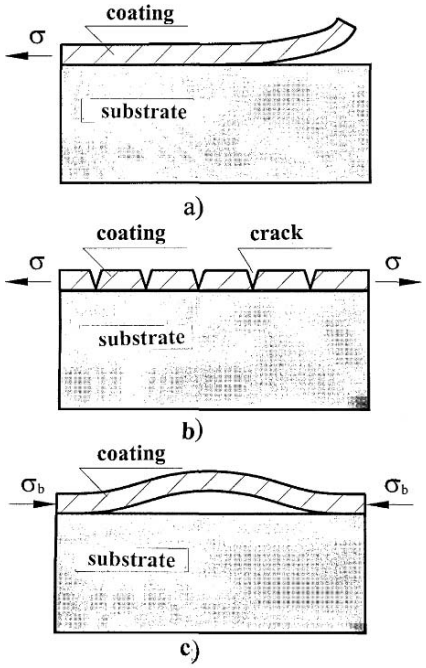

Fig. 7.15. Views of fracture of thin coatings under residual stresses: (**a**) Delamination of a coating at low adhesion from tensile stresses; (**b**) cracking of a coating from tensile stresses at good adhesion with substrate and (**c**) bulging of a coat at formation of compressive stresses and the subsequent fracture

and modulus of materials of coating and substrate. The fracture aspect is determined by degree of the coating's adhesion to the substrate, plasticity characteristic, fracture toughness [292, 293] and requirements and parameters of thermal loading [294, 295].

Thermal stresses, σ_1, in a coating of thickness h_1 originate even at uniform heating to temperature T due to a difference of coefficients of linear expansion of a coating α_1 and substrate α_2. Accepting the condition of equal deformation on the boundary line between coating and substrate, the stress in the coating can be expressed:

$$\sigma_1 = \frac{E_1 E_2 \left(\alpha_1 - \alpha_2\right) T}{\frac{h_1}{h_2} E_1 (1 - \mu_2) + E_2 (1 - \mu_1)},$$

where index 1 refers to coating and index 2 refers to substrate. E is modulus elasticity, μ is Poisson's coefficient.

Resistance of coating can be determined by the level of limiting tensile stresses at electron or laser beam heating. Initial damage of brittle coating of ThF_4 under influence of an electronic beam is developed in local layer

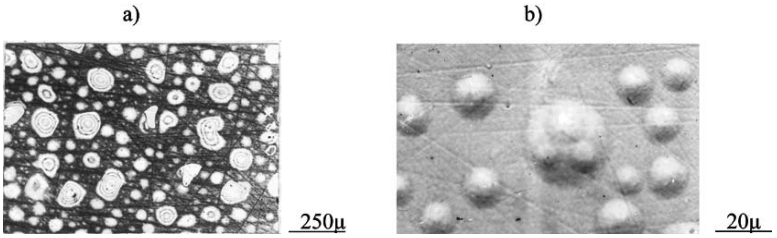

Fig. 7.16. (**a**) Damage to coating of ThF_4 0.4 μm in thickness on molybdenum substrate at thermal loading $q = 0.4\,\mathrm{kW\,sm^{-2}}$, $\tau = 0.1\,\mathrm{s}$; (**b**) Damage of silver coating 0.45 μm in thickness on SiC substrate at thermal loading $q = 1.9\,\mathrm{kW\,cm^{-2}}$, $\tau = 0.1\,\mathrm{s}$

Table 7.6. Parameters of swelling of coating of Ag (0.4 μm) on substrate of SiC

Parameters of loading		Dimensions of coating swelling			
Loading time (s)	q_1 kW cm^{-2}	Number of swelling bubbles	Radius of bubble base (r), μ	Height (H) (μm)	r/H
		50	10–20	0.3	0.09
10^{-1}	1.9	12	15–25	0.55	0.12
		3	30–40	0.8	0.09
		12	10–20	0.3	0.09
10^{-2}	3.4	5	15–25	0.55	0.12
		3	30–40	0.9	0.10

separation from the substrate. A pattern of interference rings arises on viewing a surface in reflected light (Fig. 7.16a).

Damage of plastic coating does not occur down to emersion of a residual deformation of 2% in substrate. Plastic coating repeats principally the changes of relief of the strained substrate. In this case, damage of a coating occurs usually on slip lines, scratches and on zones of disturbed adhesion. Loss of coating stability can occur only in the presence of zones of disturbed adhesion. Local layer separation of silver coating at electronic-beam loading has a regular geometric form of bubbles whose surface is close to spherical (Fig. 7.16b). Bubbles are formed chiefly of three sizes (Table 7.6) irrespective of duration of loading. Thus the relation of radius of a bubble base r on the boundary of the coating and the substrate to the height, H, of all bubbles is practically of constant magnitude.

The threshold of damageability, q, of coating ThF_4 (Table 7.7) decreases with increase in thickness of the coating and the duration of beam influence according to dependences:

$$q \sim h^{-1/2}; \quad q \sim t^{-1/2}.$$

Table 7.7. Thermal streams, q, and stresses, σ, of local spalling for coating ThF_4 on copper substrate under electron beam loading in zone of 2 mm

Loading time (s)	Thickness of coating (μ)	Substrate copper	
		q (kW sm^{-2})	σ (MPa)
	0.1	1.2	−90
10^{-1}	0.4	0.4	−50
	1.0	0.3	−40
	0.1	6.0	−300
10^{-2}	0.4	1.1	−100
	1.0	1.0	−80
	0.1	15	−350
10^{-3}	0.4	7	−130
	1.0	1.6	−140

The uncontacted method of detection of audible signal by means of the laser interferometer is used for examination of fracture of coatings at thermal-cyclic loading [296]. Correlative connection between velocity of released energy and character of audible signal is established at formation of the interphase cracks, computed by the finite element method. Convenient measurement of cohesive strength of a coating with a substrate by means of laser scratching combines, as a matter of fact, a conventional method of scratching by a quasi-static infrared pulse and laser measuring technique is observed in [297]. Residual stresses can attain 40 MPa [294] in a ceramic coating on the basis of Al_2O_3 with components ZrO_2–8%Y_2O_3 superimposed by the plasma expedient on a steel substrate. Neutron diffraction measurement of stresses has detected the presence of different tensile stresses in metal matrices and equal compression stresses in Al_2O_3 particles [298] in two composites based on aluminium and copper matrices with aluminium oxide.

Information about volume content and allocation of a metal phase in an aluminium-chromic composite, obtained by a method of a X-ray microtomography, have made it possible to calculate thermal stresses precisely by the finite element method [299].

The computational model of thermal stresses offered in [300], considered the capability of plastic deformation and creep of a material at variations of a temperature drop in coating and growth of the oxidated surface layer. Results of numerical calculations for FGM of PSZ/Ni alloy, confirmed by tests, have determined the capability of heated composite to delaminate during its cooling or at the subsequent heating cycle.

Requirements of fracture of bellied coatings [301] are determined proceeding from known theoretical positions and the analysis of experimental data at laser loading of coatings. The limiting level of energy for the beginning of fracture of a coating, $G = K_1^2/E$, is determined by the relationship:

$$G_c = (1-\nu)(1-\alpha)t(\sigma^2 - \sigma_c^2)/E$$

and the necessary and sufficient condition of fracture of a bellied coating is determined by the value:

$$\alpha_s/t \approx 1.9(E/\sigma)^{1/2},$$

where α_s is the limiting value of the radius of a bellied coat, t is the width of a coat, E is the Young module and σ is stress.

The introduction of vertical short cracks with major density increases the durability of a composite against coating delamination during cooling, and the more the width of a coating, the greater its extent [302].

It is necessary to note that thermal stress resistance of FGM made by manifold technological expedients, can vary essentially. The centrifugal casting used for preparation of FGM, allowed the content of particles SiC to vary on the width of a matrix continuously and, hence, a modulus of elasticity [303]. Interparticle matrix fracture is changed, with increase of SiC particle content on dominating fracture of particles.

For rust-proofing and oxidizing, the substrate of superalloy is coated with a barrier layer of Ni–30cr-12al-0.3 Y (mass%) by a magnetron expedient, with subsequent deposition of stabilized zirconium oxide by means of electron beam heating. At first micro-cracks are originated on the boundary lines of the columnar grains at cyclic heating of FGM in the oven at a temperature of 1,050°C, and then they pass around along the surface of the basic coating [304]. FGM with a basic coating of aluminium oxide on a steel substrate, with two or three interlayers of intermetallic Fe_3Al powder and profiled aluminium oxide composite sprayed by the plasma expedient, have appeared much more thermally resistant than usual composites without profiled strata [305]. Three or more strata of slip Al_2O_3 with components of partly stabilized zirconium oxide (PSZ) of various composition on the steel surface of a funnel formed by slip casting are sintered at 1,350°C. Tubes produced by such engineering techniques differ from the usual double-layer funnels by increased thermal resistance [306].

Two- or four-layer funnels were prepared by extrusion forming of the multilayer stock material from powder intermixture of stainless steel and PSZ of various compositions with binder and then sintered under pressure. Thermal stress resistance tests do not reveal any visible laminations on strata of the manufactured funnels [307]. The compacted multilayer disks of alum earth with nickel are sintered by means of electric current transmission through the stock material [308]. Polyfractional intermixture of Al_2O_3, deposited on a metal substrate by plasma expedient, increased the thermal stress resistance of coatings [309]. The thermal stress resistance of such coatings at a cyclic loading, in comparison with coating from mono-sized powder, is increased more than 10 times. FGM with coatings of MgO–ZrO_2 superimposed on a metal substrate by a plasma expedient possesses the greatest thermal stress resistance when porosity of a coating does not exceed 7.5% and pores of small size are uniformly distributed in the volume [310].

Substantial increase of thermal stress resistance of coatings from ZrO_2, superimposed on a metal substrate, can be attained also at reinforcement of a coating by metal mesh or fibres. Strength and thermal stress resistance of oxide coatings based on ZrO_2, HfO_2, Al_2O_3, superimposed on metal substrate of molybdenous alloys is observed in [311]. On the basis of assaying the results from temperature fields measured in the furnace and calculations of temperature stresses in a ceramic substrate, optimum regimes of thermal chemical processing are offered for the production of microchips, eliminating liability for faults and essentially increasing reliability of their operation [312].

The modelled habits of FGM in tests close to service conditions of space installations and the fracture kinetics of coatings are presented in a number of published studies [313–316]. Test limits and the fracture characters of coatings are observed in detail on an instance of loading a disk of FGM by a heat flow from a gas burner on the upper disk face and cooling by water of the bottom face [313]. FGM disks 30-mm in diameter were heated up within 1,300–1,500 K locally on a stage of 10 mm diameter before cracks occurred. FGM prepared by an elevated-temperature compaction on a substrate of stainless steel consists of five layers of a total width of 1, 2 or 3 mm with sequentially varying composition. The first layer is stabilized zirconium oxide (SZO) and four subsequent layers are the homogeneous-width intermixtures with steel at 80, 60, 40 and 20 mass%. Temperature stresses are computed by the finite element method under programme NISTRAN on the temperature field measured by a radiation pyrometer. Originating biaxial compressive stresses (Fig. 7.17) cause a plastic deformation in the surface layers of FGM at heating up to 1,400 K, which induces formation of the residual tensile stresses at cooling (Fig. 7.18), capable of organizing a system of cracks (Fig. 7.19).

The crack declines with a vertical direction of growth 200 μm in depth from the surface and starts to pass around in a direction parallel to the surface (Fig. 7.19) because the stress intensity coefficient K_{1c} for vertical cracks

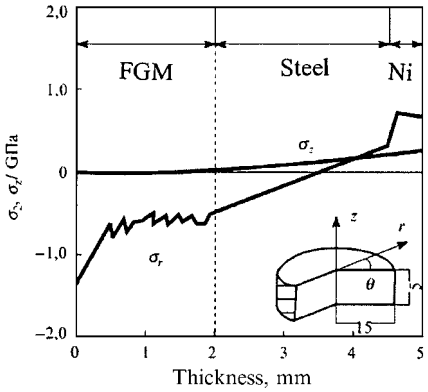

Fig. 7.17. Distribution of the thermal radial σ_r and axial σ_z stresses in a central part of the disk on FGM width

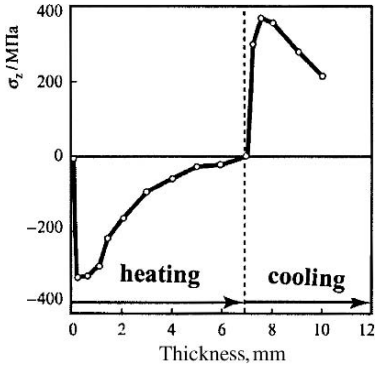

Fig. 7.18. Modification of thermal radial stresses σ_r on the surface of the central part of the disk of FGM in due course, at transition from a heating to cooling

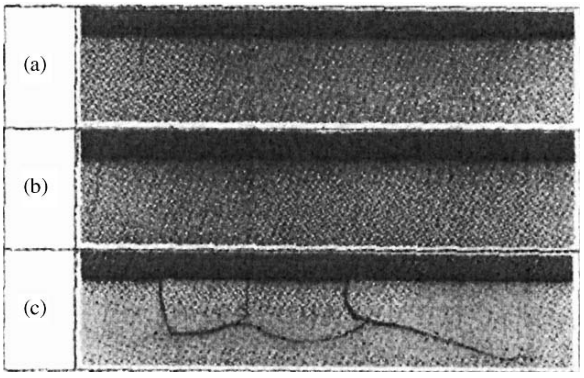

Fig. 7.19. View of the cracks that occurred after loading of FGM with the net width 1, 2 and 3 mm up to temperature 1,400 K at levels of heat flows (**a**) 1.5 MW, (**b**) 1.1 MW (**c**) 0.75 MW

is reduced in the process of their growth and value K_{1c} for cracks oriented parallel to a surface becomes predominant.

The union of the cracks system results in cleavage formation. Similar cleavages are formed in five-layer FGM of zirconium oxide with the net width of strata of 0.75 mm after five cycles of a pulsing laser loading in temperature range 1,300–700 K [314], imitating the requirements of the shut-down and starting up of gas turbines. Complex enough in a design, the thermal bench [315] allows testing large devices of components of FGM panels for space apparatuses in requirements approaching flying conditions.

The test data, simulating parameters of maintenance of the first wall of a thermonuclear reactor, are stated in [317–320]. Cracks on the boundary line of FGM of silicon carbide with coats of wolfram and intermediate laminas of copper, titanium and molybdenum for improving thermal conductivity are

detected after several thermal cycles, imitating service conditions [316]. Tubes with sputtered coats based on oxides Cr_2O_3–SiO_2 are used for prevention of tritium emersion in a thermonuclear reactor [317].

7.5 Thermal Stress Resistance of Anisotropic Bodies

It is necessary to distinguish two basic cases of the anisotropy by structural indication, sometimes existing simultaneously; homogeneous (crystalline) and heterogeneous (filamentary). Homogeneous anisotropy is caused by a crystalline structure of solids and is manifested especially sharply in single crystals, and in the presence of preferential crystallographic orientations – textures in polycrystals. Heterogeneous anisotropy is related to inhomogeneity of structure. Oriented fibres are often separated one from another by other phases which have been drawn down in determinate directions, induced by technological habits of preparation of composites.

The effect of anisotropy of polycrystal materials on thermal stress resistance is observed in [321–323]. It is established, experimentally, that the thermal stresses originating fracture change with variation of structural anisotropy of ceramic materials and cermets. The relationship of values of strength to a modulus noticeably varies depending on grain orientation in polycrystal, that result in matching variation of thermal stress resistance [322]. Impurities Ca and Si are accumulated on segments of boundary declination lines at modification of a mutual orientation of bicrystals, while there is no such impurity on the base segments of boundary lines, which naturally affects the character of propagation of micro-cracks [323]. The extent of anisotropy of coefficient of elasticity and the linear expansion factor on a level of thermal stresses is shown in [321, 324] using the finite element calculation method.

Originating microscopic thermal stresses in separate grains of anisotropic materials can lead to the directional growth of residual deformations even at both slow and volume-uniform reheating and recooling. In the presence of the certain requirements, for example preferential alignment of grains (texture), plastic detrusion and developing are manifested in macroscopic form, sometimes with strain of very considerable magnitude. This effect (a so-called cyclic thermal treatment, CTT), has been systematically studied in [325].

The thermal stress resistance of single crystals is investigated to a lesser degree, than the thermal stress resistance of the anisotropic polycrystals. Comparative test data for single crystals, bicrystals and polycrystals with preheated specimens quenched in water is shown in [326]. The authors note that cracking of specimens of MgO happens practically under equal conditions of thermal loading. Unlike polycrystals, face cracks in single crystals are oriented by a regular fashion on certain planes of spalling. Analogous regular character of fracture at pulsing plasma heating is also observed in sapphire crystal. Thus it is noted in [327] that the penetration depth of cracks in single

crystals at invariable intensity of thermal loading is more noticeable than in polycrystals.

Structural elements of sapphire are used in thermal-emission atomic power installations [328]. In view of this, the thermal stress resistance of sapphire has started to be investigated in more detail. Influence of orientation, extents of the surface and volumetric presence of crystal defects, thermal stress state on a level of thermal stress resistance and character of fracture is observed in [62], in comparison with thermal stress resistance of aluminium oxide polycrystal [329]. Available data about the strength and fracture of sapphire crystal of different alignments under mechanical loading [330] indicate capability of the significant effect of these factors under thermal loading.

Examination of thermal stress resistance of sapphire [62] was carried out on specimens of various shapes and orientations, prepared through extraction of a specified crystal profile from melting with a seed having a certain crystallographic orientation [331]. The sapphire blanks were obtained as rods 4–5 mm in diameter and 350 mm long, as pipes of 16 mm OD, 8.0 mm ID and 100–120 mm long, and as plates 40 mm wide, 4 mm thick and up to 200 mm long. The growth axes of the rods and tubes were oriented $\langle 0001 \rangle$, $\langle 01\bar{1}\bar{2} \rangle$ within 2–4° and $\{11\bar{2}0\}$ plates were $\langle 10\bar{1}0 \rangle$–oriented.

The extraction rate was 1 mm min^{-1}. Maximum 0.7 mm blocks were observed on separate sites of the crystal. Crystals with disorientation of blocks of more than 3° were rejected. The average density of dislocations on the growth surface was $10^5\,\text{cm}^{-2}$. The blanks in a batch were somewhat different in porosity. Noticeable non-uniformly distributed porosity was observed in rod batches IV and V. Pores of 1–3 μm were concentrated in the middle of the rods from batch VI with maximum pore density $10^4\,\text{mm}^{-2}$. A grid of pores was observed on the surface of the samples of batch VII. The porosity was distributed in the main on the outside of plates and tubes, which was removed by machining the specimens.

Cutting of blanks was conducted by a metal-bound diamond wheel with a 125–100 μm diamond powder. The surfaces of cylindrical bars were ground in water–oil emulsion with organic-bound diamond wheels (AC6) with 63–80 μm grain. The sapphire disks were prepared from the plates, cut into square pieces and then glued together. Such a glued unit was machined in a circular grinder by diamond wheels (AC6). The front face of the disks was subjected to successive double side polishing to remove the surface porosity by diamond wheels 125/100, 40/28 and 28/20. The edges of disk were 45° chamfered by a free abrasive of 40/28 μm. The front face was finished with diamond paste of 10/7 μm to remove damaged layers down to 20–30 μm, and then chemically superfinished on chamoise with selicole. The final roughness of the surface was no more than $R_z = 0.05$. The outside and inside and ends of the faces of the tube samples were polished in similar modes.

Thermal stress resistance was measured by non-stationary methods [31] for heating the lateral area of cold specimens in a bath with melted tin of known temperature, or by quenching of the specimen, heated up to preset

temperature, in a water bath. The procedure of water quenching of the lateral area of the disk having thermally insulated end faces, consisted in serial increase of temperature of the specimen, through steps of 10–15°C, until occurrence of first visual indications of fracture at the temperature difference ΔT between the heated sample and the water bath. In the heating test with melted tin, temperature was increased through steps of 20–30°C and the difference ΔT, initiating fracture, was registered using an acoustic sensor in the frequency range 1–20 kHz. Determination of thermal stress resistance under single and cyclical thermal loading at elevated temperatures were conducted in our high-frequency installation [163].

The three-point bending strength σ of cylindrical specimens with base $l = 20$ mm was calculated on load P from ratio $\sigma = 8Pl/\pi d^3$. Tests from above 20°C up to 1,800°C were conducted in a testing machine with tungsten heater and 250 kg load cell. The tensile strength of the hollow cylinders was determined by pressure in their internal cavity. The fracture toughness was evaluated by indentation of a diamond Vickers pyramid under load 5 N from the ratio $K_c = 0.0742\, Pc^{-3/2}$, where P is the load on indentor, and c is the radius of the hemidisk crack.

The crystallographic orientation of the specimens was measured using a DRON-3 X-Ray machine. Behaviour of cracks and twins was studied using a microscope under transparency and reflection. The fracture surfaces were examined both by optical and scanning electron microscope. The stresses after diamond processing of the sapphire surface were evaluated on copper radiation line (half of X-beam is diffracted from a 8 mm depth). Lines were recorded in a 2θ scanning mode. Integral width of (1120) line was conditionally measured from the relation between the area under curve K_α – doublet (to coincidence with the background) and the line peak height. The measurements were conducted repeatedly to avoid block structure effect; the received data were averaged.

Computational Techniques for Thermal Stresses in Anisotropic Bodies

Thermal stress resistance is defined by the value of the mean integrated temperature difference over the cross section of the sample: $\Delta T_m = T_m - T$, where T_m is the mean integrated temperature and T is temperature at an arbitrary point, either on the surface or in the bulk of the specimen. The ΔT_m is defined numerically on the measured value ΔT and on the coefficient of heat transfer in water or in melted tin. The tensile tangential thermal stresses on the surface σ_c for the cylinder and σ_d for the disk under quenching are accordingly determined per the value ΔT_m on the basis of quasistatic theory of thermal elasticity [67]:

$$\sigma_c = \alpha E \Delta T_m/(1-\mu), \sigma_d = \alpha E \Delta T_m,$$

where E is modulus of elasticity, α is coefficient of linear heat expansion.

Computation of the non-linear boundary condition of heat exchange and temperature dependence of material properties is implemented by numerical methods in determination of thermal stress resistance. Disregard of these factors gives rise to errors in calculation of thermal stresses, of up to 20–50% [74, 110, 111].

Distribution of thermal stresses in the disk and cylindrical specimens of sapphire with regard to the anisotropy and temperature dependence of properties and coefficient of thermal emission is effected by the finite elements method using an ANSYS program complex [332] through successive solution of unsteady non-linear problems of thermal conductivity and thermal stress resistance in a spatial and axisymmetrical statement. The 2D meshing for axisymmetrical and the 3D meshing for spatial state were used. The mesh division was performed with four-node rectangular elements for axial symmetry and with 20 nodes for spatial state. The number of node points and elements was dependent on the sample size. For example, the number of elements on radius, thickness and half circumference lay in the ratio of 8:5:12 for a half disk 10 mm in diameter and 2.5 mm thick; on the whole 480 elements were available and 2,491 nodes. The 2D FEM modelling of a cylinder 3 mm in diameter and 20 mm in length had 1,200 elements and 1,281 nodes. The meshes were refined near the radial-free surfaces.

The calculation of thermal stresses in sapphire, taking into account anisotropy of properties and non-linear heat exchange condition for determination of thermal stress resistance have not been made previously. The only known methods are to calculate thermal stresses in sapphire blanks grown from melts under axial temperature [333] with the aim to optimize the growth parameters and decrease the dangerous residual stresses in the crystal.

The properties of (0001) oriented sapphire are presented in Table 7.8 across ($\perp$) and along the C axis ($\parallel$). Solution of thermal elasticity problems has a number of features. The first is essential non-linearity of physical–mechanical properties of the material and change of boundary conditions during solving the problem, especially sharp changes (more than by one order) under cooling of the sample in water.

Table 7.9 shows the influence of only two parameters (heat conductivity λ and heat-transfer factor h) on the peak major stress σ_1 and the time to reach it, for oriented disks (0001) cooled in water. The last row of the table gives the solution for non-linear problem statement.

The second feature is anisotropy and scale factor. The (0001) oriented disks are transversally isotropic, disks with changed orientation possess properties of general anisotropy. Under a finite-elements simulation, the transition from transversal isotropy to general anisotropy is derived automatically, if the C-axis of the developed model is resolved to the main system of coordinates to which the preset physical–mechanical properties of a transversally isotropic body are fixed. The character of the solution changes too. The solution is axisymmetrical for disks with orientation (0001) and the problem may be solved for a two-dimension (axisymmetrical) statement. Under change of

Table 7.8. Properties of sapphire and poly-Al_2O_3 vs. temperature

Property	Orientation	Temperature (K)			
		300	500	700	900
Thermal conductivity λ (W m K^{-1})	$\parallel$	25	17.5	–	–
	$\perp$	–	–	–	–
	Polycrystal	23	15.5	8.6	8.5
Linear coefficient of thermal expansion, $\alpha \times 10^6$ (K^{-1})	$\parallel$	7.10	–	7.96	8.23
	$\perp$	5.50	–	6.60	7.22
	Polycrystal	6.30	–	7.45	7.74
Modulus of elasticity E (GPa)	$\parallel$	460	–	–	–
	$\perp$	420	–	403	387
	Polycrystal	395	–	385	362

Table 7.9. Peak values of major stresses σ_1 and time τ to reach them for water-quenched disks, with diameter 10 mm and thickness 2.5 mm, heated up to 2,000 K at varying λ and h

λ (W m K^{-1})	h (W m^2 K^{-1})	τ (s)	σ_1 (MPa)
16	30,000	0.10	241
16	14,000	0.17	176
23	14,000	0.17	147
From Table 7.6	From Fig. 3.2	0.07	160

Table 7.10. Changes of a maximum main stress σ_1 and time τ to reach it, for samples of sapphire with diameter 10 mm and height H quenched in water

Thickness of sample (mm)	Orientation	Temperature (200°C)		Temperature (220°C)	
		τ (s)	σ_1 (MPa)	τ (s)	σ_1 (MPa)
$H = 0.5$ mm	$\langle 0001 \rangle$	0.08	143	0.07	175
$H = 2.5$ mm	$\langle 0001 \rangle$	0.07	160	0.06	196
$H = 2.5$ mm	$\langle 011\bar{2} \rangle$	0.08	177	0.08	216
$H = 5$ mm	$\langle 0001 \rangle$	0.08	167	0.08	216

C-axis orientation in spite of sample/load symmetry, the symmetry of the solution disappears and the problem should be solved for a three-dimension (space) statement.

The sample's dimensions also affect significantly the stress–strain state. Plane stress state is realized for rather thin samples (thickness 1 mm and less, i.e. batches XI, XII, XIV) the axial component of stress arises and increases for thicker samples (I–VII). The plane strain state is realized principally in the transversal isotropic rod or tube, except its zones near the ends.

The anisotropy/scale effect is displayed in Table 7.10. Transition from axi-symmetrical orientation of a (0001) sample to a sample with spatial orientation

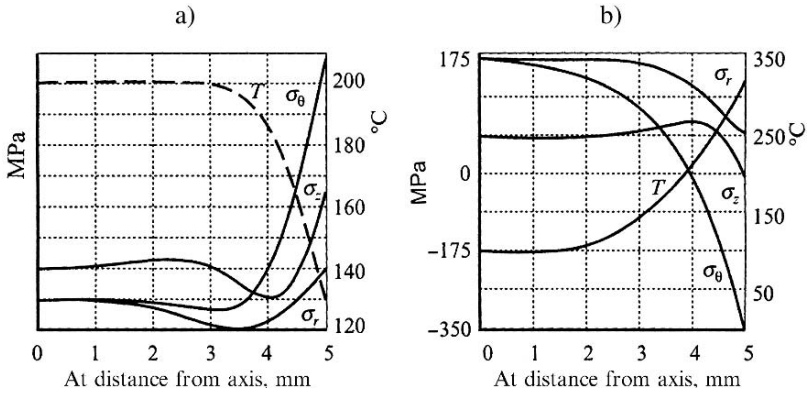

Fig. 7.20. Distribution of surface temperature T_S and stress components σ_θ, σ_r, σ_z on the radius of a cylinder $d = 10\,\text{mm}$, $h = 2.5\,\text{mm}$, orientation (0001) quenched in water from 200°C at the time of attainment of maximum tensile stress (**a**) and heated in melted tin at a temperature of 1,000°C at the moment of attainment of maximum compression stress after 0.4 s from the onset of heating (**b**)

$\langle 011\bar{2} \rangle$ as well as the transition from a plane-stress condition ($h = 0.5$) to a plane-strain state increases the level of arising stresses. The anisotropy of crystal essentially changes the spatial distribution pattern for stress components.

Distribution of stress components along the radius of a (0001) oriented disk, is changed for the heating/quenching tests (Fig. 7.20).

Note that, in water-cooled samples, the peak tensile stresses are reached in 0.025–0.09 s after cooling starts, before the peak radial temperature difference. For the tin-heated samples, peak stresses occur far later. Here, the peak tensile stresses occur after origination of the peak radial temperature drop, and the peak compression stresses appears before the peak temperature drop. Thus, compression stresses considerably exceed tensile at an initial heating-up period for specimens of batch X, but at further heating, the difference between compressive and tensile stresses is diminished.

Generally, stress calculation without taking into account the anisotropy of properties of a single crystal and non-linear conditions of heat exchange at boiling leads to net error of up to 35%.

Features of sapphire fracture in comparison with polycrystalline compounds with cubic symmetry, such as ZrC, SiC, MgO, UO_2, under thermal loading are governed by two circumstances; the fracture toughness anisotropy and the capability of deformation by twinning at rather low temperatures of 0.4–0.5 T_{melt}. This feature predetermines distinctions in the character of cracking with change of the type of thermal loading upon sapphire and polycrystalline oxide/nonoxide compounds, incapable of plastic deformation up to temperatures 0.4–0.6 T_{melt}.

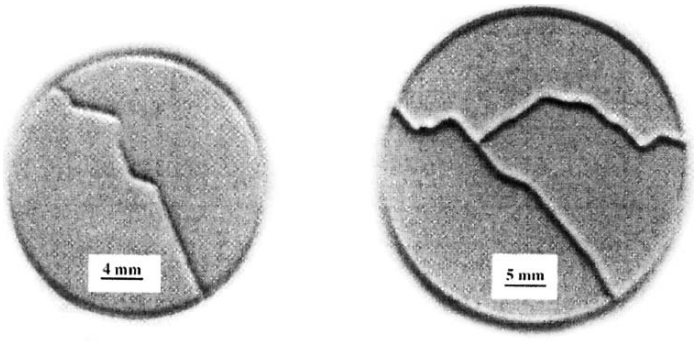

Fig. 7.21. Sapphire thin disks ($h = 1$ mm) with orientation $\{0001\}$ (**a**) and $\{11\bar{2}0\}$ (**b**) tested by quenching method

The cracks originating on the surface of quench-tested quasisotropic polycrystals stop in the compressed central zone; full fragmentation is excluded. At the same time, the heating tests lead, as a rule, to full fragmentation of the polycrystals due to tensile stresses in the central zone, despite the presence of compression stresses in the peripheral zone (Fig. 2.3).

Sapphire, unlike polycrystals, fails in a different way with change of thermal loading. Under quench test, the disks are fragmented completely (Fig. 7.21) while in the heating test, surface cracks only occur in sapphire disks (Fig. 7.22) at 500–600°C. The feature of fracture in the heating test resides in the capability of twinning in sapphire under low temperatures and stresses. For example, the critical resolved stress of twinning on the rhombohedral plane $\{1012\}$ comprises 230 MPa at 350°C and decreases to 30 MPa at 600°C [241], that is 13 times below the arising thermal stresses. Relaxation of thermal compression stresses by twinning, and formation of residual tensile stresses after cooling, close in their absolute level to the initial thermal–elastic compression stress (Table 7.11), appear to be sufficient for surface cracking. At the same time, thermal–elastic tensile stresses in the central zone of the disk as high as 120–170 MPa are below the single-axis tensile strength at the same temperature [330] and incapable of causing cracking. The plastic deformation by sliding is especially impossible because the critical stresses on the basal, prismatic and pyramidal planes even at 800°C are about 900 MPa [334].

Absence of twins in the central zone of the disk is explained by unfavourable conditions for them to be born in the tensile stress zone, as is proved in [330]. Smooth departure of the crack from its initial direction to the rim of the disk (Fig. 7.23) is caused by braking influence of compression stresses in the central zone.

The systems of twins on planes $\{0001\}, \{\bar{1}012\}$ and $\{11\bar{2}1\}$ observed under low magnification in the surface layers of disks of both orientations, as a system of fine (10–20 μm) sheets, extending up to 5,000 μm, as a rule, arise before the cracks. Twinning occurs on two planes $\{\bar{1}012\}$ and $\{11\bar{2}1\}$ in the disks of batch

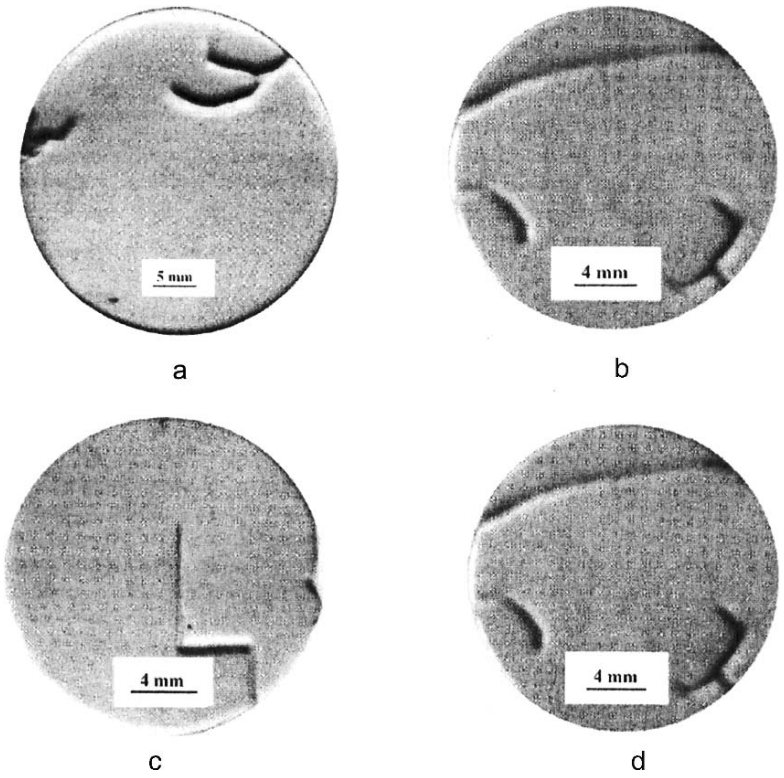

Fig. 7.22. Fracture mode of specimens with orientation $\{11\bar{2}0\}$ (**a, b**) and $\{0001\}$ (**c, d**) tested in melted tin at 500–600°C

XIII with orientation [0001]. The plane $\{\bar{1}012\}$ is located at a small angle to the plane [0001], therefore the twins when observed under a microscope, create an interference pattern with the interference bandwidth of $d \approx 800$–$1{,}000\,\mu m$ (Fig. 7.23a). The plane $\{11\bar{2}1\}$ in the disk of batch XVIII is at a large angle to the plane $\{11\bar{2}0\}$, and the twins are almost perpendicular to the surface of the disk owing to the interference band width being insignificant $d \approx 30$–$60\,\mu m$ (Fig. 7.23b). In most cases, cracks arise in a specimen after twinning.

The thermal stress resistance level of batch IX3 disks tested by quenching after 6–11 cycles of heating in melted tin up to 1,000°C increases almost twice, obviously owing to the intense twinning in the sample body and redistribution of stresses.

The disks tested by quenching fail into fragments in contrast to the surface fracture of the disks tested by heating. The tensile stresses arising on the surface are sufficient (Table 7.11) for cracking, but twinning and stress relaxation at test temperatures 200–250°C is sharply reduced. The passing of the crack through the cross section of the disk under cooling (Fig. 7.21) seems to be connected with the anisotropy of the monocrystal's fracture toughness. Various

Table 7.11. Thermal stress resistance of sapphire with various orientations [62]

Batch	Size D-diameter, l, h-length, height, mm	Orientation	No.	Thermal stress resistance				T_f (°C)	Fracture Time τ (s)
				$\Delta T_{min} - \Delta T_{max}/\Delta T_m$ (°C)	σ_r (MPa)	σ_z (MPa)	σ_θ (MPa)		
B	$D = 5$; $l = 15$	Poly Crystal	18	155–190/170			130		
IR	$D = 4.4$; $l = 40$	(0001)	24	138–200/179	0	184	150	142	0.025
IV–V	$D = 3.2$; $l = 40$	(0001)	14	158–235/210					
VI	$D = 3.2$; $l = 40$	(0001)	7	184–261/229	0	258	212		
VII	$D = 3.2$; $l = 40$	(0001)	7	221–235/229	0	258	212		
IX	$D = 10$; $h = 2.5$	$\{01\bar{1}2\}$	7	210–240/224	0	70	235	142	0.07
X	$D = 10$; $h = 2.5$	(0001)	5	180–200/180	0	59	148	130	0.07
X **	$D = 10$; $h = 2.5$	(0001)	2	980/980	175/0	0/–	175/–454	47/332	$0.4^{(1)}$
					222/0	1,000/–40	222/–374	200/457	$1.2^{(2)}$
X3	$D = 10$; $h = 2,5$	(0001)	2	280–360/320			320		
XI	$D = 20$; $h = 1$	(0001)	8	190–345/218	0	5	232	138	0.09
XII	$D = 25$; $h = 1$	$\{11\bar{2}0\}$	4	180–194/188					
XIV3	$D = 20$, $h = 1$	(0001)	2	200–234/230		7	235	135	0.09
XV	$D_o = 13$; $D_i = 9$, $l = 9$	(0001)	4	200–260/220	0	289	330	103	0.09
XVI	$D_o = 13$; $D_i = 9$, ll = 9	$\{01\bar{1}2\}$	4	200–310/230		348	359	138	0.06
XVII	$D_o = 13$; $D_i = 9$, $l = 9$	Poly Crystal	7	140–215/180	0	0	154	119	0.06
XIII*	$D = 20$; $h = 1$	(0001)	4	520–700/595	121/0	0	121/–418	23/277	$1.0^{(1)}$
					169/0	0	169/–379	113/344	$3.0^{(2)}$
XVIII*	$D = 20$; $h = 1$	$\{11\bar{2}0\}$	2	500–500					
XIX*	$D = 30$; $h = 1$	$\{11\bar{2}0\}$	2	430–500/480					

Note: D_o outside and D_i inside diameter of cylinder. The specimens of all batches are tested by quenched method except the batches X*, XIII*, XVIII*, XIX* which were tested in melted tin. IX3 and XIV3 – the specimens tested after tempering. (1) At the peak compressive stress moment; (2) At the peak tensile stress moment. Numerator: centre, denominator; edge

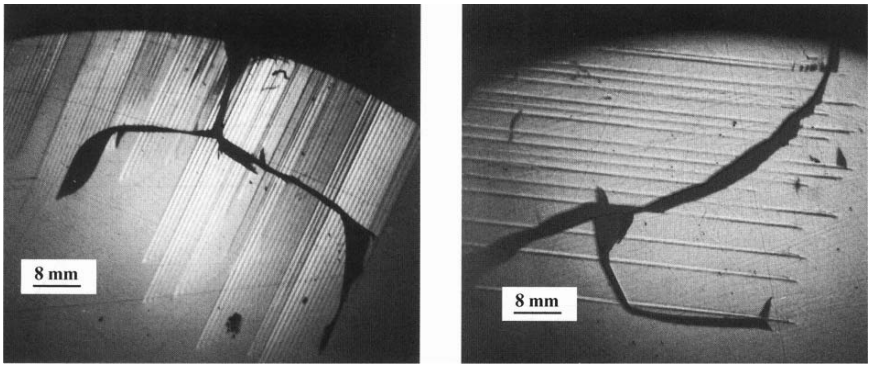

Fig. 7.23. Pattern of twins location in specimen with orientation {0001} (**a**) and $\{11\bar{2}0\}$ (**b**) after testing in melted tin at 550°C

methods of measurement [335, 336] including our own of an indentation technique, give the fracture toughness value K_{1c} or the specific fracture energy $\gamma = K_{1c}^2(1-\mu^2)/2E$, depending on the orientation, from 2 to 4.5 MPa $m^{1/2}$ or 6–22 J m^{-2}, respectively. The highest values relate to the basal plane (0001) and those lowest to the planes (1012), (1014). The fracture toughness of cold-hardened sapphire specimens having residual surface stresses is increased by 20–50% [336]. The specific fracture energy of polycrystalline Al_2O_3 varies unmonotonously with change of grain size from 20 to 100 J m^{-2} [250]. Generally, resistance to the crack propagation in Al_2O_3, as well as in other polycrystals, is noticeably higher than in the monocrystal due to additional resistance of the boundaries of variously oriented grains. Owing to a reduced fracture toughness of the monocrystal, a crack beginning its motion in the tensile zone overcomes the compression zone along more favourably oriented (least energy consuming) planes.

Thermal stress resistance, as well as the strength in a selected load mode, depends on the orientation of the specimen. The ratio between the levels of thermal stress resistance of the cylindrical specimens of batches XVI and XV is similar to the ratio between tensile strength of these batches (Table 7.12). The strength of specimens under uniaxial compression at 20°C is five to seven times greater than the uniaxial tensile strength [53]. The four-point flexure strength of the prismatic specimens having the plane $\{11\bar{2}0\}$ and the direction [0001] parallel to the tension axis, is almost twice greater than the strength of the specimens with the same plane and the direction along $[10\bar{1}0]$ axis [330]. The observable anisotropy of strength and thermal stress resistance of sapphire results from the crystallographic function of the fracture energy γ. The cylinders of batch XV fail under heating test in the main on the rhombohedral planes $\{02\bar{2}1\}$. The cylinders with the basal face surface fail on the prism planes $\{10\bar{1}0\}$.

Table 7.12. Strength of sapphire specimens under three-point flexure and tension

Batch	Number	Temperature (°C)	Dimensions (mm)	Orientation of axis	Loading mode	$\sigma_{\min} - \sigma_{\max}/\sigma_{\mathrm{m}}$ (MPa)	$W = S/\sigma_{\mathrm{m}}$ (%)
I	7	20	$D_{\mathrm{o}} = 4.4;\ l = 40$	[0001]	Flexure	420−570/490	
IV	7	20	$D_{\mathrm{o}} = 3.2;\ l = 40$	[0001]	Flexure	590−840/750	
XV	50	20	$D_{\mathrm{o}} = 13;\ D_{\mathrm{i}} = 9,\ l = 9$	[0001]	Tension	81−801/453	29
XVI	45	20	$D_{\mathrm{o}} = 13;\ D_{\mathrm{i}} = 9,\ l = 9$	$[01\bar{2}1]$	Tension	241−780/533	35
XVII	47	20	$D_{\mathrm{o}} = 13;\ D_{\mathrm{i}} = 9,\ l = 9$	Polycrystal	Tension	121−286/177	21
B	18	20	$4 \times 4 \times 15$	Polycrystal	Flexure	193−478/336	
XX[a]	3	20	$3 \times 3 \times 17$	[0001]	Flexure	800−1330/994	
XX[a]	3	600	$3 \times 3 \times 17$	[0001]	Flexure	316−600/485	
XX[a]	3	1,100	$3 \times 3 \times 17$	[0001]	Flexure	233−632/370	
XX[a]	3	1,650	$3 \times 3 \times 17$	[0001]	Flexure	269−372/314	

W is Variation coefficient, S is the mean-root-square deviation of strength, σ_{m} is the mean arithmetic value of strength
[a]Specimens were ground and then polished up to $R_a = 0.32$, edges chamfered. Tensile plane $\{10\bar{2}0\}$

Examination of the fracture pattern of sapphire from batch XX has shown that macroscopic fracture happens in the basal plane, though local fractures develop on the cleavage planes such as $\{10\bar{1}1\}$, less often on irrational surfaces and boundaries of blocks. The fracture origins are, first of all, surface defects appearing during growth and machining. The diagrams of loading (deformation – flexure) for samples of batch XX are nearly linear up to 1,100°C. Polycrystalline specimens fail mainly on the grain boundaries, only separate large grains fail by cleavage, and the level of their strength is significantly lower than that of monocrystal.

Depending on selected growth modes of monocrystal by Stepanov's method, the strength of as -grown cylindrical specimens varies from 300 to 1,100 MPa. Machining of high-strength samples, as a rule, reduces their strength. Grinding and polishing of as-grown samples with reduced strength provides strengthening due to reduction of defects and inducing of compression stresses in the surface layers (Table 7.12). Indeed, the X-rays [337] showed that 135–170 MPa compression stresses are produced in the surface layers $\leq$15 μm deep, after diamond processing of sapphire.

The thermal stress resistance of sapphire depends also significantly on the sample's surface condition. The thermal stress resistance of cylindrical specimens with as-grown surface (batch IR) is 40% lower than that of the specimens with polished surface (batches IV–VII) of the same crystallographic orientation. The presence of pores in the middle of rods of batch VI ($1-3$ μm size, maximum density 10^4 mm^2) and pores on the surface of specimens in batch VII practically did not influence thermal stress resistance, in comparison with non-porous samples (batches IV–V). In all cases the surface cracks arising in the specimens do not result in total fragmentation, preserving 30% of the initial strength after tests (Table 7.9).

A basic problem of fracture mechanics for thermally loaded bodies consists in determination of their fracture conditions. The tension-induced propagation of a crack in an elastic–brittle body is possible with reaching the critical factor of stress intensity K_{1c}. The subsequent cracking and fracture type are defined by non-uniformity of thermal stress fields [49, 50]. Materials akin to sapphire able to undergo anisotropic plastic deformation under heating are fractured in a more complex way. It becomes necessary to take into account stress relaxation due to twinning and redistribution of stresses through the whole body. The characteristic pattern of fracture of disks is associated with redistribution of thermal–elastic stresses and with strengthening of surface layers as a consequence of twinning under cyclic heating.

The computational evaluations of relaxation processes in thermal stress fields are difficult [16]. The stress relaxation could be assessed more reliably and completely by experimental using the X-ray $\sin^2\psi$ method or by the method of opening a cut in stressed bodies [61].

Features of sapphire fracture in comparison with polycrystalline materials under thermal loading are governed by two circumstances; the capability of deformation by twinning at rather low temperatures of test $\leq$400–500°C

and the fracture toughness anisotropy. Explanation of observable behaviour of cracking and thermal stress resistance with change of sample crystallographic orientation and thermal loading type is based on force fracture mechanics in view of twinning strain and physical differences in cracking in the tension and compression fields. The current models of thermal stress resistance [42, 43], using energetic principles of fracture, neglect the physical difference in cracking behaviour in the tension and compression fields and are not able to adequately describe the cracking behaviour in non-unifom thermal stress fields.

The original method of estimation of thermal stress resistance of single crystals presented in [338] deserves detailed account. The thermal stress resistance of aluminium oxide single crystals (0001), $(11\bar{2}0)$ and $(1\bar{1}02)$ faces of $1.5 \times 3\,\mathrm{cm}^2$ were tested under pulse heating in plasma of varying intensity $\sim 10\,\mu\mathrm{s}$ duration. The peak temperature on the sample surface is determined by measuring the separation Δb between fragments formed by cracks during the cooling stage of the heating–cooling cycle. Relative strain of fragments $\Delta b/b = (T_\mathrm{f} - T_0)$, enabled counting of $T_\mathrm{f} = T_0 + \Delta b/b$, where α is factor of a linear expansion, and T_0 is the initial temperature of a specimen. The critical value of fracture temperature T_f is determined by sequentially diminishing the intensity of a plasma flow, from the melting moment to formation of initial fragments in different points of a specimen. The surface peak temperature and heat flux are continuously reduced from the central hot part of the plasma-affected area in a radial direction.

On the basis of representations of fracture mechanics, the designed thermomechanical model of an estimation of thermal stress resistance in view of anisotropy of thermal, elastic and plastic properties of a crystal is offered.

Temperature deformation diagram (Fig. 7.24) illustrates the process of thermal-mechanical loading. During heating, the sample is under compressive stress until the yield stress σ_Y is reached at the temperature T_Y which corresponds to the brittle-to-ductile transition. On further heating above T_Y the yield stress decreases. Plastic deformation takes place until the peak temperature, T_p, is reached. In the diagram, the yield stress σ_y corresponds to the peak temperature, T_p, reached during the heating stage.

The sample then cools by an amount equal to ΔT_y, relieving the residual compressive stress. Upon further cooling, contraction in the surface layer is restricted by the massive matrix, forming tensile stresses and leading to the initiation of fracture when the tensile stress reaches the fracture stress σ_f. The stress–temperature diagram corresponds to the minimum heating required for the fracture stress to be just reached when the sample is cooled to its initial temperature. In this case the temperature ΔT_b represents the thermal shock resistance parameter.

According to the diagram (Fig. 7.24), ΔT_b consists of the fracture term ΔT_f and the plastic deformation term ΔT_y, so $\Delta T_\mathrm{b} = \Delta T_\mathrm{f} + \Delta T_\mathrm{y}$. Values ΔT_b, ΔT_Y and Δ_f are counted in view of fracture and deformation anisotropy of sapphire (0001), (110) and (102) which are presented for clarity in Fig. 7.25.

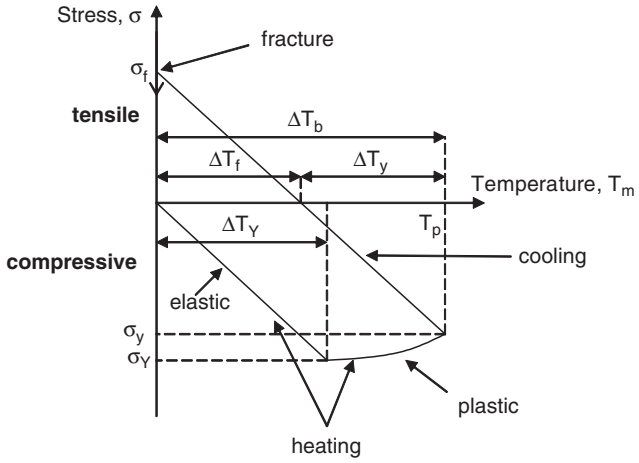

Fig. 7.24. Temperature deformation diagram of a crystal at heating stages of pulsing heat flow and subsequent cooling

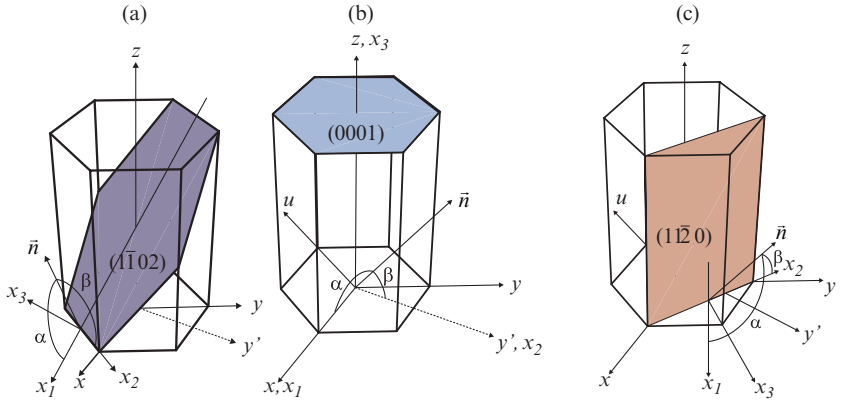

Fig. 7.25. Faces of sapphire crystal under investigation: (**a**) (0001), (**b**) (11$\bar{2}$0) and (**c**) (11$\bar{2}$0); $xy'z$ is the principal coordinate system; $x_1x_2x_3$ is the coordinate system attached to the faces with the x_3-axis normal to them

The thermal stress field is determined using the continuum mechanics approach, which utilizes the stress–strain relations (Hooke's Law) with the temperature term, the equations of equilibrium and the equations of compatibility.

A uniaxial temperature variation $\Delta T(z)$ is produced by the heat flux transferred through the surface $z = 0$ during a short period of time.
The stress field for any face due to the temperature change ΔT, is found:

$$\left.\begin{aligned}\sigma_{11} &= \frac{\alpha_1 S_{26}^2 + (\alpha_2 S_{12} - \alpha_1 S_{22}) S_{66}}{(S_{11}S_{22} - S_{12}^2)S_{66} - S_{11}S_{26}^2}\Delta T,\\ \sigma_{22} &= \frac{(\alpha_1 S_{12} - \alpha_2 S_{11}) S_{66}}{(S_{11}S_{22} - S_{12}^2)S_{66} - S_{11}S_{26}^2}\Delta T,\\ \tau_{12} &= \frac{(\alpha_2 S_{11} - \alpha_1 S_{12}) S_{26}}{(S_{11}S_{22} - S_{12}^2)S_{66} - S_{11}S_{26}^2}\Delta T\end{aligned}\right\}$$

where S_{11} and S_{22} are normal components and S_{12} is the shear component of the stress tensor, S_{ij} are the elastic compliances and $\alpha_1\alpha_2$ are the thermal expansion coefficients. Rhombohedral crystals have six independent elastic constants and two independent expansion coefficients in the principal $xy'z$ coordinate system. Using the tensor transformation equations, the compliances are transformed from the $xy'z$ system into the $x_1x_2x_3$ system for the different faces under investigation.

The shear stress, τ_{ij}, in any slip system is found by transforming the stress tensor:

$$\tau_{ik} = \sigma_{11}\cos\theta\cos\alpha + \sigma_{12}(\cos\alpha\cos\phi + \cos\beta\cos\theta) + \sigma_{22}\cos\beta\cos\phi,$$

where α and β are the angles between the normal to the (0001) plane and the x_1 and x_2 axes, respectively, and θ and ϕ are the angles between the direction of slip and the x_1 and x_2 axes, respectively.

Assuming $\tau_{ik} = \tau_c$, where τ_c is the critical shear stress, the parameter ΔT_y determines the crystal resistance to plastic deformation:

$$\Delta T_y = -\frac{(S_{11}S_{22} - S_{12}^2)S_{66} - S_{11}S_{26}^2}{\left[\begin{array}{c}\left[(\alpha_1 S_{22} - \alpha_2 S_{12})\, S_{66} - \alpha_1 S_{26}^2\right]\cos\phi\cos\alpha\\ -2\,(\alpha_2 S_{11} - \alpha_1 S_{12})\, S_{26}(\cos\alpha\cos\phi + \cos\beta\cos\theta)\\ +\,(\alpha_2 S_{11} - \alpha_1 S_{12})\, S_{66}\cos\beta\cos\phi\end{array}\right]}\tau_c.$$

Fracture is assumed to occur in a particular cleavage plane when the normal stress in that plane reaches the tensile strength, σ_f.

The solution results in the following equation for the fracture resistance parameter, ΔT_f,

$$\Delta T_f = -\frac{(S_{11}S_{22} - S_{12}^2)S_{66} - S_{11}S_{26}^2}{\left[\begin{array}{c}\left[(\alpha_1 S_{22} - \alpha_2 S_{12})\, S_{66} - \alpha_1 S_{26}^2\right]\cos^2\alpha\\ -2\,(\alpha_2 S_{11} - \alpha_1 S_{12})\, S_{26}\cos\alpha\cos\beta\\ +\,(\alpha_2 S_{11} - \alpha_1 S_{12})\, S_{66}\cos^2\beta\end{array}\right]}\sigma_f.$$

The minus sign in this equation indicates that fracture originates under tensile stresses when the temperature is decreased, $\Delta T_f < 0$.

The thermal shock resistance parameter $\Delta T_b = \Delta T_f + \Delta T_y$ is determined in sum of ΔT_f and ΔT_y, calculated by the equations given above. As is well known, plastic deformation of sapphire is produced by a slip in the basal slip system $(0001)\ \langle 11\bar{2}0\rangle$ or in the prism slip system $\{\bar{1}2\bar{1}0\}\ \langle 10\bar{1}0\rangle$.

Table 7.13. Theoretical thermal shock resistance of sapphire

Crystal face	ΔT_{f} (K)	ΔT_{y} (K)	ΔT_{b} (K)
(0001)	706	∞	–
$(11\bar{2}0)$	678	371	1049
$(1\bar{1}02)$	820	32	852

The calculations of the parameter ΔT_{b} is made for the basal slip system which, at temperature above the brittle to ductile transition, has much lower critical shear stress than that for the prism slip system. The resolved shear stress τ_{c} is assumed to be equal to 50 MPa for the basal slip system as measured at 1,000°C, this temperature roughly corresponds to the brittle-to-ductile transition in sapphire [330].

The obtained calculated estimations (Table 7.13) show that the $(11\bar{2}0)$ face is most resistant to fracture since its parameter is bigger than that for other faces. The (0001) face is the most stable face under thermal shock since shear on the prismatic and basis planes is impossible.

The pattern of cleavage of specimens of various orientations changes with peak test temperature. At rather low temperatures, when fragments of fracture are so small that it is possible to measure them only with use of scanning microscopy, cracks are propagated, primarily, on cleavage planes and fracture of specimens (0001) and $(1\bar{1}02)$ becomes preferentially isotropic. At the same time, specimens $(11\bar{2}0)$ retains the anisotropic features of fracture up to higher temperatures that indicate difference of temperature dependences of surface fracture energy and interatomic bonds over different planes and directions of the sapphire crystal.

The thermal stress resistance data for sapphire obtained at heating 500–700°C (Table 7.13), when preferential twinning is possible, nevertheless confirms the greater thermal stress resistance of specimens (0001) in comparison with $(11\bar{2}0)$ specimens.

Plasma local flow radiation of a sapphire surface causes emersion of flaws and accumulations of micro-cracks, sharply reducing thermal stress resistance [339]. Similar decrease of thermal stress resistance at radiation is observed in single crystals MgO and single crystal with orientation (111) possesses greater thermal stress resistance, in comparison with orientation (100) and (110) [340].

8

Elastic–Plastic Deformation Under Local Heating

Surfaces of components in some areas of technology experience continuous or impulsive excitation of the concentrated energy flows (laser radiation, electron beams, ions, etc.) during technological processing or at maintenance or operation [341–343]. The result of such effects is a bodily absorption of heat and origination of temperature fields, stresses and strains which can bring both undesirable deformation of a surface, and modification of its quality. The knowledge of the basic regularity of straining of surface layers in requirements of a beam heating is necessary, for example, at sampling optimum parameters of beam effect with the purpose of the directional modification of properties of a surface, and also in studying the reasons for degradation of laser mirrors [344, 345].

It is impossible to attribute the known regularity of the surface strains, established in the simple way of a mechanical loading (tension, bending, torsion), to all cases of beam effects directly. It is caused not only by the more complex aspect of a stress state and inhomogeneity of temperature and stress fields at a beam loading, but also possible specificity of interaction of a beam with the surface of a material.

Calculation of temperature fields and thermal–elastic stresses in view of the finite size of the simply supported disk at the linear boundary conditions on a cooled surface was conducted using known relationships [71]. Calculations were carried out on the computer in view of the 128 terms in the totals, with an error less than 0.1. The biaxial state of compression stress is realized in a loading spot (Fig. 8.1), thus the maximum values of temperature and stresses in its central band noticeably reduced in directions, both to the edge of a beam and to a surface deep into a specimen.

The radial σ_{r} and tangential stresses are equal in the centre of the loading spot. The relationship of heat flow magnitude to maximum value of the thermal–elastic stresses originating on a surface σ_{rr} for the given conditions of loading is possible to record in the form of

$$q = k\sigma_{\mathrm{rr}}\lambda/\alpha E,$$

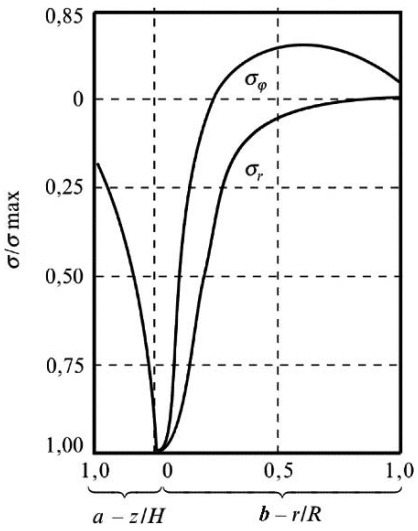

Fig. 8.1. Stress distribution $\sigma/\sigma_{\max}$ of a specimen (diameter −22 mm, width 4 mm) in depth (**a**) and on radius (**b**) at loading spot size $d = 3$ mm

where k is the factor generally depending on conditions of loading and geometry of a specimen; λ, α are, respectively, coefficients of thermal conductivity and linear expansion; E is modulus of elongation.

The strain of a surface originating at beam loading due to a non-uniform field of thermal stresses proceeds in the non-uniform properties of layers. The response of these layers is also non-uniform both in radius, and in depth of radiation zone. The damage band of single crystal Mo (100) at a local beam heating is characterized by strata whose depth and dislocation density are determined by parameters of loading [346]. The radius of a damage band exceeds its depth by 10–15 times and is 2–3 times the size of a radiation spot (Fig. 8.2).

Non-homogeneity of strain on depth of a band is related to deformation habits of surface material layers and depends on the initial state of a surface. Beam affecting results to structural change of surface layers of a material which upset an initial micro-relief since the certain level of a heat flow [347].

The onset of deformation damage of monocrystal bcc-metals (Mo, W) is expressed in emersion of the localized waviness, and in origination of slip tracks whose density is incremented with increase of a heat flow level. As well as in case of mechanical deformation of bcc-crystals, they have the wavy kind caused by simultaneous action of several families of sliding planes. The morphology of sliding traces depends on crystallographic orientations of the chosen plane loading.

Distortion of a surface is caused also by boundary grain deformation on the background of advanced intergrain slidings at beam loading of polycrystalline

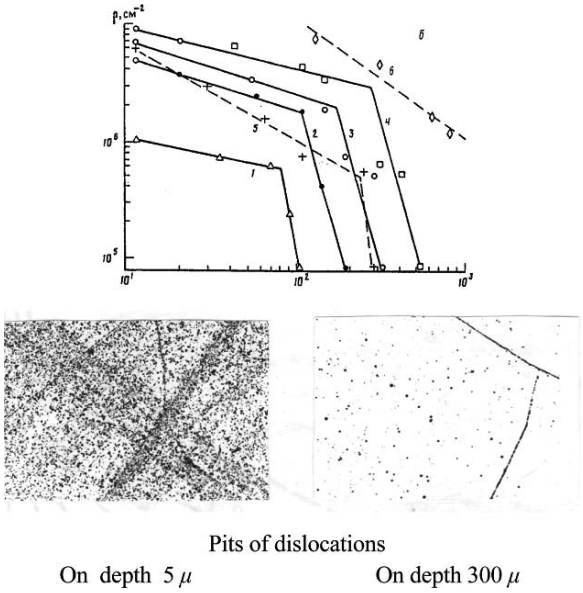

Fig. 8.2. Change of density dislocations ρ in single crystal Mo (100) on depth of the damage band depending on magnitude of a heat flow and a surface state: (1)–(4) electropolishing surface at $q = 0.4$; 1.5; 2.5 and 3.1 kW cm^{-2}, respectively; (5) after mechanical polishing; (6) after mechanical polishing and loading at heat flow $q = 3.2$ kW cm^{-2}

materials. Heterogeneity of deformation of separate grains and different sites of the same grain is characteristic for polycrystals.

A feature of local beam heating of a surface is the constrained character of deformations. Irreversible changes of surface geometry owing to its plastic deformation are observed at achievement of a certain level of thermal flow (Fig. 8.3).

The analysis of the profile record shows that a camber (Fig. 8.4) is observed in the zone of a spot loading. The extent and height of camber $H_{\max}$ increase with growth of a beam flow q and depend on the kind of material and its structural condition.

Occurrence of a deformation surface micro-relief at density of flow q_1 is fixed by the phase contrast method. The height of a surface roughness was within the limits of 0.01–0.03 μm. The beginning of plastic macro-deformation at density of flow q_2 is defined by extrapolation of corresponding dependences (Fig. 8.4) on zero value of camber. Deformation micro-relief is thus already significant, the height of roughness reaches 0.05–0.1 μm. The growth of camber size is determining in surface distortion at further increase of thermal flow level.

The choice of a material's structural condition has great significance. For example, the resistance of copper in deformed and recrystallized conditions

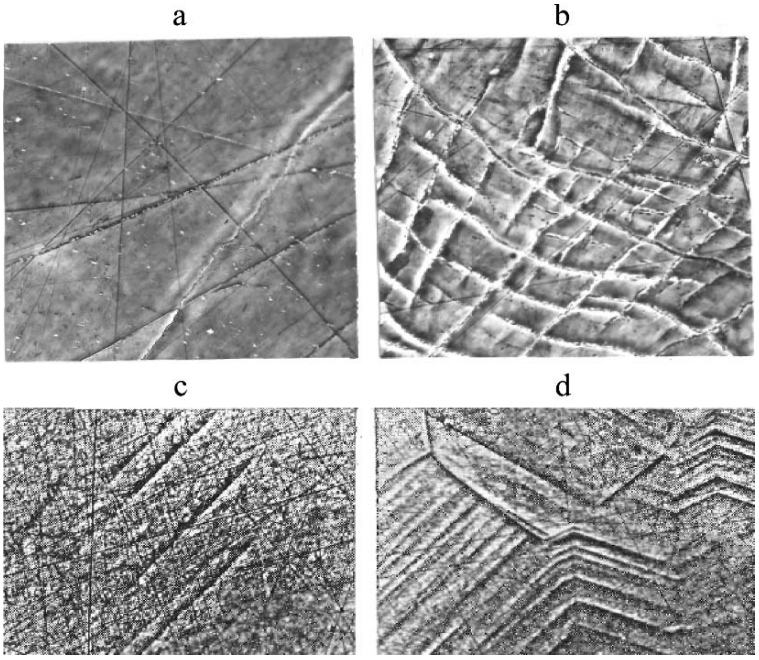

Fig. 8.3. Character of damage development of single crystal Mo (100) (**a**, **b**) and polycrystal of annealed copper (**c**, **d**) with increase of a heat density flux q(kW cm^{-2}): (**a**) 2.3; (**b**) 4.4; (**c**) 1.1; (**d**) 2.4; 120 X

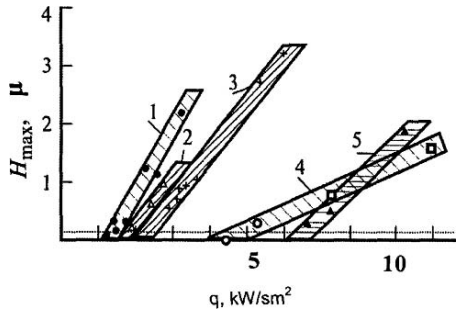

Fig. 8.4. Macroplastic deformation of a material surface depending on level of thermal loading q: (1) monocrystal of molybdenum Mo (111), (2) copper (annealed), (3) monocrystal of tungsten W (111), (4) bronze, (5) copper (deformed)

differs by four times. The received results specify the available opportunities of beam resistance increase of a material surface to examined damages by creation of the structure providing high strength characteristics.

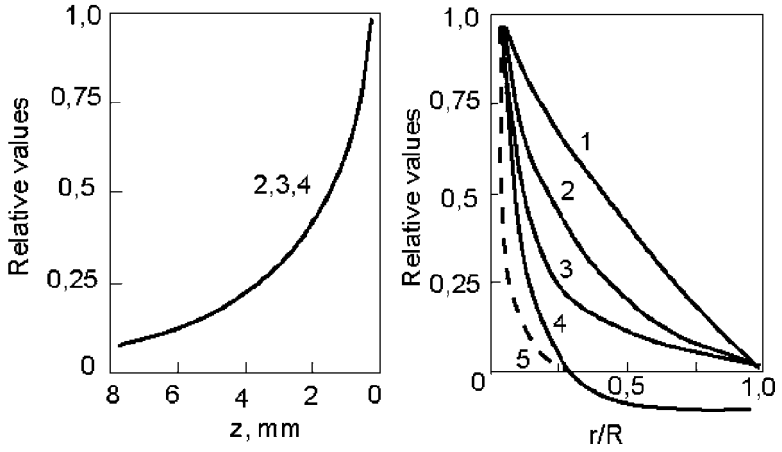

Fig. 8.5. Design values of temperature, stress and normal displacement on an axis (**a**) and on a surface (**b**) of a specimen at local thermal loading. (1) $\omega/\boldsymbol{\omega}_o$; (2) σ_r/σ_o; (3) T/T_0; (4) σ_r/σ_o; (5) q/q_o; $\omega/\boldsymbol{R} = 0.11$; $\boldsymbol{H}/\boldsymbol{R} = 0.32$; $Bio = 4.5$; $\lambda \boldsymbol{T}_0/q_o\omega = 0.60$; $\lambda\sigma_o/\alpha E q_o\omega = 0.28$; $\lambda w/\alpha q_o\omega^2 = 1.01$

Some quantitative laws of macro-plastic deformation of a metal surface in process and after local thermal loading are revealed with the use of holographic interferometer [148].

Changes of sample thickness by two times and more on the order of cooling conditions (Bio), do not influence [181] size and distribution of normal elastic displacement ω on the surface of a sample. Design of ω relative to the disk's boundary is realized in the expression:

$$8\lambda\omega/\alpha(1+\mu)q_0\omega^2 = \ln x/x_1 + E(x_1) - E(x) + [(1-\mu)/(1+\mu)](1-x/x_1)(1-e^{-x1}).$$

Distortion of a distribution profile of normal surface misalignment grows at the increase of thermal flow level and achievement of a yield limit, and more intensively on thin samples (Fig. 8.5).

The maximal values of temperature and stresses designed on the relation of a plain thermal–elasticity problem [149] have been made, respectively, for steel at 190°C and 260 MPa, and for copper at 230°C and 250 MPa. Levels of apparent stresses are close to the known values of a yield limit of materials at these temperatures. The sizes of a zone covered by plastic deformation and whole sample distortions grow with increase of thermal flow. It is natural that less rigid thin samples are deformed more strongly.

From comparison of materials it follows that the distortion of a displacement profile is defined not only by a sample's rigidity but also by higher module of copper hardening (Fig. 8.6).

The residual camber marked in [347], and deflection of a specimen aside, opposite to its position in the loading process, have grown out of the action of the stored plastic deformation. The deflection of a specimen is caused,

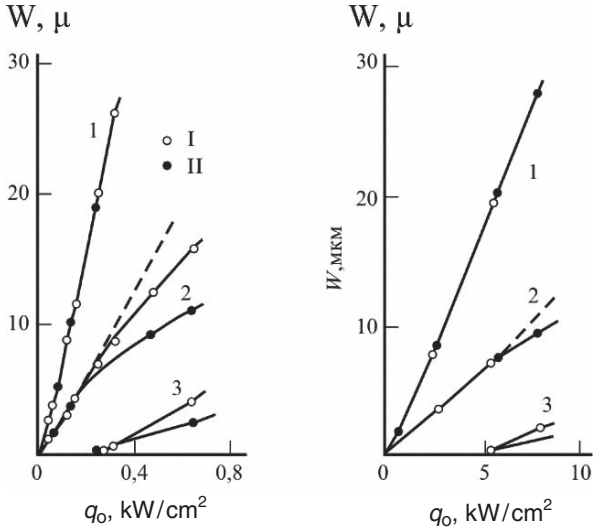

Fig. 8.6. Dependence of normal displacement of surface specimens from steel (**a**) and copper (**b**) on a level of thermal loading. (1) W_o ($r = 0$); (2) W ($r = 0.36H$); (3) W_{rs} (I) 50×8 mm; (II) 50×4 mm

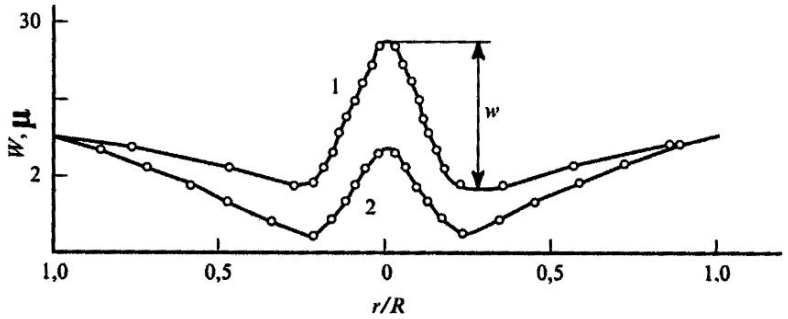

Fig. 8.7. Distribution of residual deformation ω_{rs} on surfaces of sample of steel X18H9T of dimensions 50×8 mm (1) and 50×4 mm (2) after thermal loading $q_o = 0.65\,\mathrm{kW/cm^{-2}}$

apparently, by residual stresses on the sign opposite to working in loading process. It is necessary to note that smaller distortions of a profile displacement in the loading process have led to smaller residual deflection of a sample.

Distribution of the residual displacement on the surface of the specimen in a band of thermal loading (Fig. 8.7) is the same, as well as distribution of displacement under load; only the residual displacement on magnitude is five to seven times less than the relative displacement on coordinate $0.2R$. Design values of temperature on this diameter and a stress in view of the plasticity conditions of Saint–Venant $|\sigma_r - \sigma_\theta|$ [65] are accordingly equal to 330 K and 300 MPa, that is close to the yield stress of a material, and, hence,

the diameter of the residual convexity is determined by the boundary lines of a plasticity band.

An unexpected decrease of the residual convexity height appeared on the thin specimens (compare Fig. 8.7 curves 2 and 1, though, as it is noted above, intensive growth is there on the thin specimen in a band of thermal loading). Apparently, only the solution of the thermal plasticity problem allows explanation of the effect of the residual deformation on the relationship between magnitude of convexity and bending flexure on the specimen's surface. It is necessary to note that extrapolation of the residual convexity height onto an axis q_0 offered in [347] (Fig. 8.6 curve 3) allows us to determine simply enough the threshold values of heat flows with which non-reversible modifications of geometry of a material surface are begun.

Stability of a material's surface, in particular of the surface of mirrors under affecting heat flows, can be established on the basis of deformation emersion from a requirement of yield in the form of Treska [65], according to which the plastic flow begins when the maximum shearing stress will be equal to a predetermined yield threshold, σ_o. The parameter of stability of materials on the basis of emersion of a plastic flow on an optical surface can be expressed as

$$\max \frac{\lambda \sigma_o}{\alpha E}.$$

Geometrical instability of an optical surface is determined by the difference between maximum and minimum displacement values of the mirror subjected

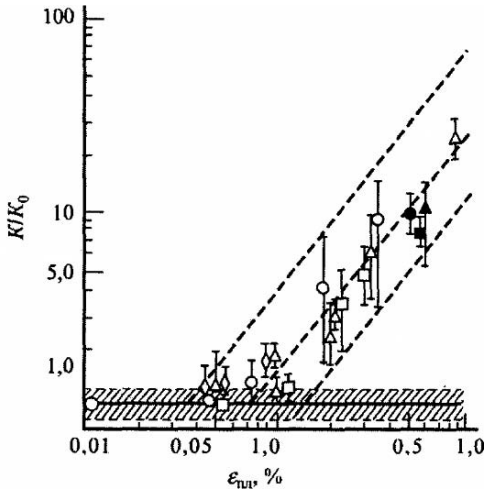

Fig. 8.8. Influence of plastic deformation of a surface mirror on the relative modification of coefficient diffusion dispersion K/K_o under the effect of laser beam (*filled square*)-strained copper, (*filled circle*)-annealed cuprum, (*filled triangle*)-single-crystal molybdenum; (*filled diamond*)-polycrystalline wolfram

to laser effect, i.e. in this case, the difference between values of axial displacement at the centre of the field of a beam spot and on its boundary line. The steady-state value of displacement $\Delta\omega$ can be computed in an explicit aspect [345].

$$\Delta\omega = \frac{\alpha(1+\mu)qR^2}{4\lambda},$$

where α is the coefficient of linear expansion, μ is Poisson's ratio, λ is heat conductivity, q is specific heat flow.

Stability criteria of materials on the basis of the thermal–elastic forming of an optical surface mirror at the continuous operational mode of the laser are expressed:

$$\max \frac{\lambda}{\alpha(1+\mu)}.$$

The parameters obtained permit the comparative analysis of metal optics materials under conditions of knowledge of critical temperature and yield stress, σ_o, exceeding which results in an intolerable decline of optical performances of a mirror (Fig. 8.8).

9

Criteria of Thermal Stress Resistance of Materials

It is possible to select two basic approaches to estimation of thermal stress resistance. The first is guided basically on the perfection of materials. Criteria used for this allow comparison of thermal stress resistance of various materials, to estimate the role and effect of different physical–mechanical characteristics in these measures [25]. The second approach is related to an estimation of bearing capacity of a detail, produced from a certain material.

In the last case, the problem of a finding of regularity change of a bearing capacity is set at a variation of conditions of thermal influence, the form and the dimensions of a body, and its stress state.

9.1 Criteria of Comparative Estimation of Thermal Resistibility of Materials

Existing criteria of resistibility of a material to thermal stresses can be subdivided into three basic groups. Criteria according to which fracture of a body comes at the moment of achievement by thermal stresses of a material strength belong to the first group. Criteria of thermal stress resistance based on energy representations about process of fracture belong to the second group. The third group considers the thermal stress resistance of materials from statistical positions according to which fracture of defective materials comes at the moment of the greatest risk of the failure, determined both by the volume of the loaded body, and the character of distribution of tensile stresses in it.

Having substituted in known formula, $\sigma = \alpha_t E/(1-\mu)\Delta T_m$, limiting the value of the stresses causing fracture (for example, tensile strength), it is possible to receive limiting mean-integrated temperature difference ΔT_m in the body conterminous on value for some forms of a body with the most known criterion [25]:

$$R = \sigma_t(1-\mu)/\alpha_t E.$$

Besides first criterion R, the next criteria can be used

$$R' = \lambda R;\ R'' = aR,$$

which reflects the ability of materials to maintain a thermal flow at stationary or non-stationary thermal influences. The more heat conductivity of the material, λ, and heat diffusivity, a, the greater thermal flow the body is able to sustain without fracture. It is necessary to note that for a choice of more thermally resistant materials used in designs as heat insulators, the estimation by criteria R' and R'' is not applicable. In this case it is necessary to use criterion R as at equal thermal insulation abilities of two materials, the best appears that which is able to sustain the greater temperature difference.

Some criteria of thermal stress resistance are offered in Hasselman's works [348]. So, for an estimation of thermal stress resistance of materials in conditions of non-stationary radiating thermal influence the criterion is entered.

$$R'_{\mathrm{r}} = \{[\sigma_t(1-\mu)\lambda]/\alpha E\varepsilon\}^{1/4}.$$

From which it follows that the less the factor of material blackness ε is integrated; the greater is the thermal stress resistance (at other constant parameters).

Ability of a material to resist to thermal loading at passing relaxation processes due to the creep characterized by coefficient of viscosity η, can be determined by criterion

$$R_{\mathrm{c}} = [\sigma_t(1-\mu)]/(\alpha\eta); \quad R'_{\mathrm{c}} = [\sigma_t(1-\mu)\lambda]/\alpha\eta.$$

Unlike the criterion accepting that fracture has a brittle character, criterion R_{c} and R_{c} define inelasticity on the basis of an elastic–viscous model. The less is the viscosity of material η, and the quicker its relaxation, the greater can be the possible change of temperature difference or a linear heat flux without risk of fracture.

Any criterion of thermal stress resistance at variation of a stressed state should vary similarly to changing of a body's strength at transferring from a tensile loading to bend, torsion, compression, etc. This dependence of a body's thermal stress resistance on stressed state causes complexity of an appropriate choice of strength value at calculation of criterion $R, R', R'', R_{\mathrm{c}}$ on physical–mechanical parameters. Therefore the comparative estimation of thermal stress resistance of materials should be conducted on samples at similarly stressed states, otherwise the variation of values of thermal stress resistance can be caused not by structurally physical parameters, but simply by varied fracture resistance at change of loading kind.

Hasselman put forward a corresponding criterion on the basis of a power view about conditions of crack distribution in thermally loaded bodies

$$R''' = E/[{\sigma_t}^2(1-\mu)]; \quad R'''' = \gamma_{\mathrm{i}}E/{\sigma_t}^2(1-\mu),$$

estimating fracture resistance of materials. According to these criteria, distribution of cracks is defined by a level of potential energy W reserved in a thermally loaded body and the value of the effective surface energy γ_{i} consumed for formation of surface cracks. The less stored energy is necessary for the beginning of a crack movement, and the greater the value of $\gamma_{\mathrm{i},}$, the less is there opportunity for the passage of a crack through the whole section of a body and only partial damage to the body is more probable, with preservation of some part of its bearing capacity.

For an estimation of inelasticity developed in some ceramic refractory, it is reasonable to use the criterion [349] representing the relation of elastic component deformation at the moment of fracture to the general deformation of fracture.

$$R_{\chi} = \sigma(1-\mu)(\chi + 3/4\chi)/\alpha_{\mathrm{t}}E.$$

Unlike the elastic–viscous approach, the estimation of a stressed state at occurrence of a plastic strain in a thermally loaded body can be conducted on the known plasticity criterion, not dependent on time and usually used at mechanical loading of sufficiently ductile bodies. In these cases, for an estimation of thermal stress resistance, it is recommended to use the criterion:

$$R_{\mathrm{p}} = \sigma_{\mathrm{y}}(1-\mu)/(Ea_{\mathrm{t}})$$

in which the ultimate strain is accepted as equal to yield point σ_{y}.

Statistical models assume that fracture at thermal loading is defined not only by values of tensile stresses, but also by body dimensions and character of stress distribution. In a general view the statistical criterion of thermal stress resistance can be presented

$$R^0 = \sigma_{\mathrm{o}}/(E\alpha_{\mathrm{t}})B^{1/m}.$$

The parameter $B = \int_V (\sigma/\sigma_{\mathrm{o}})^m \mathrm{d}V$, characterizes danger of fracture in body volume V; σ is the distribution function of tensile stresses in the volume of a body at the moment of fracture; m and $\boldsymbol{\sigma}_{\mathrm{o}}$ are strength distribution parameters.

The criterion of thermal stress resistance, with use of the statistical parameters considering heterogeneity of stress distribution A at regime factor S and Weibull uniformity of a material with an index m in volume of a body V_0, is offered in [17] as follows:

$$R_{0e} = \frac{\Delta T_{\mathrm{f}} \sqrt[m]{V_0}}{AS},$$

where ΔT_{f} is the temperature difference between surface of a body and the environment at the moment of fracture.

9.2 Criterion of an Estimation of Bearing Capacity of Thermally Loaded Body

The strength of brittle materials at transferring from a uniaxial tension to bend and compression essentially changes; this is caused by features of the kinetics of crack distribution [18, 53]. The thermal stress resistance, as well as strength (Table 9.1) does not represent a constant of a material.

Relative thermal strength $\sigma_{\text{th}}/\sigma_{\text{t}}$ (σ_{th} is level of thermal stresses, and σ_{t} is tensile strength), describing the complete fracture of a body at change of thermal loading kind, is able to change within the limits from 1 to 8–10 [16–18].

It is obvious that for establishment of a criterion for thermal stress resistance on fracture character, it is necessary to enter the quantitative characteristic of heterogeneity of a stressed state of the body, considering not only ratio of the sizes of tensile and compression zones, but also stress distribution in these zones. For this characteristic of heterogeneity of stress field, we can use the serve parameter N [49] proposed in 1973, representing the value of the relation of average value of tensile stresses $\sigma_{\varphi(z)}$ (averaging is made on the considered crack area) to the maximal value of tensile temperature stresses σ_{th} at the moment of body fracture.

For radial cracks in a disk, and also cracks parallel to an axis in a continuous or hollow cylinder with the relation of external and internal radius, $i = R_1/R_2$

$$N = \int \sigma_{\varphi} \mathrm{d}\xi/(1-i)\sigma.$$

For ring cracks in the cylinder

$$N_z = 2\int \sigma_z \xi \mathrm{d}\xi/(1-i^2)\sigma_{\text{t}},$$

where $\xi = r/R_2, i \le \xi \le 1$.

Obviously, for reflection of heterogeneity of a stressed state of a body it is possible to use another similar modification of N.

The numerical calculations executed on data of possible experimental methods have shown that parameter N can change in sufficiently wide limits.

Table 9.1. Influence of various loading kinds on strength of mono-phase ceramics with grain size $d(t = 20^{\circ}\text{C})$

Loading kind	$ZrCc_{0.95}$, $d = 9-20\,\mu$, $P = 7\%$		$ZrH_{1.9}$, $d \cong 150\,\mu$	
	$\overline{\sigma}$ (MPa)	W (%)	$\overline{\sigma}$ (MPa)	W (%)
Tension	80	22.2	44.1	11
Bending	195	22.0	93.1	7
Compression	920	26	196	12
Thermal loading[a]	102	23	68.6	10

[a] Formation of the first crack

So, with use of non-stationary methods of radiating and induction heating, and also heating in liquid environments, the parameter N for the continuous cylinder or a disk can be varied approximately from 0.39 up to 0.83 accordingly at parabolic and sharply non-uniform temperature profile.

The loading under other schema, when the disk or the cylinder heats up on a face surface by electron beam or a plasma nitrogen flow at $N = 0.3$–0.4 causes total fracture. The crack having arisen in a peripheral region at plasma heating of all face surfaces of the cylinder is bent a little in the central zone with compressing stresses, and leaves on a free surface.

Similar values of parameter N at tests by cooling method in liquid environments are accordingly 0.19 and 0.05. Values of parameter N for the continuous cylinder change in a similar way, except that the lower border of an interval of its heating change and upper at cooling are identical and equal 0.25. Change of the hole size i within the limits of from 0.05 to 0.9 allows us to vary the value of parameter N from 0.07 to 0.25 or from 0.37 to 0.26, respectively, at change of a direction of a heat flux, for the external surface of a sample, or inversely. Thus, application of non-stationary methods with stationary ones enables us to capture completely a range of parameter values N from 0.05 to 0.83.

Using all obtained data of materials tests with linear diagrams of fracture, it is possible to position unequivocally value $N < N_c$ when the crack having occurred is able to be braked, having caused only partial decrease in the bearing capacity of a body, while at $N \geq N_c$ the crack leaves on a free surface of the body. The minimal values $N_c = 0.06$, observable at quasi-stationary cooling of an internal aperture of a disk $i = 0.06$, a increasing little bit at non-stationary cooling of the lateral face of a disk up to 0.1, allow us to position values N_c in a limit $0.06 \leq N_c \leq 0.1$.

Increase of the samples sizes in the investigated range and some increase of fracture toughness (for example, zirconium hydride) in comparison with carbides and Al_2O_3 move N_c to an upper bound 0.1 [213]. The offered criterion N_c positioning conditions of fracture, obviously, can be spread to bodies of not axisymmetric form. The criterion may be applied to different materials in the elastic–brittle stage at various levels of strength, including heterogeneous structure materials, such as zirconium carbide with 3–5 wt% of carbon or as silicon carbide with 10 wt% of silicon.

Dependence of fracture stresses in the form of the dimensionless complex $\sigma\sqrt{R}/K_{1c}$ vs. the parameter of heterogeneity N can be plotted (Fig. 9.1) using methods of cooling at $N < N_c$, and methods of heating at $N > N_c$. The factor of stress intensity K_{1c} is defined during thermal loading at equilibrium propagation of a crack; for example, for zirconium carbide it is equal to $3.32\,\mathrm{MPa/m^{-1/2}}$, which practically coincides with the value $K_{1c} = 2.98\,\mathrm{MPa/m^{-1/2}}$, measured by the bend method of a beam with notch. From Fig. 9.1 it is apparent that thermal fracture at small $N \leq 0.05$–0.1 comes at values $\sigma\sqrt{R}/K_{1c}$ exceeding stresses of the start of a crack at achievement K_{1c}, on the average by 8 times for ZrC and by 10 times for ZrC + 3 mass % C.

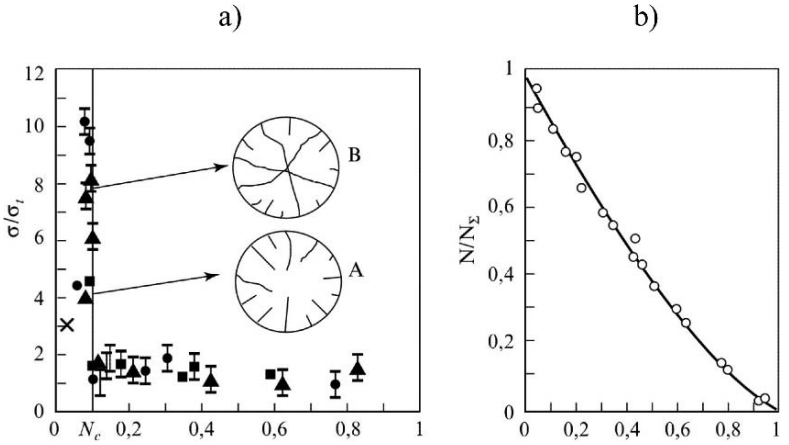

Fig. 9.1. Relative change of limiting values $\sigma\sqrt{R}/K_{1c}$ [24], causing fracture of elastic–brittle materials at change of parameter of heterogeneity N (**a**) where (*filled circle*) ZrC, (*filled triangle*) ZrC + 3 mass % C, (*cross*) SiC-5–10%Si, (*filled square*) Al_2O_3 and relative density of cracks in length l depending on size of relative length of a crack l/R (**b**); where $n_{\sum}$ is total of all cracks

Complete fracture of a disk (on an insert to Fig. 9.1b) becomes possible as a result of merging of the cracks developing towards each other from opposite points. Variation factor $W = \Delta S/\sigma$, in a test of more than 100 cylindrical test pieces 2–3 mm in diameter and 50–100 mm in length of ZrC and ZrC + 3 wt % C, makes, respectively, 20 and 35%. The probability of complete fracture of the disk samples tested by cooling in water at the greatest possible loading in this method, corresponding to value $\sigma\sqrt{R}/K_{1c} = 5$, is rather low (1–2 samples from 100). At levels of loading $\sigma\sqrt{R}/K_{1c} = 2$–4 only (on an insert to Fig. 9.1a), partial fracture of a disk with symmetric system of cracks is possible, the substantiation of which distribution law is presented above. Fracture at $N > N_c$ occurs at relative values $\sigma\sqrt{R}/K_{1c}$ by 1.5–2 times exceeding the relative level of fracture stress at uniaxial tension $N = 1$, similarly to a parity of levels of strength at a mechanical loading by bend and tension.

Fracture levels of the thermal stresses result in complete fragmentations of samples at small $N = 0.05$–0.1, that is, at a stressed state with rather great compression sections appear comparable with fracture stresses of uniaxial mechanical compression of the elastic–brittle body, exceeding by 8–13 times the stress at the beginning of a crack start [18, 213].

Similar examination [350] of development of consecutive cracks in disk samples from heterogeneous materials (basalt and quartzite), water-cooled on the lateral face, have also shown that the complete fragmentation of disks occurs due to merging of radial cracks at loadings exceeding the loadings of the crack's start.

Thus, calculations carried out on principles of force fracture mechanics and experiments on establishment of laws of distribution of cracks in finite-sized

bodies at thermal loadings have allowed us to describe features of distribution of cracks in non-uniform stress fields and to enter parameter N of a stressed state of body, and criterion N_{c}, defining fracture character and level of thermal stress resistance.

It is necessary to consider the history of a loading and the kinetics of fracture, i.e. the influence of intermediate stages of crack development on the final condition of a body, for an estimation of the bearing capacity of a thermally loaded body. The force approach of linear fracture mechanics to thermally loaded bodies, in comparison with existing energy representations, allows describing more fully and more precisely features of crack distribution in non-uniform stress fields. It becomes apparent that the account of redistribution of thermal–elastic stresses in the whole volume of a finite-sized body is necessary so the information on the initial factor of stress intensity in the mouth of a crack appears insufficient on consideration of fracture kinetics.

The criterion proposed should be used even at very high temperatures of a body's operation, up to $0.95T_{\mathrm{ml}}$ if strain rates reach $10^{-1} - 10^{2}\,\mathrm{s}^{-1}$ and, accordingly, change rates of a temperature profile are high: $10^{2} - 10^{4}\,\mathrm{deg\ s}^{-1}$. In these cases the plastic strain and the opportunity for a relaxation are not developed. For the majority of interstitial compounds and oxide systems [14, 15], the necessity to consider stress relaxation of a body becomes possible at temperatures of 0.3–$0.5T_{\mathrm{ml}}$ and loading rates 10^{-1}–$10\,\mathrm{deg\ s}^{-1}$.

The generalized criterion of thermal stress resistance is offered in [16] for cases considering relaxation of thermal stresses. Under condition of the limited temperature strain and uniform heating of a body on ΔT_0, corresponding to value of thermal stress resistance $R = \sigma_{\mathrm{b.}}(1-\mu)/E$, stresses in a body will achieve an ultimate strength. Continuation of heating of a body with some admissible speed V deg s^{-1} will not cause further stress increase owing to a relaxation and the general limited deformation of a body can be presented as follows

$$\alpha\left(\Delta T_0 + \int_0^t V\,\mathrm{d}\tau\right) - (1-\mu)\int_0^t p\,\mathrm{d}\tau - \frac{\sigma_{\mathrm{b}}(1-\mu)}{E} = 0, \tag{9.1}$$

where α is factor of linear expansion, p is creep rate at a stress equal to ultimate strength, ν is factor of transverse creep. After transformations and differentiation we obtain the further admissible heating speed for a yielded material (after creation of temperature difference ΔT_0):

$$V = \frac{p(1-\mu)}{\alpha\left(1 - \frac{\partial R}{\partial T}\right)}. \tag{9.2}$$

We obtain the same at restriction of temperature strain only on one axis:

$$V_* = \frac{p}{\alpha\left(1 - \frac{\partial R_*}{\partial T}\right)}. \tag{9.3}$$

For the majority of ceramic materials, the derivative of criterion R on temperature does not exceed 0.1 therefore value V can be calculated approximately on the formulas

$$V = \frac{p(1-\mu)}{\alpha}, \tag{9.4}$$

$$V_* = \frac{p}{\alpha}. \tag{9.5}$$

As value V depends only on material properties it can be entered into generalized criterion R_n and thus is used at an estimation of thermal resistance of a material in an elastic–viscous condition:

$$R_n = R + V\tau_0, \tag{9.6}$$

where τ_o is time of thermal loading. The value p can be calculated from the known equations of creep substituting values of stresses on ultimate strength

$$p = C\sigma_{\mathrm{b}}^n \exp\left(-\frac{Q}{kT}\right). \tag{9.7}$$

Generalized criterion R_n can be obtained by means of an apparent period of stress relaxation. For a special case, when in expression (9.7) $n = 1$, creep rate

$$p = \frac{\sigma_{\mathrm{b}}}{\eta} = \frac{\sigma_{\mathrm{b}}}{E\tau}, \tag{9.8}$$

where η is a coefficient of viscosity.

Having substituted this value in formulas (9.4) and (9.5), we obtain

$$V \approx \frac{R}{\tau}. \tag{9.9}$$

In the general case when $n \neq 1$, the period of stress relaxation cannot be obtained. Therefore the seeming coefficient of viscosity obtained from the equation is entered

$$p = \frac{\sigma_{\mathrm{b}}}{\eta_K} = C\sigma_{\mathrm{b}}^n \exp\left(-\frac{Q}{kT}\right). \tag{9.10}$$

After transformations the apparent period of stress relaxation:

$$\tau_K = \frac{\eta_K}{E} = \frac{1}{CE\sigma_{\mathrm{b}}^{n-1} \exp\left(-\frac{Q}{kT}\right)}. \tag{9.11}$$

Then there are fair expressions

$$V \approx \frac{R}{\tau_K}, \tag{9.12}$$

And the generalized criterion of thermal stress resistance of an elastic–viscous body becomes

$$R_n = R\left(1 + \frac{\tau_0}{\tau_K}\right), \tag{9.13}$$

At values τ_0/τ_k of less than 0.01, it is practically possible to neglect the influence of a relaxation on thermal stress resistance.

Finishing this chapter about the criterion of thermal stress resistance, it is necessary to note the imperative need for the further theoretical and experimental development of an estimation of bearing capacity for traditional products (refractory of mines, flowing furnaces) and even more importantly, for the elements of designs of the newest areas of technologies operating in extreme conditions of heat, loading rates and aggressive influence of the environment.

This page intentionally blank

10

Ways of Increasing Thermal Stress Resistance of Ceramic Materials

Improvement of the mechanical characteristics of the ceramics possessing limited plasticity in a wide temperature band should be made in view of its operational parameter [365]. For tool materials working in temperature range of brittle failure, the aspiration for rising strength and fracture toughness is ardently expressed and it is related, first of all, to reduction of unsoundness of the materials and creation of structural conditions which increase energy consumptions by fracture [11]. For increasing of thermal stress resistance in this area of temperatures, the methods used, basically, are connected with elimination of structural defects by optimization of modes of compaction and sintering, curing defects, thermal-mechanical programmed hardening, modification of a stressed state of a surface and introduction of a metal binding [352].

For increase of long-term thermal stress resistant characteristics in the temperature area where macro-plastic strain becomes possible, all methods used, as a rule, are applicable for metal materials. Thus in the field of temperatures, where the process of deformation is supervised by movement of dislocations [351], the methods are applied which aspire to complicate dislocation mobility by substructural hardening, doping resulting in formation of stronger chemical bonds in compounds and doping with formation of the second phases. In conditions of loading, where the dominating mechanism of deformation is grain boundary slip at high-temperature creep, an effective method of increase is recrystallization, allowing significantly to reduce the extent of borders due to increase of the grain size. It is necessary to consider using methods of hardening, so that the structural changes directed on increase of mechanical characteristics at high temperatures should not worsen the mechanical characteristics at temperatures $T < T_{\mathrm{bp}}$.

Optimization of Structural Parameters

Optimization of manufacturing modes of powder materials and realization of a certain structural condition [356, 365] promotes increase of a strength

level, fracture toughness and thermal stress resistance. For example, structural regularity of ceramics can be improved by heat treatment of a sintered material by hot isostatic pressing (HIP) at pressure 100–200 MPa and temperatures up to 1,700 K. Such processing, eliminating large pores and healing crack-like defects, allows depressing dispersion of strength and increases strength and fracture toughness in Si_3N_4, up to 600 MPa and 7 MPa $m^{1/2}$ [250].

Optimization of size distribution of the fusion mixture and some additives permits raising thermal stress resistance of materials. So, for example, the thermal stress resistance of samples of MgO [16], sintered from a fusion mixture of mono-fractional composite, with grain growth from 6 up to 2,000 μm, increases by 30%. Thermal stress resistance of the best samples with a polyfractional set of grains is lower than for samples of mono-fractional composite with a coarse grain. Propagation of cracks in coarse-grained samples is more complicated in comparison with a close-grained material, not liable to localization of cracks.

The developed technology for manufacture of silicon carbide by the sublimation method (simultaneous evaporation of a mix of powders of silicon and carbon at high temperature) allows creation of dense preform porosity to 0.3% and coarse grain up to 5,000 μm [61]. Such low porosity allows increasing strength and thermal stress resistance, in comparison with the strength of more porous silicon carbide obtained by the traditional method of reaction sintering.

Increase of thermal stress resistance and corrosion resistance becomes possible by heating of porous preform of silicon carbide in air and formation of the glassy phase SiO_2 enveloping SiC particles [354]. Optimum choice of technological parameters of silicon nitride manufacturing led to formation of ensembles of columned and spherical grains in a combination of fine pores 0.2–0.3 μm in size allowing a sharp increase in thermal stress resistance and strength up to 455 MPa, at porosity of 38% [355]. A new strategy in the technology for preparation of self-hardened alpha-sialons with needle particles of small sizes in a matrix of submicronic sizes has enabled increase of fracture toughness up to 5.1 MPa $m^{1/2}$ and, accordingly, thermal stress resistance.

The vivid example of influence of manufacturing techniques on thermal stress resistance is presented in researches into hydride materials [51, 353]. These materials, with rather limited plasticity, are used in space nuclear reactors as a moderator of neutrons. Structural parameters, such as faulty structure, phase composite, grain size and condition of grains borders, are defining for the thermal stress resistance of hydrides.

The introduction of various modifying additives promoting grain refinement of the hydrides, obtained through saturation by hydrogen of metal preforms improves thermal stress resistance by 1.5 times (Table 10.1). The increase of thermal stress resistance with grain refinement practically without change of chemical hydride composite is connected with reduction of defects at practically invariable fracture toughness. Using methods of powder metallurgy and controlling the sizes of powders fraction it is possible to obtain

Table 10.1. Influence of preparation technology of hydrides and accompanying change of grain size (d) on thermal stress resistance and strength of zirconium and yttrium hydrides

Hydride	$d\,(\mu)$	σ_b (MPa)	σ_c (MPa)	$\gamma\,(\times 10^3\ \mathrm{J\ m^{-2}})$	$\overline{R}$ (K)	R''' (mm)	$R'\,(\times 10^3\ \mathrm{W\ m^{-1}})$
	Heating in tin						
Saturation by hydrogen, $ZrH_{1.85}$	500–1,000	21.6	52.9	30	60	0.7	–
Same, $ZrH_{1.85}$	400	38	76	48	60	0.8	–
Same[a], $ZrH_{1.85}$	300	49	99	47.5	65	0.5	–
Same[a], $ZrH_{1.85}$	150	52	104	32.7	85	0.3	–
Same[a], $ZrH_{1.85}$	70	60	121	38.3	95	0.3	–
	Cooling in water						
Hot extrusion, $ZrH_{1.85}$	40	67	133	–	110	–	–
Same[b], $\perp$, $ZrH_{1.85}$	20	88	176	–	–	1.2	–
Ceramic $ZrH_{1.85}$	50	70	130		105		
Ceramic $YH_{1.95}$	130	29	59		40	22	
Saturation by hydrogen, $YH_{1.95}$	300	22	43	–	30	41	–
Same, $(Zr + 0.1Al)H_{1.85}$	500	–	68	–	65	–	23
Same, $Zr + 0.3\%Cu)H_{1.85}$	600	–	88	–	70	–	2.7
Same, $(Zr + 0.2\%Ni)H_{1.85}$	500	–	83	–	70	–	2.7

[a]Through saturation by hydrogen of metal preforms with modifying additives

[b]Hot extrusion, in a direction perpendicular to axes of extrusion

sintered hydrides preforms with diminished grain size and increased thermal stress resistance. However it is necessary to note that, besides grains, the condition of their borders and the general porosity are changed which has effects on greater scatter of strength and thermal stress resistance. The technology of hot extrusion hydrides results in grain refinement, obtaining the textured anisotropic structure and increasing strength and thermal stress resistance.

Influence on the strength of the more 'fine' structure of a material (an electronic condition, density and distribution of dislocations, vacancies) appears frequently screened. Gadolinium and erbium additives up to 10–15 mass% in solid solution of yttrium practically change in neither thermal stress resistance, nor strength of yttrium hydride. The steady influence of small additives of Al, Qu and Ni up to 0.1–0.3 weights of % on properties ε and δ-phases of zirconium hydride is not observed.

Healing of Cracks

Elimination of superficial scratches and cracks by healing at temperatures $T/T_{\mathrm{ml}} > 0.5$ can improve strength and thermal stress resistance of ceramics noticeably. Researches into crack healing with penetration depth of half of radius length in cylindrical specimens of ZrC have shown an opportunity of complete reduction of strength during some hours of annealing at temperature 2,800 K [357].

There is a shift of crack surfaces at formation of cracks in a body, as a rule, due to residual stresses in the body that result in occurrence of plural contacts between its sides. The appreciable relief of the fracture surface of samples of ZrC is apparent in electron microscopy images. Cracks propagate linearly, being wedged on greater angles (Fig. 10.1) at formation of cleavage steps in a body of grain or at transferring to the next grains in case of intercrystalline fractures. The width of a crack disclosing on local sites noticeably differs from average width (δ_0) depending on drift angle (γ) and extents of a step (I). At $l < \delta_0$ the width of a crack decreases on $l\ \sin\gamma$, in case of $l > \delta_0$ the width of disclosing of a crack is equal to $\delta_0 \cos\gamma$ and, at last, at $\gamma = 90^\circ$ there is a local clamping of the sides of a crack.

Healing is accelerated with increase of the number of contacts at reducing disclosure of the sides of crack δ. Crosspieces are formed at an early stage of annealing between the sides of a crack all along its length, the frequency of their formation increases with reduction of width of the crack disclosing. At

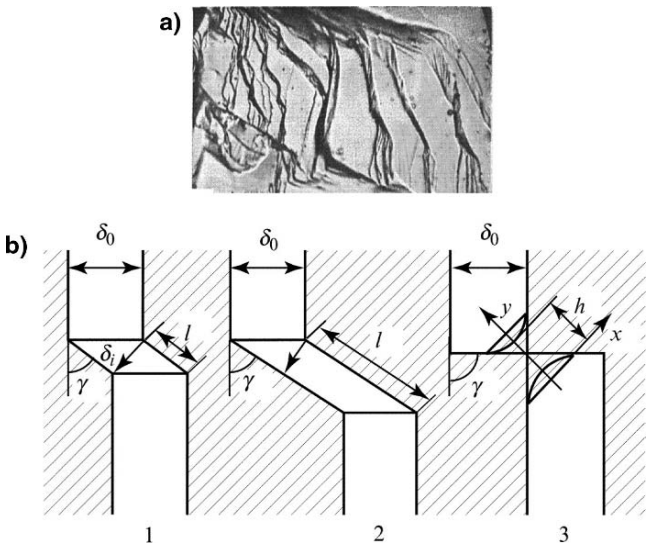

Fig. 10.1. Structure of fracture surface of sample of ZrC (**a**) and the schema of healing of a thermal crack (**b**) (1) $l < \delta_0$; $60^\circ \le \gamma \le 90^\circ$; $\delta_l \le \delta_0 - l\ \sin\gamma$, (2) $l \ge \delta_0$; $60^\circ \le \gamma \le 90^\circ$; $\delta_\mathrm{i} = \delta_0 > l\cos\gamma$; (3) $l = \delta_0$; $\gamma = 90^\circ$; $\delta_\mathrm{i} = \theta$

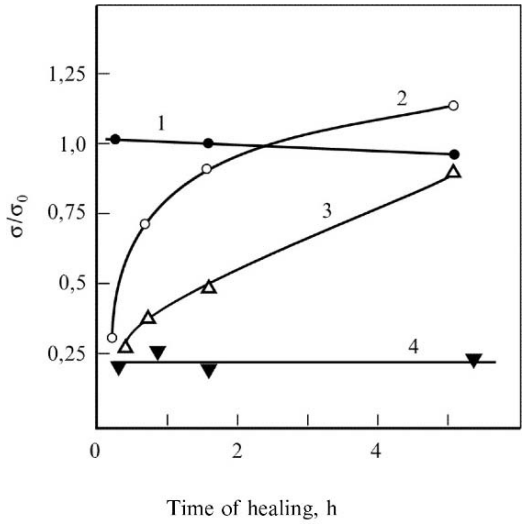

Fig. 10.2. Kinetics of strength reduction of samples of ZrC after healing at temperature 2,800 K with various sizes of disclosing of crack sides: (1) without a crack, (2) 1 μm, (3) 1.5 μm, (4) 3.5 μm

this stage, formation of contacts has the character of islands. The quantity of crosspieces and their extent increases, and the length of unhealed sites decreases in the process of increase of annealing time and/or temperatures. There is an expansion and merging of the separate 'island' contacts.

Healing of cracks with $\delta = 1$–$2\,\mu$m completely comes to an end within some hours of annealing in vacuum at temperature $T/T_{\mathrm{ml}} = 0.6$ and strength rises by 15% above the level of stress of a faultless sample (Fig. 10.2). Cracks with disclosing side $\delta > 3\,\mu$m and a very small number of contacts for the same time are not healed. The application of compression load to samples ($\sigma = 10$ MPa at $T = 2{,}500$ K) intensifies the process of healing, even at the width of a crack disclosing more than 3 μm, and provides reduction of strength in a time period of 0.4 h.

The process of healing is intensified with increase of temperature. The linear relation of healing time vs. temperature in coordinates $\ln\tau - 1/T$ for cracks with various width of disclosing is positioned. These results can be written down in the form of

$$\tau = A\exp(Q/RT),$$

where Q is activation energy of process; R and T have the usual sense; A is the factor depending on width of disclosing of cracks. Activation energy of the recovery process of zirconium carbide strength appears equal to $Q = 95$ kcal mole^{-1} and at this stage is close to the value of the activation energy of surface diffusion.

The kinetics of healing at the temporary stage proceeds rapidly and is caused by formation of contacts with rounded profile, i.e. disappearance of dangerous stress raisers on the joints of crack sides. The dominating mechanism defining kinetics at this stage is a surface diffusion of Zr in ZrC. As a result, the crack is transformed to a system of the self-contained cavities. Their healing in the second, final stages occurs at a lower rate due to the mechanism of diffusive-viscous flow, since surface diffusion only cannot provide reduction of volume of cavities.

Healing of the surface cracks which have formed after polishing of samples of single crystals Al_2O_3 may take place in a vacuum and various environments with use of the graphite container, i.e. creation of a reducing atmosphere near to a material provides steady increase of strength characteristics (Fig. 10.3). Healing of cracks in sapphire in a vacuum occurs due to surface diffusion, similarly to the healing process reported in ZrC.

The environment of annealing renders significant influence on healing. Healing of MgO is retarded in air, in comparison with vacuum, and healing of SiC increases in air. Healing anisotropy rate is observed in single crystals on various planes similarly to change of surface diffusion rates.

The structural condition of a sapphire surface after processing in different environments testifies its chemical interaction with atoms of reducing atmosphere with formation of gaseous reaction products [358]. Characteristically, the heat treatment in carboniferous atmosphere defines the significant development of a relief on a ground surface that, however, does not worsen strength, as the sharp surface cracks healing at annealing is responsible for strength level.

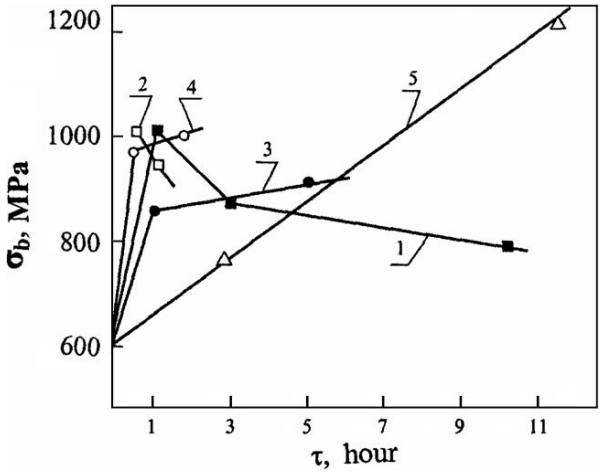

Fig. 10.3. Kinetics of change of sapphire strength at annealing in various environments. (1) 1,900°C, vacuum, (2) 1,900°C, hydrogen, (3) 1,700°C, hydrogen, (4) 1,500°C, air, (5) 1,300°C, carboniferous atmosphere

Table 10.2. Parameters of crack healing up to an initial strength level σ_i

Material		Crack depth (μm)	Conditions		Strength level, σ/σ_i
			T/T_{ml}	(τ) h	
ZrC [357]	poly	100–300	0.76	2	1.0
		5–20	0.76	0.5	1.0
SiC [359, 375]	poly	400	0.6	5	1.0
Al_2O_3 [358]	poly	800	0.85	5	0.85
		5–20	0.85	1	1.0
	mono	1,000–2,000	0.9	6	0.6
		5–20	0.9	1	1.0
MgO [360]	poly	600	0.61	2	1.0
UO_2 [361]	poly	600	0.64	6	1.0

Healing of other oxide and oxygen-free ceramics proceeds similarly to the reported process for ZrC, at quantitatively other parameters of healing defined by the crystal structure of a lattice and the structural condition of the material (Table 10.2).

Quenching Hardening

Another way of strengthening ceramic materials is the formation (in surface layers) of compressive residual stresses preventing the appearance and spreading of cracks. The formation of residual stresses on the surface of a sample or an object is based on relaxation of thermo-elastic stresses non-uniformly distributed along the section [186, 362–365, 381].

As a result of poor ductility of ceramic materials, in contrast to metals, their strengthening is performed at rather small values of *Bio* criteria ($Bio \sim 0.1$), e.g. by blowing off a cold gas stream over the heated sample or by radiation cooling. At higher *Bio* values, the rate of thermal–elastic stress relaxation turns out to be less than the rate of their increase, this leads to cracking. The strengthening of small Sc_2O_3 samples is possible by quenching in silicon oil. The optimal temperature range of refractory strengthening is limited in the lower domain by the temperature of the brittle–ductile transition and in the upper domain by the sintering temperature T_s, excess of which causes undesirable structural changes and decrease in strength [365]. The increase of temperature in the range $T_{bp} < T < T_s$ raises the strengthening effectiveness. The gain in strength of strengthened ceramics is, as a rule, 20–40% (Fig. 10.4). Quenching of polycrystalline samples of Al_2O_3, 2 mm in diameter, in oil at 1,900 K increases strength from 350 up to 700 MPa, and at quenching in air at 2,300 K up to 600 MPa. Quenching samples of Al_2O_3 in water at values $Bio = 0.5$ results in fracture [366].

Creation of compression stresses on the surfaces of a body and increase of critical intensity stress factor K_c, responsible for the beginning of fracture,

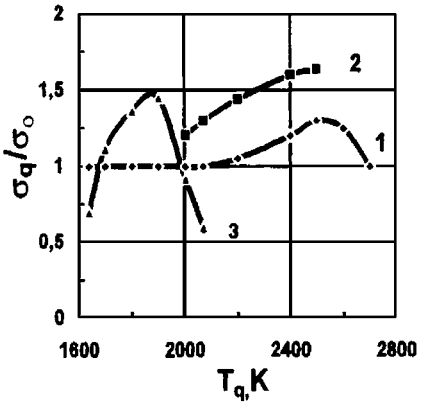

Fig. 10.4. Bending strength change of $ZrC_{0.95}$ (1, 2) and Sc_2O_3 (3) in relation to quenching temperature (T_q) and cooling methods. (1) radiation cooling; (2) gaseous helium flow; (3) cooling in silicon oil

is possible in materials undergoing phase changes as a result of the influence of the external environment or mechanical loading. For example, monoclinic phase ZrO_2 occurs with increased specific volume at surface oxidation of zirconium nitride ceramics at temperatures more than 800 K [367]. As a consequence, the compression stresses arisen on a surface can increase fracture toughness by 30–50%.

The essential hardening of ceramics due to compression stresses is possible at the formation of layers on material surface with different chemical composition, differing on a linear expansion coefficient from those values in the volume of the body. So, formation of calcium aluminates and mullite on the surface of Al_2O_3 results in increase of strength by 40–50% [368], and changes of chemical composition of silicate glasses in surface layers improves strength more than in five times [369].

The air jet quenching technology of the production of glasses allows increasing flexural strength from 30–70 MPa (for mechanically polished plate glasses) up to 100–200 MPa and more. Efficiency of normalizing hardening of glasses depends on their chemical composition, thickness and intensity of cooling. The strength of thick glass plates can be increased up to 200–300 MPa by intensification of air jet cooling. Average values of flexural strength have made 500–700 MPa on the quenched plates with thickness of 15–20 mm in which large residual stresses have been obtained.

The opportunity for further increase of strength of thin tempered glasses has been found in the use of silicon fluids. The strength of the tempered glasses has been increased up to 300–500 MPa and for thin plates (less than 5 mm) even up to 500–700 MPa as a result of application of quenching of fluids with various properties [381].

Etching of the glasses hardened by quenching in solutions of fluoric acid is a rather effective means of additional hardening. Such two-stage processing allows production of tempered glasses with strength of up to 1,000–2,000 MPa and more. It is necessary to note also other ways of hardening glasses, by ionic, neutron bombardment and UV radiation.

Thermo-Mechanical Hardening

Opportunities of thermal-mechanical hardening on single crystals of magnesia have been investigated even in R. Stokis's early works [371].

A decrease in the danger of volumetric defects as stress concentrators in polycrystals by thermal-mechanical processing (TMP), based on stress relaxation near defects due to proceeding of a microplastic strain, is considered in references [365, 370]. TMP at temperatures $T/T_{\mathrm{ml}} > 0.6$, with limited deformation ($\varepsilon < 0.15\%$) and low rates of dynamic deforming $\varepsilon' < 10^{-4}\,\mathrm{s}^{-1}$ (Fig. 10.5a), or at stresses 0.6–0.8 $\sigma/\sigma_{\max}$ and optimum time of static loading (Fig. 10.5b) permits increase in strength of ZrC in a temperature-brittle zone by almost double.

The subsequent annealing without loading at temperatures compared with the temperature at which TMP was conducted, does not remove hardening in the temperature-brittle zone. Similar hardening is observed on brittle-fractured ceramics after TMP at various kinds of loading: bending, tension, torsion, compression, including thermal loading. In the latter case, TMP was conducted by fast heating of a material to temperatures $T/T_{\mathrm{ml}} \geq 0.7$. Necessary thermal stresses for cylindrical sapphire samples 2 mm in diameter are

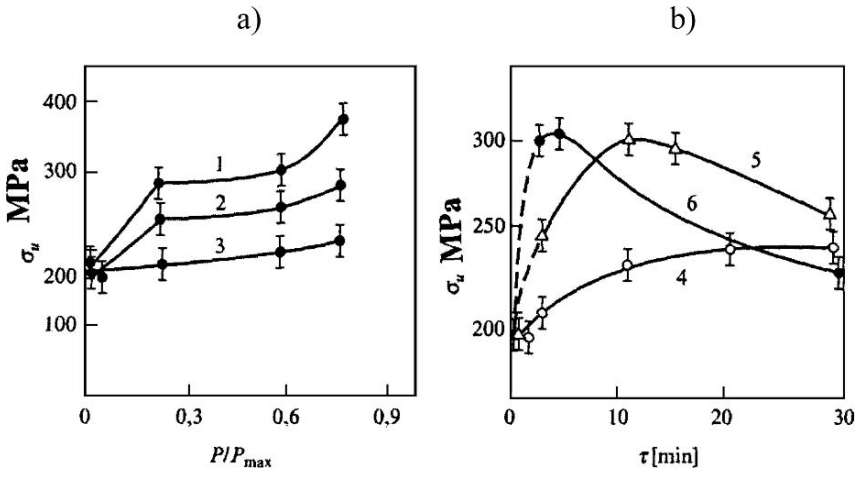

Fig. 10.5. Strength of ZrC at $T = 280\,\mathrm{K}$ after thermal-mechanical processing (TMP) ($T = 2{,}100\,\mathrm{K}, \varepsilon \leq 0.15\%$) on samples loaded with different strain rates (**a**) (1) $\varepsilon' = 10^{-4}\,\mathrm{s}^{-1}$; (2) $\varepsilon' = 10^{-3}\,\mathrm{s}^{-1}$; (3) $\varepsilon' = 10^{-2}\,\mathrm{s}^{-1}$. (**b**) TMP at static loading $T = 2{,}100\,\mathrm{K}$, (4) $\sigma/\sigma_{\max} = 0.3$; (5) $\sigma/\sigma_{\max} = 0.6$; (6) $\sigma/\sigma_{\max} = 0.8$

Table 10.3. Influence of thermal-mechanical processing on strength of cylindrical test-pieces of sapphire 2 mm in diameter with a growth surface [62]. Initial flexural strength 350 MPa

Heating temperature (°C)	Number of samples	Bending strength (MPa)
1,500	3	430, 480, 495
1,600	3	550, 620, 670
1,700	3	890, 915, 990
1,900	3	735, 800, 890
2,000	4	770, 790, 810, 1,220

created by fast input of a sample in heated chamber of induction installation [163]. At temperatures of 1,500–2,000°C on the surface of a sample again 2 mm in diameter, thermal–elastic compression stresses arise at levels of 25–50 Mpa, sufficient for the beginning movements of dislocations σ_c already at temperature 1,500°C and for the weakening of stress concentrations on defects due to relaxation [373].

The time chosen for passing stress relaxation in experiments, possibly, is superfluous. The establishment of minimum necessary exposure time at different temperature levels demands additional experiments.

It is shown in reference [373] that starting stresses found at the start of dislocations in the zone of an indentor imprint for ionic and covalent crystals at temperature 0.55 T_{ml} are at levels of, respectively, 3 and 13 MPa, that is below the stresses which have arisen at TMP. Therefore, after cooling, the strength of samples after TMP increases in 1.5–2 times (Table 10.3). Unlike quenching, hardening of samples at the subsequent isothermal heating is not eliminated.

The opportunity of thermal-mechanical hardening of sapphire is confirmed by experiments with mechanical loading of samples with cracks introduced on the surface [374]. Hardening was conducted at temperatures 1,110–1,160°C, a little exceeding the temperature of a brittle-plastic transferance, but at stresses of 0.5–0.95 from a strength level at 20°C. These experiments (which their authors state are preliminary) and the parameters of TMP used cannot be considered optimal. The maximal hardening is achieved at stresses not exceeding yield point $\sigma_{0,2}$ and at loading rates lower than the relaxation rate of local stresses.

Shot blasting of the surface of mono- and polycrystals of aluminium oxide and silicon nitride by fine solids at ambient temperature raises the density of dislocations and causes formation of subsurface cracks. Micro-cracks are healed with subsequent high-temperature annealing, and dislocations form obviously expressed sub-borders. As a result, fracture toughness of sapphire crystals increases from 1.4 up to 4.0 MPa $m^{1/2}$, and polycrystal Si_3N_4 from 6 up to 15 MPa $m^{1/2}$ [375].

Transformation Hardening

The effect of transformation hardening is based on volume change of crystal lattices of some phases during polymorphic transformation. For similar hardening, as a rule, polymorphism of zirconium dioxide, existing in three crystal modifications (monoclinic, at $T < 1{,}470\,\mathrm{K}$; tetragonal, at $1{,}470\,\mathrm{K} < T < 2{,}670\,\mathrm{K}$; cubic, at 2,670 K) [16] is used, Thus, in sense of transformation hardening, the most applicable phase change of the martensitic type, 'tetragonal-monoclinic', is accompanied with increase in volume of a crystal lattice by 3–5% [250]. Obtained zirconium dioxide solid solutions at stabilization have a rather high factor of thermal expansion owing to which products from completely stabilized zirconium dioxide possess low thermal stress resistance.

The presence of two modifications, cubic (or tetragonal) and monoclinic in products from zirconium dioxide, provide increase of spalling resistance that is related both to decrease in linear expansion and creation of a certain 'micro-fissured' structure.

The mechanism of transformation ceramic hardening, initiated by transformation of tetragonal lattice ZrO_2 into monoclinic, consists of the transformation of elastic energy at vicinities of a crack tip to the superficial energy spent for the origin and branching of micro-cracks. A tendency to depressing temperature of tetragonal-monoclinic transformation is observed with reduction of particle size of zirconium dioxide. It is possible to depress the temperature of tetragonal-monoclinic transformation to a level of ambient temperatures by alloying ZrO_2 with 6–8% CaO, Y_2O_3 or MgO and conducting the special heat treatment, reducing particle size up to 100 nm. Such materials, with the alloying additives practically completely being in tetragonal condition, can possess strength of nearly 800 MPa, fracture toughness up to $12\,\mathrm{MPa\,m^{1/2}}$ and thermal stress resistance increased by three to five times.

We note that the transformation-strengthened ceramic material is defined significantly by parameters of heat treatment and can be used efficiently only at low temperature preserving tetragonal modification [250].

Homogenizing and Recrystallization Annealing

Ceramics prepared by methods of powder metallurgy, as a rule, contain various sorts of impurity. The character of distribution of impurities in the volume of a body defined by previous technologies of preparation can essentially be changed, leading in turn, to change of mechanical characteristics.

Essential influences on the strength of ceramics and the character of fracture are rendered by annealing, as a rule, at temperatures above the temperature of previous sintering. The increase of grain size in oxygen-free and oxide ceramics after the collective recrystallization, with long annealing, more often leads to strength loss of samples, due to the strengthening impurities on the reduced area of grain borders. Fracture becomes mainly inter-crystalline.

The basic motive power of the collective recrystallization is superfluous intercrystalline energy, while primary recrystallization is defined by the volumetric energy reserved by a material at deformation.

Primary recrystallization of ceramics is conducted, also as well as in metals, after a certain critical degree of deformation of 3–7%, but much higher temperatures of annealing (0.7–0.9 T_{ml}) allows grains to grow by two to three orders exceeding their initial size [235]. A high rate of migration of grain borders at primary recrystallization prevents formation of extrinsic segregations on borders and increase of local residual stresses. Therefore strength and thermal stress resistance at temperatures below the temperature of brittle-plastic transferance T_{bp} does not vary with change of grain size, and fracture remains mainly transcrystalline. At the same time, increase of grain size at temperatures $T > T_{\mathrm{bp}}$ increases yield point and improves thermal stress resistance, owing to decreased grain boundary sliding.

Destructive and Non-Destructive Ways of Rejection

With the purpose of exception of the most defective products it is expedient to carry out rejection of faulty components by a preliminary mechanical or thermal loading. The process of mechanical rejection is well known and was used, for example, for rejection of stone wares [377, 378]. However for achievement of a positive effect of rejection, for each kind of a product it is necessary to position the method and a level of loading on the basis of statistical data about distribution of strength in view of possible damageability and economic feasibility [18].

Considering that superficial micro-cracks start to move at stresses σ_{s} equal to 0.5–0.7 of fracture stress σ_{f} at torsion loading of rod stock of ZrC of 2–3 mm in diameter, the level of rejection stresses σ_{r} must be lower than σ_{s}, in order to prevent significant damage to otherwise sound products. Under these conditions of loading, minimal and average values of stress increase and the variation factor decreases. The thermal stress resistance of samples after rejection has increased similarly to their strength values.

In some cases, thermal rejection by means of cooling products in fluid environments after their preliminary heating by a gas burner or in furnaces is easier to carry out than mechanical rejection of products using more complex methods [378]. The low level of the thermal stresses arising at cooling in oil appears insufficient for rejection of brittle samples, while the average level of values ΔT after rejection at cooling in water or spirit has been considerably raised, and the range of distribution values ΔT is narrowed.

Experiments in the use of non-destructive X-ray methods and ultrasonic testing with resolution of 70–100 µm for rejection of defective mono-phase carbide and nitride materials with porosity of 5–10% has not led to practical use as these methods in most cases did not reveal the smallest and acute stress raisers on which fracture of materials occurs.

The method [379] based on measurement of X-ray broadening lines depending on loading, applied to a sample is much more sensitive to defects present in ceramic materials. Samples of carbide materials in the form of plates $2 \times 13 \times 40$ mm were placed in a special attachment to a diffractometer and loaded with a straight bend at stresses σ, down to fracture σ_{f}. Temporary micro-stresses are calculated on change of half-width of X-line from reference state B_0 up to loaded state B.

$$\sigma_\tau = [E_{hkl}(B_2 - B_{02})^{1/2}]/4tg\theta_{hkl},$$

where E_{hkl} is elastic modulus, θ_{hkl} is X-ray line angle.

Curves of strength σ_τ vs. stress have a maximum at fracture stresses $\sigma_\tau^{\mathrm{m}} < \sigma_{\mathrm{f}}$ after which achievement growth of temporary stresses falls down, obviously due to redistribution of local stresses at interaction of defects (Fig. 10.6).

The stronger the growth rate of stresses σ_τ, the more defective were the samples tested and that is lower its strength. The dependence of strength on the parameter of material deficiency, $k = \sigma_\tau^m/\sigma$, where σ_τ^m and σ are, respectively, the maximal values of temporary and applied stresses, shows (Fig. 10.7)

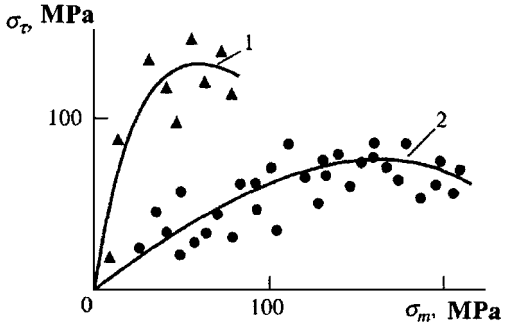

Fig. 10.6. Modification of temporary stresses σ_τ at bending loading of plates of $NbC_{0.96}$ (1) and ZrC (2)

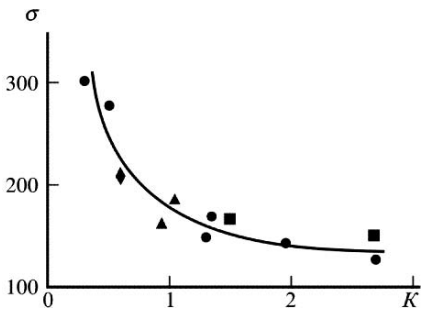

Fig. 10.7. Strength dependence of samples under bending at 20°C: (*filled circle*) ZrC, (*filled triangle*) ZrC + C, (*filled square*) NbC, (*filled diamond*) NbC + C vs. parameter of material deficiency k

the opportunity for use of a method for rejection of defective products without destroying them, operating under action of thermal stresses [379].

The method of acoustic emission is useful for estimation of defectiveness of products in some cases. The intensity of acoustic emission signals increases at a loading of a sample in a range of stresses $\sigma \approx (0.3–0.5)\sigma_f$ and defectiveness is defined on limiting intensity of signals whose level is determined by graduation [380].

A

The General Data on Properties of Constructional Materials

A.1 Structural Condition of Materials

The bases of constructional ceramics are refractory compounds that are oxygen free, and also oxide systems with high melting temperature. For such compounds, mixed ionic–covalent type of interatomic bond and high thermodynamic stability is characteristic. These compounds are characterized by a high degree of hardness, elastic modulus, chemical stability, heat resistance and high brittleness caused by features of interatomic interaction, and low dislocation mobility [14, 15]. Owing to the high structural sensitivity of the compounds, the values of properties, especially strength, are given as averages (Tables A.1 and A.2). Graphite, with low values of hardness and strength and an elastic modulus, has many times higher thermal stress resistance ($R \geq 700^{\circ}$) in comparison with other refractory compounds.

Majority of refractory compounds possess highly symmetrical cubic lattice. Majority of mono-carbides and mono-nitrides crystallize in the FCC lattice of NaCl type, with non-metallic atoms located in octahedral positions. FCC lattice of type CaF_2 is characteristic of UO_2, atoms of oxygen are in tetrahedral positions. Cubic modification of SiC possesses structure of blende ZnS, atoms of silicon are located on units of FCC cell, and atoms of carbon are in half of tetrahedral positions. The presence of numerous polytypes (more than 40) due to kinetic and dislocation features of alternation of atomic layers is characteristic of SiC.

Melting point, elastic properties and factors of thermal expansion are structurally tolerant characteristics and, in essence, they depend on bonding energy, the energy of a crystal lattice necessary for division into separate ions.

The most refractory are carbides, then borides, oxides and nitrides. Series of compounds, for example, boron nitride, Zr, Y hydrides, do not melt and dissociate. The important characteristics for an explanation of processes of creep and sintering of powders of compounds are the diffusion and crystallization phenomena. Diffusivities of metal atoms, as a rule, are below those

Table A.1. Density γ, melting point T_{ml}, linear expansion α, thermal conductivity λ, electric resistance ρ, elastic modulus E, diamond hardness H and bending strength σ_{b} of oxygen-free compounds [15]

Compound	Type of structure	γ ($\mathrm{g\,cm^{-3}}$)	T_{ml} (K)	α ($\times 10^6\,\mathrm{K^{-1}}$)	λ ($\mathrm{W\,m}K^{-1}$)	ρ ($\mu\Omega\,\mathrm{cm}$)	E (GPa)	H (GPa)	σ_{b} (MPa)
α-SiC	hcp	3.17	2,560	4.57	120	1×10^7	460	30	300–450
β-SiC	cube	3.21	–	3.9	–	5×10^8	410	–	260–300
ZrC	cube	6.73	3,690	8.6	30	50	390	27	260–350
NbC	cube	7.8	3,870	7.7	20–30	50	470	20	250–350
UC	cube	12.9	2,500	10.4	18	100	220	9.0	150
ZrB_2	hcp	6.17	3,310	6.6	30	–	495	30	200–300
WC	hcp	15.15	3,020	5.7	35	–	720	20	250–300
$Si_3N_4^-$	α-hcp	α-3.14	4,270	3.0	20–40	10^{19}	313	26	300–700
	β-cube	β-3.28						34	
AlN	hcp	3.12	2,670	5.0	50–60	10^{15}	300	12	250–350
$ZrH_{1.9}$	tetro	5.6	$\sim 2,470$[a]	7.0	30	50	69	0.16	95
YH_2	cube	4.3	$\sim 2,770$[a]	8.0	45	70	135	0.2	30

The mean value of γ, α, λ, ρ, E, H, σ_{b} in temperature range 300–700 K

[a] At pressure of hydrogen 100 MPa

Table A.2. Average values of physical–mechanical characteristics of oxide materials in a temperature band 300–700 K

Compound	Structures type	γ ($\mathrm{g\,cm^{-3}}$)	T_{ml} (K)	α ($\times 10^6\ \mathrm{K^{-1}}$)	λ ($\mathrm{W\,m}K^{-1}$)	ρ ($\mu\Omega\,\mathrm{cm}$)	E (GPa)	H (GPa)	σ_{b} (MPa)
α-Al_2O_3	hcp	α-4.0	2,320	5.8	25	10^{15}	400	24.0	300
ZrO_2	cube.	γ_{c}-5.3	3,150	10.0	2.0	10^5	165	9.0	150
	tetro.$\leq$ 2,360°	γ_{t}-6.1							500
	mono.$\leq$ 1,100°	γ_{m}-5.5							
Y_2O_3	tetro $\leq$ 2,100°	5.03	2,680	13.3	3.5	10^9	138	6.5	150
UO_2	cube	10.97	3,080	10.6	2–5	10^6	230	6.5	180
BeO	α-hcp	3.02	2,840	9–10	25–30	10^{14}	300	10.0	200
SiO_2									
Mullite	romb.	3.18	2,120	5.2	3–5	10^{10}	150		40
$SiO_2 + Al_2O_3$									
MgO	cube	3.58	3,000	13.4	20	–	305	9.0	200
Spinel	cube	3.58	2,420	7.6	3–5	10^{11}	180		50
$MgAl_2O_4$									

of non-metallic atoms by two to three orders, and in oxides by some orders. The presence of structural vacancies in compounds with a deviation from stoichiometry essentially increases diffusion of atoms and affects passing of creep and sintering processes. Processes of diffusion at elevated temperatures appear responsible for processes of healing of surface cracks in products and, therefore, for increases of their strength.

High brittleness of compounds is caused by low dislocation mobility owing to an orientation of bonding, high value of Pierls–Nabarro forces and low rates of multiplication of dislocations. Dislocations submit to the same laws in compounds as in metals. However, in polyatomic compounds with ionic–covalent bonding, more complex geometry of dislocation structure is observed. Dislocation reorganization in ionic compounds with structure NaCl should not disorder the electro-neutrality of a crystal. Sliding in crystals of cubic system proceeds on planes {110}, {111}, {100}, and directions of sliding coincide with the direction in ionic crystals along which charges of one sign ⟨100⟩ lay [381].

Starting stresses of movement of dislocations in crystals with high Pierls barrier are one to two orders greater than in metals. The stresses demand for the yield beginning, in turn, exceed the starting stresses by two orders at moderate temperatures ($0.3\,T_{\mathrm{ml}}$) as the further advance of dislocations after start is defined by interaction with point defects [382, 383]. With temperature rise there are secondary systems of sliding and transverse sliding, owing to high energy of packing defects.

By virtue of limited plasticity, hardness of the majority of the compounds is high. The greatest hardness, up to 35 GPa, is possessed by carbides and borides, while oxides have two to three times lower hardness. Hardness is the characteristic reflecting bonding energy and specificity of structure and consequently is widely used in physical–structural researches. On the other hand, hardness is the deformation characteristic correlating with mechanical characteristics at simple kinds of a loading and is used for an estimation of a product's resistance (for example, the cutting tool).

A.2 Fracture Toughness

Features of ceramics production technology define the kind and character of the structure. For ceramics obtained by methods of powder metallurgy, porosity and micro-cracks located between grains or phase components and interaction between them are common. Micro-cracks in heterogeneous compounds develop due to various linear expansion and elastic characteristics of the matrix and inclusions.

Superficial fracture energy of refractory compounds with mixed ionic–covalent bonding owing to low dislocation mobility is defined basically, by rupture processes of interatomic bonds. Their effective superficial energy γ_{ii} is close to thermodynamic superficial energy, γ_0.

The effective superficial energy representing work, necessary for the formation of a new surface unit in a solid body, contains actually free superficial body energy and the summands connected with features of a plastic strain. The expression for γ_i is usually written in the form

$$\gamma_i = \psi\gamma_0 + \gamma_p + \gamma_s + \gamma_c + \gamma_b,$$

where ψ is the geometrical factor depending on how much true fracture surface differs from the nominal area of section of a sample (ψ = 2–4); γ_p is the energy spent for a micro-plastic strain; γ_s and γ_c are the energy spent for the formation of accompanying cracks and cleavage step and γ_b is the summand for the account of blunt cracks.

Values γ_0, as well as in the case of metal crystals, approach 1 J m^{-2}, and the effective superficial energy of oxide and oxygen-free compounds exceeds γ_0 no more than by ten times.

Effective superficial energy γ_i is defined experimentally on measurement of values K_{1c}:

$$\gamma_i = K_{1c}\sqrt{2E},$$

where E is an elastic modulus. Values γ_i and K_{1c} characterize fracture toughness of materials. For majority of ceramic mono-phase materials, value K_{1c} does not exceed 5 MPa m$^{1/2}$. Change of K_{1c} with temperature, as a rule, is non-monotonic, K_{1c} falls again at temperature rise or remains constant and only with development of plasticity it starts to increase. The value of effective superficial energy is anisotropic, that is found out at test of single crystals so, for example, for a plane (1010) Al_2O_3 γ_i makes 7.3 J m^{-2}, and for a plane (1012) 6 J m^{-2}. Complex influence on effective superficial energy is rendered by the environment. Fracture of single crystals MgO, Al_2O_3 in water proceeds with smaller energy expenses, than fracture in dry air.

Making heterogeneous ceramics by introduction of metal or ceramic particles, whiskers and continuous filaments permits raising considerably the fracture toughness and strength. For example K_{1c} can be increased in alloys WC–Co to 15–20 MPa m$^{1/2}$.

Reinforcement of a matrix by ceramic particles or fibres increases fracture toughness, strength and resistance to cyclic loadings, mainly due to increased forces directed on disclosing of a crack at elongation of fibres and reorientation of a crack at its interaction with borders of the matrix-inclusion. Display of these mechanisms and efficiency of a fracture toughness increase depends on the form and sizes of inclusions, the strength of their bonding with a matrix and the level of residual stresses.

Individual toughening mechanisms including phase transformations, micro-cracking, twinning, ductile reinforcement, fibre/whisker reinforcement and grain bridging are treated thoroughly in [250, 376]. The optimum structure of ZrC with small grain, pore size below 1 μm and medium porosity 8–10% has the maximum K_{1c} = 3.3 MPa m$^{1/2}$ and bending strength near 650 MPa [14, 15]. The K_{1c} of most refractory carbides, nitrides and borides

does not exceed 5 MPa $m^{1/2}$ [15]. The polycrystals based on two modifications of boron nitride with large internal local stresses have extremely high K_{1c} up to 18 MPa $m^{1/2}$ [352]. The composites based on Si_3N_4 with small particles of SiC retain the $K_{1c} = 8$ MPa $m^{1/2}$ at operating temperature up to 1,700 K [250].

Considering the importance of the fracture toughness characteristic in research into thermal stress resistance, we pause for a more detailed consideration of existing measurement methods. For definition of the fracture toughness, K_{1c}, tests of samples with macro-cracks or macro-notches simulating cracks, or with introduction of an indenter, were conducted in [57, 250]. It is believed that the linear-elastic movement of a crack becomes possible at achievement of critical stress intensity K_{1c}, at separation of a crack sites from each other. It is assumed that K_{1c} does not depend on length of a crack and is invariant in relation to the form and the size of a sample, i.e. it can be considered as a property of a material. Standard methods for definition of K_{1c} were developed with reference to metals, as tests of brittle ceramic materials were not always convenient. This is due to the complexity of manufacturing of samples with a cut or with a crack of the set standard form, the great sensitivity of brittle materials to skews and to a number of other methodical factors.

The most effective methods of definition of fracture toughness for brittle materials are the tests in conditions of intermediate instability, when the condition is satisfied:

$$\partial K_1/\partial l < 0 \text{ at } K_I \leq K_{1a} \text{ and } l \geq l_a,$$

i.e. the stress intensity factor (SIF) K_1 is decreased with increase of a crack length to the critical size l_c. Thus the crack jumps to the length l_a, stopping on achievement of the threshold level SIF at unitary loading $K_{1a} < K_{1c}$. This condition is realized at compression of a sample. The further propagation of a crack becomes possible only at achievement of K_{1c} with increase of external loading. Thus, the values K_{1a} and K_{1c} are defined repeatedly on one sample at each jump of a crack [372]. The condition of propagation of a crack $\partial K_1/\partial l < 0$ at $\sigma = \text{const.}$ is practically realized also at indentation of an indenter. Although this method provides researchers with simplicity of tests, accuracy and reliability, measurement of fracture toughness is limited by difficulty of correct definition of true length of micro-cracks at their plural occurrence as during loading, and unloading, and also the complexity of analytical definition of a stress field in a body at indentation.

However in majority of known methods of definition of fracture toughness at tension and bending, the condition of a crack propagation is positioned $\partial K_1/\partial l > 0$ at $\sigma = \text{const.}$, owing to which there is an unceasing avalanche propagation of a crack until complete fracture of the sample into parts, and tests are limited to only one gauging.

An eccentric tension and a two-console loading [250, 372] has been used recently for testing with more convenient condition of a crack propagation $\partial K_1/\partial l = 0$ at $\sigma = \text{const.}$, allowing K_{1c} not to be limited with one measurement at rigid loading in certain range of crack lengths.

Propagation of a crack at axial compression of a flat or disk sample with the central cut located under angle to an axis of loading occurs in conditions of intermediate instability on curvilinear trajectories, asymptotically coming from both tops of a cut to the central axis of loading. The crack trajectory at a complex stressed state in brittle materials is defined by direction of the maximal tension stresses (or K_I), which at any moment of the fracture process operate in a direction perpendicular to trajectories of a crack propagation. Corresponding shear stresses (or K_{II}) are equal to zero [57, 372].

A so-called method of the R-curves, consisting in plotting of dependence of an increment of crack length (l) vs. SIF finds wide application in the practice of researchers for estimation of fracture toughness. As was underlined above, conditions of propagation of cracks $\partial K_1/\partial l = 0$ or $\partial K_1/\partial l < 0$ at $\sigma = \text{const.}$ can be satisfied at certain kinds of a loading, and then a plotting of dependences $K_I = f(l)$ becomes possible. The variation of character of these curves can reflect change of a structural dissipation of energy due to phase changes, micro-cracking fissuring, micro-plasticity, either elastic or inelastic, overlapping of crack sites by bonding bridges, for example by whiskers, fibres, ductile crystals, etc. However, a method of R-curves is not invariant in relation to different kinds of loading, or to the geometrical sizes of tested samples. In particular, even at one chosen kind of a loading, change of relative length of an initial crack can change the kind of R-curves essentially.

Consideration of the influence of the method of manufacturing an initial stress concentrator on gauged value K_{1c} is the important question at a substantiation of methods of definition of fracture toughness.

As a rule, for this purpose, fatigue crack is applied. Making of such a concentrator in known types of samples for brittle materials is rather problematic; therefore notches and sharp cracks are used at measurements. Competency of such replacement is caused, first, by the fact that propagation of cracks in brittle materials, unlike metals, occurs without appreciable plastic strain, resulting in irreversible changes in the field of a crack top, so the requirement of minimization of amplitude SIF at production of an initial crack is not proposed. Second, owing to low fracture toughness of brittle materials at a primary loading of a sample, micro-cracks are formed in length of up to 200 μm on the end of a notch, carrying out the functions of a sharp crack.

Indentation methods are used for definition of fracture toughness at a micro-structural level, when the size of a formed crack is comparable to elements of a micro-structure. Empirical or semi-empirical relation between loading on an indenter and the size of half-disk micro-cracks are used for direct definition K_{1c} on parameters formed at indentation micro-cracks. Some such relations are known. In a general view they can be written down as

$K_{1c} = \chi P c^{-3/2}$, where χ is a factor, P is loading on an indentor, c is radius half-disk crack. In particular, at indentation:

$$K_{1c} = 0.016\,(E/H)^{1/2} P c^{-3/2},$$

where H is Knoop hardness, E is an elastic modulus.

It is necessary to note that fracture toughness fixed on the beam samples and at indentation can differ noticeably, owing to distinction of interaction of macro-notches and micro-cracks with borders of grains.

A.3 Dependences of Strength Change

The strength of ceramics in brittle condition is defined predominantly by the surface and volume defects [15, 250] and alloying with formation of solid solution has practically no influence on the strength. Severe surface relief on sintered ceramic samples or micro-cracks appearing after electro-machining or diamond cutting is responsible for the low strength level [18]. Elimination of these surface defects by mechanical grinding and polishing increases the strength by 50–70% leaving the strength variance practically constant at the expense of volume flaws. The volume defects in the form of large rounded flaws with sizes of 100–400 μm are responsible for 40% of all the cases of fracture in mono-phase ceramics. In some cases, the fracture occurs at lower stress at the cost of zone peculiarities appearing during inhomogeneous forming and subsequent inhomogeneous shrinkage during sintering. These zones in the form of friable porous layers lower the strength by 30–50%. Maximum of strength and T_{bp} is increased by 300–400 K in comparison with ceramics having the same porosity level but without these zones. In most cases, sources of failure of ceramic materials are small cracks faintly visible at the magnification of 1,000 with a radius many orders of magnitude lower than for large pores; so the former are able to cause more dangerous stress concentration.

The availability of pores decreasing the body's cross section clearly reduces the strength. The pore size increased from 3 to 90 μm and emergence of ellipsical pore form at a constant porosity level led to strength reduction of ZrC under bending from 300 to 170 MPa with constant porosity level of 5–7%. The exact influence of porosity on the strength is difficult to determine as in most cases, simultaneously with porosity, other structural parameters are varied: grain size, surface and volume defects and impurity segregation [14].

The strength of ceramics is dispersed in brittle condition in considerably greater degree than the strength of metals. This feature is defined, first of all, by variation of both superficial and volumetric deficiency and lack of stress relaxation on stress concentrators. Dispersion of strength in an engineering practice most often is appreciated by Weibull distribution function:

$$P(\sigma) = 1 - \exp\left\{\int \left[(\sigma - \sigma_n)/\sigma_0\right]^m \mathrm{d}V\right\}; \cdots\cdots \sigma \geq \sigma_n,$$

where σ_n is a stress below which the probability of fracture is equal to zero, irrespective of the dimensions of a body; σ_o is the normalizing parameter; m is the parameter describing uniformity of a material, i.e. degree of distribution uniformity of defects on the body's volume. The distribution of stress estimated on the basis of a bend-and-torsion test of hundreds of samples of Cr_2C_3, ZrC and NbC submits to the normal law and is described conveniently by the Weibull function.

The variation of loading conditions radically altering the strength level has no influence on the variation coefficient $W = S/\sigma$, and Weibull coefficient m (Table A.3), where S is a mean root square strength deviation and σ_m is a mean arithmetic strength value. Between distribution parameters m and W there is a correlation. Comparative tests of large and small sets of samples have shown that reliable enough estimation σ can be obtained from a test of 5–7 samples, and distribution parameters σ_n, W and m on 25–30 samples. The W and m are in the range of 20% and 3–5 respectively for mono-phase dense and porous ceramics. The W value increases by double for hetero-phase carbides with carbon inclusions, owing to damage of carbide matrix.

The strength level of ceramics in brittle condition in most cases depends considerably on the stress state, so while passing from tension to bending and compression the strength increases in relation 1: (1.5–2.0): (8–10) (Table A.3). This phenomenon is associated with the kinetic peculiarities of crack propagation. The start of a crack in tension begins under attainment of critical coefficient of stress intensity K_{1c}, which gives rise to a further avalanche of

Table A.3. Strength variation of refractory compounds at various loading conditions ($T = 280\,\mathrm{K}$)

Kind of sample, material	Stress condition, base (mm)	Test number	$\sigma/\sigma_{min} - \sigma_{max}$ (MPa)	S (MPa)	W (%)	m
Cylinder, ZrC,	I, 80	703	195/105 – 135	43	22.0	4.0
$d = 3$–$4\,\mathrm{mm}$, $P = 7\%$	II, 15	603	217/45 – 345	47	21.7	4.2
$d_g = 9$–$20\,\mu\mathrm{m}$	III, 50	60	80/57 – 129	18	22.2	4.3
	IV, 4	40	97/36 – 158	28	29.3	2.6
	V, 6	36	920/230 – 1240	24	26.0	2.5
Cylinder, $d = 3\,\mathrm{mm}$	I, 80	256	215/45 – 345	56	26.0	3.8
NbC $P = 8\%$, $d_g = 15\,\mu\mathrm{m}$	II, 15	340	210/145 – 375	50	21.1	5.0
ZrC + 5 wt%C, $P = 20\%$, $d_g = 15\,\mu\mathrm{m}$	I, 80	120	85/28 – 220	43	51	2.3
ZrC, $P = 75\%$	VI	35	6.5/2.8 – 8.1	1.3	20.2	
ZrC + 50%NbC, $P = 65\%$	VI	48	9.1/2.3 – 13	2.2	24	
Si_3N_4, $P = 8\%$, $d_g = 5\,\mu\mathrm{m}$	VII, 40	120	244/150 – 380	45.5	18.5	4.8
ZrB_2, $P = 7\%$, $d_g = 15\,\mu\mathrm{m}$	VII, 30	38	265/105 – 360	53.0	20	3.7

(I) four-point bending, (II) torsion, (III) tension, (I–VII) diametrical compression, (V) compression, (VI) hydrostatic tension (hollow cylinder $d = 30$–$50\,\mathrm{mm}$, $\delta = 4\,\mathrm{mm}$, $H = 50\,\mathrm{mm}$), (VII) three-point bending

crack propagation until full body fragmentation. The crack initiated under compression at K_{1c} is able to grow uniformly under increase of continuous load only on a curved trajectory, and tends to take its orientation towards the compression axis. Eventually the transition of equilibrium crack propagation into avalanche crack stage, leading to full fragmentation, is made possible after interaction of equilibrium growth of cracks at loads many times higher than the initial load for crack start. In case of a non-uniform stressed state of a body with compression and tensile sections, for example at body bending, an artificially entered crack (length 100 μm and depth 2–4 μm) is increased again at equilibrium with the length in the superficial extended layers, and then the crack intergrows non-stop through all sections of the body at stresses twice greater than the starting stress. The strength of polycrystalline Al_2O_3 at a biaxial compression loading increases in comparison with axial compression twice, and at a uniaxial tension it drops by 12 times.

With the variation of loading types, changing strength level practically does not influence on variation coefficient. Calculated estimations of a strength change of mono-phase and heterogeneous carbide materials on the Weibull model at transference from tensile to torsion and bending coincide well with experimental data and miss with experiments on 30–50% in a tensile-compression octant. Calculated estimations become absolutely uncertain in octant compression–compression, as accepted by statistical models of strength, the assumption about an instantaneous strength loss at fracture of the weakest part at compression, is not justified.

The scale effect predicted by statistical theories is displayed in all investigated materials in restricted limits, only for small volumes of a body up to 150 mm^3, as at increases in length l from 10 up to 100 mm at a uniform cross section, and at l = const. and variations of the area of section S from 4 up to 20 mm^2. Therefore calculated estimations on the Weibull model for large volumes appear strongly underestimated. It is known that the scale effect is most strongly displayed on whiskers, fine fibres 50–100 μm in diameter, when the sizes of defects (in particular, superficial) are commensurable with the sizes of a body.

It is significant to note that the strength variation parameters of various ceramics in the brittle state are not affected markedly by electron band structure and atomic bonding but are governed primarily by the variation of surface and volume flaws.

Non-monotonic strength dependence on temperature is characteristic for refractory compounds with high resistance level to dislocation mobility. Observing the strength temperature dependencies, one can see that the temperature increase in a wide temperature range does not lead to a considerable change of fracture strength (Fig. A.1a). The strength increases with the development of micro-plasticity and it reaches a maximum value only at the temperature of brittle-plastic transition T_{bp} [18], as a result of thermally activated relaxation of local peak stresses near the structural defects always found in ceramics. The further temperature increase $T > T_{bp}$ causes progression

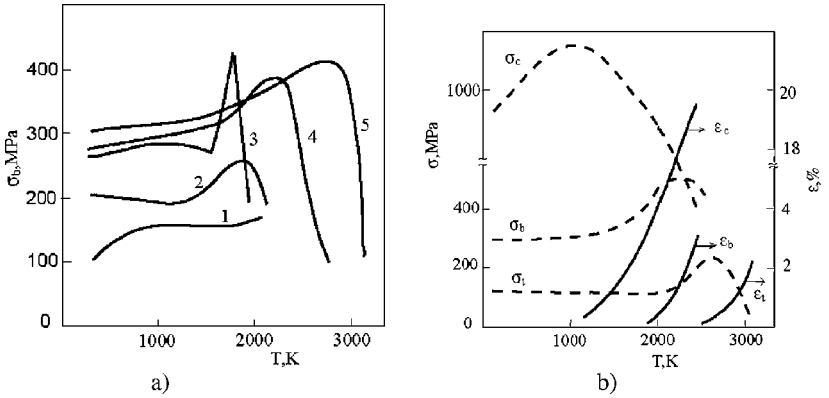

Fig. A.1. Temperature dependence of bending strength of some refractory compounds in vacuum: $1 - Y_2O_3; 2 - Sc_2O_3; 3 - Al_2O_3; 4 - NbC; 5 - NbC + 50\%$ ZrC; (**a**) and dependence of ZrC strength and relative deformation ε_f according to kind of loading: tension σ_e, bending σ_b and compression σ_c with deformation rate $5 \times 10^{-3}\,s^{-1}$ (**b**)

of macro-ductility and a monotonous decrease of yield stress and strength as well as in metals. The fracture of transition metal carbides in the temperature range up to 0.3 T_m occurs transgranularily by cleavage on {100} planes. The rise of temperature increases the inter-granular fracture. The change from tension loading to bending and compression for carbides at the deformation rate $10^{-3}\,s^{-1}$ decreases T_{bdt} from 0.6–0.65, 0.47–0.52 to 0.32–0.4 T_{ml}, respectively, and raises the level of ductile deformation (Fig. A.1b). The transition from tension to compression loads and decrease of deformation rate increases the fraction of inter-granular fracture [14], but a marked drop of strength is observed as a rule only with development of macro-ductility. The availability of non-metal (O_2, N_2, C, Si) and metal (Fe, Co, Ni) additives resulting in phases and eutectics with low-melting point can change the typical curve of temperature strength significantly. An abrupt fall of strength can be seen at moderate temperature or the appearance of two peaks of strength [15].

Departure from the stoichiometry of a refractory compound is accompanied as a rule by strength decrease, which can be observed in titanium carbide, zirconium nitride and zirconium carbide [14]. Observable non-monotonic dependencies of strength in the homogeneous range on times can be associated with the influence of porosity and grain size.

The deformation rate increase from 10^{-3} to $10^{-1}\,s^{-1}$ enhances T_{bp} from 0.55–0.6 to 0.8 T_m for ZrC under tension. The T_{bp} of ceramics changes more (by hundreds of degrees) in comparison with metals while varying the stress state. The T_{bp} decreases to 0.3 T_m at the deformation rate $10^{-5}\,s^{-1}$.

Transition from axial compression to multi-axial compressive loading by intrusion of indenter initiates the ductile deformation in carbides of transition metals even at 80 K [382]. Temperature dependence of micro-hardness reveals

deformation peculiarities undetectable under other kinds of loading. The first bend on the curve of micro-hardness takes into account the transition of gliding system $\{110\}\langle 110\rangle$ to the system $\{111\}\langle 100\rangle$. This is typical for transition metal carbides [14]. The second bend is associated with further development of ductile deformation and disappearance of cracks near indentations. The variation of load on indenter from 200 to 1,000 g changes the temperature of crack disappearance from 800 to 1,400 K.

Observation for changes of elastic distortion and dislocation motion after annealing of carbide samples with indentations at various temperatures permits determination of the starting stress σ_s for dislocation motion and yield stress σ_y [373]. The σ_s for ZrC and other refractory carbides is high in the low temperature range of 0.15–0.3 T_m as in covalent crystals (Ge, Si) with high Pierls stress (intrinsic lattice resistance to dislocation motion). The σ_y is three orders of magnitude higher than the σ_s. This suggests the controlling rate of dislocation generation and dislocation pinning. This value of σ_s for metals is three orders lower than in ZrC and Ge. At temperatures above 0.4 T_m the deformation mechanism changes and the diffusion rate of metal and carbon atoms increases markedly. An active non-conservative motion of dislocations causes the relaxation of local stresses and subsequent decrease of yield stress. Elongated dipoles and dislocation loops disappear and the generation of dislocation networks begins [383]. The further temperature increase up to 0.6 T_m brings into existence the cell appearance. The formation of dislocation in carbides and metals during deformation are very much similar. However the temperature levels for initiation of dislocation motion and formation of cell structure are higher for carbides.

Mechanical characteristics of single crystals with reduced quantity of defects are noticeably above the polycrystals. At the same time, strong anisotropy of properties is displayed. Temperature dependence of bending strength of sapphire essentially changes at change of orientation of a sample (Fig. A.2). This observable distinction is caused by facilitated twinning at compression of sapphire samples oriented parallel to an axis of compression at low temperatures and low stresses [330], in comparison with sliding which becomes possible at greater temperatures and stresses.

The relationship between strength and grain size is rather complicated due to simultaneous variation with grain size of flaws, segregation additives on the grain boundaries and ratio of grain and boundary volumes in ceramics [232]. The primary recrystallization (annealing of material after preliminary deformation) makes it possible to vary the grain size of ZrC in the wide range from 5 up to 2,500 μm without altering the boundary conditions [235]. In this case, the variation of grain size retains carbide strength at 280 K constant while a decrease of strength of ZrC samples is observed after accumulative recrystallization (Fig. A.3). The latter is more common for ceramics, as mentioned in [14, 232]. The yield stress $\sigma_{0.2}$ of ceramics follows Hall–Petch law in the temperature range $0.6 < T > T_{bp}$ [234].

$$\sigma_{0.2} = \sigma_0 + k_y d_g^{-1/2}, \qquad (A_1)$$

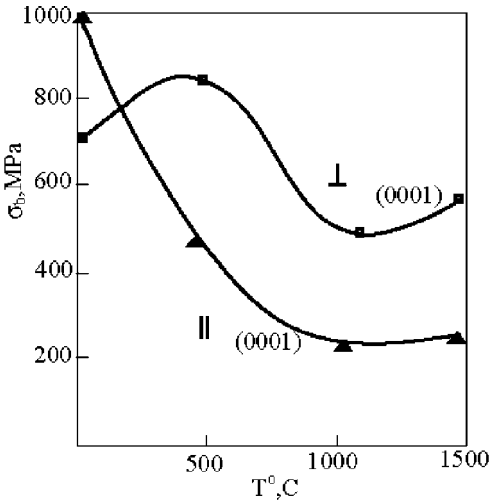

Fig. A.2. Bending strength change of sapphire depending on crystallographic alignment [352]

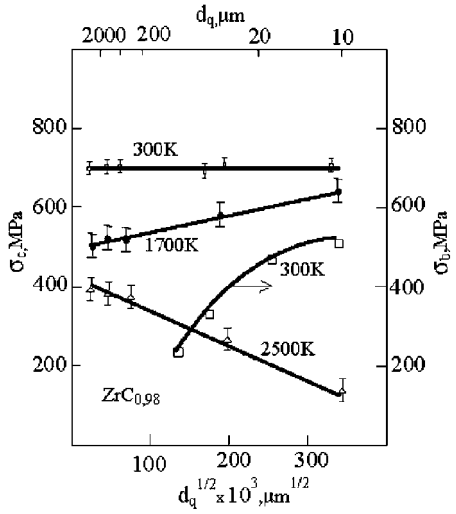

Fig. A.3. Compression strength σ_c for ZrC in vacuum after primary recrystallization and bending strength σ_b for ZrC obtained by accumulative recrystallization against grain size [232]

where σ_0 is the Pierls stress and k_y is the coefficient of deformation resistance through grain boundaries. Relationship (A1) is altered radically at temperatures above $0.6\,T_m$. The yield stress $\sigma_{0.2}$ decreases owing to the grain boundary sliding and rotation of crystals.

Deformation on grain borders as well as inter-grain deformation, develops irregularly. Cavities are formed on joints of grain borders owing to grain boundary sliding and turn of grains as a result of the raised level of local stresses. Fracture is exclusively of the grain boundary in this temperature range. Ceramic materials, unlike metals, possess the increased propensity to grain boundary sliding that is caused, in particular, by presence on grain borders of pores and independence of strength vs. grain size in a low-temperature range.

Silicon and boron carbides, and also silicon, aluminium and zirconium nitrides are resistant enough to oxidizing atmosphere, and strength at heating up to 1,300 K varies weakly at rather short endurances up to 100 h. Oxidizing resistance of these materials drops with increase of open porosity. Mono-phase and hetero-phase systems of oxides Al_2O_3, ZrO_2, BeO, Y_2O_3, MgO [56, 382] are used successfully for long operation of products in oxidizing atmospheres at temperatures up to 1,800 K.

Display of fatigue processes at the cyclic loadings observable in ductile metals is limited in ceramic materials by lack of micro-plastic strains in a wide temperature band down to 0.3–0.5 T_{ml}. At the same time in the polycrystalline ceramics prepared by usual methods of powder metallurgy, owing to thermal anisotropy of expansion and elasticity of crystals, there are always local residual stresses. Therefore, irreversible processes proceed at ceramics loading in the vicinity of a crack: disclosings and displacement of a crack sites in loading cycle, removal of a part of residual stresses and occurrence of residual stresses of a revertive sign in the grains proximate at unloading and crack formation in these places at a repeated loading.

The various variants of cyclic fatigue defining an invariance or decrease or growth, of strength can be realized depending on a ratio of power expenses for formation of a local zone of fracture and energy dissipation at crack propagation. The local mechanism and thus attained effect is defined by structure and deficiency, level of residual stresses, temperature, type and loading parameters. Strength at cyclic loadings of the polycrystals fractured inter-crystalline at rather low temperatures, as a rule, drops at smaller threshold values of SIF, than at static loads. Processes of corrosion reduce cyclic strength. For example, tests on Al_2O_3 in a damp atmosphere or in water reduce static rupture life and, especially, cyclic by 30–50% depending on duration of a loading, stress level and numbers of cycles.

At cyclic loading of ceramic samples of ZrC, SiC, Si_3N_4 in non-aggressive environments at bending, tension or torsion at ambient temperature and loadings making 0.9 from average value of ultimate strength, samples collapse either on the first cycle, or do not fracture for comprehensible time of tests 10^7–10^8 cycles.

The laws of cyclic crack propagation are convenient for investigating conditions of loading of a ceramic sample in the form of a two-console beam, when the SIF K_{I}, at constant external stress σ, does not vary with propagation of a crack, or, especially, at compression of a plate or a disk with a slanting

notch, when the condition for crack propagation is satisfied at $\partial K_{\mathrm{I}}/\partial l < 0$, $\sigma = \mathrm{const}$.

The sample with an initial cut l_0 is statically loaded up to a start stress of a crack at the top of the cut. SIF reaches at this moment the critical value $K_{1\mathrm{c}}$, owing to which the crack makes jump and stops, in view of reduction of SIF up to K_{Ia}, describing condition of crack retardation at single-pass loading. After that the sample is exposed to cyclic deforming with constant stress amplitude. Sub-critical crack velocity is described by:

$$\mathrm{d}l/\mathrm{d}N = a(K_1/K_{1\mathrm{c}})^n,$$

where K_1 is a current stress intensity, $K_{1\mathrm{c}}$ is the fracture toughness, a and n constants depending on type of loading and the environment. $K_{1\mathrm{c}}$ is determined by our developed method under uniaxial compression for plate specimens of ZrC, graphite, silicate glass and aluminium oxide with a central cut at a certain angle to an axis [372, 385]. The crack starts at $K_{1\mathrm{c}}$ and after sporadically increasing in length, stress intensity drops to a lower $K_{1\mathrm{a}}$ value. The subsequent crack growth is possible only at increasing external load, this permits us to multiply determination of the fracture toughness on one specimen. The results of cyclic tests show that the crack propagates even at $K_1 < K_{1\mathrm{a}}$ with velocities of $1\text{–}3 \times 10^{-3}\,\mathrm{mm\ s^{-1}}$. The value $\mathrm{d}l/N$ increases to $1\,\mathrm{mm\ s^{-1}}$ at $K_1 \to K_{1\mathrm{c}}$ with n value in the range 75–89. The observed sub-critical crack growth under compression at room temperature is connected with accumulated localized micro-cracking and crushing of fracture-surface roughness at the unloading stage. Internal local stresses play an important role in the fatigue behaviour of ceramics [21]. The origin of these local stresses depends on heterogeneity of chemical composition, structure and anisotropy of sintered ceramic blanks. Cyclic loading of cylindrical ZrC samples at room temperature

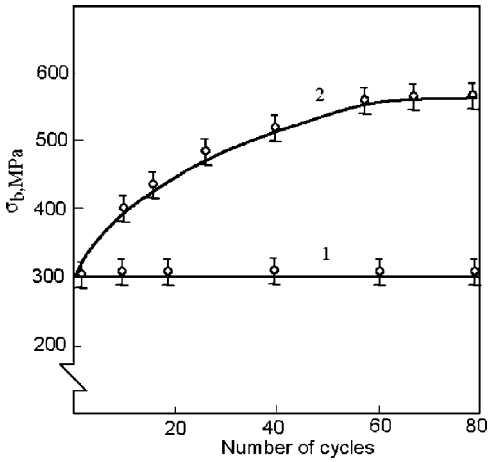

Fig. A.4. Change of the cyclic bending strength σ_{b} under stresses $\sigma_{\max} = 0.8\sigma_{\mathrm{b}}$, $\sigma_{\min} = 0.1\sigma_{\mathrm{b}}$ at 300 K (1) and at 2300 K (2)

does not decrease the strength σ_b under constant bending stresses equal to 0.8–0.9 of the mean σ_b for a number of cycles up to 10^6. The cyclic bending of ZrC samples at temperature above 2,300 K increases the strength because of viscous inter-granular flow and stress relaxation of local stresses (Fig. A4). The growth of a crack induced by stress/corrosion, taking place in aluminum oxide at constant load, especially in wet air at ambient temperatures [56], is not observed in ZrC.

Structural heterogeneity and deficiency of ceramics cause appreciable variation of time and geometrical non-uniformity of crack propagation. The increment of crack length occurs by jumps prepared by processes of structural reorganization of a zone in the crack vicinity. The growing crack undergoes local deviations, both on the surface of a sample, and in its thickness on fracture front.

The kinetics of crack propagation at cyclic compression is limited by conditions of the crack propagation and commensurable with relaxation rate of stresses [384, 385]. The fatigue effect is not displayed naturally, in those cases, when relaxation rate of stresses are essentially below the rise of the stress rate at ambient temperature. At the same time, frictional flow on grain borders and local relaxation of dangerous stresses increase strength at a cyclic loading, when a micro-plastic strain proceeding in overstressed sites of a body becomes possible at elevated temperatures.

So, cyclic strength at bending loading of samples ZrC is increased, when the ratio of maximal stress σ_{max} to yield point $\sigma_{0.2}$ lies within the limits of $0.2 < \sigma_{max}/\sigma_{0.2} \leq 0.5$, and total deformation does not exceed 0.1%. Increase rate of strength is most significant for the first ten cycles, then, at the further cycling, it remains constant. Generally change of frequency and cycle form alter hardening. Strength sharply drops at a cyclic loading, when $\sigma_{max}/\sigma_{0.2} \geq 1$. The cyclic loading at $\sigma_{max}/\sigma_{0.2} = 1.2$ ($T = 2{,}700$ K) with average cycle rate $10^{-3}\,c^{-1}$, resulting in sharp increase of residual deformation from cycle to cycle and fracture on 8–9 cycles at stresses lower on ∼30% than at a unitary loading with the same speed. Fracture occurs at total residual deformation 2.3% in 2.5 times less than at unitary loading.

A.4 Creep and Rupture Life

Laws of creep kinetics inherent to metals are observed also for ceramic materials [382, 386]. In a general view, dependence of creep rate ε' on applied stress σ can be written as:

$$\varepsilon' = \boldsymbol{\sigma}^n (A/L^m)\tau^b \exp(-Q/RT),$$

where L is size of grain, τ is time, Q is activation energy of creep; n, m, b, A are the constants depending both from properties of a material, and from conditions of experience.

Creep rate depends from σ mostly under the linear law in an interval of small stresses of 10–20 MPa at high temperatures of 0.6 T_{ml}. According to this we usually distinguish threshold (i.e. developed at stresses surpassing some stress $\boldsymbol{\sigma} \geq \boldsymbol{\sigma}_{\mathrm{t}}$) and not-threshold creep; the last can be observed at any as much as small σ. Not-threshold creep is carried out by the directed diffusion of atoms and proceeds on the vacancy-diffusion mechanism of Nabarro-Herring. Creep rate is inversely proportional to the square size of grain and in a large degree depends on stoichiometry of the compound (Fig. A.5).

At stresses $\boldsymbol{\sigma} > \boldsymbol{\sigma}_{\mathrm{t}}$ along with diffusive processes, conservative movement of dislocations is initiated. Dependence ε' from σ becomes power mode $\varepsilon' \sim \sigma^{3-4}$ (Fig. A.6) and the inter-granular sliding at the final stage of creep generates micro-porosity on the grain boundaries that causes appreciable decrease of density. Generally creep deformation is caused by passing not one, but several processes (diffusive fluidity, sliding on grain borders, dislocation moving), the contribution of each process depends on conditions of carrying out of experiences (temperature, stress, duration) and structural characteristics of the object.

The instantaneous and unsteady stages of creep are absent in most cases at stresses of greater $\boldsymbol{\sigma}_{\mathrm{t}}$, but smaller yield point $\sigma_{0.2}$. Accumulation of a plastic strain basically occurs at stages of the stationary and accelerated creep, and duration of a final site leaves approximately one-third from the time before fracture. The general accumulated plastic strain during creep

$$\varepsilon = \varepsilon' \tau + \varepsilon_{\mathrm{III}}(\tau),$$

where ε' – creep rate on the stationary stage; $\varepsilon_{\mathrm{III}}$ – deformation on the accelerated stage; τ – time.

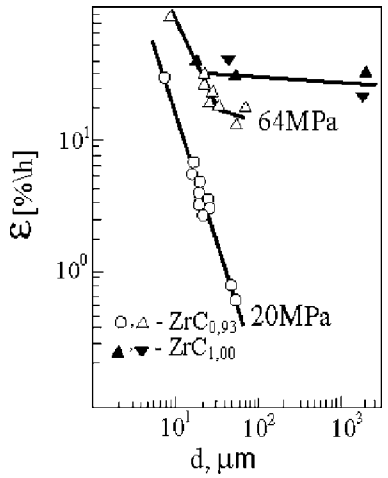

Fig. A.5. Dependence of creep rate of ZrC ($T = 2{,}900$ K) vs. grain size at threshold stress $\sigma_{\mathrm{t}} = 20$ MPa and at stress above threshold

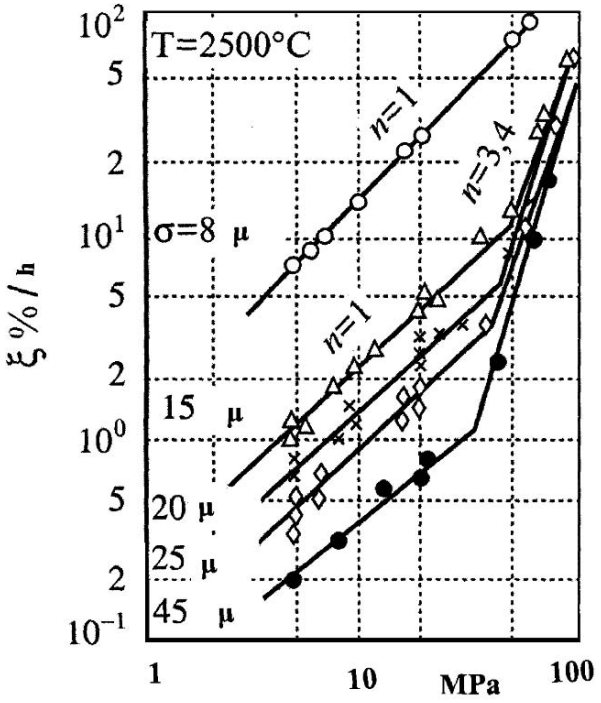

Fig. A.6. Dependence of creep rate of zirconium carbide with various grain size vs. stress

The structure of ceramics changes with increase of creep strain, when agglomeration of micro-pores in the form of chains on borders occur in grains, perpendicular to the action of loading. Structural changes result in change of density and physical properties. Increase of porosity, for example, in beryllium from 1.4 up to 12% raises ε' by two to four times. Generally dependence of creep can be expressed by the empirical expression

$$\varepsilon' \sim (1 - p^{2/3})^{-1} \quad or \quad \varepsilon' \sim (1 - p)^{-3},$$

where p is porosity of a product.

Deformation and creep rupture strongly depend on heterogeneity of a micro-structure and presence of phase components. For example, cluster of grain boundary phases can render double influence: to promote fracture owing to internal stresses, and also to slow down this process because of 'blunting' of a crack top. The last effect is realized in the materials of type SiC–Si containing up to 30 vol% binding phases.

Introduction of less refractory phase in a ceramic matrix resulting in reduction of creep-resistance is considered in detail on alloys WC–Co, with the various contents of Co. In systems of carbides of transitive metals with

graphite, forming an eutectic with melting point lower than the melting points of carbides and graphite, the creep rate of an alloy drops in comparison with ε' of both components.

Small oxide additives variously influence temperature dependence of creep UO_2, the additive of 1% SiO_2 increases ε' and the additive of 0.5% CaO, Y_2O_3 and ZrO_2 reduces ε' almost on order. Aprioristic estimations of an additives influence on ε' are mostly inconvenient, as doping can affect mobility of dislocations and diffusive fluidity, and sliding of grain borders. Formation of solid solutions of transitive metal carbides ZrC–TaC, ZrC–NbC equimolar composites resulting in appreciable decrease of creep rate, due to increase of interatomic-pair bonds.

Time of fracture τ and stationary creep rate ε' are connected with applied stress σ

$$\varepsilon' = A\sigma^n \exp(-Q/RT)$$
$$\tau = B\sigma^{-m} \exp(U/RT)$$

where *A, B, n, m* are constants, Q and U are activation energy of creep and long fracture processes. For carbide materials tested in a temperature band 2,500–3,000 K, activation energy Q and U and exponents n and m of stresses practically coincide. Dependence of rupture life on temperature at the set time base is well described by the Ito–Shishokin equation:

$$\sigma_\tau = C \exp(-\alpha T),$$

where C and α are constants.

A long-held strength σ_l of ceramic therewith decreases with time linearly in most cases and depends on temperature as: $\sigma_\text{l} = C \exp^{Q/RT}$. The failure time τ_f varies with stress as: $\tau_\text{f} = B\sigma^m \exp^{U/RT}$, where C, B are constants and Q, U activation energy in both relationships [382, 386].

The establishment of a stress level at which the material can work reliably in service and under technological processing at high temperatures without fracture is necessary in conditions of creep along with the criterion describing strength properties of a material. The most popular plasticity criterion is a product of the stationary creep rate on fracture time

$$\varepsilon' \tau_\text{p} = \text{const.},$$

where the constant has dimension of deformation. The average ε' on II and III creep stages are mostly used.

The phenomenon of superplasticity in ceramic materials, especially with ultradispersible structure, also as well as in metal alloys, can be observed at temperatures, as a rule, above 0.5 T_ml. For example, nitride–silicon ceramics with ultradispersible structure can be deformed by creep with specific elongation more than 200% at 1,900 K and stress 50 MPa. The main role in superplasticity is played by diffusive processes. Presence of the developed grid of interfaces is one of the indispensable conditions of superplasticity display. However there is no common opinion about the mechanism of superplasticity.

References

1. V.A. Kuznetsov, *Atomic Reactors of Space Power Plant* (Atomizdat, Moscow, 1977), 239p. (in Russian)
2. M.T. Simnad (ed.), Energy Int. J. **16**(1/2), 609 (1991)
3. A.S. Kosolapova (ed.), *Nuclear Rocket Engines* (Norma-form, 2001), 414p. (in Russian)
4. T.S. Liu, A. Tomsett, H. Zhang, Carbon **38**(9), 1401 (2000)
5. IAU, J. Franklin Inst **333A**(2–6), 113–276
6. A.K. Sikder, N. Sikder, J. Hazard Mater. **112**(1–2), 1 (2004)
7. Lee In, Roh Jin Ho, Oh Il-Kwon, in *Proceedings of the 5th Int. Congress on Thermal Stresses and Related Topics. Thermal Stresses 03*, ed. by L. Librescu, P. Marzocca, USA, 2003, vol. 1, KNL 2-1–2-6
8. E.G. Butler, M.H. Lewis, in *Proceedings of the 4th International Symposium on Ceramic Materials and Components for Engines,* Gothenburg, Sweden, June 10–12, 1991, ed. by R. Carlsson, T. Johansson, L. Kahlman. (Elsevier, London, 1992), pp. 32–49
9. J.I. Federer, T.N. Tiegs, *Advances in Ceramics. Vol. 14, Ceramics in Heat Exchangers* (American Ceramic Society, Columbus, OH, 1985), pp. 315–34
10. B. Schwartz, in *Electronic Ceramics—Properties. Devices and Applications,* ed. by L.L. Levinson (Marcel Dekker, New York, 1988), chap. 1, p. 27
11. F. Wayne, S.T. Buljan, J. Am. Ceram. Soc. **72**(5), 754 (1989)
12. V.A. Shmakov, Power Optics 320 (2003) (in Russian)
13. Shatt (ed.), *Powder Metallurgy. Sintered and Composite Materials* (translated under edition. R.A. Andrievskij) (Metallurgy, 1983), 518p. (in Russian)
14. R.A. Andrievsky, A.G. Lanin, G.A. Riamashevsky, *Strength of Refractory Compounds* (Metallurgy, 1974), 232p. (in Russian)
15. R.A. Andrievsky, I.I. Spivak, *Strength of Refractory Compounds* (Metallurgy, 1989), 367p. (in Russian)
16. V.I. Dauknis, K.A. Kazakjavichjus, Pranzkevichus et al., *Research of Spalling Resistance of Refractory Ceramics* (Mintis, Vilnius, 1971). 148p. (in Russian)
17. K.A. Kazakjavichjus, A.A. Janulovichus, *Law of Thermal Fracture Prismatic Bodies* (Mokslas, Vilnius, 1981) 164p. (in Russian)
18. A.G. Lanin, *Strength and Thermal Stress Resistance of Constructional Ceramic* (Moscow State Engineer Physical institute, Moscow, 1998), 111p. (in Russian)
19. Symposium on thermal shock, J. Am. Ceram. Soc. **38**(1), 1 (1955)

20. Symposium on thermal shock, Trans. Br. Ceram. Soc. **57**(10), 591 (1958)
21. G.A. Schneider, G. Petzow (eds.), *Thermal Shock and Thermal Fatigue Behavior of Advanced Ceramics.* Proceedings of the International Conference. Nato ASI Series E: Applied Sciences, vol. 241 (Kluwer, Dordrecht, 1993), 588p
22. Proceedings of International Symposium on Thermal Stresses and Related Topics, Hamamatsu, Japan, 5–7 June 1995
23. Bradt, Hasselman (eds.), in *Proceedings of Sixth International Symposium on Fracture Mechanics of Ceramic,* vol. II, Karlsruhe, Germany, 18–20 July 1995 (Plenum, New York, 1996), 670p.
24. Proceedings of 7th Intern. Symposium on Fracture Mechanics of Ceramics FMC'99, vol. 13 (Kluwer, Dordrecht, 2002), 527p
25. W.D. Kingery, *Properties Measurement at High Temperature* (Wiley, New York, 1959), 465p.
26. Pisarenko, V.N. Rudenko, G.N. Tretjachenko et al., *Strength of Materials at High Temperature* (Naukova Dumka, Kiev, 1966), 791p. (in Russian)
27. S.S. Manson, *Thermal Stress and Low-Cycle Fatique* (McGraw-Hill, New York, 1970), p. 344
28. *Non-Metallic Constructional Materials,* vols. 2–4 (Mashinosroenie, 2005), 464p. (in Russian)
29. A. Lanin, V.B. Feodorov, V.S. Egorov, Thermal Phys. High Temp. **6**, 865 (1966) (in Russian)
30. H. Wang, R. Singh, Int. Mater. Rev. **39**(6), 228 (1994)
31. A.G. Lanin, Ind. Lab. **64**(3), 168 (1998)
32. E. Glenny, M.G. Royston, Trans. Brit. Cer. Soc. **57**, 645 (1958)
33. W.B. Crandall, J. Ging, J. Am. Cer. Soc. **38**(1), 44 (1955)
34. G.R. Irwin, *Handbuch der Physik,* vol. 6 (Springer, Berlin, 1958)
35. M. Fellner, P. Supanic, Key Eng. Mater. **223**, 97 (2002)
36. S.S. Manson, R.W. Smith, J. Am. Ceram. Soc. **38**(1), 18 (1955)
37. S.D. Volkov, *Statistical Theory of Strength* (Mashgiz, 1960), 175p. (in Russian)
38. D.M. Shur, in *Strength of Materials* (Plenum, New York, 1972)
39. V.I. Melkin, D.M. Shur, V.S. Egorov et al., Mashinostroenie **2**, (1970) (in Russian)
40. D.P.H. Hasselman, J. Am. Ceram. Soc. **46**(11), 535 (1963)
41. D.P.H. Hasselman, J. Am. Ceram. Soc. **52**(11), 600 (1969)
42. H. Bahr, H.J. Weis et al., in *Current Topics in Material Science*, ed. by E. Kaldis (North Holland, Amsterdam, 1985), pp. 317–359
43. H.A. Bahr, U. Bahr, H. Balke et al., in *Thermal Shock and Thermal Fatigue Behavior of Advanced Ceramics*, ed. by G.A. Schneider, G. Petzow. Nato ASI Series E: Applied Sciences, vol. 241 (Kluwer, Dordrecht, 1993), pp. 143–153
44. G.A. Schneider, in *7th CIMTIC World Ceramics Congress*, Montecatini Terme, Italy, June 1990
45. G.T.M. Stam, Giessen E. van der, P. Meijers, Int. J. Sol. Struct. **31**, 1923 (1994)
46. C.S. Yu, D.K. Shetty, M.C. Shaw, D.B. Marshall, J. Am. Ceram. Soc. **75**, 2991 (1992)
47. G. Rauchs, D. Munz, T. Fett, in *Fracture Mechanics of Ceramics*, vol. 13, ed. by R.C. Bradt et al. (Kluwer/Plenum, New York/New York, 2002), pp. 1–8
48. T. Fett, D. Munz, G. Thun, H.A. Bahr, J. Am. Ceram. Soc. **78**(4), 949 (1995)

49. A.G. Lanin, V.V. Borunov, V.S. Egorov, V.P. Popov, *Fracture of the Cylindrical Bodies from Brittle Materials at a Thermal Loading* (Plenum, New York, 1973) Strength of Materials
50. V.S. Egorov, A.G. Lanin, I.I. Fedik, *Fracture of Thermally Loaded Disks from the Elastic–Brittle Materials* (Plenum, New York, 1981) Strength of Materials, pp. 183–189
51. A.G. Lanin, in *Thermal Shock and Thermal Fatigue Behavior of Advanced Ceramics*, ed. by G.A. Schneider, G. Petzow. Nato ASI Series E: Applied Sciences, vol. 241 (Kluwer, Dordrecht, 1993), pp. 523–529
52. A.G. Lanin, V.S. Egorov, in *Proceedings of 7th Intern. Symposium on Fracture Mechanics of Ceramics FMC'99*, Moscow (Kluver, Netherlands, 2001), pp. 395–411
53. A.G. Lanin, N.A. Bochkov, V.S. Egorov, B.A. Sokolov, Fracture of materials in a brittle condition at compression (Plenum, New York, 1986) Strength of Materials, pp. 1274–1278
54. M.F. Ashby, S.D. Hallam, Acta metal. **34**(4), 497 (1986)
55. C.G. Sammis, M.F. Ashby, Acta metal. **34**(4), 511 (1986)
56. A.G. Lanin, V.A. Sorolov, V.S. Egorov, (Plenum, New York, 1984) Strength of Materials
57. G.A. Gogozi, Powder Metallurgy **7–8**, 55 (2004)
58. A.G. Lanin, V.P. Popov, N.A. Bochkov, Fracture of ceramic materials at local thermal loading. (Plenum, New York, 1986) Strength of Materials
59. A.G. Lanin, V.P. Popov, N.A. Bochkov, Fracture of silicon carbide at local thermal loading. (Plenum, New York, 1990) Strength of Materials
60. A.G. Lanin, V.S. Egorov, Phys. Chem. Process. Mater. **2**, 78 (1999) (in Russian)
61. A.G. Lanin, I.I. Deryavko, J. Eur. Ceram. Soc. **20**, 209 (2000)
62. A.G. Lanin, E.L. Muravin, V.P. Popov, V.N. Turchin, J. Eur. Ceram. Soc. **23**(3), 455 (2003)
63. C.P. Demidov, M. Vyashaya Shcola, Elastic theory 1979, 432p. (in Russian)
64. N.N. Malinin, *Applied Theory of Plasticity and Creep* (Nauka, 1975), 399p. (in Russian)
65. *Dynamics and Machines Strength*, vols. 1–3, book 1 (*The Encyclopedia Mechanical Engineering*, 1995), 430p. (in Russian)
66. V.V. Panasjuk, A.E. Andrejkiv, V.Z. Parton, in *Mechanics of Fracture and Strength of Materials* (Naykova Dumka, Kiev, 1988), Handbook in 4 volumes (in Russian)
67. B. Boly, J.H. Weiner, *Theory of Thermal Stresses* (Wiley, New York, 1960) p. 517
68. A.V. Lykov, M. Vyashaya Shcola, *Theory of Thermal Conductivity*. 596 (1967) (in Russian)
69. I.I. Fedik, V.S. Kolesov, V.N. Michailov, *Temperature Profiles and Thermal Stresses*. Theory of thermal conductivity (Energotomizdat, 1985), 280p. (in Russian)
70. A.I. Pehovich, V.M. Zhydkich, *Calculation of Thermal Conditions of Solid Bodies* (Energy, Leningrad, 1968), p. 240 (in Russian)
71. A.D. Kovalenko, *Basis of Thermal-Elasticity* (Naykova Dumka, Kiev, 1970), p. 180 (in Russian)
72. N.J. Tajtz, *Technology of Heating of Steel*. (Publishing house of the literature on black and nonferrous metallurgy, Moscow, 1962), p. 566 (in Russian)

73. M. Kalyon, B.S. Yilbas, Proc. Inst. Mech. Eng. C J. Mech. Eng. Sci. **215**(12), 1429 (2001)
74. H. Awaji, T. Takahashi, N. Yamamoto, T. Nishikawa, J. Ceram. Soc. Jpn. **106**(4), 358 (1998)
75. N. Noda, in *Thermal Shock and Thermal Fatigue Behavior of Advanced Ceramics*, ed. by G.A. Schneider, G. Petzow. Nato ASI Series E: Applied Sciences, vol. 241 (Kluwer, Dordrecht, 1993), pp. 15–26
76. Thermal stress resistance of machine's details. Eds. I.A. Birger, B.F. Shorr et al., Mashinostroenie. 1975, 455pp. (in Russian)
77. V.P Popov, A.G. Lanin, N.A. Bochkov, *Test Method of Thermostability of Samples From Brittle Electroconductive Materials with Use Electron Beam Heating* (Plenum, New York, 1984) Strength of Materials
78. S. Sato, Y. Imamura, A. Kurumada, K. Kawamata, R. Ishida, H. Awaj, in *Thermal Shock and Thermal Fatigue Behavior of Advanced Ceramics*, ed. by G.A. Schneider, G. Petzow. Nato ASI Series E: Applied Sciences, vol. 241 (Kluwer, Dordrecht, 1993), pp. 253–268
79. V.S. Egorov, V.P. Popov, About limiting temperature pressure in disks from fragile materials (Plenum, New York, 1975) Strength of Materials
80. T.R. Hsu, Appl. Mech. **1,** 121 (1970) (Russian translation)
81. S. Sato, K. Sato, Y. Imamura, Carbon **13**, 309 (1975)
82. L.A. Kozdoba, Phys. Chem. Process. Mater. **5**, 3 (1970) (in Russian)
83. N.S. Koksal, M. Toparli, Key Eng. Mater. **264**, 1783 (2004)
84. A.G. Lanin, A.L. Tkachev, J. Mater. Sci. **35**, 2553 (2000)
85. V.I. Subbotin, D.N. Sorokin, A.A. Ziganov, in *Thermal-74th A Science*, 1975, p. 229 (in Russian)
86. T. Andersson, D.J. Rowcliffe, J. Am. Ceram. Soc. **79**(6), 1509 (1996)
87. Y. Takeshita, H. Uchimura, J. Ceram. Soc. Japan **103**(6), 563 (1995)
88. N.I. Tikhonov, Ind. Lab. **30**(9), 1103 (1962) (in Russian)
89. J.C. Glandus, P. Boch, Interceram **5**, 33 (1984)
90. J.P. Singh, J. Tree, D.P.H. Hasselman, J. Mater. Sci. **16**(8), 2109 (1981)
91. P.F. Becher, D. Lewis, K.R. Carman et al. Am. Cer. Soc. Bull. **59**(5), 542 (1980)
92. I.P. Morrell, in *Thermal Shock and Thermal Fatigue Behavior of Advanced Ceramics*, ed. by G.A. Schneider, G. Petzow. Nato ASI Series E: Applied Sciences, vol. 241 (Kluwer, Dordrecht, 1993), pp. 27–32
93. F. Osterstock, B. Legendre, J. Phys III **7**(3), 561 (1997)
94. R.W. Davidge, G. Tappin, Trans. Brit. Cer. Soc. **66**, 405 (1967)
95. T. Sakuma, U. Iwata, J. Ceram. Soc. Jpn. **104**(8), 743 (1996)
96. A.G. Tomba, A.L. Cavalieri, J. Eur. Ceram. Soc, **20**(7), 893 (2000)
97. T. Gao, T. Nishikawa, M. Hibi, M. Takatsu, J. Ceram. Soc. Jpn. **101**(7), 788 (1993)
98. A. Lanin, V.V. Borunov, V.S. Egorov et al., in *Thermal Strength Resistance of Materials and Constructive Elements*, no. 5 (Naukova Dumka, Kiev, 1969), pp. 284–293 (in Russian)
99. C.J. Mustacchi, Nucl. mater. **12**(3), 330 (1964)
100. D.P.H. Hasselman, W.B. Crandall, J. Am. Cer. Soc. **46**, 434 (1963)
101. S. Aratani, K. Sato, J. Cer. Soc. Japan. **103**(4), 365 (1995)
102. M. Oguma, C.J. Fairbanks, D.P.H. Hasselman, J. Am. Cer. Soc. **69**(4), 87 (1986)

103. S.S. Manson, R.W. Smith, ASME **78**(3), 533 (1956)
104. K. Niihara, J.P. Singh, D.P.H. Hasselman, J. Mater. Sci. **17**, 2553 (1982)
105. W.D. Kingery, J. Am. Cer. Soc. **38**(1), 3 (1955)
106. J.C. Glandus, P. Boch, J. Thermophysics **2**(1), 89 (1981)
107. L. Petrash, V. Quenching mediums. M. Mashgiz, 1959. 110p. (in Russian)
108. N.A. Neduzhnij, A. Alabovskij, Engineering thermodynamics and a heat transfer. Kiev, Vish'a Skola, 1978, 223p. (in Russian)
109. L.A. Kozdoba, *The Solution of Nonlinear Problems Thermal Conductivity* (Naukova Dumka, Kiev, 1976), p. 135 (in Russian)
110. Sakuma Toshio, U. Iwata, J. Ceram. Soc. Jpn. **304**(8), 743 (1996)
111. G.M. Kondratyev, Thermal measurements. M. Mashgiz, 1957, p. 244 (in Russian)
112. J. Absi, J.C. Glandus, J. Eur. Ceram. Soc. **24**(9), 2835 (2004)
113. H. Wang, W. Porter, J. Compos. Mater. **37**(1), 73 (2003)
114. M. Collin, D. Rowcliffe, Acta Mater. **48**(8), 1655 (2000)
115. R.E. Faber, M.D. Huang, A.G. Evans, J. Am. Ceram. Soc. **64**(5), 296 (1981)
116. M. Hamidouche, N. Bouaouadja, C. Olagnon, G. Fantozzi, Ceram. Int. **29**(6), 599 (2003)
117. K. Tagashira, T. Mikami, J. Okamura, T. Sasa, M. Obata, JSME Int. J. A Solid Mech. Mater. Eng. **45** (4), 612 (2002)
118. A.G.T. Martinez, M.A. Camerucci, G. Urretavizcaya, A.L. Cavalieri, Br. Ceram. Trans. **101**(3), 94 (2002)
119. D.P.H. Hasselman, J. Am. Ceram. Soc. **46**(5), 229 (1963)
120. J.R. Thomas, J.P. Singh, D.P.H. Hasselman, J. Am. Ceram. Soc. **64**(3), 163 (1981)
121. V.R. Vedula, D.J. Green, J.R. Hellmann, A.E. Segall, J. Mater. Sci. **33**(10), 5427 (1998)
122. E.M. Baroody, E.M. Simons, W.H. Duckworth, J. Am. Ceram. Soc. **38**(1), 38 (1955)
123. W.R. Bussem, E.A. Bush, J. Am. Ceram. Soc. **38**(1), 27 (1955)
124. G.A. Gogozi, Ind. Lab. **33**(5) 627 (1967) (in Russian)
125. H. Awaji, T. Endo, J. Ceram. Soc. Jpn. **103**(9), 960 (1995)
126. S. Honda, T. Suzuki, T. Nishikawa, H. Awaji, J. Ceram. Soc. Jpn. **110**(1), 38 (2002)
127. P. Supancic, Key Eng. Mater. **223**, 69 (2002)
128. G.A. Gogozi, V. Kravchuk, R.I. Kuriat et al., Therm. Phys. High Temp. **7**(3), 515 (1969) (in Russian)
129. Y. Wakamatsu, T. Saito, S. Ueda et al., in *Thermal Shock and Thermal Fatigue Behavior of Advanced Ceramics*, ed. by G.A. Schneider, G. Petzow. Nato ASI Series E: Applied Sciences, vol. 241 (Kluwer, Dordrecht, 1993), pp. 555–565
130. W.C. Spicer, P.T. Ross, R.L. Newman, Rev. Sci. Instrum. **43**(2), 236 (1972)
131. A. Moskalev, E. Pigida, L.G. Kerekiliza, *Destruction of Rocks at Thermal-Cycle Affecting* (Naukova Dumka, Kiev, 1987), p. 248 (in Russian)
132. G.C. Wei, J. Walsh, J. Am. Ceram. Soc. **72**, 1286 (1989)
133. C.Y. King, W.W. Webb, J. Appl. Phys. **42**(6), 2386 (1971)
134. N.A. Bochkov, V.S. Egorov, Phys. Chem. Process. Mater. **2**, 53 (1993) (in Russian)
135. H. Takahashi, T. Jshikawa, D. Okugawa et al., in *Thermal Shock and Thermal Fatigue Behavior of Advanced Ceramics*, ed. by G.A. Schneider, G. Petzow. Nato ASI Series E: Applied Sciences, vol. 241 (Kluwer, Dordrecht, 1993), pp. 543–554

136. S. Deschka, N. Nickel, in *Thermal Shock and Thermal Fatigue Behavior of Advanced Ceramics*, ed. by G.A. Schneider, G. Petzow. Nato ASI Series E: Applied Sciences, vol. 241 (Kluwer, Dordrecht, 1993), pp. 331–341
137. R. Duqdale, R. McVickers, S. Ford, J. Nucl. Mater. **12**, 1 (1964)
138. H. Takahashi, T. Hashida, JSME Int. J. Ser. I **33**, 281 (1990)
139. O. Minin, A. Stolayrov, N. Yarishev, *Installation for Comparative Tests of Refractories for Thermal Stability* (Plenum, New York, 1970) Strength of Materials
140. V.S. Egorov, G.V. Koroleva, Appl. Mech. **11**(3), 115 (1975) (in Russian)
141. J. Lamon, D. Pherson, J. Am. Ceram. Soc. **74**(6), 1188 (1991)
142. G. Kirchoff, in *Thermal Shock and Thermal Fatigue Behavior of Advanced Ceramics*, ed. by G.A. Schneider, G. Petzow. Nato ASI Series E: Applied Sciences, vol. 241 (Kluwer, Dordrecht, 1993), pp. 245–251
143. S. Amada, W.Y. Nong, S. Akiyama, Ceram. Int. **25**, 61 (1999)
144. S. Akiyama, S. Amada, M. Shimada, T Yoshii, JSME Int. J. Ser. A-Mech. Mater. Eng. **38**(4), 594 (1995)
145. N. Morita, J. Ceram. Soc. Jpn. **101**(5), 522 (1993)
146. J. Linke, M. Akiba, Marul, in *Thermal Shock and Thermal Fatigue Behavior of Advanced Ceramics*, ed. by G.A. Schneider, G. Petzow. Nato ASI Series E: Applied Sciences, vol. 241 (Kluwer, Dordrecht, 1993), pp. 343–354
147. C. Schubert, H.A. Bahr, M. Weiss, Carbon **24**, 21 (1986)
148. N.A. Bochkov, V.I. Sh'ipalkin, Surface J. **2**, 59 (1992) (in Russian)
149. A.G. Lanin, N.A. Bochkov, V.I. Sh'ipalkin, Phys. Chem. Process. Mater. **1**, 50 (1991) (in Russian)
150. A. Lanin, V.P. Popov, V.I. Sh'ipalkin, Phys. Chem. Process. Mater. **1**, 56 (1992) (in Russian)
151. V.V. Pasechny, A.V. Choba, Kuznetzov et al., Heliotechnics **1**, 26 (1985) (in Russian)
152. A. Choba, F.F. Egorov, V.V. Pasechny, Powder Metallurgy **11**, 19 (1990) (in Russian)
153. H. Away, T.J. Endo, J. Ceram. Soc. Jpn. **103**(9), 960 (1995)
154. K. Kokini, in *Thermal Shock and Thermal Fatigue Behavior of Advanced Ceramics*, ed. by G.A. Schneider, G. Petzow. Nato ASI Series E: Applied Sciences, vol. 241 (Kluwer, Dordrecht, 1993), pp. 531–541
155. A. Kumakawa, M. Nino, in *Thermal Shock and Thermal Fatigue Behavior of Advanced Ceramics*, ed. by G.A. Schneider, G. Petzow. Nato ASI Series E: Applied Sciences, vol. 241 (Kluwer, Dordrecht, 1993), pp. 567–577
156. G.A. Schnider, G. Petzow, J. Am. Ceram. Soc. **74**(1), 98 (1991)
157. V.I. Shvidenko, B.A. Ljashenko, G.V. Isachanov, Ind. Lab. **8**, 1001 (1966) (in Russian)
158. Iu. Anufriev, D. Trapeznikov, V.A. Ursin, Ind. Lab. **9**, 1132 (1967)
159. T. Log, J. Melas, B. Larsen, Carbon **31**(6), 931 (1993)
160. Z. Zudans, T.C. Yen, W.H. Steigelman, *Thermal Stress Technique in the Nuclear Industry* (Elsevier, New York, 1965), p. 350
161. S. Sato, K. Sato, Y.I. Ymamura, Carbon **13**, 309 (1975)
162. S. Sato, Y. Ymamura, A. Kurumada et al., in *Thermal Shock and Thermal Fatigue Behavior of Advanced Ceramics*, ed. by G.A. Schneider, G. Petzow. Nato ASI Series E: Applied Sciences, vol. 241 (Kluwer, Dordrecht, 1993), pp. 253–268

163. A. Lanin, V. Popov, J. Therm. Stresses 87 (1995) (in Russian)
164. V.I. Melkin, A.G. Lanin, V.S. Egorov, in *Coll.: Methods of Research of Refractory Materials* (Atomizdat, Moscow, 1970), pp. 121–128 (in Russian)
165. B. Schultrich, H.J. Weiss, H. Bahr, in *Thermal Shock and Thermal Fatigue Behavior of Advanced Ceramics*, ed. by G.A. Schneider, G. Petzow. Nato ASI Series E: Applied Sciences, vol. 241 (Kluwer, Dordrecht, 1993), pp. 355–363
166. R.M. Jones, H.S. Starret, AIAA J. **15**, 1116 (1977)
167. A.E. Carden, R.W. Andrae. J. Am. Ceram. Soc. **53**(6), 339 (1970)
168. P.B. Goldstein, N.M. Osipenko, About one model of formation of cracks systems at thermal stress resistance, Institute of problems of mechanics of the Russian Academy of Science. preprint 577, 1997, p. 26
169. Dzh. Rais, in *Fracture*, vol. 2, (World, 1975), pp. 204–335
170. E.M. Morozov, Proc. RAN USSR, **156**(3) (1964)
171. A.L. Tkachev, A. Lanin, V.S. Egorov, G.V. Koroleva, *End Effect of Fracture at Heating of Brittle Cylinder* (Plenum, New York, 1975) Strength of materials (in Russian)
172. A.G. Lanin, V.P. Popov, S.A. Pritchin et al., Series: Nucl. Mater. Sci. **2**(25), 39 (1987) (in Russian)
173. A.G. Lanin, I.M. Zalivin, V.P. Popov, Series: Nucl. Mater. Sci. **5**(16), 19 (1982) (in Russian)
174. W.P. Rogers, A.E. Emery, R.C. Bradt, J. Am. Ceram. Soc. **79**, 406 (1987)
175. R.L. Barnett, R.L. McGuire, Am. Ceram. Soc. Bull. **45**, 595 (1966)
176. C. Lin, T. Kuo, J. Ceram. Soc. Jpn. **105**(12), 1062 (1997)
177. B. Cotterell, S.W. Ong, C.D. Qin, J. Am. Ceram. Soc. **78**(8), 2056 (1995)
178. C.K. Lin, T.C. Kuo, J. Ceram. Soc. Jpn. **105**(12), 1062 (1997)
179. J.C. Glandus, P. Boch, Int. J. Thermophys. **2**(1), 89 (1981)
180. A.A. Uglov, Phys. Chem. Process. Mater. **3**, 3 (1976) (in Russian)
181. V.S. Kolesov, N.A. Bochkov, Appl. Mech. **21**(5), 73 (1985) (in Russian)
182. V.S. Kolesov, N.A. Bochkov, Appl. Mech. **26**(6), 31 (1990) (in Russian)
183. I.I. Derjavko, A.G. Lanin, N.A. Bochkov, Powder Metallurgy **5**, 60 (1984) (in Russian)
184. A.G. Lanin, I.I. Derjavko, M.A. Fedotov, in *Technics of Radiating Experiment* (Atomizdat, Moscow 1975), pp. 88–91 (in Russian)
185. I.I. Derjavko, A.G. Lanin, V.P. Maximov, in *Physics and Mechanics of Deformation and Destruction*, vol. 7 (Atomizdat, Moscow, 1979) pp. 47–54 (in Russian)
186. K.K. Strelov, *Theoretical Basis of Technology Fire-Resistant Materials* (Metallurgy, 1985), 480p. (in Russian)
187. B.L. Wang, Y.W. Mai, J. Am. Ceram. Soc. **87**(5), 929 (2004)
188. X.J. Zheng, J.Y. Li, Y.C. Zhou, Acta Mater. **52**(11), 3313 (2004)
189. A. Nisar, M.J.J. Schmidt, M.A. Sheikh, L. Li, Proc. Inst. Mech. Eng. B.J. Eng. Mater. **217**(8), 1085 (2003)
190. X. Wang, P. Xiao, Acta Mater. **52**(9), 2591 (2004)
191. P.T. Rybalkin, S.D. Ivanov, G.N. Tchernyshev, *Thermal Processing of Electric Melting Refractories* (Metallurgy, 1981), 199p. (in Russian)
192. G. Fargas, D. Casellas, L. Llanes, M. Anglada, J. Eur. Ceram. Soc. **23**(1), 107 (2003)
193. K. Zeng, A. Giannakopoulos, D. Rowcliffe, P Meier, J. Am. Ceram. Soc. **81**(3), 689 (1998)

194. M. Leoni, P. Scardi., V. Sglavo, J. Eur. Ceram. Soc. **18**, 1663 (1998)
195. S. Akiyama, S. Amada, N. Kotani, J. Therm. Stresses **26**(4), 297 (2003)
196. A.A. Pozdeev, J.I. Njashin, P.V. Trusov, *Residual Stresses, the Theory and Practice* (Science, 1982), 112p. (in Russian)
197. G.N. Chernyshev, A.L. Popov, A.A. Antonov, S.D. Ivanov, Technological Stresses in Welded Connections (MGOU, 2004), 254p. (in Russian)
198. A.G. Tomba, A.L. Cavalieri, J. Eur. Ceram. Soc. **8**, 1205 (2001)
199. A.G. Lanin, M.A. Fedotov, S.A. Pritchin, R.N. Maraginskij, Powder Metallurgy **1**, 51 (1986) (in Russian)
200. A.N. Rakitskij, B.N. Trefilov, Powder Metallurgy **9**, 62 (1977) (in Russian)
201. O.N. Grigor'ev, A. Krell, V.I. Trefilov, Factory. Lab. **7**, 36 (1990) (in Russian)
202. O.N. Grigor'iev, A. Krell, V. Pompe, V.I. Trefilov, Powder Metallurgy **1**, 43 (1987) (in Russian)
203. V.I. Kruglov, D. Gurevich, V.I. Groshev et al., Powder Metallurgy **1**, 59 (1979) (in Russian)
204. I.I. Derjavko, A.G. Lanin, M.L. Taubin, Powder Metallurgy **2**, 67 (1978) (in Russian)
205. H. Tomaszewski, M. Boniecki, H. Weglarz, J. Eur. Ceram. Soc. **21**, 1021 (2001)
206. I.I. Derjavko, A.G. Lanin, in *M. Proceed. of II All-Union symposium*, 1985, 390p. (in Russian)
207. B.D. Miracle, H.A. Lipsitt, J. Am. Ceram. Soc. **66**, 592 (1983)
208. A.G. Lanin, V.P. Popov, in *Proceedings of the International Symposium on Thermal Stresses and Related Topics*, Hamamatsu, Japan, 5–7 June 1995
209. D.M. Vasil'ev, Factory Lab. N**8**, 972 (1965) (in Russian)
210. I.A. Birger, *Residual Voltage* (Mashgiz, 1963), 232p. (in Russian)
211. P. Agrawal, K. Konlon, K.J. Bowman et al., Acta Met. Mater. **51**, N4, 1143, (2003)
212. G.S. Pisarenko, A.P. Jakovlev, V.V. Matveev, *Directory on Resistance of Materials* (Naukova Dumka, Kiev, 1988), p. 734 (in Russian)
213. A.G. Lanin, V.S. Egorov, Phys. Chem. Process. Mater. **6**, 71 (1998) (in Russian)
214. S.R. Levine, E.J. Opila, M.C. Halbig, J.D. Kiser, M. Singh, J. Eur. Ceram. Soc. **22**(14–15), 2757 (2002)
215. J. Pascualcosp, A.J.R. Delvalle, J. Garciafortea, P.J. Sanchezsoto, Mater. Lett. **55**(4), 274 (2002)
216. NPO "Luch", affairs and people, Podolsk, scientific research institute NPO "LUCH", ed. by I.I. Fedik, 2004, p. 455 (in Russian)
217. D. Sciti, S. Guicciardi, C. Melandri, A. Bellosi, J. Am. Ceram. Soc. **86**(10), 1720 (2003)
218. Fracture mechanics of ceramics. *Fatique, Composites and High Temperature Behaviour*, vol. 12, (Plenum, New York, 1996), p. 500
219. Y. Wakamatsu, in *Thermal Shock and Thermal Fatigue Behavior of Advanced Ceramics*, ed. by G.A. Schneider, G. Petzow. Nato ASI Series E: Applied Sciences, vol. 241 (Kluwer, Dordrecht, 1993), pp. 555–563
220. J. Linke, M. Akiba, in *Thermal Shock and Thermal Fatigue Behavior of Advanced Ceramics*, ed. by G.A. Schneider, G. Petzow. Nato ASI Series E: Applied Sciences, vol. 241 (Kluwer, Dordrecht, 1993), pp. 343–350
221. M. Saadaoui, J. Chevalier, G. Fantozzi, in *Thermal Shock and Thermal Fatigue Behavior of Advanced Ceramics*, ed. by G.A. Schneider, G. Petzow. Nato ASI Series E: Applied Sciences, vol. 241 (Kluwer, Dordrecht, 1993), pp. 381–393

222. T. Volkov-Husovic, R.M. Jancic, M. Cvetkovic, D. Mitrakovic, Z. Popovic, Thermal shock behavior of alumina based refractories: fracture resistance parameters and water quench test **38**(5), 5372 (1999)
223. J.H. Schneibel, S. Sabol, J. Morrison, E. Ludeman, J. Am. Ceram. Soc. **81**(7), 1888 (1998)
224. T. Baskin, G. Arenberg, J. Handwerk, J. Am. Ceram. Soc. **43**, 489 (1960)
225. I.W. Donalg, P.W. McMillan, J. Mater. Soc. **11**, 949 (1976)
226. X.W. Yin, L.F. Cheng, L.T. Zhang, Y.D. Xu, Carbon **40**(6), 905 (2002)
227. P.K. Panda, T.S. Kannan, J. Dubois, C. Olagnon, G. Fantozzi, J. Eur. Ceram. Soc. **22**(13), 2187 (2002)
228. J.Q. Li, X.R. Zeng, J.N. Tang, P. Xiao, J. Eur. Ceram. Soc. **23**(11), 1847 (2003)
229. N.D. Sobolev, V.I. Ugorov, Ind. Lab. No. 9, 1098 (1969) (in Russian)
230. O.I. Romaniv, I.A. Iarema, I.A. Mahutov et al., *Fatigue and Cyclic Fracture Toughness of Constructional Materials* (Naukova Dumka, Kiev, 1990), p. 680
231. M. Arnold, A.R. Boccaccini, G. Ondracek, J. Mater. Sci. 43
232. A.G. Lanin, O.N. Erin, V.N. Turchin, Refract. Mater. Hard Met. **9**(3), 139 (1990)
233. A.G. Evans, J. Am. Ceram. Soc. **73**, 187 (1990)
234. A.G. Lanin, M.A. Fedotov, V.V. Glagolev, in *Proceedings of Plannsee seminar 6. High Temperature Materials*, Vienna, 1969, pp. 663–671
235. A.G. Lanin, V.N. Turchin, O.N. Erin, S.N. Sul'ianov, Powder Metallurgy **2**, 86 (1986) (in Russian)
236. H. Kawamura, H. Kita, in *Thermal Shock and Thermal Fatigue Behavior of Advanced Ceramics*, ed. by G.A. Schneider, G. Petzow. Nato ASI Series E: Applied Sciences, vol. 241 (Kluwer, Dordrecht, 1993), pp. 59–74
237. T.K. Gupta, J. Am. Ceram. Soc. **55**(5), 249 (1988)
238. M.J. Hoffmann, G.A. Schneider, G. Petzow, in *Thermal Shock and Thermal Fatigue Behavior of Advanced Ceramics*, ed. by G.A. Schneider, G. Petzow. Nato ASI Series E: Applied Sciences, vol. 241 (Kluwer, Dordrecht, 1993), pp. 49–58
239. P. Pettersson, Z.J. Shen, M. Johnsson, M. Nygren, J. Eur. Ceram. Soc. **22**(8), 1357 (2002)
240. Q.H. Chen, J.L. He, K.X. Tan et al., Science in China Series and-Technological Sciences **45**(4), 337 (2002)
241. A.G. Lanin, P.V. Zubarev, K.P. Vlasov, Atomnay Energiya **74**, 42 (1993) (in Russian)
242. D. Hasselman, Fulrath, J. Am. Ceram. Soc. **49**, 68 (1966); **50**, 399 (1967)
243. V.N. Turchin, A.G. Lanin, Powder Metallurgy **1**, 31 (1980) (in Russian)
244. R.A Dorey, J.A Yeomans, P.A. Smith, J. Eur. Ceram. Soc. **22**(4), 403 (2002)
245. J.H. She, J.F. Yang, D.D. Jayaseelan, N. Kondo, T. Ohji, S. Kanzaki, Y. Inagaki, J. Am. Ceram. Soc. **86**(4), 738 (2003)
246. L.J. Vandeperre, Y. Inagaki, W.J. Clegg, J. Mater. Res. C **18**(11), 2724 (2003)
247. T. Ohji, N. Kondo, Y. Inagaki, Y. Shigegaki, Key Eng. Mater. **223**, 91 (2002)
248. V.N. Antsifirov, V.G. Gilev, A.G. Lanin, V.P. Popov, Powder Metallurgy **11**, 66 (1992) (in Russian)
249. J.R.G. Evans, R. Stevens, J. Mater. Sci. **19**, 3692 (1984)
250. S.M. Barinov, V.J. Shevchenko, *Strength of Technical Ceramics* (Science, 1996), 158p. (in Russian)
251. T. Fett, D. Munz, R.D. Geraghty, K.W. White, J. Eur. Ceram. Soc. **20**, 2143 (2000)

252. O. Raddatz, G.A. Schneider, W. Mackens, N. Claussen, J. Eur. Ceram. Soc. **20**, 2261 (2000)
253. N. Schmitt, A. Burr, Y. Berthaud, J. Poirier, Mech. Mater. **34**(11), 725 (2002)
254. K. Niihara, Mem. Inst. Sci. Res. Osaka Univ. **49**(1), 21 (1992)
255. S. Maensiri, S.G. Roberts, J. Am. Ceram. Soc. **85**(8), 1971 (2002)
256. G. Pezzotti, M. Sakai, J. Am. Ceram. Soc. **77**(10), 3039 (1994)
257. R.I. Todd, B. Derby, Acta Mater. **52**(6), 1621 (2004)
258. L. Wang, J.L. Shi, J.H. Gao, D.S. Yan, J. Eur. Ceram. Soc. **21**, 1213 (2001)
259. Y.Q. Wu, Y.F. Zhang, G. Pezzotti, J.K. Guo, J. Eurp. Ceram. Soc. **22**, 159 (2002)
260. T. Kusunose, Y.H. Choa, T. Sekino, K. Niihara. Key Eng. Mater. **161**, 475 (1999)
261. M.I. Nieto, R. Martinez, L. Mazeerolles, C. Baudin, J. Eur. Ceram. Soc. **24**(8), 2293 (2004)
262. L.J. Broutman (ed.), *Modern Composite Manerials* (Addison Wesley, Reading, 1967), p. 671
263. G.M. Song, Y. Wu, Q. Li, J. Eur. Ceram. Soc. **22**(4), 559 (2002)
264. Y.H. Koh, H.W. Kim, H.E. Kim, J.W. Halloran, J. Eur. Ceram. Soc. **24**(8), 2339 (2004)
265. X.W. Yin, L.F. Cheng, L.T. Zhang, Y.D. Xu, Carbon **40**(6), 905 (2002)
266. S.Q. Li, Y. Huang, Y.M Luo, C.A Wang, C.W. Li, Mater. Lett. **57**(11), 1670 (2003)
267. F.A. Fehretdinov, I.S. Belevich, G.A. Kudintseva et al., Inorganic Materials **7**, 1457 (1971) (in Russian)
268. A.G. Lanin, V.P. Popov, A.S. Maskaev, V.A. Sokolov, V.N. Turchin, Strength Carbide Graphite Compositions at Thermal Loading (Plenum, New York, 1982) Strength of Materials
269. L.W. Donald, P.W. McMillan, J. Mater. Sci. **11**, 949 (1976)
270. D.P.H. Hassellman, J. Am. Ceram. Soc. **46**(2), 103 (1963)
271. P.V. Gerasimov, V.S. Egorov, A.G. Lanin, L.B. Nezhevenko, V.A. Sokolov, Powder Metallurgy **1**, 67 (1982) (in Russian)
272. L.B. Nezhevenko, I.I. Spivak, P.V. Gerasimov, Powder Metallurgy **8**, 23 (1980) (in Russian)
273. G.A. Gogozi, Refrectory **5**, 45 (1977) (in Russian)
274. G.A. Gogotsi, in *Thermal Shock and Thermal Fatigue Behavior of Advanced Ceramics*, ed. by G.A. Schneider, G. Petzow. Nato ASI Series E: Applied Sciences, vol. 241 (Kluwer, Dordrecht, 1993), pp. 279–291
275. G.A. Gogotsi, A.V. Drozdov, M. Swein, *Strength, Fracture Toughness and Acoustic Emission of Ceramics on Basis of Partially Stabilized Zirconium Dioxide* (Plenum, New York, 1991) Strength of Materials
276. G.A. Gogozi, A.V. Drozdov, V.G. Peichev, Mechanical behaviour of zirconium dioxide crystals partially stabilized by yttrium oxide. (Plenum, New York, 1992) Strength of Materials
277. E.H. Lutz, in *Thermal Shock and Thermal Fatigue Behavior of Advanced Ceramics*, ed. by G.A. Schneider, G. Petzow. Nato ASI Series E: Applied Sciences, vol. 241 (Kluwer, Dordrecht, 1993), pp. 75–85
278. M.V. Swain, in *Thermal Shock and Thermal Fatigue Behavior of Advanced Ceramics*, ed. by G.A. Schneider, G. Petzow. Nato ASI Series E: Applied Sciences, vol. 241 (Kluwer, Dordrecht, 1993), pp. 269–278

279. A.H. Heur, F.F. Lange, M. Swain, A.G. Evans, J. Am. Ceram. Soc. **69**(3), i (1986)
280. D. Han Jr., J. Mecholsky, J. Am. Ceram. Soc. **73**(12), 3692 (1990)
281. Arias Alan, J. Am. Ceram. Soc. **49**, 339 (1966)
282. D. Sherman, J. Am. Ceram. Soc. **84**(12), 2819 (2001)
283. D.T. Rankin, J. Stiglich, P. Petrak, J. Am. Ceram. Soc. **54**, 277 (1971)
284. O. Sbaizero, G. Pezzotti, Mater. Sci. Eng. A Struct. Mater. **343**(1–2), 273 (2003)
285. Y. Ootao, Y. Tanigawa, T. Fukuda, J. Therm. Stresses **14**, 201 (1991)
286. Y. Tanigawa, N. Oka, T. Akai, R. Kawamura, JSME Int. J. A **40**, 117 (1997)
287. T. Elperin, G. Rudin, Heat Mass Transfer **38**(7–8), 625 (2002)
288. Y.M. Shabana, N. Noda, J. Therm. Stresses **25**(12), 1133 (2002)
289. L.A. Rastrigin, *Statistical Methods of Searching* (Science, 1968), 374p. (in Russian)
290. A.S. Chernikov, V.S. Kolesov, L.N. Permjakov et al., Proc. Belarus Acad. Sci. Ser. Phys. Energetic Sci. **3**, 77 (1982) (in Russian)
291. M. Kalyon, B.S. Yilbas, Proc. Inst. Mech. Eng. C J. Mech. Eng. **215**(12), 1429 (2001)
292. Y.M. Shabana, N. Noda, in *Proceedings of the 5th International Congress on Thermal Stresses and Related Topics*, *TS2003*, Blacksburg, VA, 8–11 June 2003, MA-2-1-1–MA-2-1-5
293. Jian Zhao, V. Silberschmidt Vadim, in *Proceedings of the 5th International Congress on Thermal Stresses and Related Topics, 2003*, Blacksburg, VA, 8–11 June 2003
294. H. Waki, K. Ogura, I. Nishikawa, Y. Kashihara, JSME Int. J. Ser. A Solid Mech. Mater. Eng. **46**(4), 590 (2003)
295. R. Asmatulu, R.O. Claus, I. Tuzcu, in *Proceedings of the 5th International Congress on Thermal Stresses and Related Topics, TS2003*, Blacksburg, VA, 8–11 June 2003, MA-6-3-1–MA-6-3-4
296. S. Nishinoiri, K. Nozawa, M. Enoki, Mater. Sci. Forum **449**, 717 (2004)
297. A.X. Feng, Y.K. Zhang, H.K. Xie, L. Cai, M. Zhou, Y.S. Liu, Key Eng. Mater. **259**, 615 (2004)
298. P. Agrawal, K. Conlon, K.J. Bowman, C.T. Sun, F.R. Cichocki, K.P. Trumble, Acta Mater. **51**(4), 1143 (2003)
299. G. Geandier, A. Hazotte, S. Denis, A. Mocellin, E. Maire, Microstructural Analysis of Alumina Chromium Composites by X-Ray Tomography and 3-D Finite-Element Simulation of Thermal-Stresses, **48**(8), 1219 (2003)
300. Y.C. Zhou, T. Hashida, Trans. ASME **124**(4), 922 (2002)
301. R.L. Loh, C. Rossington, A.G. Evans, J. Am. Ceram. Soc. **69**(2), 139 (1996)
302. B. Zhou, K. Kokini, Mater. Sci. Eng. A Struct. Mater. **348**(1–2), 271 (2003)
303. R. Rodriguezcastro, R.C. Wetherhold, M.H. Kelestemur, Mater. Sci. Eng. A Struct. Mater. **323**(1–2), 445 (2002)
304. M.H. Li, Z.Y. Zhang, X.F. Sun, H.R. Guan, W.Y. Hu, Z.Q. Hu, Oxid. Met. **58**(5–6), 499 (2002)
305. Y.S. Yin, J.D. Zhang, H. Zhang, J. Li, Mater. Sci. Forum **437**, 77 (2003)
306. H. Kobayashi, Mater. Sci. Forum **423**, 235 (2003)
307. W.Q. Zhang, J.X. Xie, Z.G. Yang, S. Chen, Y.Q. Liu, C.Z. Wang, Mater. Sci. Forum **423**, 275 (2003)
308. G. Jin, T. Nishikawa, S. Honda, H. Awaji, Mater. Sci. Forum **423**, 693 (2003)

309. D.M. Karpinos, V.G. Zil'berberg, Powder Metallurgy **10**, 46 (1971) (in Russian)
310. L.C. Celic, O. Saricava, Mater. Sci. Eng. A **379**(2), 11 (2004)
311. G.V. Isachanov, *Strength of Nonmetallic Materials at Non-uniform Heating* (Naukova Dumka, Kiev, 1971), p. 176 (in Russian)
312. L.C.K. Liau, T.C.K. Yang, S.P. Huang, C.C. Chang, J. Chin. Inst. Chem. Eng. **34**(2), 219 (2003)
313. A. Kawasaki, R. Watanabe, in *Thermal Shock and Thermal Fatigue Behavior of Advanced Ceramics*, ed. by G.A. Schneider, G. Petzow. Nato ASI Series E: Applied Sciences, vol. 241 (Kluwer, Dordrecht, 1993), pp. 509–520
314. A. Kumakawa, M. Niino, in *Thermal Shock and Thermal Fatigue Behavior of Advanced Ceramics*, ed. by G.A. Schneider, G. Petzow. Nato ASI Series E: Applied Sciences, vol. 241 (Kluwer, Dordrecht, 1993), pp. 567–577
315. H. Takahashi, T. Ishicawa, D. Ocugawa, T. Hashida, in *Thermal Shock and Thermal Fatigue Behavior of Advanced Ceramics*, ed. by G.A. Schneider, G. Petzow. Nato ASI Series E: Applied Sciences, vol. 241 (Kluwer, Dordrecht, 1993), pp. 543–554
316. Y. Wakamatsu, T. Saito, S. Ueda, M. Niino, in *Thermal Shock and Thermal Fatigue Behavior of Advanced Ceramics*, ed. by G.A. Schneider, G. Petzow. Nato ASI Series E: Applied Sciences, vol. 241 (Kluwer, Dordrecht, 1993), pp. 555–565
317. M. Nakamichi, H. Kawamura, T. Teratani, J. Nucl. Sci. Technol. **38**(11), 1007 (2001)
318. A. Kurumada, Y. Imamura, Y. Tomota, T. Oku, Y. Kubota, N. Noda, J. Nucl. Mater. **313**, 245 (2003)
319. S. Ueda, J. Therm. Stresses **25**(1), 83 (2002)
320. E. Celik, O. Sarikaya, J.M. Linke, T. Hira, M. Rodig, L.A. Singheiser, Fusion Sci. Technol. **46**(1), 142 (2004)
321. S. Ishihara, T. Goshima, S. Iwawaki, M. Shimizu, S. Kamiya, J. Therm. Stresses **25**(7), 647 (2002)
322. J.H. She, J.F. Yang, D.D. Jayaseelan, N. Kondo, T. Ohji, S. Kanzaki, Y. Inagaki, J. Am. Ceram. Soc. **86**(4), 738 (2003)
323. B.J. Hockey, S.M. Wiederhorn, J.E. Blendell, J.S. Lee, M.K. Kang, J. Am. Ceram. Soc. **86**(4), 612 (2003)
324. J.E. Blendell, R.L. Coble, J. Am. Ceram. Soc. **66**(3), 174 (1982)
325. N.N. Davidenkov, V.A. Lichachev, *Irreversible Forming of Metals at Cyclic Thermal Action* (Mashgiz, 1962), 223p. (in Russian)
326. G.D. Miles, F.J. Clarke, Philos. Mag. **6**(72) (1961)
327. R.A. Dugdale, Trans. Brit. Ceram. Soc. **64**, 287 (1965)
328. Y.V. Nicolaev, A.V. Vasilchenko, N.V. Lapochkin, in *Proc. of 12th Symposium on Space Nuclear Power and Propulsion*, ed. by M.S. EL-Genk. AIP Conference Proceedings, vol. 324 (American Institute of Physics, New York,) pp. 289–294
329. T.K. Gupta, J. Am. Ceram. Soc. **55**(5), 249 (1988)
330. F. Schmid, D.C. Harris, J. Am. Ceram. Soc. **81**(4), 885 (1998)
331. A.V. Stepanov, J. Technical Phys. **29**(3), 381 (1959) (in Russian)
332. ANSYS Programmer's Manual. Revision 5.5. (ANSYS, 1999)
333. N. Miyazaki, H. Uchida, T. Tsukada, T. Fukuda, J. Cryst. Growth 162(1–2), 83 (1996)
334. W.D. Scott, K.K. Orr, J. Am. Ceram. Soc. **66**(1), 27 (1983)
335. S.M. Wiederhorn, J. Am. Ceram. Soc. **52**(9), 485 (1969)
336. Monocrystal corundum in the jeweller industry. Under J.V. Derjugina's edition. L. Mechanical engineering, 1984, p. 147 (in Russian)

337. F.F. Lange, M.R. James, D.J. Green, J. Am. Ceram. Soc. **64**, 504 (1983)
338. V.N. Gurarie, P.H. Otsuka, Mater. Chem. Phys. **75**(1–3), 246 (2002)
339. V.N. Gurarie, D.N. Jamieson, R. Szymanski, A.V. Orlov, J.S. Williams, M. Conway, Nucl. Instrum. Methods Phys. Res. Sect. B **147**(1–4), 221 (1999)
340. V.N. Gurarie, P.H. Osuka, J.S. Williams, M.J. Conway, Nucl. Instrum. Methods Phys. Res. B **178**, 138 (2001)
341. N.N. Riakalin, A.A. Uglov, I.V. Zuev, *Electron-ray Processing of Materials.* (Mashinostroenie, 1985), 469p. (in Russian)
342. V.S. Kovalenko (ed.), *Directory on Technology of Laser Processing* (Technics, Kiev, 1985), p. 167 (in Russian)
343. N.N. Riakalin, I.V. Zuev, A.A. Uglov, M. Mashinostroenie 245 (1978) (in Russian)
344. N.M. Vlasov, V.S. Kolesov, I.I. Fedik, *Stability of Optical Surfaces for Lazer Mirrors* (FGUP. Zniiatominform, 2005), 213p. (in Russian)
345. N.A. Bochkov, V.S. Kolesov Lanin et al., Surface **11**, 89 (1983) (in Russian)
346. V.M. Kostin, A.G. Lanin, V.N. Fedjrova, Surface. Physics, Chemistry, Mechanics **4**, 32 (1993) (in Russian)
347. V.S. Kolesov, V.M. Kostin, A.G. Lanin et al., Surface. Physics, Chemistry, Mechanics **12**, 124 (1982) (in Russian)
348. D.P.H. asseIman, Am. Ceram. Soc. Bull. **49**, 1033 (1970)
349. G.A. Gogozi, Refrectory **5**, 45 (1977) (in Russian)
350. R.L. Marovelly, T.S. Chen, K.F. Veith, Trans. Soc. Mining Eng. **3**, 1 (1966)
351. N.M. Vlasov, V.S. Kolesov, I.I. Fedik, *Stability of Optical Surfaces for Lazer Mirrors* (FGUP. Zniiatominform, 2005), 213p. (in Russian)
352. A.G. Lanin, Proc. RAN, Series physical **68**, 1503 (2004) (in Russian)
353. R.A. Andrievsky, *Material Science of Hydride* (Metallurgy, 1986), 129p. (in Russian)
354. J.H. She, T. Ohji, S. Kanzaki, J. Eur. Ceram. Soc. **24**(2), 331 (2004)
355. C. Kawai, A. Yamakawa, J. Am. Ceram. Soc. **80**(10), 2705 (1997)
356. S.M. Kaz, *High temperature thermal insulating materials* (Metallurgy, 1981), 232p. (in Russian)
357. A.G. Lanin, O.N. Erin, V.N. Turchin et al., Physika Chimiaya Obrabotki Materialov **3**, 124 (1990) (in Russian)
358. A.G. Lanin, V.N. Turchin, D.J. Kovalev, Surface **6**, 112 (1992) (in Russian)
359. F.F. Lange, J. Am. Ceram. Soc. **53**(5), 290 (1970)
360. T.K. Gupta, J. Am. Ceram. Soc. **58**(3–4), 143 (1975)
361. G. Bandyopadhyay, C.R. Kennedy, J. Am. Ceram. Soc. **60**(1–2), 48 (1977)
362. R.M. Gruver, H.P. Kirchner, J. Am. Ceram. Soc. **51**(4), 232 (1968)
363. W.R. Buessem, R.M. Gruver, J. Am. Ceram. Soc. **55**(2), 101 (1972)
364. Hiroyuki Ohira, Richard C. Bradt, J. Am. Ceram. Soc. **71**(1), 35 (1988)
365. A.G. Lanin, in *Proceedings of World Ceramic Congress,* Italy, 1991 (Elsevier, Amsterdam, 1991)
366. J. Gebauer, D.P.H. Hasselman, J. Am. Ceram. Soc. **54**, 468 (1971)
367. F.F. Lange, J. Am. Ceram. Soc. **63**(1–2), 38 (1980)
368. H.P. Kirchner, R.M. Gruver, R.E. Walker, J. Am. Ceram. Soc. **50**(4), 169 (1967)
369. D.A. Duke, J. Megles, J.E. Macdowell, H.F. Bopp. J. Am. Ceram. Soc. **51**(2), 98 (1968)
370. A.G. Lanin, A.V. Yemelyanov, V.N. Turchin, P.V. Zubarev, Phys. Chem. Process. Mater. **2**, 88 (1982) (in Russian)

371. R.J. Stokes, J. Am. Ceram. Soc. **49**(1), 39 (1966)
372. A.G. Lanin, V.A. Sokolov, N.A. Bochkov, *Definition's Method of Fracture Toughness of Brittle Materials* (Plenum, New York, 1984) Strength of Materials, pp. 161–165
373. A.G. Lanin. V.N. Turchin, D.J. Kovalev, Metallophysica **13**(4), 120 (1991) (in Russian)
374. H. Kim, S. Roberts, J. Am. Ceram. Soc. **77**(12), 3099 (1994)
375. M.-C. Chu, S.-J. Cho, Y.-C. Lee, H.-M. Park, D.Y. Yoo, J. Am. Ceram. Soc. **87**(3) (2004)
376. W.I. Moon, T. Ito, S. Uchimure, H. Sake, J. Mater. Sci. Eng. A 387 (2004)
377. J.E. Ritter, P.B. Oates, E.R. Fuller, S.M. Wiederhorn, J. Mater. Sci. **15**, 2275 (1980)
378. N. Kamiya, in *Thermal Shock and Thermal Fatigue Behavior of Advanced Ceramics*, ed. by G.A. Schneider, G. Petzow. Nato ASI Series E: Applied Sciences, vol. 241 (Kluwer, Dordrecht, 1993), pp. 473–482
379. I.I. Derjavko, A.G. Lanin, A.S. Maskaev, Powder Metallurgy **10**, 84 (1984) (in Russian)
380. K.J. Konsztowich, in *Thermal Shock and Thermal Fatigue Behavior of Advanced Ceramics,* ed. by G.A. Schneider, G. Petzow. Nato ASI Series E: Applied Sciences, vol. 241 (Kluwer, Dordrecht, 1993), pp. 429–441
381. I.A. Boguslavsky, Stroyizdat 207 (1969), 305 p (in Russian)
382. A.G. Evans, T.G. Langdon, Structural ceramics. Pergamon press, 256 p, (1976)
383. V.F. Britun, O.N. Erin, A.G. Lanin, V.N. Turchin, Poroshkovay Metallurgia **12**, 72 (1992) (in Russian)
384. *Proceedings of the 5th International Congress on Thermal Stresses and Related Topics, TS2003*, Blacksburg, VA, 8–11 June 2003
385. A.G. Lanin, V.A. Sokolov, V.S. Egorov, *Cyclic Strength of Brittle Materials at Compression* (Plenum, New York, 1984) Strength of Materials, pp. 101–107
386. P.V. Zubarev, *High temperature strength.* M. Metallurgy 100 (1985) (in Russian)

Index

Allocation of stresses, 34, 78, 88, 91
Alumina, 120
Analytical methods of definition of thermal stresses, 13
Anisotropy, 3, 51, 101, 115, 117, 129, 135
  effect on thermal stress resistance, 3, 155
  of strength, 164

Bearing capacity, 65, 76, 85, 107, 111, 128, 182, 185
Bio criterion, 42, 63
Boundary conditions, 14, 24, 158, 171

Calculation of thermal stresses
  for bodies with a volumetric heat generation, 18
  for bodies with temperature dependent, 20
  for finite size body, 171, 185
  for quenched bodies, 104
Carbon inclusions, 131, 132, 134–137, 211
Ceramic materials, 1, 2, 9, 37, 52, 195, 199, 216
  borides, 2, 111, 112
  carbides, 2, 133, 135, 190, 193, 200, 201
  mono-phase, 101, 115, 117, 118, 121, 125, 130, 133, 135, 182, 200, 207, 210–212
  nitrides, 2, 131, 142, 196, 198, 200, 221
  oxides, 120, 127, 129–131, 141, 142, 195, 198, 199
Characteristic of test methods, 66
Combined force and thermal loading, 107
Complete fragmentations, 10–12, 87, 106, 108, 111, 161, 184, 212
Composites
  heterogeneous
    with carbon inclusion, 131, 132, 134
    with functionally gradient materials, 145
    with metal inclusions, 119, 143, 145
Computation of thermal stresses in construction elements of atomic reactors, 18
Convective heat transfer, 33, 35, 100
Corrosion, 1, 55, 56, 65, 190, 216
Crack
  growth, 7–11, 38, 70, 72, 74, 108, 110, 117, 212, 217
  initiation, 11, 127, 212
  interaction, 11, 70, 72, 75, 111, 125, 128, 129, 206
  reorientation, 128, 207
Creep
  creep kinetics, 218
Creep rate *versus* stress, 220
Creep rupture, 220

Criterion
of bearing capacity, 182
of comparative estimation of thermal resistibility, 179
Criterion Fourier, 82
Cyclic thermal loading, 56, 115, 119, 140

Damage, 85, 96, 122, 127, 148–150, 172, 174
Damage of plastic coating, 150
Dependence of rupture life on temperature, Design estimates of thermal stress resistance criterion, 111
Destructive and non-destructive ways of rejection, 200
Determination of heat resistance by cooling in water, 41
Developed technology for manufacture of ceramics, 190
Diffusion, 193, 194, 203, 206
Dislocations, 172, 189, 198, 206, 214, 219
Dispersion of the physical–mechanical properties, 33
Displacement of surface, 176
Distribution of residual deformation, 176

Effect on thermal stress resistance, 136, 180
of carbon inclusions, 136
of effective surface energy, 181
of elastic stress state, 20, 30
of physical–mechanical characteristics, 179
of porosity, 125
Elastic–brittle fracture, V
Elastic–plastic calculation, 26
Elements of a force optics, 1
Energy
energy for crack spreading, X
energy fracture model, 78
release, 9, 80
release rate, 8
Environmental effects, 3
Equilibrium propagation of cracks, 11, 183

Failure, 40, 46–50, 52, 53, 55, 56, 60, 61, 64, 94, 210, 221
Fatigue
fatigue mechanisms, 115
Features of sapphire fracture, 160, 166
Finite element method
program ANSIS, 36
Flaws, 3, 6, 76, 115, 125, 136, 210
Force fracture mechanics, 10, 11, 184
Formation of residual stresses, 99, 102, 105, 129, 195
Fracture
fracture character, 81, 82, 86, 87, 127, 141, 153, 182, 185
fracture complete, 91, 95, 141, 182, 184
fracture condition, 166
fracture kinetics, 10, 74
fracture mechanics, 6, 11, 87, 166, 167, 185
fracture of coatings, 151
fracture partial, 7, 10, 184
fracture pattern of sapphire, 166
fracture surface, 82, 133, 157, 192
fracture toughness, 41, 46, 70, 76, 101, 122, 127–130, 137, 139, 142–144, 157, 160, 164, 183, 190, 198, 206–209
fracture view, 10, 87
Fragmentation, 67, 76, 111, 133, 212
Fuel elements, 18, 19, 147, 148

Glass, 53, 99, 196, 197
Grain size, 101, 121, 123, 190, 199, 200, 215, 219
Graphite, 10, 35, 43, 48, 49, 55, 63, 64, 131–133, 135
Growth of cracks, 38, 107, 212

Healing of cracks, 190, 192, 193
in ceramic, 192
in sapphire, 194
Heat transfer, 13–17, 22, 32–35, 42–44, 52, 64, 78, 85, 89, 103, 104, 148, 157, 158
by radiation, 14, 103
in boiling water, 22, 36, 42, 44, 46
in liquid media, 22, 42, 45, 46, 78, 104, 157

High-temperature, V, 1, 2, 49, 52, 61, 105, 131, 144, 147, 189, 198
Homogenising and recrystallization annealing, hydrides, 199

Improvement
  of mechanical characteristics, 189
  of thermal stress resistance, V, 1, 3, 103, 105, 113, 120, 125, 126, 130, 131, 144
Impurities, 2, 121, 125, 199
Inclusions, 101, 115, 125, 127, 129, 135
Indentation, 75, 164, 208, 209, 214
Influence, 121, 213
  of grain size, 121, 213
  of manufacturing, 190
  of temperature on thermal stress, 111
  preparation technology of hydrides, 191
Instability of an optical surface, 177
Integrated temperature difference, 15, 16, 109, 157
Interaction of cracks, 10, 111, 125

Kinetics of fracture, 109, 185

Limit equilibrium of cracks, 67
Loading history, 76
Loading velocity, 3, 113
Local heating, 92
Long term loading, 103
Long-term strength, 221

Macrocracks, 11, 67, 75, 76, 208
Measurement of residual stresses, 99, 100
Method for testing, 49
  by induction heating, 64
  by plasma heating, 55
  in a gas stream, 47, 52
  in molten salts and metals, 53
  of cylinders and disks, 49
  of prismatic specimens, 51
  with use of focusing mirrors, 61
Micro-scopic structure, 123, 126, 145
Microhardness, 75, 213
Micromechanical fracture models, 128
Microplasticity, 3, 113, 115, 209, 212
Mixed form of fracture, 87

Modelling, 102
  of residual stress formation in operating conditions, 102
  of the origination of residual stresses, 102

Non-uniform fields of thermal stresses, 67
Non-uniform local stress fields, V
Nondestructive testing techniques, 42
Numerical calculation of residual stresses, 103

Optimization of structural parameters, 189

Parameter, 185, 195
  of a stressed state of body N, 185
  of crack healing, 195
  of fracture mode, 92
  of heterogeneity, 183, 184
Plain stress state, 21, 26
Plane problem, 18
Plastic deformation, 21, 78, 81
Porous ceramics, 127, 211
Powder metallurgy, 2, 15, 190, 199, 206, 216
Probability of brittle fracture, 6
Problems of thermal stress resistance, 4
Process of healing, 193
Property
  mechanical characteristics
    bending, 6, 197
    compression, 180, 197
    hardness, 2, 203, 206
    modulas of elasticty, 74, 98, 152, 159
    tension, 6, 197
    torsion, 6, 197
  thermal characteristics
    coefficient of heat transfer, 16
    coefficient of linear expansion, 33, 130
    melting point, 54, 203
    thermal conductivity, 19, 20, 88, 159

Quantitative assessment of thermal stress resistance, 5, 13
Quantitative evaluations of the heat resistance, 46

Quenching, 7, 44, 105, 156, 161, 195, 197
Quenching hardening, 195

R-curves, 9, 101, 102, 128, 141, 209
Rearrangement of stresses, 70
Recrystallization annealing, 199
Refractory materials, 3, 27, 62
Regularity of the strength and fracture, 4
Regularity of thermal stress resistance with temperature, 111
Residual displacement, 176
Residual stresses, of technological origin, 98

Spalling, 39, 54, 94, 96, 100, 151, 155
Statistical concepts of strength, 6
Statistical estimates of strength, 6
Steady cracking motion, 9
Stoichiometric composite affects, 2
Strength, 2, 3, 5, 6, 13, 30, 32, 33, 35, 37, 38
Stress, 122
  concentration, 122, 125, 134, 135
  field, 3, 10, 13, 33, 56, 60, 61, 63, 85, 106, 168, 208
  intensity factor, 7, 209, 216
  relaxation, 3, 28, 30, 41, 113, 114, 144, 162, 186, 198
Structural anisotropy, 101, 117, 126, 155
Structural defects, 2, 189, 212
Surface residual stresses, 100, 106

Technological expedients, V, 2, 152
Temperature dependence, 111
  of criterion of thermal stress resistance, 111
  of strength, 112, 124, 138
Temperature fields, 13, 15, 22, 24, 31, 34, 40, 49, 51
Temperature gradients, 3, 14, 68, 98, 103
Thermal elasticity, 13, 17, 18, 24, 55, 103, 157
Thermal loading modes, V, 5, 85
Thermal stress resistance, 2, 3, 5
  at local radiation heating, 30
  criteria, 179
  improvement, 120, 131, 136, 144
  of anisotropic materials, 155
  of composites with metal inclusions, 119, 143
  of fissured materials, 113, 140
  of functionally graded materials, 145
  of sapphire, 156, 163, 164, 166
Thermal stress resistance testing, 39, 64
Thermal stresses, 1–3, 5, 16, 18, 19
  for specimens of finite sizes, 30
  for thermally loaded end surface, 89
Thermo-mechanical hardening, 197
Transformation strengthening, 115, 199
Twinning, 160–162, 166, 167, 207, 214

Unstable crack, 7, 9–11, 75
  development and propagation, 8, 9, 67, 71, 75

Variation coefficient of thermal stress resistance, 89, 127
Variation of stress state, 91

Weibull's theory, 6

X-ray $\sin^2\psi$ method, 100, 104, 105, 107, 166